Flexible aircraft flight dynamics and loads model identification

from flight test data including unsteady aerodynamic effects

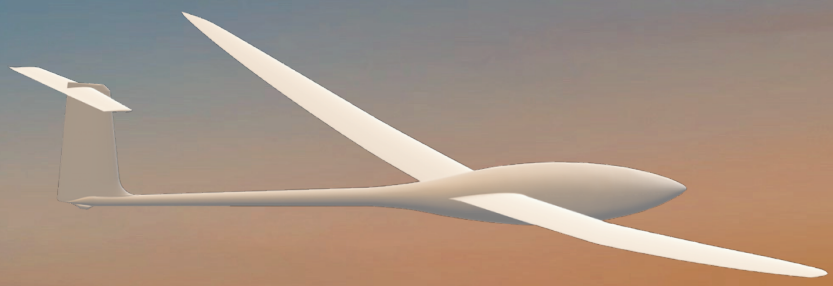

Andres Jürisson

Flexible aircraft flight dynamics and loads model identification from flight test data including unsteady aerodynamic effects

Flexible aircraft flight dynamics and loads model identification from flight test data including unsteady aerodynamic effects

Dissertation

for the purpose of obtaining the degree of doctor
at Delft University of Technology,
by the authority of the Rector Magnificus Prof. dr. ir. H. Bijl,
chair of the Board for Doctorates,
to be defended publicly on Monday, 1 June 2026 at 15:00

by

Andres JÜRISSON

This dissertation has been approved by the promotors.

Composition of the doctoral committee:

Rector Magnificus,	chairperson
Prof. dr. ir. R. De Breuker,	Delft University of Technology, *promotor*
Dr. ir. C.C. de Visser,	Delft University of Technology, *promotor*
Independent members:	
Prof. dr. T. Keviczky,	Delft University of Technology
Prof. dr. C.E. Cesnik,	University of Michigan, USA
Prof. Dr.-Ing. W.R. Krüger,	Technical University Berlin and German Aerospace Center, Germany
Prof. Dr.-Ing. F.J. Silvestre,	Technical University Berlin, Germany
Prof. dr. ir. M. Mulder,	Delft University of Technology, *reserve member*
Other members:	
Ir. B.J.G. Eussen,	Royal Netherlands Aerospace Centre

Keywords: aeroelasticity, flight testing, system identification,

Printed by: Ipskamp Printing

Front and back: Andres Jürisson and Iida Kaisa Urm

ISBN 978-94-6384-965-4

An electronic copy of this dissertation is available at
https://repository.tudelft.nl/.

CONTENTS

SUMMARY

To reduce emissions and improve efficiency, modern aircraft designs are moving towards higher aspect ratios and lighter materials. While these design choices enhance performance, they also result in more flexible aircraft structures. This flexibility leads to greater interaction between rigid body motion and structural dynamics. Accurate modelling of these interactions is critical for evaluating aircraft handling qualities, predicting structural loads, tuning control laws for stability and performance, and developing simulators for pilot training.

System identification techniques provide a means to derive these models from flight test measurements. State-of-the-art system identification methods successfully capture the effects of structural dynamics. However, they rely on the assumption of (quasi-) steady aerodynamics. In steady aerodynamic models, changes in parameters such as angle of attack or control surface deflections are assumed to result in instantaneous changes in aerodynamic forces and moments. In reality, due to wake effects from unsteady aerodynamics, these forces and moments take time to develop, introducing delays in the response. Accurately capturing these delays is crucial for correctly predicting and modelling the aircraft's dynamic behaviour. Failure to account for unsteady aerodynamics can lead to errors in load predictions, degraded handling quality assessments, and suboptimal control law design.

This dissertation develops a methodology for identifying a parametric flight dynamics and loads model from flight test measurements for a flexible aircraft that also include the effects of structural dynamics and unsteady aerodynamics. A two-step approach was adopted where the identification procedure consists of separate state estimation and parameter estimation steps. This allowed to perform model parameter estimation using a linear least squares approach. In contrast, alternative methods such as the output-error approach perform state estimation and model parameter estimation in a single nonlinear optimisation process. While this method can provide accurate results, it requires accurate initial parameter estimates to achieve convergence and a good fit, and it imposes a significantly higher computational load, making it less efficient for larger and more complex models.

A scaled Diana 2 glider unmanned aerial vehicle (UAV) was used as the flight test platform in this research. Using a UAV allowed to conduct flight testing with much fewer rules and regulations compared to full-scale aircraft testing, while also significantly lowering costs. A glider configuration was selected due to its high aspect ratio and flexible structure, making it well-suited for studying aeroelastic effects. Furthermore, the flight tests could be conducted at airspeeds and reduced frequencies corresponding to unsteady aerodynamic conditions,

ensuring that unsteady aerodynamic effects are present in measured responses.

The aircraft needed to be instrumented to measure both its rigid body and structural responses. A custom-built data acquisition system (DAQ) was developed and integrated into the aircraft. The system was designed to be low-cost and accessible, using widely available consumer electronic sensors and leveraging open-source Robot Operating System (ROS) software. This approach improves accessibility to aeroelastic flight testing and is highly customisable. To ensure accurate and meaningful measurements, all sensors underwent careful calibration. Calibration procedures included wind tunnel tests for the aeroprobe, load tests for strain gauges with temperature bias corrections, inertial measurement unit (IMU) alignment tests, and actuator model identification.

Flight tests were conducted using a range of excitation manoeuvres to capture the aircraft's response under various conditions. Tests were performed at airspeeds that maximised the influence of unsteady aerodynamics to ensure the most significant deviations from steady aerodynamic assumptions. The data acquisition system was capable of collecting over 130 different response signals during flight, with some sensors reaching sampling rates above 400 Hz.

To determine the structural properties and modal parameters of the scaled Diana 2 UAV, a ground vibration test (GVT) was conducted. The aircraft was elastically suspended and excited using a modal hammer at multiple locations while acceleration, rotational rate, and strain responses were recorded across the aircraft structure. From these measurements, the modal frequencies, damping and mode shapes of the Diana 2 were estimated. The acceleration, rotational rate, and strain responses were used together as well as individually to evaluate their accuracy in the modal analysis process. The obtained results were validated by comparing them to a reference high-end system, which also served to verify the accuracy of the integrated DAQ. The results showed that the modal estimates obtained with the custom DAQ closely matched those derived from the reference system, confirming its accuracy and sensitivity.

Using different types of sensors together for estimation resulted in mode shapes that included displacement, rotation, and strain responses. This allowed for a more detailed overview of the vibration modes. Specifically, this approach provided better insight into how strains corresponded to displacements, while gyroscope data improved the capture of twisting motions without requiring additional accelerometers. This could lead to faster testing times for large aircraft as less setup is required and improved fitting of aircraft structural models through additional data from rotational and strain mode shapes.

To estimate the states of a flexible aircraft, the flight path reconstruction (FPR) approach was extended to also account for structural dynamics. The developed method is based on the Extended Kalman Filter and uses the additional measurements from accelerometers, gyroscopes, and strain gauges, combined with the structural mode shapes, to estimate the states related to aircraft rigid-body motion together with modal amplitude and velocity states. This approach was formulated based on flexible aircraft kinematic equations, making it applicable to various aircraft configurations. A significant advantage of this

approach is that it enables the estimation of modal states without requiring an aeroelastic flight dynamics model or high-resolution strain measurements.

A simulation study, where the true model states were known, demonstrated that the filter could accurately estimate these states from noisy measurements. The accuracy and consistency of the modal state estimates were confirmed, showing insensitivity to the number of modes included in the filter and robustness to random errors in the provided mode shapes. The filter was then applied to the scaled Diana 2 UAV flight test measurements. The estimated rigid body states were compared with results from a traditional FPR filter, showing close agreement. Modal state estimates remained consistent regardless of the number of modes included, and the addition of structural modes reduced the error in gyro and strain response predictions across the aircraft. The filter was also capable of identifying consistent sensor biases, particularly in the aeroprobe measurements.

A limitation of the approach was observed in capturing local wing torsion deformations resulting from aileron deflections. This limitation was due to the use of global vibration mode shapes, which could not represent local deformation effects. Future enhancements to the filter could include incorporating local mode shapes to improve estimation accuracy. Overall, the developed filter provided reliable estimates of modal amplitude and velocity states, making them available for direct use in parameter estimation of flexible aircraft models.

To include the effects of delays and response amplitude changes caused by unsteady aerodynamics in the identified models, a correlation-based approach was developed to estimate aerodynamic lag poles directly from flight test measurements. These poles define the dynamics of aerodynamic lag states that are used to model unsteady aerodynamics. The developed method was applied to the scaled Diana 2 flight test manoeuvres, and the identified poles closely matched values predicted by aeroelastic numerical theory, validating the approach.

Using the collected flight test responses and the filtered state estimates, flight dynamics and loads models were identified. The identified models included rigid body force and moment coefficients, generalised forces corresponding to structural modes, and loads models for wing root bending, torsion moments, and tail loads. Two models were developed: a rigid model, constructed using only parameters related to rigid body responses, and a flexible model, which also included structural modes and aerodynamic lag states. The inclusion of these flexible dynamics and aerodynamic lag states improved the accuracy of model fitting, with the most notable improvement seen in the roll moment coefficient due to the addition of aerodynamic lag term associated with aileron deflections. This result emphasised the importance of including unsteady aerodynamics in the identification process to be able to accurately capture the aircraft responses.

To ensure model stability and prevent self-exciting modes, constraints were introduced during the fitting of generalized force coefficients. Finally, the identified models were validated through open-loop simulations, demonstrating good agreement with flight test measurements and numerical simulation model predictions. The results showed that the identified models could accurately

predict rigid body motions, structural dynamic responses, and external loads and that the identification process was able to accurately estimate and model the modal states from flight test measurements.

This dissertation resulted in the publication of an open-access dataset that includes aeroelastic flight test data, modelling results, and calibration test outcomes. The availability of this dataset increases the accessibility of aeroelastic flight data for future research. Along with the data, scripts related to the DAQ setup are provided, allowing other researchers to adapt and customise their own flight test systems, potentially leading to the creation of more open-access datasets in the future.

Recommendations for future work include further development of the flight test platform to improve reliability and implementing an automatic excitation system to allow for advanced excitation manoeuvres, such as orthogonal multisines, and increase the reproducibility of the tests. Advancements in the identification framework are also suggested, including the exploration of more flexible test configurations and incorporating nonlinearities. Additionally, working towards eliminating the need for a separate ground vibration test by using operational modal analysis methods could simplify future model identification efforts and allow for continuous identification and aircraft structural health monitoring. Finally, the identified models could be used to synthesise load alleviation control laws for the scaled Diana 2 glider, allowing for in-flight evaluation of model accuracy and assessing their feasibility for control law design and implementation.

SAMENVATTING

Om de emissies te verminderen en de efficiëntie te verbeteren, gaan moderne vliegtuigontwerpen steeds meer in de richting van hogere vleugelslankheden en lichtere materialen. Hoewel deze ontwerpkeuzes de prestaties verbeteren, resulteren ze ook in flexibelere vliegtuigstructuren. Deze flexibiliteit leidt tot meer interactie tussen bewegingen van starre lichamen van het vliegtuig en structurele dynamica. Nauwkeurige modellering van deze interacties is essentieel voor het evalueren van de bestuurbaarheid van vliegtuigen, het voorspellen van structurele belastingen, het afstemmen van de besturingswetten voor stabiliteit en prestaties en het ontwikkelen van simulatoren voor de training van piloten.

Systeemidentificatietechnieken bieden de mogelijkheid om deze modellen af te leiden uit metingen van testvluchten. De nieuwste systeemidentificatiemethoden vangen met succes de effecten van structurele dynamica. Ze gaan echter uit van een (quasi-) stabiele aerodynamica. In stabiele aerodynamische modellen wordt aangenomen dat veranderingen in parameters zoals invalshoek of doorbuigingen van het stuurvlak resulteren in onmiddellijke veranderingen in aerodynamische krachten en momenten. In werkelijkheid, als gevolg van de instabiele aerodynamica, hebben deze krachten en momenten tijd nodig om zich te ontwikkelen, waardoor vertragingen in de respons ontstaan. Het nauwkeurig vastleggen van deze vertragingen is cruciaal voor het correct voorspellen en modelleren van het dynamische gedrag van het vliegtuig. Als er geen rekening wordt gehouden met de instabiele aerodynamica, kan dit leiden tot fouten in de voorspellingen van de belasting, een slechtere beoordeling van de kwaliteit van de besturing en een suboptimaal ontwerp van de besturingswet.

Dit proefschrift ontwikkelt een methodologie voor het identificeren van een parametrisch vluchtdynamica- en belastingsmodel uit testvluchten voor een flexibel vliegtuig, waarin ook de effecten van structurele dynamica en instabiele aerodynamica zijn opgenomen. Er is gekozen voor een tweestapsbenadering waarbij de identificatieprocedure bestaat uit afzonderlijke stappen voor het schatten van de staat en het schatten van de parameters. Dit maakte het mogelijk om modelparameterschattingen uit te voeren met behulp van een lineaire kleinste kwadratenmethode. Alternatieve methoden, zoals de output-error benadering, voeren de schatting van de staat en de schatting van de modelparameters daarentegen uit in één niet-lineair optimalisatieproces. Hoewel deze methode nauwkeurige resultaten kan opleveren, zijn er nauwkeurige initiële parameterschattingen nodig om convergentie en een goede fit te bereiken en is de rekenbelasting aanzienlijk hoger, waardoor deze methode minder efficiënt is voor grotere en complexere modellen.

Een onbemand Diana 2 zweefvliegtuig op schaal (UAV) werd gebruikt

als platform voor testvluchten in dit onderzoek. Het gebruik van een UAV maakte het mogelijk om testvluchten uit te voeren met veel minder regels en voorschriften in vergelijking met het testen van vliegtuigen op volledige schaal, terwijl ook de kosten aanzienlijk verlaagd werden. Er werd gekozen voor een zweefvliegtuigconfiguratie vanwege de hoge hoogte-breedteverhouding en flexibele structuur, waardoor het heel geschikt is voor het bestuderen van aero-elastische effecten. Bovendien konden de testvluchten worden uitgevoerd bij luchtsnelheden die overeenkomen met instabiele aerodynamische omstandigheden, zodat instabiele aerodynamische effecten aanwezig zijn in de gemeten respons.

Het vliegtuig moest worden uitgerust met instrumenten om zowel de stijfheid van het lichaam als de structurele respons te meten. Er werd een op maat gemaakt data-acquisitiesysteem (DAQ) ontwikkeld en geïntegreerd in het vliegtuig. Het systeem werd ontworpen om goedkoop en toegankelijk te zijn, met behulp van algemeen verkrijgbare elektronische consumentensensoren en gebruikmakend van open-source Robot Operating System (ROS) software. Deze aanpak verbetert de toegankelijkheid van aero-elastische testvluchten en is in hoge mate aanpasbaar. Om nauwkeurige en zinvolle metingen te garanderen, werden alle sensoren zorgvuldig gekalibreerd. De kalibratieprocedures omvatten windtunneltests voor de aeroprobe, belastingtests voor rekstrookjes met temperatuurcorrecties, uitlijningstests voor de traagheidsmeeteenheid (IMU) en identificatie van het actuatormodel.

Er werden testvluchten uitgevoerd met een reeks excitatiemanoeuvres om de reactie van het vliegtuig onder verschillende omstandigheden vast te leggen. De tests werden uitgevoerd bij luchtsnelheden die de invloed van de instabiele aerodynamica maximaliseerde, om de grootste afwijkingen van de stabiele aerodynamische aannames te verkrijgen. Het data-acquisitiesysteem was in staat om meer dan 130 verschillende responssignalen te verzamelen tijdens de vlucht, waarbij sommige sensoren samplingsnelheden bereikten van meer dan 400 Hz.

Om de structurele eigenschappen en modale parameters van de Diana 2 UAV te bepalen, werd een grondtrillingstest (GVT) uitgevoerd. Het vliegtuig werd elastisch opgehangen en op verschillende plaatsen aangeslagen met een modale hamer terwijl versnelling, rotatiesnelheid en rekresponsen werden geregistreerd over de hele vliegtuigstructuur. Uit deze metingen werden de modale frequenties, demping en modusvormen van Diana 2 geschat. De versnellings-, rotatie- en rekresponsen werden zowel samen als afzonderlijk gebruikt om hun nauwkeurigheid in het modale analyseproces te evalueren. De verkregen resultaten werden gevalideerd door ze te vergelijken met een high-end referentiesysteem, wat ook diende om de nauwkeurigheid van het op maat gemaakte data-acquisitiesysteem te verifiëren. De resultaten toonden aan dat de modale schattingen, verkregen met de aangepaste DAQ, nauw overeenkwamen met die van het referentiesysteem, wat de nauwkeurigheid en gevoeligheid bevestigt.

Het gebruik van verschillende soorten sensoren samen voor de schatting resulteerde in modusvormen die verplaatsings-, rotatie- en rekrespons omvatten.

Dit maakte een gedetailleerder overzicht van de trillingsmodes mogelijk. Specifiek gaf deze aanpak een beter inzicht in hoe vervormingen overeenkwamen met verplaatsingen, terwijl gyroscoopgegevens het vastleggen van draaiende bewegingen verbeterden zonder dat er extra versnellingsmeters nodig waren. Dit zou kunnen leiden tot snellere testtijden voor grote vliegtuigen omdat er minder instellingen nodig zijn en een betere passing van vliegtuigstructurele modellen door aanvullende gegevens van rotatie- en rekmodusvormen.

Om de toestanden van een flexibel vliegtuig te schatten, werd de vliegbaanreconstructie (FPR) uitgebreid om ook rekening te houden met structurele dynamica. De ontwikkelde methode is gebaseerd op het Extended Kalman Filter en gebruikt de aanvullende metingen van versnellingsmeters, gyroscopen en rekstrookjes, gecombineerd met de structurele modusvormen, om de toestanden te schatten die gerelateerd zijn aan de starre-lichaamstoestanden van het vliegtuig, samen met de modale amplitude en snelheidstoestanden. Deze benadering is geformuleerd op basis van flexibele kinematische vergelijkingen voor vliegtuigen, waardoor het toepasbaar is op verschillende vliegtuigconfiguraties. Een belangrijk voordeel van deze aanpak is dat het de schatting van modale toestanden mogelijk maakt zonder dat een aero-elastisch vluchtdynamicamodel of hoge-resolutie vervormingsmetingen nodig zijn.

Een simulatiestudie, waarbij de ware model staten bekend waren, toonde aan dat het filter deze toestanden nauwkeurig kon schatten uit ruismetingen. De nauwkeurigheid en consistentie van de schattingen van de modale staten werden bevestigd, waarbij ongevoeligheid voor het aantal modi in het filter en robuustheid voor willekeurige fouten in de aangeleverde modusvormen werd aangetoond. De filter werd vervolgens toegepast op de geschaalde Diana 2 UAV testvluchten. De geschatte staten van de starre lichamen werden vergeleken met de resultaten van een traditionele FPR filter, met een goede overeenkomst. De schattingen van de modale staten bleven consistent ongeacht het aantal opgenomen modi en de toevoeging van structurele modi verminderde de fout in gyroscoop- en rekresponsvoorspellingen voor het hele vliegtuig. Het filter was ook in staat om consistente sensorvertekeningen te identificeren, met name in de aeroprobe-metingen.

Een beperking van de benadering werd waargenomen in het vastleggen van lokale vleugeltorsievervormingen als gevolg van rolroeruitslagen. Deze beperking was te wijten aan het gebruik van globale trillingsmodevormen, die de lokale vervormingseffecten niet konden weergeven. Toekomstige verbeteringen aan het filter zouden kunnen bestaan uit het opnemen van lokale modusvormen om de schattingsnauwkeurigheid te verbeteren. Over het geheel genomen leverde het ontwikkelde filter betrouwbare schattingen van modale amplitude en snelheidsstaten, waardoor ze beschikbaar zijn voor direct gebruik in parameterschattingen van flexibele vliegtuigmodellen.

Om de effecten van vertragingen en responsamplitudeveranderingen veroorzaakt door instabiele aerodynamica op te nemen in de geïdentificeerde modellen, werd een correlatiegebaseerde aanpak ontwikkeld om aerodynamische vertragingspolen rechtstreeks uit testvluchten te schatten. Deze polen definiëren

de dynamica van aerodynamische vertragingstoestanden die worden gebruikt om de instabiele aerodynamica te modelleren. De ontwikkelde methode werd toegepast op de manoeuvres van de Diana 2 testvluchten en de geïdentificeerde polen kwamen nauw overeen met de waarden die voorspeld werden door de aero-elastische numerieke theorie, wat de aanpak valideert.

Met behulp van de verzamelde testvluchten en de gefilterde toestandsschattingen werden vluchtdynamica- en belastingsmodellen geïdentificeerd. De geïdentificeerde modellen omvatten kracht- en momentcoëfficiënten voor starre lichamen van het vliegtuig, gegeneraliseerde krachten die overeenkomen met structurele modi en belastingsmodellen voor buiging van de vleugelwortel, torsiemomenten en staartbelastingen. Er werden twee modellen ontwikkeld: een star model, geconstrueerd met alleen parameters die betrekking hebben op de reacties van starre lichamen, en een flexibel model, dat ook constructiemodi en aerodynamische achterlooptoestanden omvatte. Het opnemen van deze flexibele dynamica en aerodynamische vertragingstoestanden verbeterde de nauwkeurigheid van de modelpassing, waarbij de meest opmerkelijke verbetering werd gezien in de rolmomentcoëfficiënt door de toevoeging van de aerodynamische vertragingsterm in verband met rolroerafbuiging. Dit resultaat benadrukte het belang van het opnemen van instabiele aerodynamica in het identificatieproces om de respons van het vliegtuig nauwkeurig te kunnen vastleggen.

Om de stabiliteit van het model te garanderen en zelfexciterende modi te voorkomen, werden beperkingen geïntroduceerd tijdens de aanpassing van de gegeneraliseerde krachtcoëfficiënten. Tot slot werden de geïdentificeerde modellen gevalideerd door middel van open-loop simulaties, waarbij goede overeenstemming werd aangetoond met testvluchten en voorspellingen van numerieke simulatiemodellen. De resultaten toonden aan dat de geïdentificeerde modellen nauwkeurig bewegingen van het starre lichaam, structurele dynamische reacties en externe belastingen konden voorspellen en dat het identificatieproces in staat was om de modale staten van testvluchten nauwkeurig in te schatten en te modelleren.

Dit proefschrift resulteerde in de publicatie van een open-access dataset met aero-elastische testvluchten, modelresultaten en resultaten van kalibratietesten. De beschikbaarheid van deze dataset vergroot de toegankelijkheid van aero-elastische vluchtdata voor toekomstig onderzoek. Samen met de gegevens worden scripts met betrekking tot de DAQ-opstelling geleverd, zodat andere onderzoekers hun eigen testvluchten kunnen aanpassen, wat in de toekomst kan leiden tot de creatie van meer open-access datasets.

Aanbevelingen voor toekomstig werk zijn onder andere de verdere ontwikkeling van het testvluchtenplatform om de betrouwbaarheid te verbeteren en de implementatie van een automatisch excitatiesysteem om geavanceerde excitatiemanoeuvres mogelijk te maken, zoals orthogonale multisinus, en de reproduceerbaarheid van de tests te vergroten. Er worden ook verbeteringen in het identificatieraamwerk voorgesteld, waaronder het onderzoeken van flexibelere testconfiguraties en het opnemen van niet-lineariteiten. Bovendien zou het werken aan het elimineren van de noodzaak voor een aparte grondtrillings-

test door het gebruik van operationele modale analysemethoden toekomstige modelidentificatie-inspanningen kunnen vereenvoudigen. Tenslotte kunnen de geïdentificeerde modellen gebruikt worden om belastingsverlagende controlewetten te ontwikkelen voor het Diana 2 zweefvliegtuig op schaal, waardoor de nauwkeurigheid van de modellen tijdens de vlucht geëvalueerd kan worden en hun haalbaarheid voor het ontwerp en de implementatie van controlewetten beoordeeld kan worden.

NOMENCLATURE

LIST OF SYMBOLS

A_x, A_y, A_z	Aircraft centre of gravity accelerations
$\boldsymbol{A^b_{xyz}}$	Vector of accelerations in aircraft body frame
$\boldsymbol{A^S_{xyz}}$	Vector of accelerations in sensor frame
$\boldsymbol{A_N}$	Vector of measured accelerations
$\boldsymbol{A_0}$, $\boldsymbol{A_1}$, $\boldsymbol{A_2}$, $\boldsymbol{A_{2+i}}$	Aerodynamic matrices for rational function approximation
$\boldsymbol{A_{lag}}$	Aerodynamic matrix for lag state contributions in RFA
b	Wing span
$\bar{b}$	Semi-chord
$\bar{c}$	Mean chord
$\boldsymbol{C}$	Damping matrix
C_D	Drag coefficient
C_L	Lift coefficient
C_Q	Generalised force coefficient
C_X, C_Y, C_Z	Aerodynamic force coefficient
C_l, C_m, C_n	Aerodynamic moment coefficient
C_l^{AC}, C_m^{AC}, C_n^{AC}	Moment coefficient around aerodynamic centre
C_l^{CG}, C_m^{CG}, C_n^{CG}	Moment coefficient around centre of gravity
C_F^*, C_M^*	External force and moment load coefficients
C_α, C_β	Aeroprobe calibration coefficients for AoA and AoS
C_{e0}, C_{e1}, C_{e2}	Elevator angle calibration coefficients
d	Distance between swing suspension points
$\boldsymbol{F}$	Frequency spectrum of input force
$\boldsymbol{f}$	Excitation forces
g	Gravitational acceleration
G	Transfer function of actuator model
G_{GF}	Gauge factor
$\boldsymbol{G_k}$	Combined modeshape matrix
h	Heave degree of freedom for a typical section
H	Magnetic field strength
$\boldsymbol{H}$	Frequency response matrix
$\boldsymbol{H^\epsilon}$	Strain frequency response matrix
$\boldsymbol{H_k}$	Rotational modeshape matrix
I_x, I_y, I_z, I_{xz}	Aircraft moments of inertia
$\boldsymbol{I}$	Identity matrix
k	Reduced frequency
$\boldsymbol{K_s}$	Structural stiffness matrix
l	Distance between swing axis and centre of gravity
L_{ext}	External load on aircraft structure

m	Aircraft mass
m_i	Generalised mass for mode i
$\boldsymbol{M_s}$	Structural mass matrix
p, q, r	Aircraft rotational rates
p_i	Aerodynamic lag state pole
$\boldsymbol{Q}$	Generalised force
$\bar{q}$	Dynamic pressure
$\boldsymbol{r}$	Sensor distance to aircraft centre of gravity
S	Aircraft wing area
$\hat{S}_{yu}$, $\hat{S}_{uu}$	Cross-spectrum and input power spectrum estimate
T	Measured temperature
T_d	Time delay in actuator models
$T_{b\alpha}$	Transformation matrix from aerodynamic to body frame
T_{Eb}	Transformation matrix from body to Earth frame
T_{ref}	Reference temperature
$\boldsymbol{T_{bS}}$	Transformation matrix from sensor to body frame
u, v, w	Aircraft body velocities
u_i	Aerodynamic lag state input
$\boldsymbol{U}$	Vector of system inputs
V	Airspeed
V^{α}_{probe}	Airspeed measured by Aeroprobe
V^{E}_{GPS}	Aircraft velocity measured by GPS
V_m	Voltage difference across strain gauge
V_{ref}	Strain gauge excitation voltage
$\boldsymbol{v}$	Vector of measurement noise
v_*	Measurement noise
w	Beam out-of-plane displacement
$\boldsymbol{w}$	Vector of process noise
$\boldsymbol{W^E}$	Wind speed vector in Earth frame
x, y, z	Aircraft position
x^*_{lag}	Aerodynamic lag state
$\boldsymbol{x}$	State vector
$\boldsymbol{x_{lag}}$	Aerodynamic lag state vector
$\boldsymbol{X_{reg}}$	Regression matrix
$\boldsymbol{X}$	Frequency spectrum of displacement responses (Chap. 3)
$\boldsymbol{X}$	Vector of system states
$\boldsymbol{X^{\epsilon}}$	Frequency spectrum of strain responses
$\boldsymbol{Y}$	Vector of system outputs
$\boldsymbol{y}$	Vector of true states
$\bar{\boldsymbol{y}}$	Vector of predicted responses
$\boldsymbol{z}$	Measurement vector

GREEK LETTERS

α	Angle of attack
β	Angle of sideslip
δ_a^{sym}, δ_a^{asym}	Symmetric and asymmetric aileron deflections
δ_e	Elevator deflection
δ_r	Rudder deflection
Δp_α	Pressure difference in α-channel
Δp_β	Pressure difference in β-channel
Δp_V	Pressure difference in airspeed channel
Δt	Sampling time
ΔX_{CG}, ΔY_{CG}, ΔZ_{CG}	Distance from aircraft's centre of gravity to aerodynamic centre
ϵ_0	Constant bias for strain-gauge bridge
ϵ_i	Calculated strain for sensor i
ϵ_k	Measured strain of sensor k
ϵ_T	Strain-gauge temperature gradient
ϵ_{max}	Maximum surface strain on a beam
ζ_n	Mode n damping ratio
η_n	Mode n amplitude
$\boldsymbol{\eta}$	Vector of modal amplitudes
θ_x, θ_y, θ_z	Sensor frame to aircraft body frame rotations
$\boldsymbol{\theta}$, $\hat{\boldsymbol{\theta}}$	Parameter vector and parameter estimate vector
ϑ	Beam-displacement derivative
κ	Wing curvature (Chap. 3)
κ	Matrix condition number (Chap. 4)
λ_{A_x}, λ_{A_y}, λ_{A_z}	Centre of gravity accelerometer biases
λ_α, λ_β	Aerodynamic angle biases
λ_G	Accelerometer scaling factor
λ_p, λ_q, λ_r	Centre of gravity rotational rate biases
$\boldsymbol{\lambda}$	Vector of biases
$\boldsymbol{\lambda_{A_{xyz}}}$	Vector of accelerometer biases
$\boldsymbol{\lambda_{\omega_{xyz}}}$	Vector of gyroscope biases
μ_i	Calibration coefficient for external loads
τ	Time constant for actuator model (Chap. 2)
τ	Swing-oscillation period (Chap. 3)
ϕ, θ, ψ	Aircraft Euler angles
$\boldsymbol{\Phi}$	Modeshape matrix
ψ_1, ψ_2	Jones's coefficients to Wagner function
$\boldsymbol{\Psi}$	Strain modeshape matrix
ω	Oscillation frequency
ω_n	Mode n frequency
$\boldsymbol{\omega^S}$	Vector of rotational rates in sensor frame
$\dot{\boldsymbol{\omega}}_{\boldsymbol{N}}$	Vector of measured rotational accelerations

SUBSCRIPTS AND SUPERSCRIPTS

CG	Centre of gravity
LI	Left wing, inner section
LM	Left wing, middle section
LO	Left wing, outer section
LTI	Left wingtip, inner sensor
LTO	Left wingtip, outer sensor
LWB	Left Wing Bending
LWT	Left Wing Torsion
PX	Pixhawk
RI	Right wing, inner section
RM	Right wing, middle section
RO	Right wing, outer section
RTI	Right wingtip, inner sensor
RTO	Right wingtip, outer sensor
RWB	Right Wing Bending
RWT	Right Wing Torsion
TL	Tail Lift
TS	Tail Side Force
TT	Tail Torsion
WB	Wing Bending
WT	Wing Torsion

ACRONYMS

ADC	Analog to Digital Converter
AoA	Angle of Attack
AoS	Angle of Sideslip
CFD	Computational Fluid Dynamics
DAQ	Data Acquisition System
DLM	Doublet Lattice Method
DOF	Degrees of Freedom
EMA	Experimental Modal Analysis
FEM	Finite Element Method
FES	Front Electric Self-launch
FPR	Flight Path Reconstruction
FRF	Frequency Response Function
GPS	Global Positioning System
GVT	Ground Vibration Testing
IMU	Inertial Measurement Unit
MAC	Modal Assurance Criterion
MEMS	Micro-electromechanical System
NLR	Royal Netherlands Aerospace Centre

OLS	Ordinary Least Squares
OMA	Operational Modal Analysis
RC	Radio Control
RFA	Rational Function Approximation
RMS	Root Mean Square
RMSE	Root Mean Square Error
RMS_{rel}	Relative Root Mean Square Error
ROS	Robot Operating System
RTK	Real-Time Kinematics
SFRF	Strain Frequency Response Function
SHM	Structural Health Monitoring
TIC	Theil's Inequality Coefficient
TSM	Two-Step Method
UAV	Unmanned Aerial Vehicle

1

INTRODUCTION

To improve aircraft fuel efficiency, modern aircraft wing designs are becoming longer, more slender, and are built using lightweight composite materials. These design changes result in increased structural flexibility and reduced natural frequencies of the aircraft. As a result, the aircraft rigid body mode frequencies move close to the structural modes which can lead to significant interactions between them [1].

Understanding and accurately modelling these interactions is crucial to ensuring aircraft safety, characterising handling qualities, assessing aerodynamic loads, and determining flight dynamic stability coefficients. Furthermore, precise modelling is also needed for the development of high-fidelity flight simulators for pilot training.

Accurate flight dynamics and load models of flexible aircraft are necessary for the synthesis and optimisation of advanced control systems. These systems include gust load alleviation, manoeuvre load alleviation, and flutter suppression systems, which are active areas of research due to their potential to enhance fuel efficiency and overall aircraft performance [2, 3].

The flight dynamics of and loads on a flexible aircraft are thoroughly studied during the aircraft design process. Traditional analysis methods often involve high-fidelity aerodynamic simulations, such as computational fluid dynamics (CFD), and lower-fidelity methods like the doublet lattice methods (DLM). Structural dynamics are typically modelled using finite element methods (FEM). These methods are based on first principles and produce detailed models that can include millions of elements and thousands of parameters. The results from these simulations are validated through structural, wind tunnel and flight testing.

To develop these numerical models, detailed information about the aircraft's geometry, structural layout, and material properties is required. However, such information might be unavailable, uncertain, or subject to change throughout the aircraft's operational life due to wear, repairs, or modifications. This can lead to inaccuracies in the predicted and actual aircraft behaviour. Therefore, a modelling approach based on aircraft flight response measurements would be required.

1

1.1. Aircraft System Identification

System identification methods can be applied to derive aircraft flight dynamics and loads models directly from collected flight test response measurements. System identification is a scientific discipline focused on constructing models of systems based on input and output data [4]. This process is typically divided into three key phases: model structure selection, parameter estimation, and model validation, which are iterated until the required accuracy criterion is met.

During the model structure selection phase, a specific mathematical framework for the model is chosen, along with the parameters to be estimated. This step may incorporate prior knowledge of the system's dynamics to guide model formulation. The selected model structures can vary widely, including polynomial representations of various orders, spline functions, and both parametric and non-parametric models. Klein and Morelli [5] state that an adequate model should fit the data well, enable the estimation of unknown parameters that can be justified by physical principles, and demonstrate strong predictive capabilities. To achieve these objectives, models are often designed to be parsimonious, striking a careful balance between simplicity and explanatory power by including only components that are essential to capturing the underlying physical phenomena [4, 5]. This results in models that are generally much smaller and more computationally efficient than those produced by traditional numerical methods.

The parameter estimation phase involves determining the values of the model's parameters by minimizing the differences between the measured responses and the model outputs. Both frequency-domain and time-domain methods are available for this step, each with their specific advantages and applications. Following parameter estimation, model validation assesses the model's accuracy, standard deviation of the estimated parameters, and model predictive capabilities. If the model fails to meet the established criteria, the model structure is adjusted, and the identification process is repeated [4]. System identification for flight mechanics and loads modelling is critical for flight testing and certification, and it has a long history supported by well-established methods in both the time-domain and frequency-domain [4, 6].

One of the most widely utilized techniques for aircraft flight dynamics system identification is the output error method [4], in which system model parameters are iteratively adjusted to minimize the difference between measured aircraft responses and model-predicted responses. This optimisation problem is nonlinear which can be computationally expensive and requires good initial parameter estimates to successfully converge to a desirable solution. The method assumes that noise is present only in the measured responses, while process noise, such as atmospheric disturbances, is considered negligible. Therefore, flight testing should be conducted in steady atmospheric conditions.

To account for both measurement and process noise, an additional state estimator can be implemented to propagate the model states, most often in the form of a Kalman filter. This method is then referred to as filter error method. Although computational demands increase with this approach, it offers greater robustness to disturbances, reduces the likelihood of encountering local minima,

and improves the convergence properties of the optimisation [4].

An alternative approach is the Two-Step Method (TSM) [7], where the nonlinear identification and optimisation process are divided into separate state estimation and parameter estimation steps. In the first step, a Kalman filter is applied to remove noise and biases from the measured responses and estimate the aircraft's true states. In the second step, model parameters are estimated using the equation error method with linear least-squares regression techniques. This approach is computationally less expensive, as it provides a closed-form solution and does not require prior parameter estimates.

Numerous additional system identification methods have also been applied to aeroelastic systems, including ARM and (N)ARMAX models [8–11], state-space and eigensystem realization algorithms [12–16], and machine learning techniques like neural networks [17–21]. These methods typically result in black-box models, which can be effective for matching the system input-output behaviour but lack physical interpretability and insights into the underlying system dynamics. Due to these limitations, these approaches were not considered for this work.

1.2. Flexible aircraft identification

Traditionally, system identification methods for aircraft flight dynamics have assumed a rigid aircraft model, justified by the sufficient frequency separation between the rigid body dynamics and structural dynamics. However, as aircraft designs evolve to become lighter, more slender, and fuel-efficient, this assumption no longer holds. In flexible aircraft, the flight dynamics and structural dynamics become coupled due to the reduced frequency separation [1]. For this reason, recent research has focused on adapting identification methods to include the effects of structural flexibility on flight dynamics and load models.

The model developed by Waszak and Schmidt [22] is most often used when describing the equations of motion of a flexible aircraft. This model uses a mean-axis formulation where the origin is at the aircraft's centre of gravity and small elastic displacements are assumed for the structural deformations. This formulation integrates structural dynamics into the flight mechanics model through a set of structural vibration modes characterised by their damping ratios, natural frequencies, and modal masses. The interaction between rigid-body and structural motion is captured through aerodynamic forces and moments, as well as generalized forces acting on the flexible structure. The goal of system identification is to derive models capable of describing and predicting these aerodynamic forces, moments, and generalised forces acting on the aircraft and its structure directly from flight test data. For a flexible aircraft, the identified models can be expressed as a function of quantities related to the rigid-body motion such as the angle of attack, body rotational rates and control surface deflections as well as structural mode responses.

While system identification methods for rigid aircraft are well-established, there is limited reference literature focused on the identification of flexible aircraft, particularly using flight test data. Grauer [23] highlights several challenges in this

domain, including the complexity of larger models, the need to excite a wide range of frequencies during flight tests, the requirement for numerous additional sensors, the lack of direct observability of modal states, and the reliance on nonlinear methods that require accurate initial parameter estimates.

Previous studies have explored various identification methods for different aircraft models. One early example is presented by Theodore et al. [24], who used the Waszak and Schmidt model to identify the lateral-directional flight dynamics of a large transport aircraft in the frequency-domain. By including an asymmetric wing bending mode and a lateral fuselage bending mode, they developed a model which is accurate across a broader frequency range, even beyond the included structural modal frequencies. However, due to significant frequency separation between rigid-body and structural dynamics, there was minimal interaction between these modes.

Grauer and Boucher [23, 25] applied both the equation-error approach and output-error approach in the frequency-domain to identify the longitudinal dynamics models of the X-56A flying-wing aircraft including two structural modes. Using orthogonal multisine inputs, they effectively excited multiple control surfaces simultaneously during flight tests, allowing for a wide frequency range excitation from a single test manoeuvre. Output-error method applied on frequency-domain data allowed to reduce the number of data points and make the estimation process computationally more efficient. Initial parameter values were obtained from a separate panel method aeroelastic analysis, while ground vibration tests and FEM models provided structural frequencies and mode shapes.

Danowsky et al. [26] used output-error methods in the frequency-domain to identify the flight dynamics model of a scaled version of the X-56A aircraft. Their step-by-step approach estimated and fixed rigid-body dynamics coefficients first, subsequently incorporating structural modes to refine the model. The final model included four structural modes, with modal frequencies and damping ratios derived from ground tests.

Silva [1] identified the flight dynamics model of a SB10 glider aircraft. Measurements related to the rigid body motion were first filtered using a Kalman filter to ensure consistency and remove noise and biases. This was followed by time-domain identification using the output-error method to determine the quasi-steady aerodynamic forces and aircraft modal parameters. A step-by-step approach was used where first a rigid aircraft model was identified that was then gradually expanded by adding structural modes with previous parameter estimates as the initial guess. In total 5 structural modes were included in the final model. Flight tests were conducted at two different airspeeds to obtain different dynamic pressures which allowed to separate the aerodynamic and structural contributions in the responses.

Viana [27] followed a similar approach by also applying a Kalman filter to the rigid body measurements followed by the output-error method in the time-domain to identify the quasi-steady aerodynamic model for the Discus-2c glider aircraft. The identified model included the aircraft flight dynamics together with local loads at seven different points on the aircraft. This comprehensive model, which

integrated six structural modes, proved valuable for monitoring operational loads and developing load alleviation control systems.

1.3. UNSTEADY AERODYNAMICS

In all of the existing flexible aircraft identification approaches presented previously, the aerodynamic forces and moments are assumed to be quasi-steady, meaning they respond instantaneously to condition changes [28]. However, in unsteady aeroelastic models, the forces and moments are frequency-dependent which results in changes in response amplitude and additional delays. The frequency dependence of unsteady aerodynamic effects is characterised using the reduced frequency, a non-dimensional parameter expressed as the ratio between the oscillation frequency, the wing's semi-chord length, and the airspeed.

The Theodorsen function is central to aeroelastic theory and describes the amplitude and phase lag of unsteady aerodynamic forces [29]. At reduced frequencies below 0.05, the amplitude and phase differences between unsteady and quasi-steady forces remain small and quasi-steady conditions can be assumed [28]. As the reduced frequency increases, the magnitude of the unsteady aerodynamic response decreases sharply compared to the quasi-steady case. For instance, the force amplitude drops to about 90% of the quasi-steady value at a reduced frequency of 0.06, to roughly 80% at 0.15, and to around 60% by 0.57 and ultimately converges to 50% for higher reduced frequencies. The phase lag between the unsteady and quasi-steady forces also increases as the reduced frequency is increased, reaching a maximum of 15 deg around a reduced frequency of 0.3 before gradually decreasing again [28]. For reference, in an aircraft with a rigid-body or structural mode at 1 Hz, a 15 deg phase lag would correspond to a time delay of approximately 40 ms. More information and figures about the Theodorsen function are presented in Chapter 2 and 5.

In Fig.1.1, the relation between the reduced frequency and oscillation frequency is presented for common transport aircraft types evaluated at their respective cruise speeds and chord lengths.

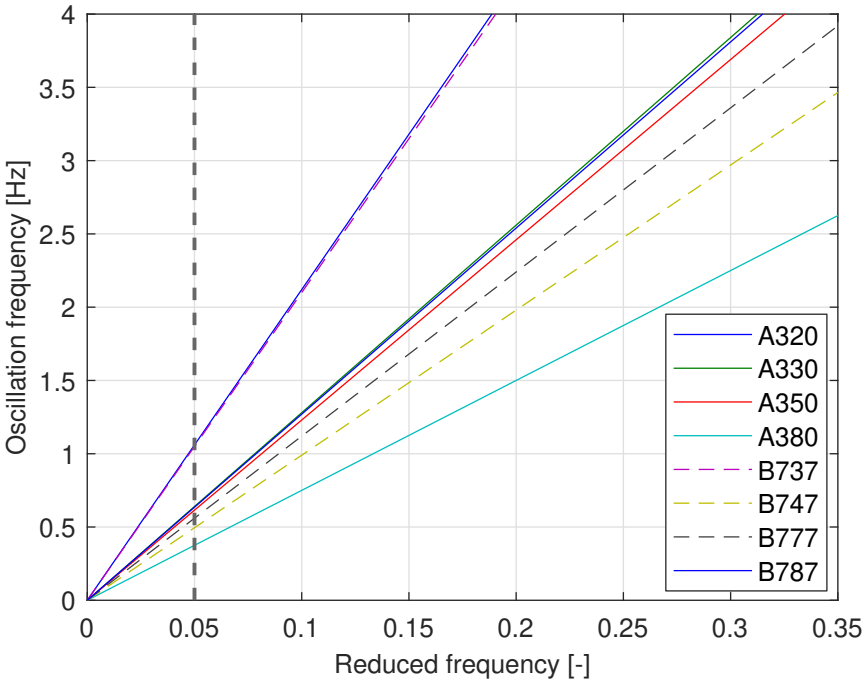

Figure 1.1: Reduced frequencies for transport aircraft at cruise speed.

As can be seen, already at oscillation frequencies above 0.5-1.0 Hz the reduced frequencies become larger than 0.05 and enter the region of unsteady aerodynamics. Therefore, the structural modes present or control surfaces that operate at those frequencies experience unsteady aerodynamic loads. Capturing these delays and amplitude changes in the aircraft responses becomes especially important when designing and implementing control laws for active load alleviation or flutter suppression as it often requires higher actuation frequencies.

To model the dynamics of a 2D aeroelastic airfoil with unsteady aerodynamics in the frequency-domain, the Theodorsen function [29] is commonly used. However, to formulate these effects in the time-domain, aerodynamic lag states are often introduced, which behave as first-order time delays. These are characterised by a pole value scaled by the airspeed, which determines the amount of delay and an input signal that is being delayed. Typically, the states that are considered as inputs for aerodynamic lag states include aircraft rotational rates, control surface deflections, and structural modal velocities. In the case of a 2D airfoil, the aerodynamic lag pole values can be obtained from Jones's [30] approximation. However, in 3D aeroelastic analyses, such analytical solutions are not available, and numerical panel methods or CFD must be used instead. These numerical analyses result in generalised aerodynamic forces at specified discrete reduced frequencies, describing the harmonic loads and the aerodynamic interactions

between aircraft rigid-body, structural, and control surface modes.

The aerodynamic lag states are then incorporated into the time-domain models through a Rational Function Approximation (RFA) process [31]. In RFA, aerodynamic coefficients related to the aircraft states as well as aerodynamic lag states are fitted to match the frequency-domain aerodynamic forces obtained from the numerical analysis. Aerodynamic lag states are assigned to each mode and the number of lag states is increased iteratively until satisfactory fitting accuracy between the time-domain model and the frequency-domain solution is achieved. Multiple lag states are associated with each mode, each with different lag poles corresponding to shorter or longer delays. Both Roger's method [31] and ZONA software [32] distribute the lag poles evenly based on the highest reduced frequency of interest. While a good fit can be achieved, this can also result in large model sizes where not all lag states are required.

With flight test response measurements, such detailed frequency-domain aerodynamic solutions are not available. Therefore, an alternative approach is required to identify both the relevant aircraft states for the aerodynamic lag states and the corresponding pole values directly from measured flight data. This would allow to accurately capture the unsteady aerodynamic effects by including the aerodynamic lag states in the model identification process.

1.4. Research goal

To address the limitations of existing methods and to expand the capabilities of system identification approaches for flexible aircraft by also including the frequency-dependent effects of unsteady aerodynamics, the following goal is set for this thesis:

> *Develop a methodology for identifying a parametric flight dynamics and loads model from flight test measurements for a flexible aircraft that includes the effects of structural dynamics and unsteady aerodynamics.*

To achieve this goal, it is necessary to acquire unsteady aeroelastic flight test data, which can be challenging due to the need for extensive set of sensors and the requirement to excite a broad range of aircraft dynamic responses. Moreover, such datasets are rarely publicly shared and published [1]. Conducting full-scale aeroelastic flight testing is very expensive. As a result, researchers have increasingly turned to alternative solutions such as unmanned aerial vehicles (UAVs) or scaled demonstrator aircraft to perform aeroelastic flight experiments in a practical and cost-effective manner. Examples of such aeroelastic demonstrators include AlbatrossONE [33], T-FLEX [34, 35] and TU-Flex [36], X-HALE [37, 38], X-56A [39] and its smaller scale versions [40–42].

However, there is limited information available about the specific hardware and instrumentation used for flight testing and the performance capabilities achieved by these systems. Documentation on sensor configurations and system

setups could provide valuable references for future projects, especially if such systems can be built using widely available, low-cost consumer electronics and open-source software. This leads to the first research question and supporting subquestions:

Research question 1:

How feasible is an open-source, low-cost sensor-based flight test system for capturing both rigid body and structural dynamic responses of an aeroelastic aircraft in flight?

Subquestions:

1. What sampling rates can be achieved with such a system?
2. What are the system's measurement capabilities in terms of the number and types of responses captured, as well as its impact on aircraft weight and power consumption?
3. How accurately can the system estimate modal parameters, including natural frequencies, damping ratios, and mode shapes?
4. What are the required sensor accuracy and noise statistics for aeroelastic flight testing?

For the identification procedure, the two-step approach [7] is chosen over the output-error method as it has the benefits of performing parameter estimation using linear regression methods which does not require any prior information about the model parameters and is less computationally demanding. However, this requires performing state estimation to ensure the consistency of the collected flight data and remove noise and biases from measured responses. In addition to measuring the rigid body responses, additional sensors are needed for a flexible aircraft in order to also capture the dynamic responses of the aircraft structure. It is therefore necessary to combine the information from all the local deformation measurements to estimate the structural response in terms of more general modal states which could then be used for modelling. This presents the second research question:

Research question 2:

How can information from GPS, aeroprobe, accelerometers, gyroscopes and strain gauges be combined to simultaneously estimate the aircraft rigid body states and modal states?

Similarly, also the states related to the unsteady aerodynamic contributions need to be estimated from the flight test response measurements. As described previously, aerodynamic lag states can be used to represent unsteady aerodynamic effects in the time-domain. These aerodynamic lag states are characterised by the lag poles which determine the delay amount and need to

be estimated from the flight response measurements. In addition, it is also necessary to determine which aircraft states are relevant to be used as inputs to the aerodynamic lag states.

As explained in Section 1.3, the most significant delays in aerodynamic forces due to unsteady effects occur at reduced frequencies between 0.05 and 0.5. These frequency ranges should therefore be specifically targeted during flight testing. This raises the question of how to most effectively excite these reduced frequencies in flight in order to obtain meaningful measurements of the unsteady aerodynamic responses. This leads to next research question and subquestions:

Research question 3:

How to estimate aerodynamic lag poles and reconstruct aerodynamic lag states from flight test response measurements?

Subquestions:

1. Is the first-order lag structure suitable for identifying aerodynamic lag dynamics from flight test data?
2. What adjustments to flight testing are required to estimate the aerodynamic lag states?

Once the aerodynamic and structural states can be estimated and integrated into the model, the key question becomes whether incorporating these elements leads to an improvement in model predictive accuracy. This presents the final research question:

Research question 4:

How much are the identified model predictions improved by incorporating structural dynamics and unsteady aerodynamic effects in the model?

Subquestions:

1. What is the improvement in aerodynamic force and moment coefficient predictions?
2. What is the improvement in wing root and tail load predictions?

1.5. Research contributions and publications

The main contributions of this research can be summarised as follows:

- Development, implementation and experimental validation of a low-cost and modular data acquisition system for flexible aircraft flight testing (Chapter 2).
- Execution of a flight test campaign and publication of an aeroelastic flight test dataset for a scaled Diana 2 glider UAV (Chapter 2 to 5).

- Demonstrated experimental modal analysis through the combined use of acceleration, rotational rate and strain measurements and validated the modal parameters with reference sensor and FEM model results (Chapter 3).
- Extended the Kalman filter based flight path reconstruction approach to estimate also the modal amplitude and velocity states by including additional accelerometer, gyroscope and strain measurements together with modeshapes (Chapter 4).
- Development and validation of a correlation based method for estimating the aerodynamic lag state poles and reconstructing the aerodynamic lag states from flight test measurements (Chapter 5).
- Identification of a flight dynamics and loads model of the scaled Diana 2 glider UAV including states related to structural modes and aerodynamic lags. Model performance validation with flight data and comparison with a rigid aircraft model structure and a numerical model (Chapter 5).

The research covered in this thesis has resulted in a number of publications in peer reviewed scientific journals and conference proceedings. An overview of these publications is as follows:

1. Jürisson, A., Eussen, B. J. G., de Visser, C. C., & De Breuker, R., ”Low-cost flight test instrumentation system development for aeroelastic flight testing” in *Journal of Aircraft (submitted)*, 2026
2. Jürisson, A., De Breuker, R., de Visser, C. C., Eussen, B. J. G., & Timmermans, H, ”Aeroservoelastic flight testing platform development for system identification” in *AIAA SCITECH 2022 Forum*, 2022
3. Jürisson, A., Eussen, B. J. G., de Visser, C. C., & De Breuker, R., ”Combined Estimation of Structural Displacement, Rotation and Strain Modes on a Scaled Glider” in *MDPI Applied Sciences*, 2026
4. Jürisson, A., Timmermans, H., Eussen, B. J. G., de Visser, C. C., & De Breuker, R., ”Ground vibration testing and FEM model updating of scaled Diana 2 glider model using accelerometer, gyro and strain measurements” in *Proceedings of the International Forum of Aeroelasticity and Structural Dynamics 2022*, 2022
5. Jürisson, A., Eussen, B. J. G., de Visser, C. C., & De Breuker, R., ”Flight path reconstruction filter extension for flexible aircraft state estimation” in *Journal of Aircraft (submitted)*, 2026
6. Jürisson, A., Eussen, B. J. G., de Visser, C. C., & De Breuker, R., ”Flight path reconstruction filter extension for tracking flexible aircraft modal amplitudes and velocities” in *AIAA SciTech Forum 2023*, 2023

7. Jürisson, A., Eussen, B. J. G., de Visser, C. C., & De Breuker, R., "Flexible aircraft model identification from flight test data in unsteady conditions" in *Journal of Aircraft (submitted)*, 2026

8. Jürisson, A., Eussen, B. J. G., de Visser, C. C., & De Breuker, R., "Flexible aircraft flight dynamics and loads model identification from flight test data in unsteady conditions" in *Aeroelasticity & Structural Dynamics in a Fast Changing World, IFASD 2024*, 2024

1.6. Outline of the thesis

This thesis is divided into four main parts, each addressing a critical aspect of developing and validating a methodology for identifying flexible aircraft models incorporating structural dynamics and unsteady aerodynamics. Each chapter has been written with the intention of publication in a peer-reviewed scientific journal and includes a separate survey of relevant literature.

Chapter 2 focuses on the development of an aeroelastic flight test platform using a scaled Diana 2 glider UAV. The aircraft was instrumented with an extensive set of various types of sensors to capture its rigid-body and structural responses. The capabilities and performance of the developed flight test system is presented together with the experiments conducted to calibrate the sensors.

Chapter 3 investigates the structural properties of the UAV through a ground vibration test (GVT) and an experimental modal analysis. Structural parameters were estimated using onboard sensors such as accelerometers, gyroscopes, and strain gauges, and the results were validated using external reference sensors and a finite element method (FEM) model. The FEM model was tuned using the experimental data to improve its accuracy.

Chapter 4 extends the traditional flight path reconstruction (FPR) methodology by incorporating additional onboard sensor measurements, including accelerometers, gyroscopes, and strain gauges, to estimate states associated with structural modes. The performance of this extended FPR method is compared against the standard approach while varying the number of structural modes used in state estimation. Additionally, the robustness of the approach to errors in modeshapes is analysed and presented.

Chapter 5 introduces a correlation-based method for estimating aerodynamic lag poles from flight test response data. Using this method, aerodynamic lag states are reconstructed, and parametric models are identified for aerodynamic forces and moments, as well as loads acting on the aircraft wing root and tail. The identified flexible aircraft models, incorporating structural and aerodynamic states, are compared against traditional rigid-body identification approaches. The identified models are validated by simulating flight test responses using measured control surface deflections and are further compared with numerical results obtained via aerodynamic panel methods.

Finally, Chapter 6 summarises the findings of this thesis, and provides recommendations for future research.

1

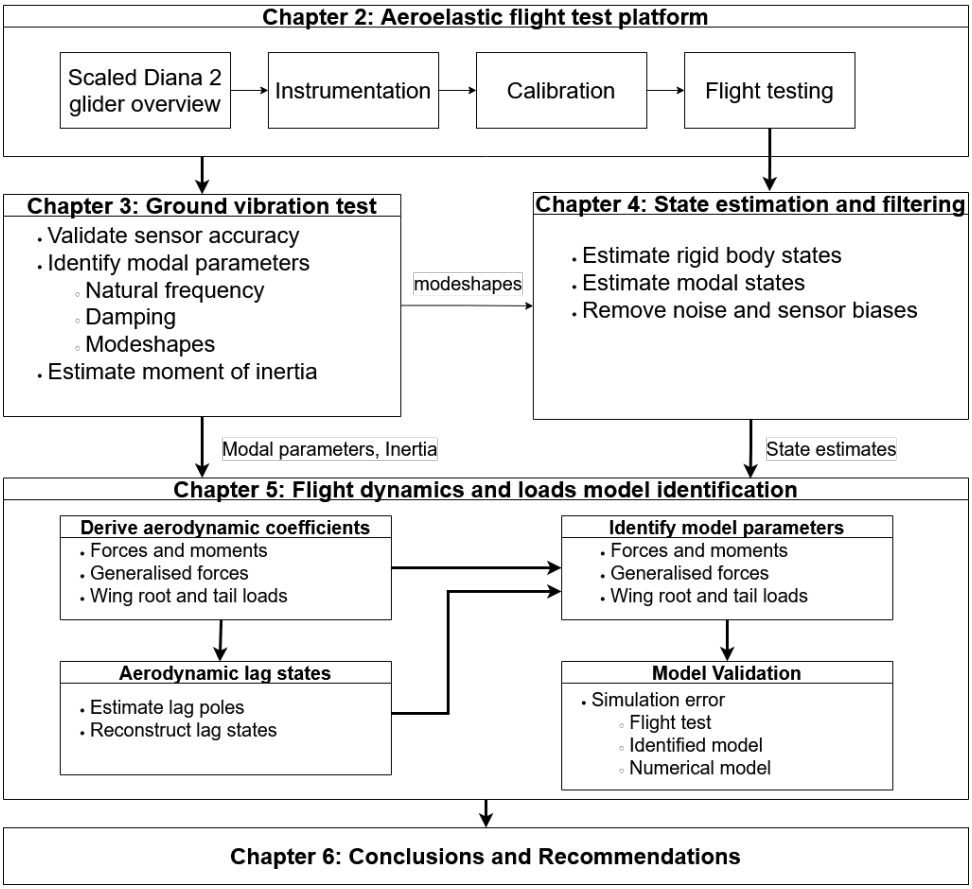

Figure 1.2: Structure of the thesis.

REFERENCES

[1] B. G. de Oliveira Silva. “System Identification of Flexible Aircraft in Time Domain”. PhD thesis. Technical University of Braunschweig, Aug. 2018, p. 225.

[2] E. Livne. “Aircraft Active Flutter Suppression: State of the Art and Technology Maturation Needs”. In: *Journal of Aircraft* 55.1 (Jan. 2018), pp. 410–452. ISSN: 0021-8669. DOI: 10.2514/1.C034442.

[3] M. Kopf, E. Bullinger, H.-G. Giesseler, S. Adden and R. Findeisen. “Model Predictive Control for Aircraft Load Alleviation: Opportunities and Challenges”. In: *2018 Annual American Control Conference (ACC)*. Milwaukee, WI: IEEE, June 2018, pp. 2417–2424. DOI: 10.23919/ACC.2018.8430956.

[4] R. V. Jategaonkar. *Flight Vehicle System Identification: A Time Domain Methodology*. Vol. 216. Progress in Astronautics and Aeronautics. AIAA, Aug. 2006. ISBN: 1563478366.

[5] E. A. Morelli and V. Klein. *Aircraft system identification: Theory and Practice*. en. AIAA Education Series. Reston, VA: American Institute of Aeronautics & Astronautics, Aug. 2006.

[6] P. G. Hamel and R. V. Jategaonkar. “Evolution of flight vehicle system identification”. In: *Journal of Aircraft* 33.1 (1996), pp. 9–28. ISSN: 0021-8669. DOI: 10.2514/3.46898.

[7] J. A. Mulder, Q. P. Chu, J. K. Sridhar, J. H. Breeman and M. Laban. “Non-linear aircraft flight path reconstruction review and new advances”. In: *Progress in Aerospace Sciences* 35.7 (7 Oct. 1999), pp. 673–726. ISSN: 03760421. DOI: 10.1016/s0376-0421(99)00005-6.

[8] J. Sjöberg, Q. Zhang, L. Ljung, A. Benveniste, B. Delyon, P.-Y. Glorennec, H. Hjalmarsson and A. Juditsky. “Nonlinear black-box modeling in system identification: a unified overview”. en. In: *Automatica (Oxf.)* 31.12 (Dec. 1995), pp. 1691–1724. DOI: 10.1016/0005-1098(95)00120-8.

[9] T. Cowan, A. Arena Jr and K. Gupta. “Acceleration CFD-based aeroelastic predictions using system identification”. In: *23rd Atmospheric Flight Mechanics Conference*. Boston,MA,U.S.A.: American Institute of Aeronautics and Astronautics, Aug. 1998. DOI: 10.2514/6.1998-4152.

[10] K. Gupta, L. Voelker, C. Bach, T. Doyle and E. Hahn. “CFD-based aeroelastic analysis of the X-43 hypersonic flight vehicle”. In: *39th Aerospace Sciences Meeting and Exhibit*. Reno,NV,U.S.A.: American Institute of Aeronautics and Astronautics, Jan. 2001. DOI: 10.2514/6.2001-712.

[11] S. L. Kukreja and M. J. Brenner. “Nonlinear aeroelastic system identification with application to experimental data”. en. In: *J. Guid. Control Dyn.* 29.2 (Mar. 2006), pp. 374–381. DOI: 10.2514/1.15178.

[12] W. Silva and D. Raveh. “Development of unsteady aerodynamic state-space models from CFD-based pulse responses”. In: *19th AIAA Applied Aerodynamics Conference*. Vol. 1213. American Institute of Aeronautics and Astronautics, June 2001, p. 2001. DOI: 10.2514/6.2001-1213.

[13] R. A. De Callafon, B. Moaveni, J. P. Conte, X. He and E. Udd. “General realization algorithm for modal identification of linear dynamic systems”. en. In: *J. Eng. Mech.* 134.9 (Sept. 2008), pp. 712–722. DOI: 10.1061/(ASCE)0733-9399(2008)134:9(712).

[14] W. A. Silva, V. N. Vatsa and R. T. Biedron. “Development of Unsteady Aerodynamic and Aeroelastic Reduced-Order Models Using the FUN3D Code”. In: *2009 International Forum on Aeroelasticity and Structural Dynamics (IFASD)*. June 2009.

[15] S. L. Brunton, S. T. Dawson and C. W. Rowley. “State-space model identification and feedback control of unsteady aerodynamic forces”. In: *Journal of Fluids and Structures* 50 (2014), pp. 253–270. ISSN: 10958622. DOI: 10.1016/j.jfluidstructs.2014.06.026.

[16] R. C. Machado, D. Fernando, C. Zúniga, A. D. Souza, T. Rosado, L. Carlos and S. Góes. “Open-Loop Subspace Identification of a Flexible Unmanned Aerial System”. In: *33rd Congress of the International Council of the Aeronautical Sciences (ICAS)*. ICAS, Sept. 2022, pp. 5463–5476.

[17] F. D. Marques and J. Anderson. “Identification and prediction of unsteady transonic aerodynamic loads by multi-layer functionals”. en. In: *J. Fluids Struct.* 15.1 (Jan. 2001), pp. 83–106. DOI: 10.1006/jfls.2000.0321.

[18] M. K. Samal, M. Garratt and S. Anavatti. “Identification of a flexible aircraft using neural network”. In: *Proceedings of the 27th IASTED International Conference on Modelling, Identification and Control*. Feb. 2008, pp. 515–520. ISBN: 9780889867123.

[19] H. Song, J. Qian, Y. Wang, K. Pant, A. W. Chin and M. J. Brenner. “Development of Aeroelastic and Aeroservoelastic Reduced Order Models for Active Structural Control”. In: *56th AIAA Structures, Structural Dynamics, and Materials Conference*. 2015, p. 13. DOI: 10.2514/6.2015-2055.

[20] K. Li, J. Kou and W. Zhang. “Deep neural network for unsteady aerodynamic and aeroelastic modeling across multiple Mach numbers”. en. In: *Nonlinear Dyn.* 96.3 (May 2019), pp. 2157–2177. DOI: 10.1007/s11071-019-04915-9.

[21] R. Halder, M. Damodaran and B. C. Khoo. “Deep learning based reduced order model for airfoil-gust and aeroelastic interaction”. en. In: *AIAA J.* 58.10 (Oct. 2020), pp. 4304–4321. DOI: 10.2514/1.J059027.

[22] M. R. Waszak and D. K. Schmidt. “Flight dynamics of aeroelastic vehicles”. In: *Journal of Aircraft* 25.6 (1988), pp. 563–571. ISSN: 0021-8669. DOI: 10.2514/3.45623.

[23] J. A. Grauer and M. J. Boucher. “Real-time parameter estimation for flexible aircraft”. In: *2018 Atmospheric Flight Mechanics Conference*. Atlanta, Georgia: American Institute of Aeronautics and Astronautics, June 2018. DOI: 10.2514/6.2018-3155.

[24] C. Theodore, C. Ivler, M. Tischler, E. Field, R. Neville and H. Ross. “System Identification of Large Flexible Transport Aircraft”. In: *AIAA Atmospheric Flight Mechanics Conference and Exhibit*. American Institute of Aeronautics and Astronautics, Aug. 2008. DOI: 10.2514/6.2008-6894.

[25] J. A. Grauer and M. J. Boucher. *Output Measurement Equations for Flexible Aircraft Flight Dynamics*. TM–2018–220102. NASA Langley Research Center, 2018, pp. 1–36.

[26] B. P. Danowsky, D. K. Schmidt and H. Pfifer. “Control-Oriented System and Parameter Identification of a Small Flexible Flying-Wing Aircraft”. In: *AIAA Atmospheric Flight Mechanics Conference*. American Institute of Aeronautics and Astronautics, Jan. 2017, p. 25. ISBN: 978-1-62410-448-0. DOI: 10.2514/6.2017-1394.

[27] M. V. Preisighe Viana. “Time-Domain System Identification of Rigid-Body Multipoint Loads Model”. PhD thesis. Technical University of Braunschweig, June 2016, p. 385. DOI: 10.2514/6.2016-3706.

[28] J. R. Wright and J. E. Cooper. *Introduction to Aircraft Aeroelasticity and Loads*. Wiley, Dec. 2014. ISBN: 9781118700440. DOI: 10.1002/9781118700440.

[29] T. Theodorsen. *General Theory of Aerodynamic Instability and the Mechanism of Flutter*. Tech. rep. TR-496. NACA, 1935.

[30] R. T. Jones. *Operational Treatment of the Nonuniform-Lift Theory in Airplane Dynamics*. Tech. rep. NACA TN 667. NACA, 1938.

[31] K. L. Roger. “Airplane Math Modeling Methods for Active Control Design”. In: *AGARD CP-228*. Aug. 1977.

[32] ZONA Technology Inc. *ZAERO Theoretical Manual, Version 9.0*. Scottsdale, Arizona, 2014.

[33] T. Wilson, J. Kirk, J. Hobday and A. Castrichini. “Small scale flying demonstration of semi aeroelastic hinged wing tips”. In: *International Forum on Aeroelasticity and Structural Dynamics*. Savannah, Georgia, USA: IFASD, June 2019, pp. 1–19.

[34] J. Bartaševičius, S. Koeberle, D. Teubl, C. Roessler and M. Hornung. “Flight Testing of 65kg T-FLEX subscale Demonstrator”. In: *32nd Congress of the International Council of the Aeronautical Sciences, ICAS 2021*. Shanghai, China: International Council of the Aeronautical Sciences, Sept. 2021, pp. 1–16.

[35] M. Wüstenhagen, O. Suelozgen, L. Ackermann and J. Bartasevicius. “Validation and Update of an Aeroservoelastic Model based on Flight Test Data”. In: *2021 IEEE Aerospace Conference*. Big Sky, MT, USA: IEEE, Mar. 2021, pp. 1–18. ISBN: 978-1-7281-7436-5. DOI: 10.1109/AERO50100.2021.9438354.

[36] P. Gonzalez, G. Starvorinus, F. J. Silvestre, A. Voß, Y. M. Meddaikar and W. Krueger. “TU-Flex: A Very-Flexible Flying Demonstrator with a Generic Transport Aircraft Configuration”. In: *AIAA SCITECH 2023 Forum*. National Harbor, MD, USA: American Institute of Aeronautics and Astronautics, Jan. 2023. ISBN: 978-1-62410-699-6. DOI: 10.2514/6.2023-1312.

[37] C. E. S. Cesnik, P. J. Senatore, W. Su, E. M. Atkins and C. M. Shearer. “X-HALE: A Very Flexible Unmanned Aerial Vehicle for Nonlinear Aeroelastic Tests”. In: *AIAA Journal* 50 (12 Dec. 2012), pp. 2820–2833. ISSN: 0001-1452. DOI: 10.2514/1.J051392.

[38] A. B. G. Neto, G. C. Barbosa, J. A. Paulino, R. M. Bertolin, J. S. M. Nunes, P. J. González, F. L. Cardoso-Ribeiro, M. A. V. Morales, R. G. A. da Silva, F. L. S. Bussamra, F. J. Silvestre, F. J. O. Moreira and C. E. S. Cesnik. “Flexible Aircraft Simulation Validation with Flight Test Data”. In: *AIAA Journal* 61 (1 Jan. 2023), pp. 285–304. ISSN: 0001-1452. DOI: 10.2514/1.J060960.

[39] J. A. Grauer and M. J. Boucher. “Identification of aeroelastic models for the X-56A longitudinal dynamics using multisine inputs and output error in the frequency domain”. In: *Aerospace* 6 (2 2019). ISSN: 22264310. DOI: 10.3390/aerospace6020024.

[40] D. K. Schmidt. “Stability Augmentation and Active Flutter Suppression of a Flexible Flying-Wing Drone”. In: *Journal of Guidance, Control, and Dynamics* 39 (3 Mar. 2016), pp. 409–422. ISSN: 1533-3884. DOI: 10.2514/1.G001484.

[41] C. D. Regan. “mAEWing2: Conceptual design and system test”. In: *AIAA Atmospheric Flight Mechanics Conference, 2017*. Grapevine, Texas, USA: American Institute of Aeronautics and Astronautics Inc, AIAA, 2017. ISBN: 978162410448. DOI: 10.2514/6.2017-1391.

[42] C. D. Regan, A. Kotikalpudi, D. K. Schmidt and P. J. Seiler. “mAEWing2: Initial Flight Test and System Identification of a Flexible UAV”. In: *AIAA Scitech 2020 Forum*. Orlando, FL: American Institute of Aeronautics and Astronautics, Jan. 2020. ISBN: 978-1-62410-595-1. DOI: 10.2514/6.2020-1965.

2

AEROELASTIC FLIGHT TEST PLATFORM DEVELOPMENT

To develop flight dynamics and loads models that include effects from structural dynamics and unsteady aerodynamics, a suitable test aircraft was required, one that is both flexible and capable of operating in unsteady aerodynamic conditions. This chapter provides an overview of the scaled Diana 2 glider UAV, which was used for flight testing. The aircraft was equipped with a wide range of sensors to capture the responses of the aircraft and its structure in flight. For this purpose, a custom data acquisition system was developed, and a series of calibration tests were performed to ensure measurement accuracy. A detailed overview of the integrated sensors and calibration procedures are also presented in this chapter.

This chapter is based on the following article: Jürisson, A., Eussen, B., de Visser, C. C., & De Breuker, R., ”Low-cost flight test instrumentation system development for aeroelastic flight testing” in *Journal of Aircraft (submitted)*, 2026

2.1. Introduction

To improve aircraft performance and reduce fuel consumption, aircraft designs incorporate longer and more slender wings to reduce the induced drag. Combined with more lightweight structures, this can lead to increased aeroelastic interactions between the aircraft flight dynamics and structural modes, which can negatively impact the aircraft's handling qualities, structural loads, and stability. Therefore, addressing these challenges has become an active research area, focusing on topics such as manoeuvre and gust load alleviation, flutter suppression, and flexible aircraft modeling.

Aeroelastic flight test data is essential for studying and evaluating new approaches and methods, but such data is often scarce and not publicly available [1]. Full-scale flight testing campaigns can be very costly and complex, motivating the use of unmanned aerial vehicles (UAVs) as more accessible experimental platforms. Several UAV-based aeroelastic demonstrators have been developed in recent years, including AlbatrossONE [2], T-FLEX [3–6], TU-Flex [7], X-HALE [8, 9], and X-56A and its scaled variants [10–14]. These platforms have been used to design and test new aircraft concepts and flight test innovative control laws.

While UAV-based aeroelastic demonstrators have shown the potential of flight testing on scaled platforms, the implementation of suitable data acquisition systems (DAQ) remains challenging. Such systems must balance measurement accuracy with constraints on cost, weight, power consumption, and system robustness. In many cases, high-performance instrumentation can become overly expensive relative to the aircraft platform, which is undesirable given the inherent risk of loss during flight testing. Moreover, existing demonstrators often rely on specialized or custom-built hardware, which can limit accessibility, adaptability, or reproducibility. In addition, while demonstrator platforms are described in detail, the complete measurement chain, including hardware selection and calibration, is not always presented as a complete workflow. Yet, these steps are essential to transform raw sensor data into physically meaningful aeroelastic quantities and to ensure reproducibility of the system and measurements. This motivates the development of accessible and well-characterized DAQs that enable aeroelastic flight testing and the generation of high-quality datasets.

This paper addresses these challenges by presenting a modular, low-cost DAQ for aeroelastic flight testing of flexible UAVs, along with an overview of calibration tests and system performance assessment. The proposed system is based on widely available off-the-shelf components and open-source software, and is designed to be easily adaptable to different sensor configurations and aircraft platforms. The contribution of this work lies in demonstrating how a complete measurement system can be realized, calibrated, and evaluated to provide aeroelastic flight test data suitable for model identification.

The measurement capabilities of the system are demonstrated through flight testing using a scaled Diana 2 glider UAV. The collected data are compared with aeroelastic simulation model predictions, and frequency-domain analyses are performed to evaluate the system's ability to capture both rigid-body and structural dynamic responses. By combining system design, calibration procedures, and

evaluation of system performance, this work provides a reproducible and adaptable framework for acquiring aeroelastic flight test data. To support further research, the calibration data, data acquisition software, and flight test datasets are made publicly available [15].

The chapter is organized as follows. First, an overview of the test aircraft is presented in section 2.2. Section 2.3 gives an overview of the hardware and sensors used in the DAQ, while section 2.4 covers the tests performed to calibrate these sensors. Section 2.5 presents example flight test response measurements captured by the developed DAQ and compares them with open-loop simulation predictions from an aeroelastic flight dynamics model. Finally, conclusions are drawn in section 2.6.

2.2. AEROSERVOELASTIC TEST PLATFORM

The main goal of the test platform is to collect experimental data about the aircraft's responses to various excitations during flight in unsteady airflow conditions. These measurements are then used to develop a methodology for identifying flight dynamics and load models for flexible aircraft.

Therefore, a suitable test aircraft needs to meet the following requirements:

- The aircraft should exhibit flight dynamic responses influenced by the structural dynamics.
- The aircraft should be able to operate in unsteady aerodynamic conditions.
- An existing aircraft needs to be available as the design and manufacturing is out of the scope of this research.

To quantify the aerodynamic unsteadiness, reduced frequency is often used in aeroelasticity. Reduced frequency, denoted by k, is defined in Eq. (2.1).

$$k = \frac{\omega \bar{b}}{V} \tag{2.1}$$

Here ω is the oscillation frequency, $\bar{b}$ is the semi-chord length, and V is the airspeed. This oscillation frequency relates both to the control surface inputs used to excite the aeroelastic system and the resulting structural responses.

In Fig. 2.1, the Theodorsen function, which models the amplitude and phase differences between unsteady and quasi-steady aerodynamic forces, is evaluated for varying reduced frequencies. As can be seen, reduced frequencies between 0.15 and 0.5 should be targeted to observe the largest difference in phase between unsteady and quasi-steady forces, with the peak in phase difference occurring at 0.3.

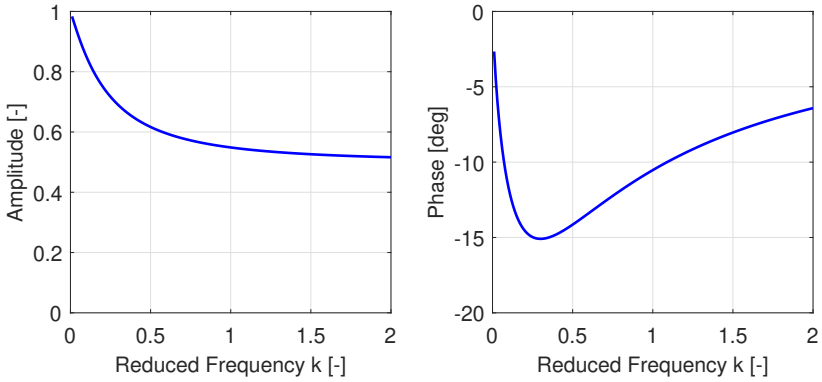

Figure 2.1: Theodorsen function amplitude and phase lag effects [16].

Based on these requirements, a scaled glider model was chosen as the test platform for the research. Gliders have wings with very high aspect ratios, making them aerodynamically efficient, but they can also result in more significant deformations and influence flight dynamic responses. The chosen test aircraft is a 1:3 scaled model of the Diana 2 glider manufactured by Baudismodel [17]. This scaled glider model has a wing span of 5 m and an aspect ratio of 24.3. It is a composite aircraft manufactured using both carbon and glass fibre sheets. An overview of the technical data is presented in Table 2.1, and an image of the model is presented in Fig. 2.2.

Table 2.1: Diana 2 model technical parameters.

Property	Value	Units
Aspect ratio	24.3	-
Mean chord	0.206	m
Weight	10.7	kg
Wing area	1.03	m^2
Wingspan	5.0	m

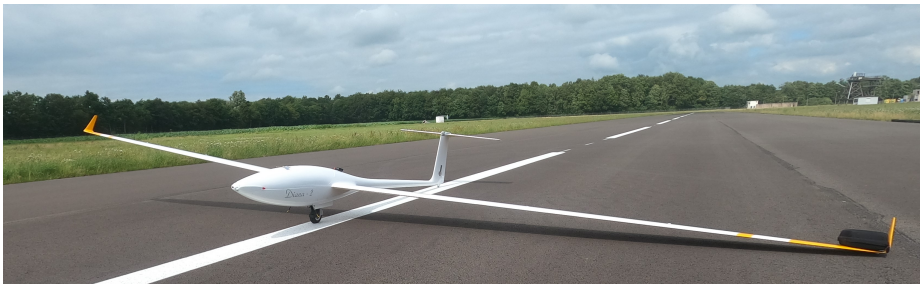

Figure 2.2: Diana 2 scaled glider.

The model has three ailerons on both wings, which can also be configured as flaperons or spoilerons, two control surfaces for the elevator, and a rudder. A Front Electric Self-launch/Self-sustainer (FES) propulsion system with folding propellers allows for take-offs without a winch and greatly increases endurance while simplifying operations. Table 2.2 presents an overview of the servos used for the control surfaces, retractable main landing gear, and electric motor.

Table 2.2: Diana 2 servos and FES specifications.

	Hardware	Voltage range [V]	Torque range [kg-cm]
Ailerons	KST X10	6.0-8.4	7.5-10.8
Elevators	MKS HV6110	6.0-8.4	2.6-3.4
Rudder	MKS HV6130H	6.0-8.4	6.0-8.1
Landing gear	HS 5585MH	6.0-7.4	14.0-17.0
FES	Hacker A40-8L V4 14-Poles	18.0-25.2	-

In Fig. 2.3, the described control surface locations and naming conventions are presented with letters specifying the inner (I), middle (M), and outer (O) ailerons and also the right (R) and left (L) side.

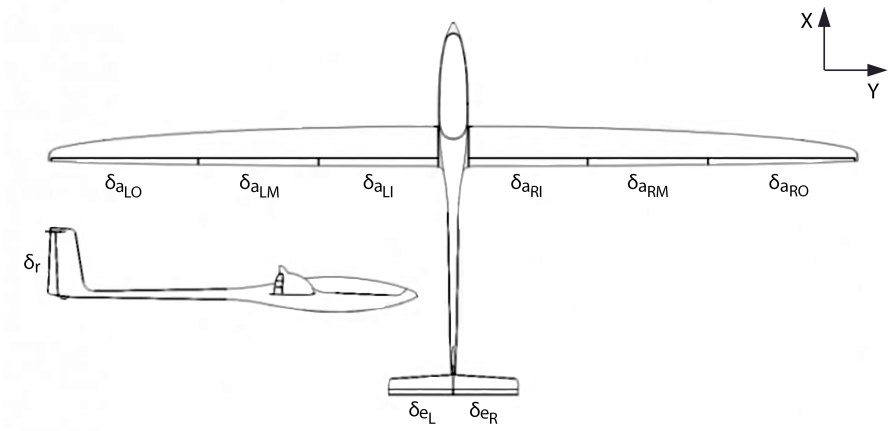

Figure 2.3: Control surface locations and naming conventions.

In Fig. 2.4, the reduced frequency is determined for varying airspeeds and oscillation frequencies using the Diana 2 model chord length in Eq. (2.1). A target airspeed range of 20 to 25 m/s is used for flight testing to maintain a safety margin before stalling while achieving higher reduced frequencies at lower oscillation frequencies. With the natural frequency of the first structural mode at 7.5 Hz and the control surfaces reaching a bandwidth up to 10 Hz as shown

in Sec. 2.4.2, the platform is capable of operating at the targeted reduced frequencies between 0.15 and 0.5.

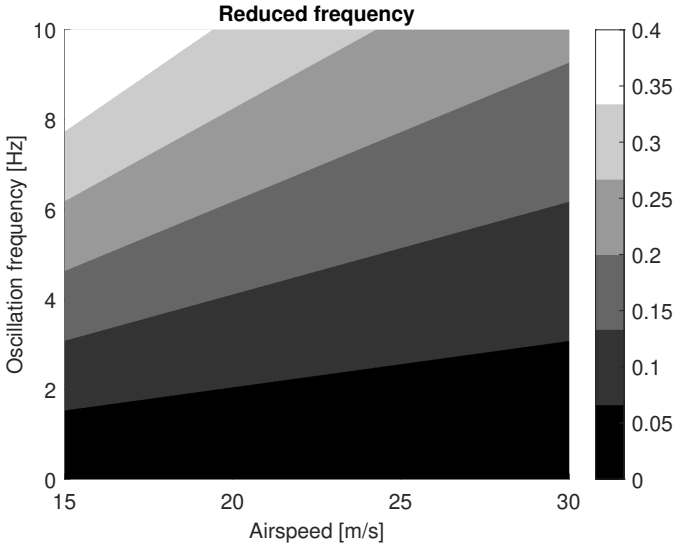

Figure 2.4: Reduced frequency for varying airspeeds and oscillation frequencies.

2.3. Instrumentation

To capture the dynamic responses of the aircraft and its structure during flight, together with the loads acting on the structure, a data acquisition system (DAQ) with various sensors is required. However, the instrumentation of the scaled Diana 2 glider presented several challenges. The space available inside the aircraft's fuselage, wings, and tail is limited. The additional weight that can be added to the aircraft and the electrical power available for the sensors are also restricted. Additionally, to capture the response of the aircraft structure, a considerable number of sensors are needed across the entire aircraft, necessitating a cost-effective solution. In order to meet these requirements and explore the capabilities of widely available consumer electronics sensors, a custom DAQ was developed for the scaled glider. An overview of the sensors, along with the developed DAQ, is presented in this section.

2.3.1. Pixhawk 4 autopilot hardware

To model the forces and moments acting on the aircraft in a flight dynamics model, it is necessary to measure the translational and rotational accelerations at the aircraft's centre of gravity. Then, the forces and moments can be calculated using the aircraft mass and moment of inertia.

The Pixhawk 4 autopilot hardware is a central piece of the instrumentation system for the Diana 2. In terms of sensors, it includes an inertial measurement unit (IMU) for measuring the acceleration, rotational rate, and magnetic field on 3 axes and a barometer for altitude measurement. In addition, all the commands given by the pilot via the RC transmitter are received by the Pixhawk board and assigned to the correct servos. This allows to log the pilot inputs and implement different control loops to enhance the aircraft behaviour. During the flight, the pilot's workload can be reduced by the autopilot by stabilizing the aircraft and counteracting atmospheric disturbances. Furthermore, when the signal between the pilot and the glider is lost, the autopilot can take over the command and safely return the glider to base and loiter until the signal can be restored. Pixhawk 4 autopilot hardware was selected for the scaled glider due to its widespread usage and support for the Ardupilot and PX4 open-source autopilot software. Both software solutions allow real-time monitoring of the aircraft's state during flight using a 433 MHz telemetry module.

2.3.2. Aircraft Position

The aircraft's position is determined using a GPS receiver placed on the top of the fuselage. A ground-based reference station is used to improve positioning accuracy, implementing a correction technique known as Real-Time Kinematics (RTK). The base station, whose position is known with high precision, estimates local measurement biases and transmits real-time correction data to the glider via telemetry. The Diana 2 glider is equipped with a Reach M+ receiver, while the ground station uses the corresponding Reach RS+ unit, both developed by Emlid. This setup enables position measurements at a rate of up to 14 Hz. While traditional GPS receivers offer positional accuracy in the order of a few metres, the GPS-RTK system can achieve centimetre level accuracy, according to Emlid. While the RTK corrections were successfully received and applied during flight testing, no independent ground-truth validation was conducted to experimentally evaluate the accuracy of the GPS-RTK position estimates used in this setup.

2.3.3. Aerodynamic Angles

To model the aircraft's flight dynamics, it is necessary to measure the dynamic pressure, angle of attack, and angle of sideslip. A 5-hole probe from Aeroprobe Corporation is used for these measurements, connected to three differential pressure sensors. Ideally, the probe should be placed in the nose of the aircraft, where the fuselage or wings do not influence the airflow. However, this was not possible due to the electric motor. Instead, an L-shaped probe positioned to the side of the fuselage is used, as shown in Fig. 2.5. This configuration provides a maximum clearance angle of approximately 40 degrees relative to the fuselage. Although the propeller wake can affect the aeroprobe measurements, all test manoeuvres were performed during the gliding phase of the flight, with the propeller folded, thereby minimising its influence. The 18-bit DLLR differential pressure sensors by Amphenol are used to measure the pressure difference

between the individual channels in the aeroprobe, with a measurement resolution of 0.01 Pa.

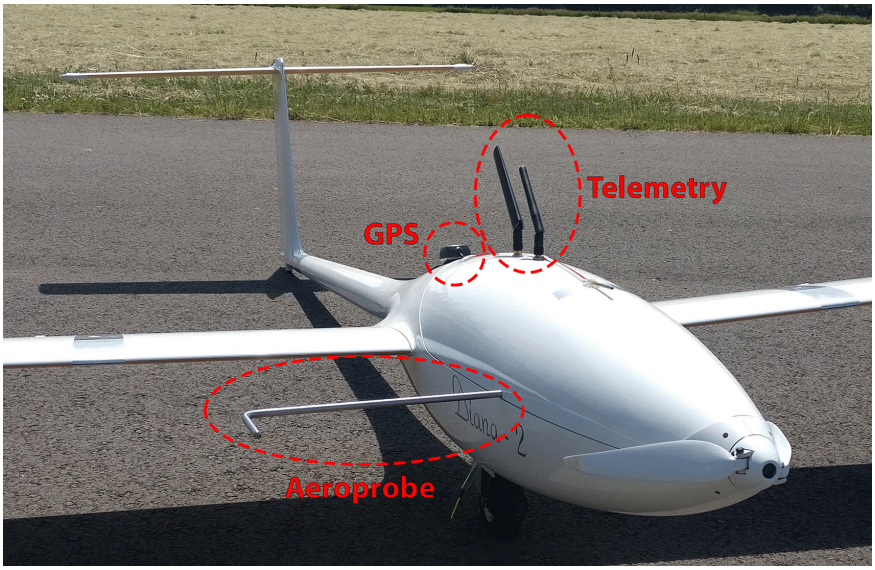

Figure 2.5: Aeroprobe installation location.

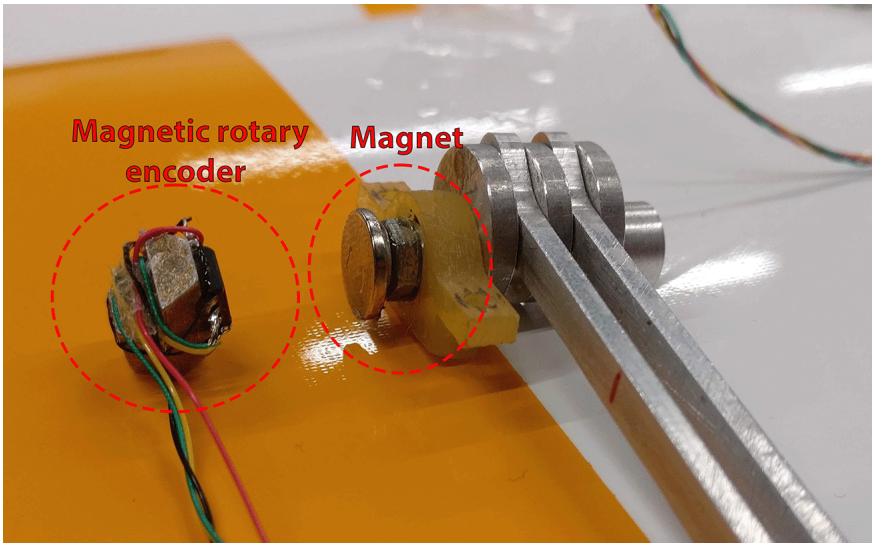

Figure 2.6: Magnetic rotary encoder and magnet on the axis of the control surface linkage.

2.3.4. CONTROL SURFACE ANGLES

The control surface deflection angles are measured using AS5600 rotary encoders that measure the orientation of a magnetic field. These sensors are placed adjacent to the rotation axis of the servos while the magnetic field is created with a diametrical magnet connected to the servo. The sensor has a 12-bit resolution, which allows it to measure angle changes as small as 0.09 degrees without interfering with the servo. Fig. 2.6 illustrates the sensor and magnet attached to the control surface linkage before installation inside the wing.

2.3.5. STRAIN GAUGES

Strain gauges are used on the wings and tail to measure the loads experienced by the aircraft structure. All the strain gauges are installed in a full Wheatstone bridge configuration to maximize the output sensitivity and reduce the influence of temperature effects. For bending the EA-06-250PD-350 and for shear, the CEA-06-250US-350 strain gauges by Micro-Measurements are used as shown in Fig. 2.7 and 2.8.

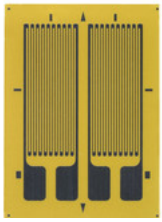

Figure 2.7: Bending stain gauge [18].

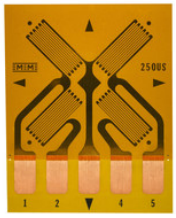

Figure 2.8: Shear strain gauge [18].

To measure the voltage difference over the Wheatstone bridge, the ADS1115 analog-to-digital converter (ADC) is used. This sensor can be configured to amplify the input signals by 16x, which allows the measurement of voltages in the range of ± 0.256 V with a resolution of 7.8 µV. An applied strain gauge excitation voltage of 5.0 V and a gauge factor of 2 allows the measurement of strains up to ±25600 microstrain with a resolution of 0.78 microstrain. Furthermore, an ADS1115 sensor is also used to monitor the strain gauge excitation voltage during the flight. To compensate for possible thermal effects in the strain gauge measurements, TMP102 temperature sensors are also fitted in each wing and tail.

2.3.6. ACCELERATION AND ROTATIONAL RATE OF STRUCTURE

To complement the strain gauges, additional IMUs are placed inside the wings and the tail to also capture the acceleration and rotational rate responses of the structure. For this purpose, the ICM-20948 IMUs are used, which include a 3-axis accelerometer and gyroscope. The sensor also contains a magnetometer,

which is currently not used in this setup. The accelerometers are configured to measure up to 8g-s while also supporting 2g, 4g, and 16g limits. Similarly, the gyros are configured to measure rotational rates up to 250 deg/s while also supporting 500, 1000, and 2000 deg/s limits.

2.3.7. Data acquisition system

The data acquisition system that collects measurements from all the individual sensors and stores them centrally consists of a Raspberry Pi 4 single-board computer that is connected to multiple Teensy 4.0 development boards. The Raspberry Pi is running Ubuntu Linux operating system and uses ROS to communicate with all the components. More specifically, the *MAVROS* module allows to connect the Raspberry Pi to the Pixhawk 4 board and retrieve all the sensor data and other parameters of interest from the autopilot while *rosserial* module allows to communicate with the Teensy 4.0 boards. All the individual sensors described previously are connected to the Teensy 4.0-s, which reads the sensor measurements and passes them to the Raspberry Pi, where they are stored on an SD card. The sensor measurements are not collected according to a fixed and uniform sampling time. Instead, measurements are collected whenever they become available while ROS synchronizes the time signals between all the modules, giving each measurement an accurate time stamp. Each set of sensors connected to a Teensy board can easily be modified, and boards can be added or removed. This modular design makes it easy to adapt or extend to different sensor configurations. Moreover, the system also becomes more robust as the individual Teensy nodes can stop working without disrupting the rest of the system. In Fig. 2.9, an illustration of the interconnections between all the elements in the described DAQ is presented.

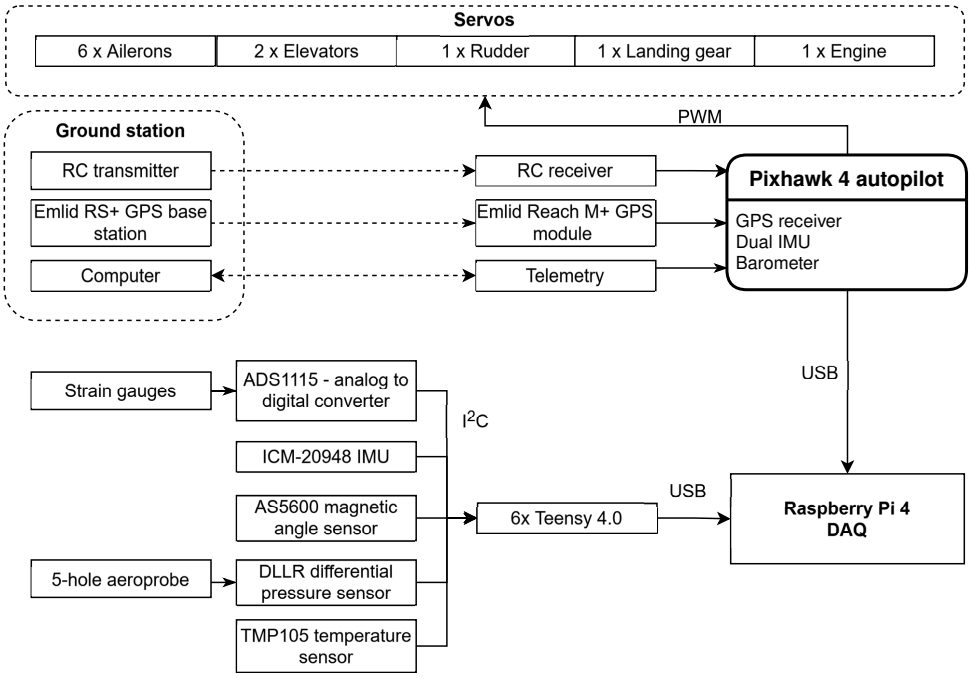

Figure 2.9: Diana 2 DAQ system overview.

As can be seen, six Teensy boards were installed in total. There are two in both wings and one in the tail collecting the strain gauge, IMU, and control surface angle measurements. Finally, there is one in the fuselage for the 5-hole aeroprobe.

2.3.8. SENSOR PLACEMENT OPTIMISATION

After selecting the sensors, it was necessary to determine the number of sensors required and their optimal placement. For some sensors, such as the rotary encoders and the L-shaped aeroprobe, their placement was straightforward. The rotary encoders were placed on all eight control surface servos, while the aeroprobe was positioned on the right side of the fuselage to avoid interference from the propeller, as discussed earlier. The Pixhawk 4 board and the GPS receiver are also placed in the fuselage near the aircraft's centre of gravity to minimize the influence of structural dynamics on their measurements.

As mentioned before, strain gauges are used to estimate the load distribution on the aircraft structure. For this, the wings were divided into three sections according to the ailerons, and the strain gauges were placed at the wing root side of each aileron. To avoid the region where the main spar connects both wings to the fuselage, the inner strain gauges were placed near the middle of

the inner flap as seen in Fig. 2.10. At each location on the wing, there are two full bridge shear strain gauges for monitoring the torque loads on the wings and a single full bridge strain gauge to capture the bending due to lift. The shear gauges are placed in front of and behind the main spar, while the bending gauges are on the top and bottom skin to complete the full bridge. At the tail, there is a single full bridge shear strain gauge, while the full bridges for bending are completed by having strain gauges on the top and bottom sides and left and right sides. This allows to monitor the torque, side force and lift at the tail. An example of the strain gauge installation can be seen in Fig. 2.10. In total, 21 strain responses are measured.

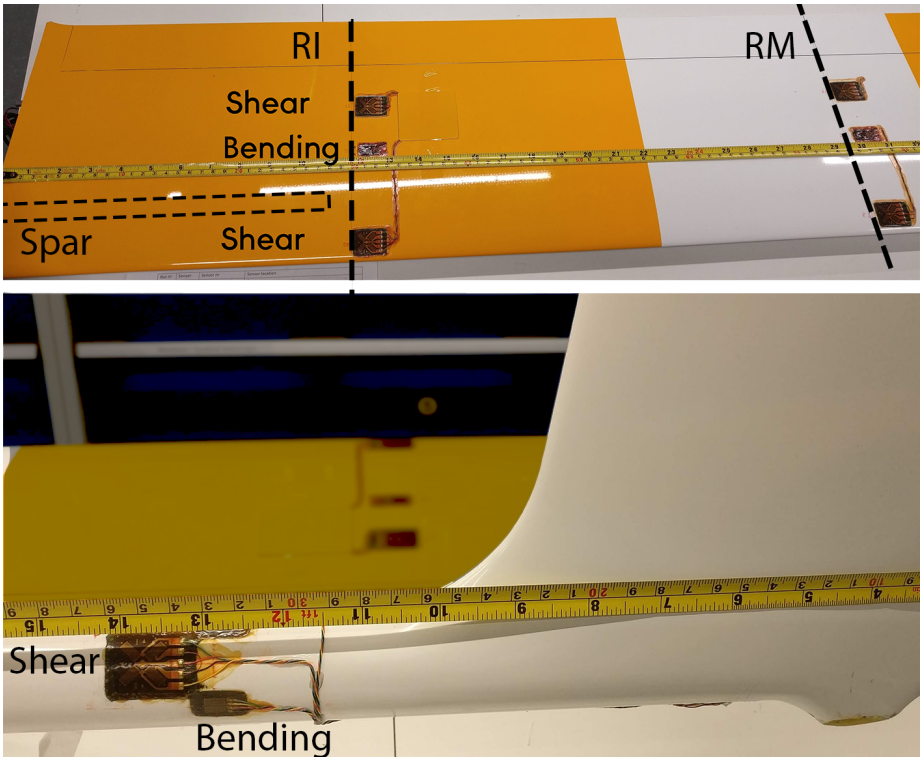

Figure 2.10: Strain gauge placement on the wings and tail.

In addition to estimating loads, the strain gauges also provide information about the structural deformations during flight. Additional IMUs are installed across the structure to complement the strain gauge measurements with acceleration and rotational rate response measurements to capture the structural response. To be able to evaluate different IMU placement configurations, a finite element method (FEM) model was used that has been updated using ground vibration test results from Chapter 3. The structural mode shapes obtained from the FEM model allowed to find the most effective locations for the IMUs. The advantage of using

IMUs instead of only accelerometers is the ability to measure the rotation of the wing using a single sensor instead of requiring a pair of accelerometers. This allowed placing the IMUs in a single line along the wings. To capture all the structural modes below 60 Hz, a configuration with 12 IMUs was determined. Therefore, in addition to the Pixhawk 4 board in the fuselage, four additional IMUs are placed on both wings and three IMUs on the tail.

In Fig. 2.11, an overview of the final integrated sensor positions is presented. Sensor positions on both wings are identical, while in Fig. 2.11, the strain gauge locations are presented on the right wing and IMUs together with magnetic rotary encoders on the left wing for clarity. There are three full bridge strain gauges at each strain gauge location, as described before.

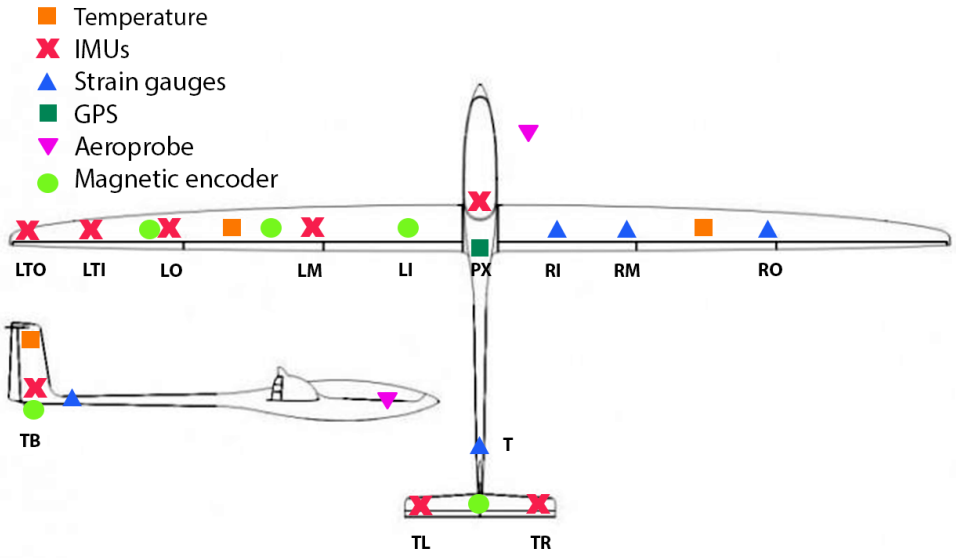

Figure 2.11: Diana 2 sensor placement overview and node naming convention.

2.4. CALIBRATION

After building the DAQ, it was necessary to calibrate many of the sensors before meaningful data could be obtained. This section presents an overview of the experiments conducted for sensor calibration and the calibration procedures.

2.4.1. AEROPROBE CALIBRATION FOR AERODYNAMIC ANGLE MEASUREMENTS

In order to establish an accurate relation between the measured pressure differences and the corresponding angle of attack and sideslip, a wind tunnel

calibration of the aeroprobe was conducted within the controlled environment of the TU Delft M-tunnel. The M-tunnel, characterised by an open jet configuration, features a test section measuring 0.4 x 0.4 m and supports velocities up to a maximum of 35 m/s. During the calibration procedure, the aeroprobe was securely positioned within the wind tunnel, and its angular position relative to the airflow was systematically varied along a single axis while maintaining a fixed angle on the orthogonal axis. A series of angle sweeps were performed at various constant angle offsets at airspeeds of 20, 25, and 30 m/s for both the angle of attack and sideslip measurements. To determine the aeroprobe angle with respect to the airflow, an IMU functioning as an inclinometer was mounted to the probe, enabling the measurement of gravitational acceleration. By leveraging this information to determine the probe's orientation relative to the gravitational vector, the aeroprobe angle was precisely monitored throughout the angle sweeps conducted within the wind tunnel. The constant offset angle was determined manually. Figure 2.12 provides an overview of the wind tunnel setup employed during the calibration process.

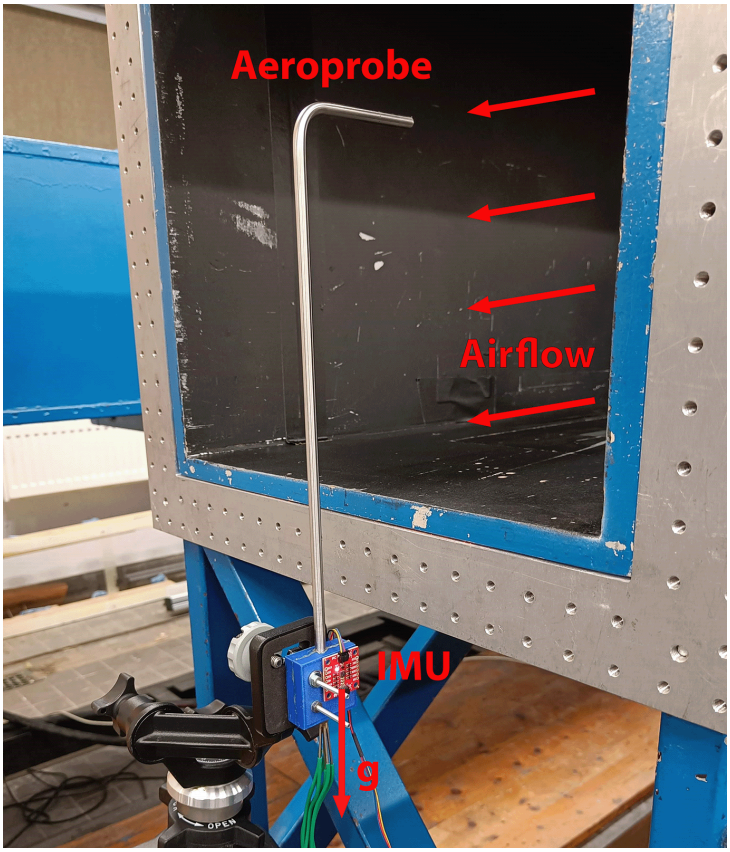

Figure 2.12: Aeroprobe calibration setup.

To model the aeroprobe, the aerodynamic angles covering the range of ±20 degrees were used. A linear model structure was adopted for the probe, as shown in Eq. (2.2) [19].

$$\alpha = C_\alpha \frac{\Delta p_\alpha}{\Delta p_V} \tag{2.2}$$

$$\beta = C_\beta \frac{\Delta p_\beta}{\Delta p_V} \tag{2.3}$$

Here, Δp_α and Δp_V represent the pressure differences measured in pascals by the angle of attack and dynamic pressure channels, respectively. The fitting coefficient C_α was obtained from the measurements to determine the angle of attack α in radians. The same procedure was applied to determine the sideslip angle β.

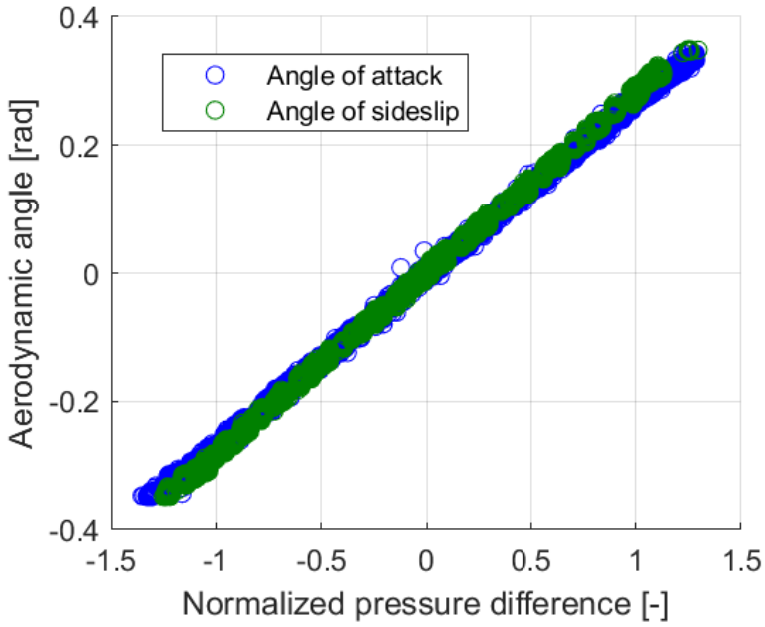

Figure 2.13: Angle of attack and angle of sideslip calibration responses.

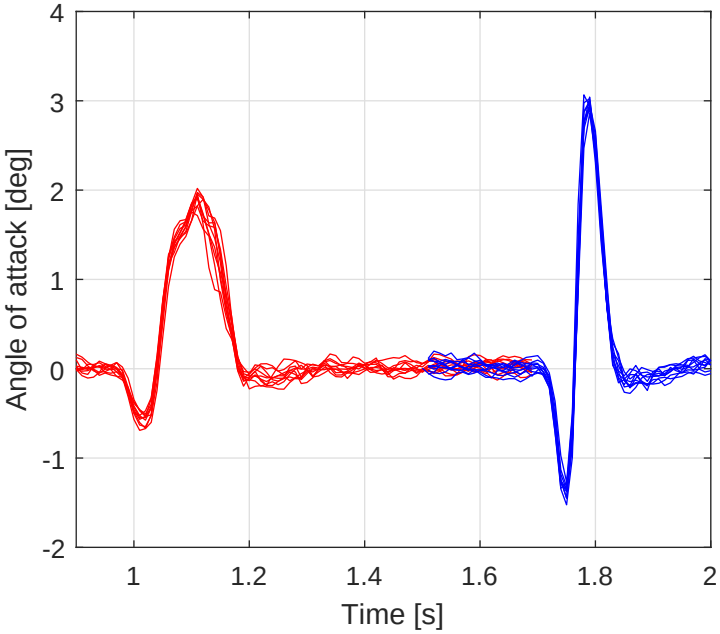

Figure 2.14: Wind tunnel gust response measurements - 5 Hz gusts (red), 10 Hz gusts (blue) at 12 m/s airspeed.

The wind tunnel measurements are presented in Fig. 2.13, where the experimental results exhibit a distinct linear trend between the aerodynamic angle and the measured probe pressure difference scaled by the dynamic pressure. Based on these responses, the slopes for $C_\alpha = 0.27$ and $C_\beta = 0.28$ were derived. The root mean square error (RMSE) for the fitting process amounted to 0.19 degrees and 0.21 degrees for the angle of attack and sideslip, respectively.

Furthermore, the aeroprobe was also tested in a dynamic setting by measuring the responses of a gust generator in the wind tunnel. Figure 2.14 presents the superimposed gust responses, with 5 Hz gusts shown in red and 10 Hz gusts depicted in blue. As observed, both the gust generator and the aeroprobe demonstrated consistent measurements, indicating their reliability in capturing fast and dynamic responses.

2.4.2. Control surface dynamics modelling

Control surface deflection angles are measured using a rotary encoder positioned at the servo axis. However, since there is a linkage between the servo and the control surface, it is necessary to calibrate the rotary encoders to obtain accurate deflection measurements. For this purpose, the control surface positions were varied and measured across their entire range to properly zero the trim positions and normalize the measurements to a -1 to 1 range. Furthermore, the physical

limits for each control surface deflection angle were also measured and are presented in Table 2.3.

The magnet and the rotary encoder were attached directly to the servo axis for all control surfaces except the elevator. The elevator is divided into two control surfaces operated by individual servos facing each other, as illustrated in Fig. 2.15. Consequently, there is no space available to place a sensor on the servo axis. However, the AS5600 sensor can also measure the magnetic field strength. Therefore, a magnet was placed on the servo linkage instead, and the sensor was positioned next to it. This configuration allows to measure the magnetic field strength as the magnet moves closer to or farther away from the sensor during surface movement.

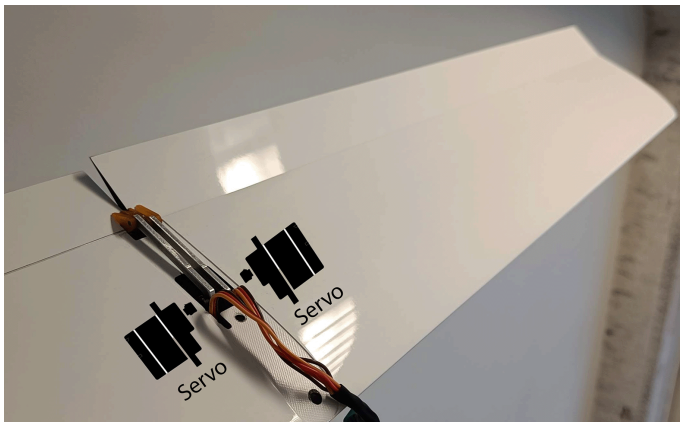

Figure 2.15: Elevator servo placement.

To correlate the magnetic field measurement with the elevator angle, a calibration test was conducted in which the elevator position was gradually varied across its entire range. Using the collected responses, a model for the elevator angle was created according to Eq. (2.4). Some outliers can be observed at the upper end of the deflection range. These were likely caused by accidentally moving the surface too fast during calibration, resulting in a mismatch between the commanded and actual surface deflection.

$$\delta_e = C_{e2} \log^2(H) + C_{e1} \log(H) + C_{e0} \tag{2.4}$$

Here, δ_e represents the normalized elevator angle, H stands for the magnetic field strength, and C_{e0}, C_{e1}, and C_{e2} are the fitting coefficients. The measurement points and the fitted model with coefficients $C_{e0} = 2.3630$, $C_{e1} = -1.8179$, and $C_{e2} = 0.2345$ are presented in Fig. 2.16. The fitted model achieved a root mean squared error of 0.055 on the normalized elevator angle data corresponding to 1.32 deg.

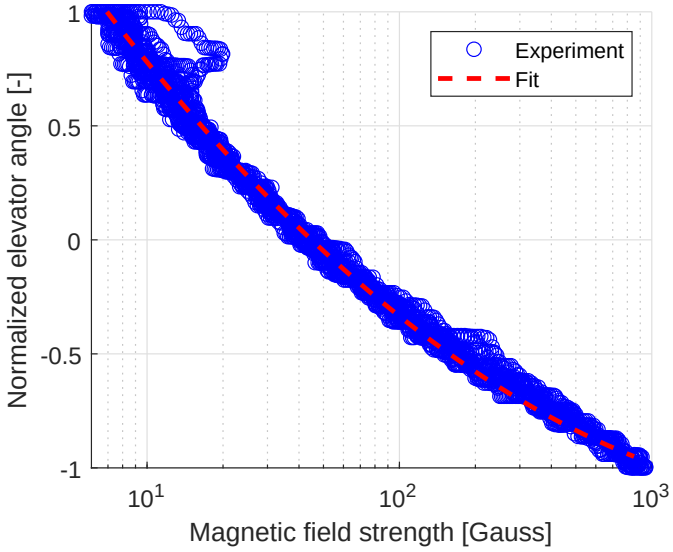

Figure 2.16: Elevator angle modelling using magnetic field measurement.

To evaluate whether the control surfaces have sufficient bandwidth to control or excite the structural frequencies during flight testing, their dynamic models were identified. For this purpose, a reference command consisting of a sine sweep and step references was given to each surface, and their responses were measured. The sine sweep was conducted up to a frequency of 10 Hz at an amplitude of 25% of each control surface's full range. In Fig. 2.17, the reference signal and the right wing outer aileron response are presented as an example.

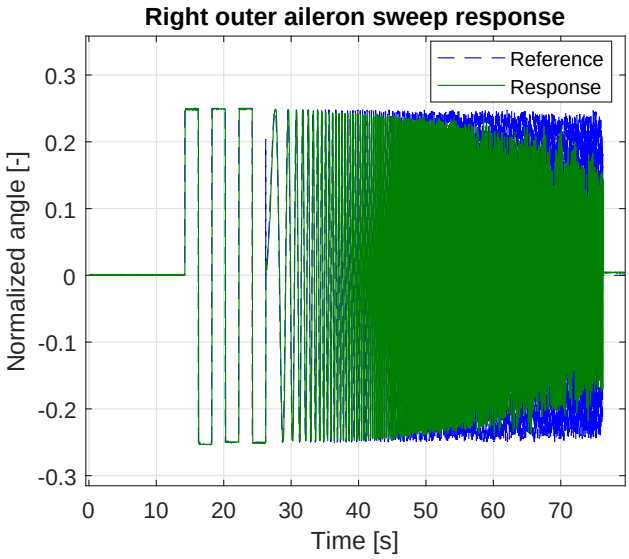

Figure 2.17: Control surface reference signal and right outer aileron response.

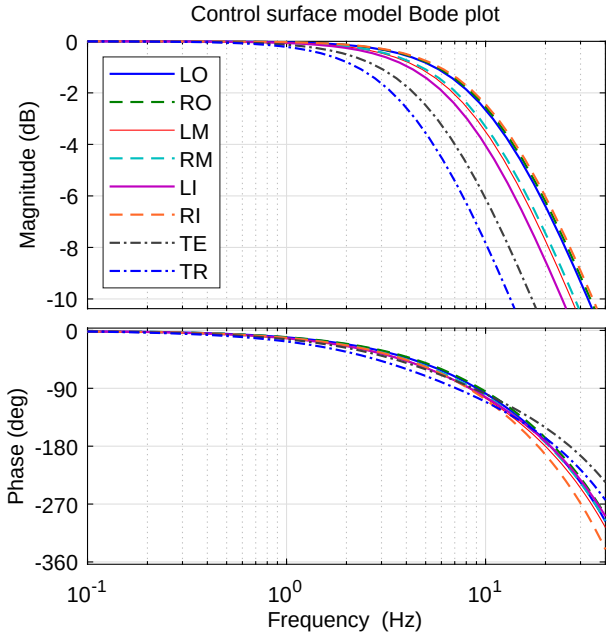

Figure 2.18: Identified actuator model Bode plots.

The reference and response angle signals were used to model the control surfaces as a first-order transfer function together with a delay term, as presented in Eq. (2.5). The identified parameters are presented in Table 2.3 along with the corresponding Bode plots shown in Fig. 2.18.

$$G(s) = \frac{1}{1+\tau s} e^{-T_d s} \tag{2.5}$$

Table 2.3: Identified control surface parameters.

Control surface	Abbrv.	Delay [ms]	Time constant (τ)	Fit [%]	Min [deg]	Max [deg]
Aileron, left wing, outer	LO	15.4	0.0146	87.1	-24	23
Aileron, right wing, outer	RO	14.8	0.0142	86.4	-25	23
Aileron, left wing, middle	LM	15.9	0.0177	86.8	-18	20
Aileron, right wing, middle	RM	15.2	0.0170	89.2	-19	23
Aileron, left wing, inner	LI	14.6	0.0197	88.8	-29	27
Aileron, right wing, inner	RI	18.5	0.0138	87.6	-28	30
Elevator	TE	10.7	0.0279	87.3	-24	20
Rudder	TR	12.5	0.0358	87.2	-31	39

In general, the identified parameters are consistent between the left and right wings, as expected given the use of identical servo types. An exception is observed for the right inner aileron, which exhibits a slightly higher delay and a lower time constant. This discrepancy may be attributed to variations among individual servos, highlighting the importance of identifying each control surface.

Differences are also observed between the inner, middle, and outer ailerons, with the outer control surfaces exhibiting faster dynamics than the inner ones. This trend is consistent with the variation in control surface size, which is approximately 386, 378, and 281 cm^2 for the inner, middle, and outer sections, respectively, corresponding to relative sizes of 100%, 98%, and 73%.

2.4.3. STRAIN GAUGE LOAD CALIBRATION AND TEMPERATURE BIASES

The strain gauges were installed at multiple sections of the wings and at the tail to measure the structural deformations and loads during the flights. However, a calibration process is required before the loads can be determined from the strain measurements. This involves subjecting the aircraft to known loads while recording the resulting strains. Subsequently, a model can be developed to establish the relationship between the measured strains and the equivalent static loads.

Before conducting the load calibration, it is necessary to eliminate constant biases and temperature effects from the strain measurements. The strain gauges are supplied by an excitation voltage, and the resulting voltage difference is measured using the ADC sensors. The strain for strain gauges configured in a full-bridge arrangement can then be calculated using Eq. (2.6).

$$\varepsilon_i = -\frac{V_m}{V_{ref}} \frac{1}{G_{GF}} \tag{2.6}$$

Here, ε_i is the calculated strain, V_m is the voltage difference measured across the strain gauge, V_{ref} is the excitation voltage, and G_{GF} is the gauge factor. The gauge factors for the shear and bending gauges used in the scaled glider are 2.08 and 2.105, respectively.

Differences in wire sizes or properties connecting the strain gauges to the ADC can cause a nonzero voltage output even in the absence of load on the structure and, therefore, cause biases in the calculated strains. Additionally, temperature variations can lead to changes in calculated strains even under constant load due to different thermal expansion coefficients.

To account for these biases, the aircraft was placed in an unloaded condition within a heated room and subsequently cooled. The temperature was gradually adjusted from 24 deg to 15 deg over approximately 2 hours. Figure 2.19 provides an example response displaying the strains measured at the tail.

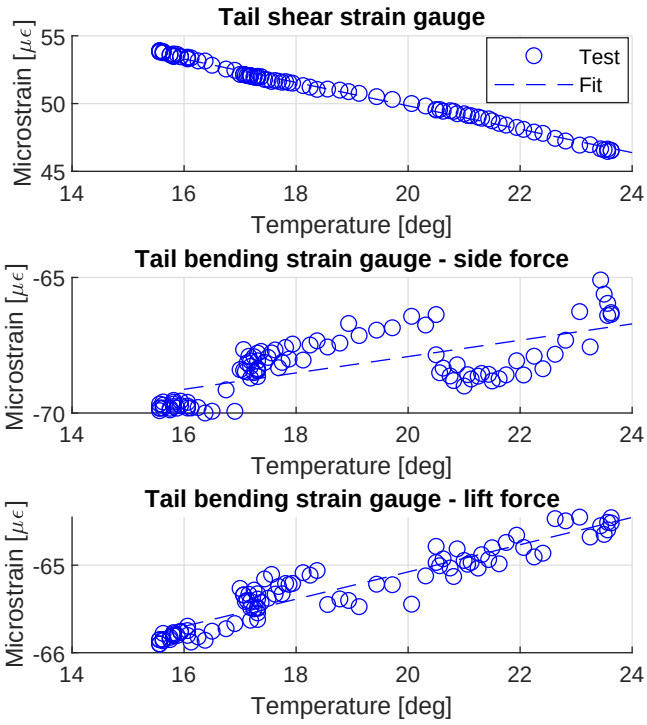

Figure 2.19: Tail strain gauge constant offset and temperature bias.

The calculated strain ε_i can be described by three separate contributions as

shown in Eq. (2.7).

$$\varepsilon_i = \varepsilon_0 + \varepsilon_T(T - T_{ref}) + \mu_i L_{ext} \tag{2.7}$$

where ε_0 is the constant bias, ε_T is the temperature gradient and T, T_{ref} are the measured and reference temperature, respectively. L_{ext} corresponds to the external load and μ_i is the corresponding calibration coefficient. A reference temperature of $T_{ref} = 15.0\ °C$ was used for the modelling.

Since no external load was applied during the temperature testing, it was possible to determine the constant offset bias and temperature gradient terms. As shown previously in Fig. 2.11, the placement of the strain gauges allows the splitting of the main wings into three sections - inner, middle, and outer. The biases were estimated for all the strain gauges, and the results are presented in Table 2.4. It can be seen that the bending strain gauges were generally affected more by the temperature changes than the shear strain gauges. This was expected, as the full bridge configuration was completed by placing all the bending gauge patterns in parallel. This makes them highly sensitive to the bending strains but offers less temperature compensation. Instances with low fit values did not indicate a strong temperature influence on the strain gauges, and therefore, the fitted parameters were unable to predict the measurements. However, they can still be applied to remove the constant offset biases from the measurements.

Table 2.4: Strain gauge constant offset (ε_0) and temperature gradient (ε_T) biases.

		Left wing			Right wing		
Segment	Direction	ε_0 [$\mu\varepsilon$]	ε_T [$\mu\varepsilon/deg$]	R^2 fit [%]	ε_0 [$\mu\varepsilon$]	ε_T [$\mu\varepsilon/deg$]	R^2 fit [%]
Outer	TE shear	23.81	-0.27	83.15	-85.50	0.76	49.93
	LE shear	314.05	-0.55	73.71	-150.98	0.09	95.49
	Bending	192.75	1.63	93.13	207.71	1.07	83.78
Middle	TE shear	124.55	-1.48	43.25	47.29	0.15	98.17
	LE shear	-28.25	-0.17	91.79	-44.32	1.19	40.21
	Bending	-51.92	1.82	74.98	229.63	2.07	90.73
Inner	TE shear	62.59	-0.64	55.96	24.80	-0.41	59.68
	LE shear	46.03	0.26	84.98	-31.26	0.17	93.03
	Bending	138.01	0.46	27.96	283.66	1.65	87.11
Tail	Side force	-69.43	0.30	45.05			
	Lift force	-65.86	0.16	88.21			
	Torque	54.15	-0.86	99.27			

With the strain gauge bias terms determined, performing a load-to-strain calibration was now possible. For this purpose, the aircraft's wings and tail were loaded with lead weight blocks and a water ballast to produce different combinations of bending moments and torques. A lift force corresponding to 1.5 times the aircraft weight was applied to the wings at maximum loading. Examples of different loading arrangements are presented in Fig. 2.20. The lead weights were attached to the structure directly, while the water ballast was attached using a clamp. The clamp also allowed to place the lead weights at the leading and trailing edge of the wing to create different bending and torque load combinations.

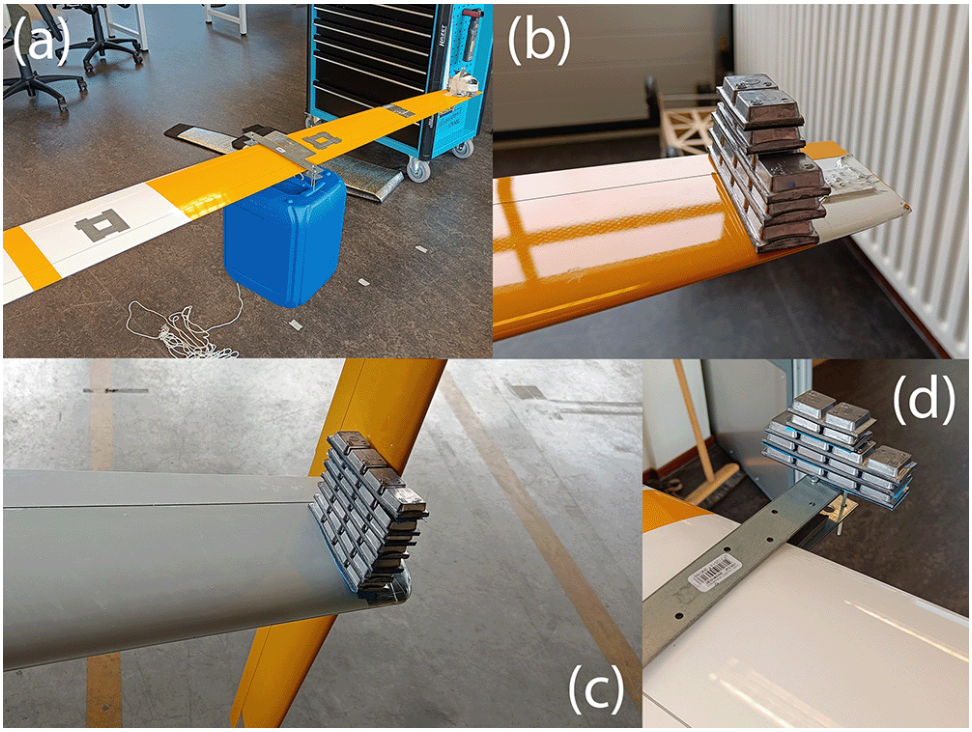

Figure 2.20: (a) Wing lift loading with water ballast and tip weights, (b) wing tip loading weights, (c) tail torque loading on the vertical tail, (d) wing torque loading with weights in front of the wing leading edge.

In total, 98 loading cases were applied to the wings and 91 to the tail. Using the collected strain gauge responses and the applied bending and torque loads, it was then possible to determine the relation between the two for each section of the wings.

Initially, a calibration approach based on the method of Skopinski et al. [20] was considered, in which both bending and shear strain gauge measurements are used simultaneously to estimate the applied loads. However, the measured responses exhibited a clear linear relationship between bending loads and bending strain gauge measurements, as well as between torque loads and shear strain gauge measurements. This behaviour could be accurately captured using a single strain gauge input for each load component. Therefore, a simplified linear model structure with a single strain gauge input was selected, reducing model complexity while maintaining accurate load estimation. In Fig. 2.21, the bending and torque responses and the model fittings are shown for both wings.

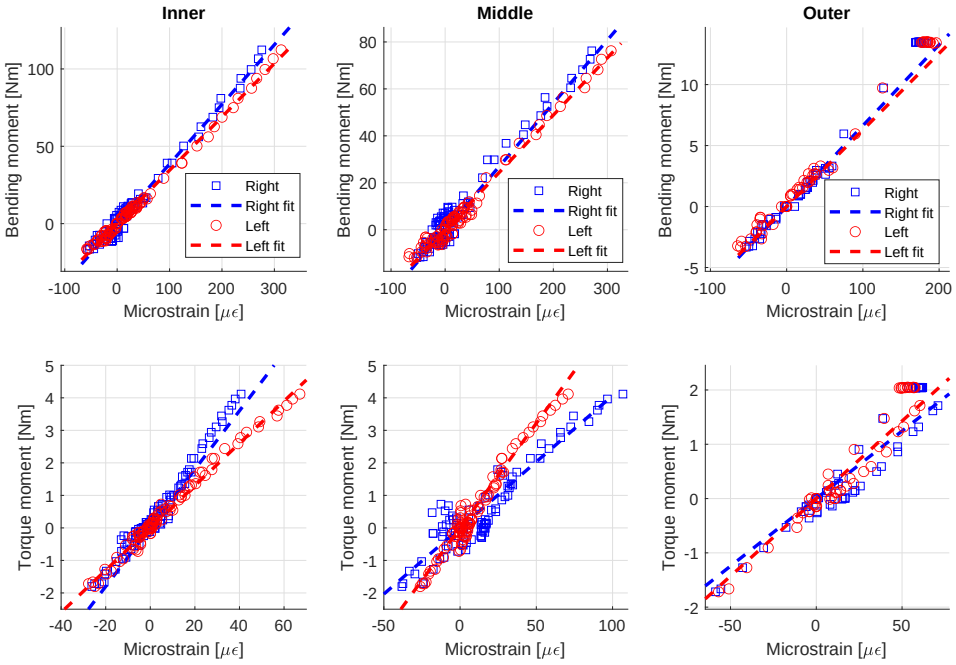

Figure 2.21: Wing bending and torque load calibration for right and left wing inner, middle and outer sections.

In some regions, more scatter can be observed. This is assumed to be mainly due to uncertainties in the applied load location measurements, as the applied weights could sometimes shift, and the clamp would start to warp at higher loads.

A similar approach was followed for the tail load calibration. Weights were placed on horizontal tail tips to produce both positive and negative lift at varying torque moments. To produce side forces, weights were placed on the top and bottom sections of the vertical tail to again achieve different force and torque moment combinations. A linear model structure with a single strain gauge input was also used for the tail calibration to model the loads. The response measurements and the fitted model are presented in Fig. 2.22.

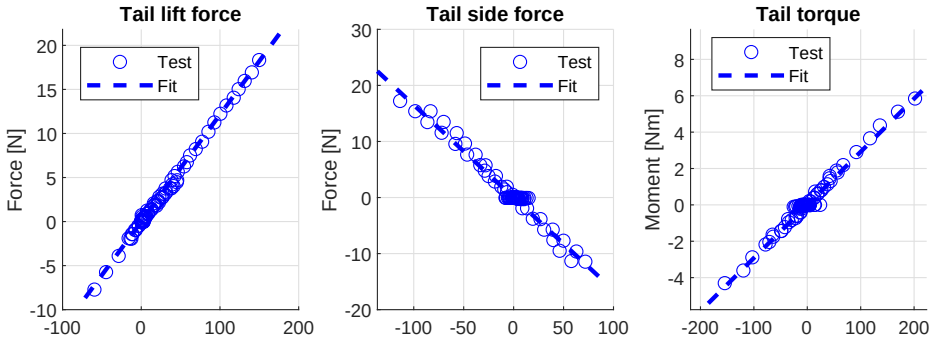

Figure 2.22: Tail load calibration.

Finally, in Table 2.5, all the estimated load calibration coefficients are presented together with the fitting results.

Table 2.5: Load calibration results.

		Left wing		Right wing	
Segment	Direction	$\mu_i[Nm/\mu\varepsilon]$	R^2 fit [%]	$\mu_i[Nm/\mu\varepsilon]$	R^2 fit [%]
Outer	Bending	0.063	96.72	0.066	97.29
	Torque	0.029	90.84	-0.025	88.24
Middle	Bending	0.244	98.17	0.269	94.95
	Torque	0.064	95.56	-0.041	86.29
Inner	Bending	0.345	99.52	0.385	97.93
	Torque	0.065	98.60	-0.090	93.82
Tail	Lift	0.121	99.53		
	Side	-0.165	97.17		
	Torque	0.029	97.67		

2.4.4. INERTIAL MEASUREMENT UNIT CALIBRATION AND ALIGNMENT

During the installation of the IMUs, the sensors are placed across the aircraft structure. In some locations, it is possible to align the sensor according to the aircraft body axis reference frame as defined in Fig. 2.23. However, in most cases, the sensor orientation is dictated by the orientation of the structure it is attached to. Therefore, an alignment correction needs to be applied to the measured signals. This correction transforms the sensor measurements from the sensor axis to the aircraft body axis as shown in Eq. (2.8) and (2.9).

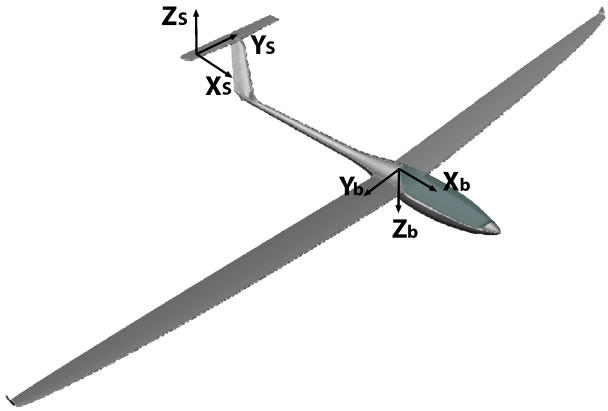

Figure 2.23: Aircraft body axis reference frame.

$$\boldsymbol{A}^{\boldsymbol{b}}_{\boldsymbol{xyz}} = \boldsymbol{T}_{\boldsymbol{bS}}(\theta_x, \theta_y, \theta_z)\boldsymbol{A}^{\boldsymbol{S}}_{\boldsymbol{xyz}} \tag{2.8}$$

$$\boldsymbol{T}_{\boldsymbol{bS}}(\theta_x, \theta_y, \theta_z) = \begin{bmatrix} 1 & 0 & 0 \\ 0 & \cos\theta_x & \sin\theta_x \\ 0 & -\sin\theta_x & \cos\theta_x \end{bmatrix} \begin{bmatrix} \cos\theta_y & 0 & -\sin\theta_y \\ 0 & 1 & 0 \\ \sin\theta_y & 0 & \cos\theta_y \end{bmatrix} \begin{bmatrix} \cos\theta_z & \sin\theta_z & 0 \\ -\sin\theta_z & \cos\theta_z & 0 \\ 0 & 0 & 1 \end{bmatrix} \tag{2.9}$$

Here $\boldsymbol{A}^{\boldsymbol{S}}_{\boldsymbol{xyz}}$ represents the measured acceleration vector in the sensor frame and $\boldsymbol{A}^{\boldsymbol{b}}_{\boldsymbol{xyz}}$ in the aircraft body frame, and the transformation matrix $\boldsymbol{T}_{\boldsymbol{bS}}$ between the two reference frames consists of three rotations $\theta_X, \theta_y, \theta_z$.

A calibration measurement was conducted to determine these rotations for each sensor. During this test, the aircraft was kept steady at various roll and pitch angles while the IMU acceleration and gyro measurements were recorded. The spar surface connecting both wings was chosen as the reference XY-plane for the body axis frame. As these accelerometers also capture the gravity vector, it is possible to use gravity as a reference for the alignment at given roll and pitch angles. Furthermore, the constant offset biases of the accelerometer and gyro can be estimated during the steady test conditions. In total, nine different roll and pitch angle combinations were recorded as presented in Table 2.6.

Table 2.6: IMU alignment test cases.

Test	1	2	3	4	5	6	7	8	9
Roll angle [deg]	0.0	5.3	10.5	-5.1	-10.4	0.0	0.0	0.0	0.0
Pitch angle [deg]	0.0	0.0	0.8	0.0	1.5	5.4	10.0	-4.9	-10.4

For the accelerometers, the constant biases are estimated together with a scaling factor λ_G, while for the gyros, only the constant biases are estimated.

The inclusion of the scaling factor provides an indication of the accuracy of the measured acceleration magnitudes.

$$\boldsymbol{A^S_{xyz}} = \boldsymbol{A^S_{xyz_m}} \lambda_G + \boldsymbol{\lambda_{A_{xyz}}} \tag{2.10}$$

$$\boldsymbol{\omega^S} = \boldsymbol{\omega^S_m} + \boldsymbol{\lambda_{\omega_{xyz}}} \tag{2.11}$$

Here $\boldsymbol{A^S_{xyz_m}}$ and $\boldsymbol{\omega^S_m}$ are the measured accelerations and rotational rates while $\boldsymbol{\lambda_{A_{xyz}}}$ and $\boldsymbol{\lambda_{\omega_{xyz}}}$ are the corresponding constant biases. The calibration and alignment results for all the sensors are presented in Table 2.7 according to the naming convention presented in Fig. 2.11. The offset biases for the Pixhawk IMU (PX) are estimated and corrected by the PX4 autopilot software.

Table 2.7: IMU alignment calibration and bias estimation results.

	Calib. angles [deg]				Accel. biases [m/s^2]			Gyro biases [rad/s]		
Sensor	θ_x	θ_y	θ_z	λ_G	λ_{Ax}	λ_{Ay}	λ_{Az}	$\lambda_{\omega x}$	$\lambda_{\omega y}$	$\lambda_{\omega z}$
PX	0.0	180.1	179.4	1.00	0.000	0.000	0.000	0.000	0.000	0.001
RTO	0.5	1.1	-1.9	0.97	0.004	0.003	0.005	0.016	-0.002	0.005
RTI	182.9	178.2	0.0	0.98	0.000	0.000	0.000	0.016	-0.016	0.004
RO	2.4	-3.6	0.2	0.97	-0.001	-0.002	0.010	0.013	-0.013	-0.003
RM	3.5	-2.9	8.1	0.99	0.002	0.003	0.008	0.005	-0.008	0.005
LTO	-1.7	1.3	179.2	1.00	0.024	-0.013	0.023	0.007	0.006	0.009
LTI	-2.6	1.6	0.3	0.98	-0.001	0.000	0.013	0.019	-0.009	0.002
LO	-5.0	-4.3	1.6	1.00	-0.021	0.094	0.050	0.023	-0.018	-0.006
LM	-0.4	-16.3	71.9	0.99	0.006	0.001	-0.008	0.007	-0.007	-0.003
TB	89.0	0.0	177.1	0.98	0.001	0.000	0.000	-0.005	0.001	-0.002
TR	179.5	2.5	181.1	1.00	0.017	0.008	-0.017	-0.009	-0.009	-0.008
TL	180.3	2.4	0.9	1.03	-0.013	0.009	-0.044	0.010	0.009	0.005

2.4.5. DATA ACQUISITION SYSTEM PERFORMANCE OVERVIEW

As described before, the data acquisition system consists of Teensy 4.0 development boards that collect the measurements from individual sensors and a Raspberry Pi 4, which receives the data from all the boards and stores it. The individual sensors do not have a common trigger signal to start the measurements, but instead, each Teensy board has its own continuous loop where all sensor measurements are triggered, then read and sent to the Raspberry Pi. As the number and type of sensors connected to each Teensy board are different, so are the corresponding sampling rates. Table 2.8 presents an overview of the sampling rate ranges for each type of sensor and the average noise standard deviations to indicate the data acquisition system performance. In total, over 130 different measurements are collected in flight by the system.

The additional weight due to the integration of the DAQ is estimated to be only around 500 g without including the weight of the batteries. In total, the entire DAQ power consumption was measured to be 2.0 amperes at a supply voltage of 8 V, resulting in 16 W, which demonstrates its energy efficiency and suitability for integration into UAV platforms.

Table 2.8: Overview of the measured signals.

Parameter	Hardware	Sampling rate [Hz]	Noise std.
Acceleration	ICM-20948	350-420	0.018 m/s^2
Aerodynamic angles	Amphenol DLLR	100	0.09 Pa
Aircraft position	Emlid Reach M+	14	-
Attitude	Pixhawk 4	30	-
Control surface angle	AS5600	45-80	0.05 deg
Control surface command	Pixhawk 4	40	-
Dynamic pressure	Amphenol DLLR	100	0.21 Pa
Elevator angle	AS5600	45-80	0.24 deg
Rotational rate	ICM-20948	350-420	0.0018 rad/s
Strain	ADS1115	185-260	0.47 microstrain
Temperature	TMP102	0.2	-

The noise values were determined from ground test measurements where the aircraft was stationary. The elevator angle measurement shows larger noise levels than other control surfaces as it is calculated using the magnetic field strength instead. However, as the control surface commands are also recorded, it is possible to create a filter using the control surface model to improve the signal tracking if necessary. The noise for aerodynamic angles is given in pascal, as the angle measurement also depends on the dynamic pressure.

2.5. Flight testing and validation

The flight testing was conducted on the airfield at the Royal Netherlands Aerospace Centre in Marknesse, the Netherlands. The flights were conducted within the pilot's line of sight, with the pilot controlling the glider manually via an RC transmitter. At the start and end of each flight, the aircraft was kept steady and level on the ground for roughly one minute to also record measurements for potential sensor bias corrections. The flights were initiated by taking off and climbing to a maximum flight altitude of 150-200 metres using the electric motor. The climb was followed by the gliding flight phase, during which different excitation manoeuvres were performed for data collection. This sequence was repeated multiple times within a single flight until the engine battery was depleted and the aircraft was landed. In Fig. 2.24, an example segment of a flight trajectory during one of the test flights is presented.

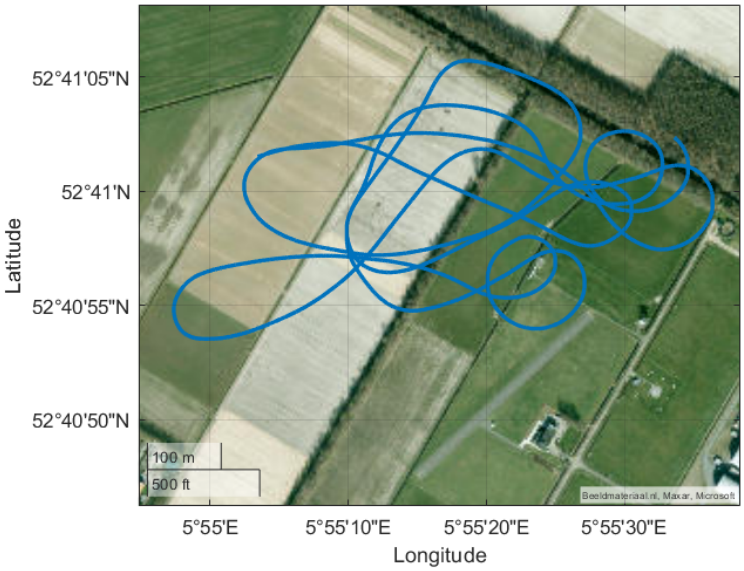

Figure 2.24: Segment of a flight test trajectory.

2.5.1. Excitation Manoeuvres

A total of nine successful test flights were completed across four separate test days, during which various excitation manoeuvres were executed to gather steady and dynamic response data. The excitation inputs included standard system identification manoeuvres - impulse, doublet, 3211, and frequency sweep excitations. Impulse inputs were generated by quickly deflecting a control surface and then returning it immediately to the neutral position. Doublet inputs involved a rapid deflection in one direction, followed by an equally rapid deflection in the opposite direction. The 3211 manoeuvres consisted of four sequential control inputs with varying pulse durations and alternating signs. Frequency sweep inputs were applied by continuously oscillating a control surface while gradually increasing the oscillation frequency throughout the manoeuvre. These inputs were conducted manually by the pilot and applied individually to all control surfaces.

Additional test scenarios included angle of attack sweeps, where the pitch attitude was slowly increased, and sideslip sweeps, in which rudder input was increased to vary the sideslip angle while holding a level wing attitude. Phugoid oscillations were initiated by small pitch increases that led to periodic climb and descent cycles. Some manoeuvres also featured simultaneous excitation of multiple control surfaces, as well as turns at various bank angles.

As mentioned before, the system collects over 130 different measurements during each flight. After the flight, the calibration corrections presented in this

Chapter are applied to the collected measurements.

2.5.2. Flight test and simulation comparison

To validate the sensor calibrations and the resulting flight test measurements, they were compared with open-loop simulation results obtained from an aeroelastic flight dynamics model. This model was developed using ZAERO software, based on potential flow aerodynamics, and coupled with a structural model tuned using ground vibration test (GVT) results from Chapter 3. A more detailed description of the simulation model is provided in Appendix 2.A.

For this comparison, the simulation was initialized using measured flight conditions, and the system response was simulated in open-loop by applying the measured control surface deflections. The resulting simulated responses were then compared with the flight test measurements. It should be noted that open-loop simulations are inherently sensitive to modelling errors, as even small discrepancies accumulate over time and may lead to divergence. In addition, atmospheric disturbances such as turbulence are not represented in the simulation model but were present during flight testing. This can be seen in lateral-directional responses, such as sideslip angle and yaw rate, as the tests were conducted in windy conditions with wind speeds of approximately 5 m/s. Therefore, the simulation results should not be interpreted as ground truth, but rather as a consistency check to assess whether the measured responses are realistic and correctly capture the dominant aircraft dynamics and aeroelastic effects.

To reduce drift in the simulated attitude response and improve comparability, constant trim offsets were applied to the control surface inputs, together with small initial offsets in pitch and roll angles. These offsets were determined through an optimisation routine that minimized the difference between measured and simulated responses, with limits of 10% of the control surface range and 6 deg for the attitude angles.

In Fig. 2.25 and Fig. 2.26, the Diana 2 glider responses to elevator and aileron excitations are compared with the corresponding open-loop simulation results. The presented variables include control surface deflections, rigid-body states (airspeed, aerodynamic angles, body rotational rates, and attitude), as well as differential acceleration and rotational rate measurements between the wing tip and fuselage IMUs to highlight structural dynamics. In addition, distributed wing bending loads at three spanwise locations are shown.

The presented flight test measurements are raw measurements that were resampled to a uniform 200 Hz sampling time, and the presented calibration corrections were applied. The aircraft attitude is obtained from the Pixhawk 4 Kalman filter state estimates.

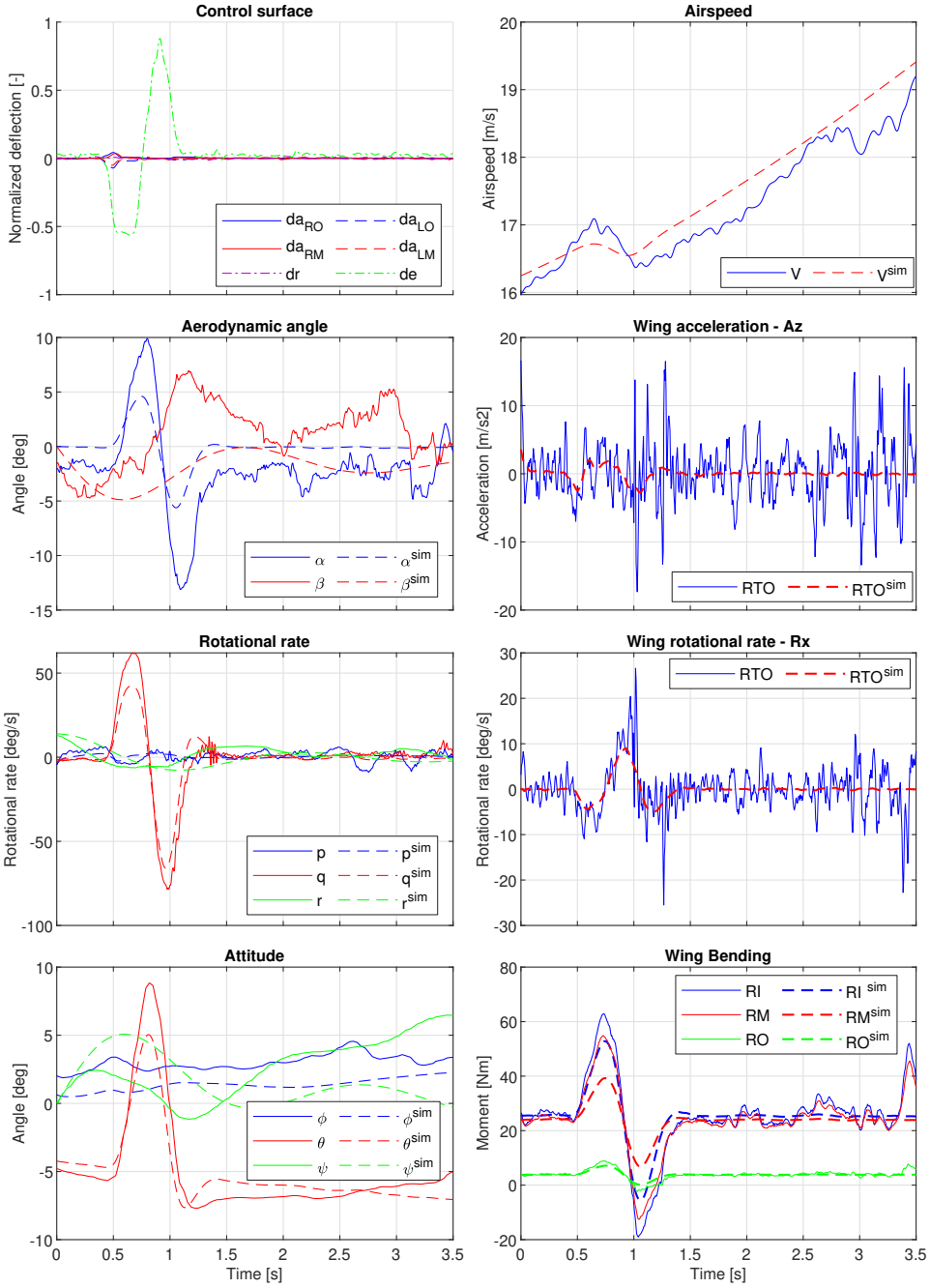

Figure 2.25: Elevator doublet response comparison.

Overall, good agreement is observed between the measured and simulated rigid-body responses. The airspeed is captured accurately, and the main trends in aerodynamic angles, angular rates, and attitude are well reproduced. Remaining discrepancies are assumed to be due to wind disturbances encountered during flight and simplifications in the aerodynamic model, such as the absence of aerodynamic drag forces.

The structural response signals exhibit higher levels of excitation in the flight data compared to the simulation, indicating continuous excitation from turbulence during flight. Nevertheless, the dominant trends match well between the measured and simulated responses. In particular, wing tip acceleration responses during aileron excitation are well reproduced, although the simulation tends to underestimate peak magnitudes.

The distributed wing bending loads show good agreement with the simulation results during elevator excitations, although the load magnitudes for the inner and middle span locations are underestimated by the simulation. For aileron excitations, the responses are noisier but still follow the main trends. As the simulation model is linearized about a trim condition and provides incremental outputs, a constant offset was applied to align the load signals with the measured data.

Figure 2.27 presents the response to a rudder excitation, including horizontal tail IMU differential signals and tail load measurements. Similar to the previous cases, the rigid-body responses show good agreement in terms of overall trends, with deviations mainly attributed to disturbance effects and accumulated errors. The structural response signals again exhibit higher excitation levels in the measurements, while matching the simulation trends. Moreover, the tail load responses show very good agreement in both phase and amplitude.

The observed agreement between measured and simulated responses across multiple excitation cases provides confidence that the developed data acquisition system and calibration procedures are able to capture both rigid-body and aeroelastic responses.

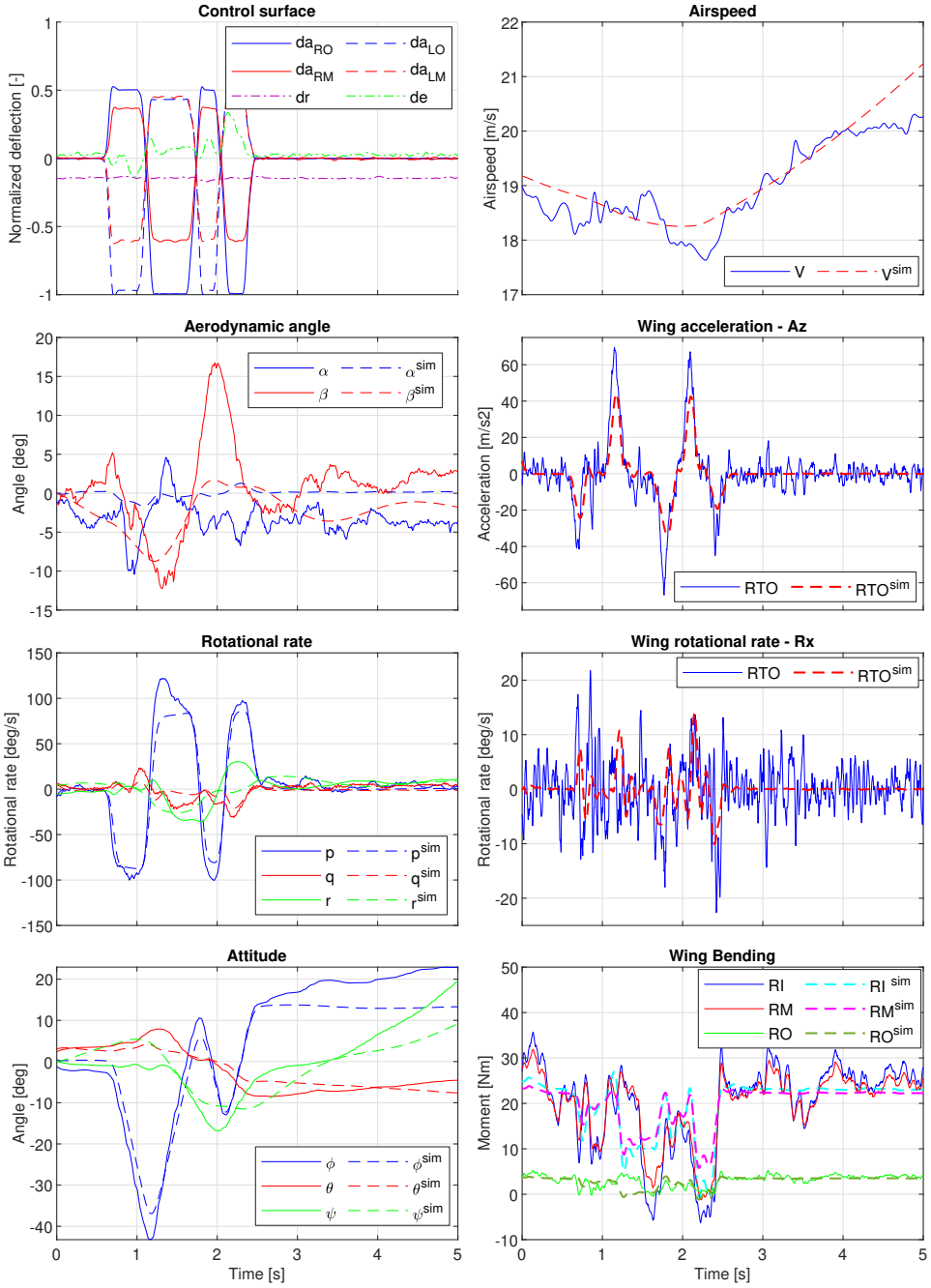

Figure 2.26: Aileron excitation response comparison.

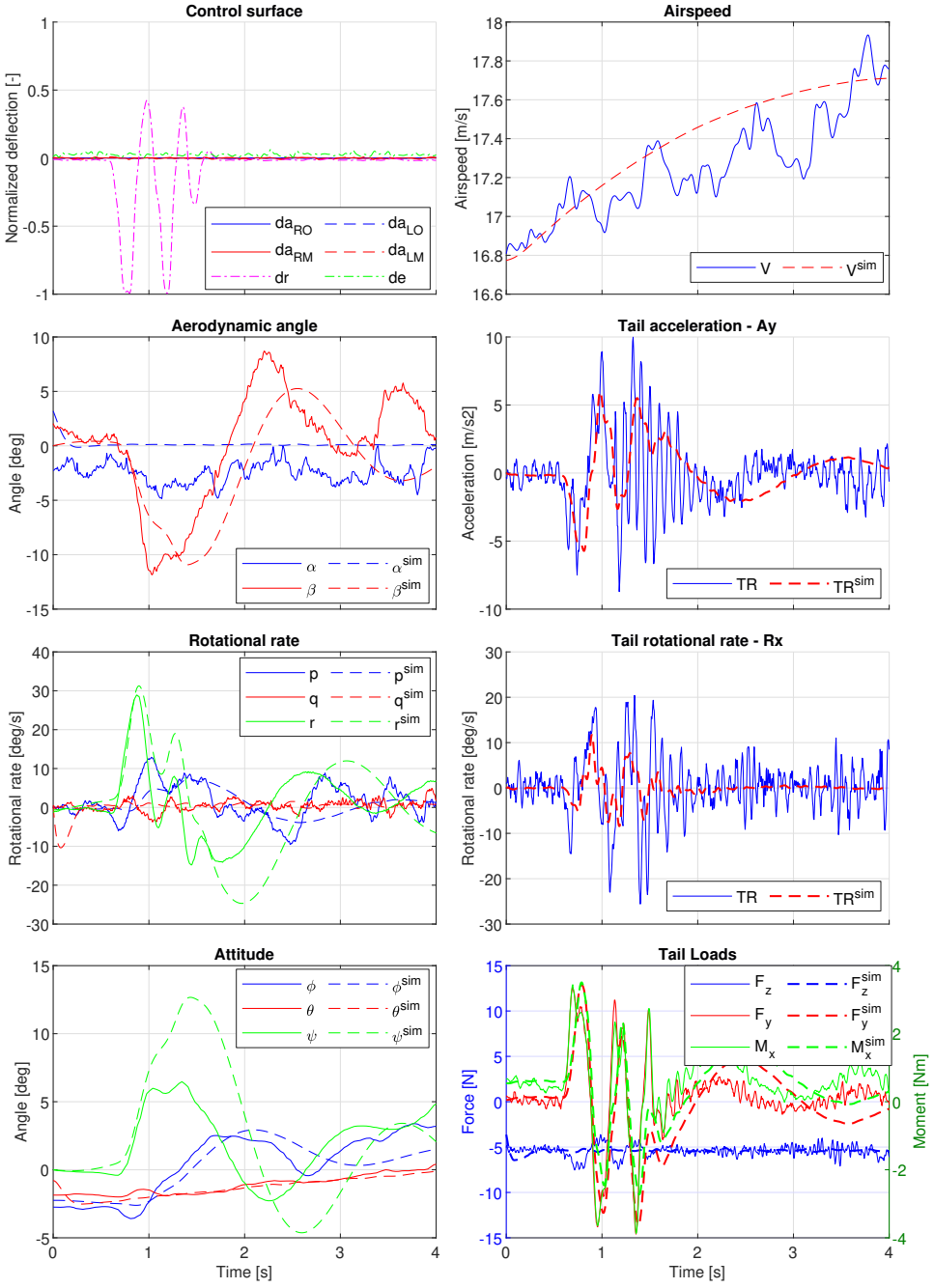

Figure 2.27: Rudder excitation response comparison.

An additional assessment of the sensor sensitivity to aeroelastic responses is performed by analysing the frequency content of the measured signals. Figures 2.28 and 2.29 present the power spectral density of load, acceleration, and rotational rate signals for the wing and tail during elevator and rudder excitation manoeuvres, respectively. The first 12 structural mode frequencies identified from GVT are indicated by dashed vertical lines as a comparison.

As can be seen, frequency content from both the wing and tail sensors includes many peaks matching with the modal peaks obtained during GVT. Small discrepancies in peak locations are expected, as the GVT results do not include aerodynamic effects, which can shift modal frequencies in flight. These results confirm that the developed DAQ system provides sufficient sensitivity to capture the aircraft's aeroelastic responses and that these standard excitation manoeuvres were also able to excite the structural modes.

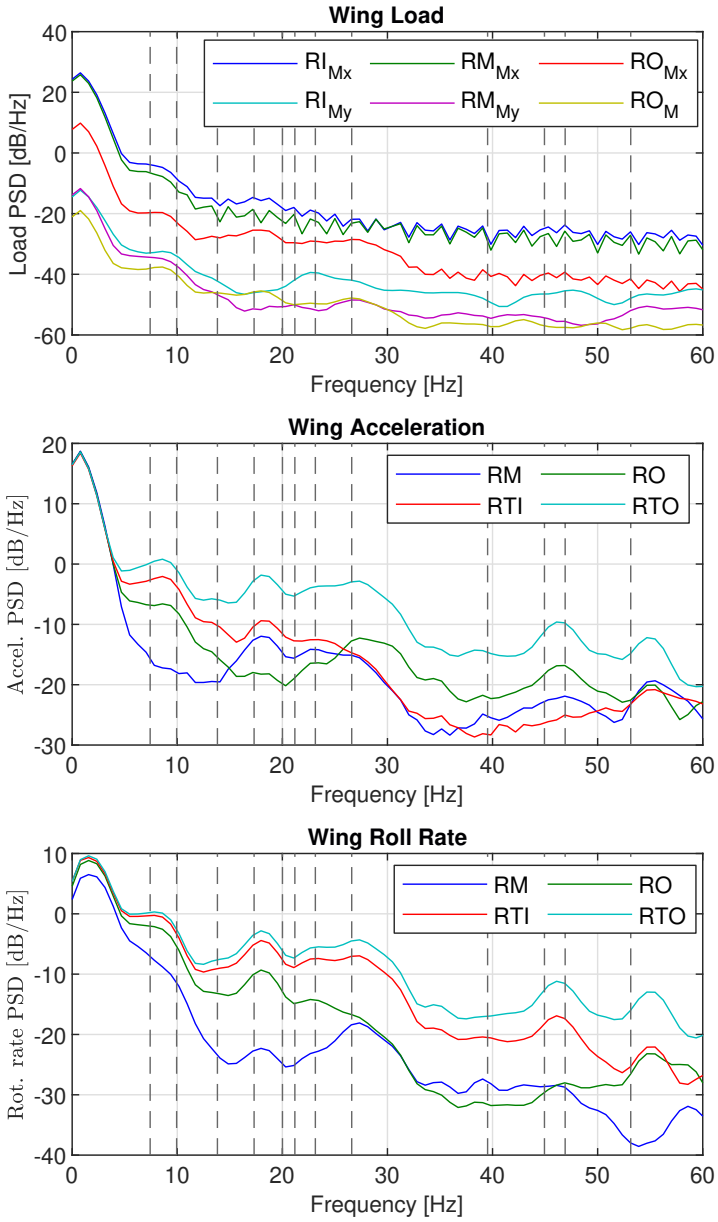

Figure 2.28: Power spectral density of wing load, acceleration, and rotational rate signals from elevator excitation responses.

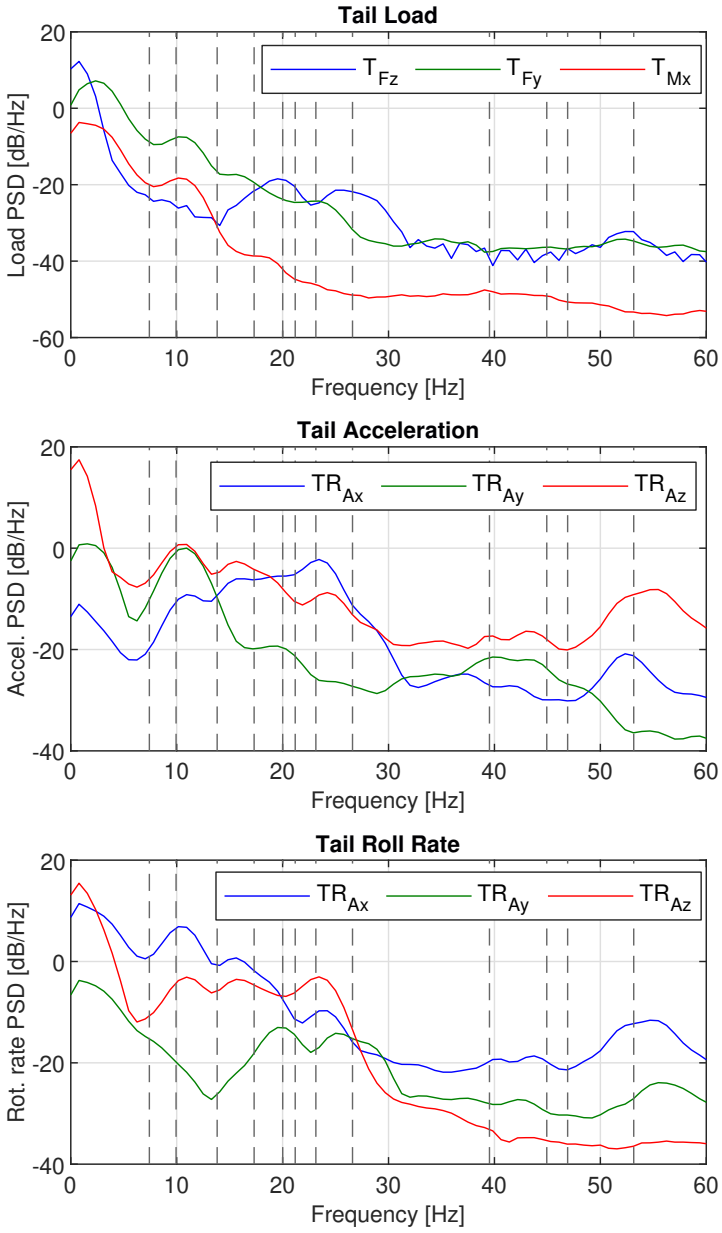

Figure 2.29: Power spectral density of tail load, acceleration, and rotational rate signals from rudder excitation responses.

2.5.3. Data repository

The research data related to this work has been published in the 4TU.ResearchData repository [15]. This includes all the response measurements collected during the flight tests, together with the presented calibration measurements and fitting results. In addition, the configuration files related to the DAQ setup, such as the Teensy 4.0 code and ROS launch files, are also provided. These resources provide a reference system to help streamline implementation for future projects and facilitate customization for other UAV platforms.

2.6. Conclusion

In conclusion, this chapter introduces a low-cost and capable flight test instrumentation system tailored for aeroelastic research, using a scaled Diana 2 glider UAV as a test platform. The system is built with widely available consumer electronic sensors and hardware and implemented using open-source Robot Operating System (ROS) software. The system's modular design allows it to be easily extended or modified to meet different test requirements. To ensure data accuracy, various calibration tests were conducted and presented. These included wind tunnel tests for the 5-hole aeroprobe, load and temperature calibrations for the strain gauges, IMU alignment calibration, and control surface modelling. The developed instrumentation system captures a wide range of flight parameters, including aerodynamic angles, aircraft position and attitude, control surface deflections, structural responses, and loads experienced at various locations on the aircraft. The system was successfully used to gather aeroelastic flight test data, and examples of gathered aircraft responses are given for different excitation manoeuvres. The full dataset with all the collected response measurements has also been published in an open-access repository. Finally, the chapter presents the achieved sampling rates and noise levels as indicators of the system's performance capabilities and as benchmarks for future projects.

REFERENCES

[1] B. G. de Oliveira Silva. “System Identification of Flexible Aircraft in Time Domain”. PhD thesis. Technical University of Braunschweig, Aug. 2018, p. 225.

[2] T. Wilson, J. Kirk, J. Hobday and A. Castrichini. “Small scale flying demonstration of semi aeroelastic hinged wing tips”. In: *International Forum on Aeroelasticity and Structural Dynamics*. Savannah, Georgia, USA: IFASD, June 2019, pp. 1–19.

[3] J. Bartaševičius, S. Koeberle, D. Teubl, C. Roessler and M. Hornung. “Flight Testing of 65kg T-FLEX subscale Demonstrator”. In: *32nd Congress of the International Council of the Aeronautical Sciences, ICAS 2021*. Shanghai, China: International Council of the Aeronautical Sciences, Sept. 2021, pp. 1–16.

[4] M. Wüstenhagen, O. Suelozgen, L. Ackermann and J. Bartasevicius. “Validation and Update of an Aeroservoelastic Model based on Flight Test Data”. In: *2021 IEEE Aerospace Conference*. Big Sky, MT, USA: IEEE, Mar. 2021, pp. 1–18. ISBN: 978-1-7281-7436-5. DOI: 10.1109/AERO50100.2021.9438354.

[5] K. I. Soal, M. Nagy, D. Teubl, R. Volkmar, C. Thiem, M. Y. Meddaikar, B. Vanek, Y. Govers and M. Böswald. “Hardware-in-the-loop testing of a miniaturized real time flutter monitoring system for UAVs”. In: *Proceedings of ISMA 2022 - International Conference on Noise and Vibration Engineering and USD 2022*. Sept. 2022. ISBN: 978-908289315-1. URL: https://elib.dlr.de/188371/.

[6] K. I. Soal, C. Thiem, T. Meier, R. Volkmar, J. Sinske, Y. Govers and M. Böswald. “Embedded flight vibration testing system for online flutter monitoring of UAVs”. In: *19th International Forum on Aeroelasticity and Structural Dynamics, IFASD 2022*. June 2022. ISBN: 978-840942353-8. URL: https://elib.dlr.de/188373/.

[7] P. Gonzalez, G. Starvorinus, F. J. Silvestre, A. Voß, Y. M. Meddaikar and W. Krueger. “TU-Flex: A Very-Flexible Flying Demonstrator with a Generic Transport Aircraft Configuration”. In: *AIAA SCITECH 2023 Forum*. National Harbor, MD, USA: American Institute of Aeronautics and Astronautics, Jan. 2023. ISBN: 978-1-62410-699-6. DOI: 10.2514/6.2023-1312.

[8] C. E. S. Cesnik, P. J. Senatore, W. Su, E. M. Atkins and C. M. Shearer. “X-HALE: A Very Flexible Unmanned Aerial Vehicle for Nonlinear Aeroelastic Tests”. In: *AIAA Journal* 50 (12 Dec. 2012), pp. 2820–2833. ISSN: 0001-1452. DOI: 10.2514/1.J051392.

[9] A. B. G. Neto, G. C. Barbosa, J. A. Paulino, R. M. Bertolin, J. S. M. Nunes, P. J. González, F. L. Cardoso-Ribeiro, M. A. V. Morales, R. G. A. da Silva, F. L. S. Bussamra, F. J. Silvestre, F. J. O. Moreira and C. E. S. Cesnik. “Flexible Aircraft Simulation Validation with Flight Test Data”. In: *AIAA Journal* 61 (1 Jan. 2023), pp. 285–304. ISSN: 0001-1452. DOI: 10.2514/1.J060960.

[10] J. A. Grauer and M. J. Boucher. “Identification of aeroelastic models for the X-56A longitudinal dynamics using multisine inputs and output error in the frequency domain”. In: *Aerospace* 6 (2 2019). ISSN: 22264310. DOI: 10.3390/aerospace6020024.

[11] J. A. Grauer and M. Boucher. “System identification of flexible aircraft: Lessons learned from the X-56A phase 1 flight tests”. In: *AIAA Scitech 2020 Forum*. Orlando, FL: American Institute of Aeronautics and Astronautics, Jan. 2020.

[12] D. K. Schmidt. “Stability Augmentation and Active Flutter Suppression of a Flexible Flying-Wing Drone”. In: *Journal of Guidance, Control, and Dynamics* 39 (3 Mar. 2016), pp. 409–422. ISSN: 1533-3884. DOI: 10.2514/1.G001484.

[13] C. D. Regan. “mAEWing2: Conceptual design and system test”. In: *AIAA Atmospheric Flight Mechanics Conference, 2017*. Grapevine, Texas, USA: American Institute of Aeronautics and Astronautics Inc, AIAA, 2017. ISBN: 978162410448. DOI: 10.2514/6.2017-1391.

[14] C. D. Regan, A. Kotikalpudi, D. K. Schmidt and P. J. Seiler. “mAEWing2: Initial Flight Test and System Identification of a Flexible UAV”. In: *AIAA Scitech 2020 Forum*. Orlando, FL: American Institute of Aeronautics and Astronautics, Jan. 2020. ISBN: 978-1-62410-595-1. DOI: 10.2514/6.2020-1965.

[15] A. Jürisson, B. Eussen, C. C. de Visser and R. De Breuker. *Flexible Diana 2 Scaled Glider UAV - Aeroelastic Flight Test Measurements*. Dataset. 4TU.ResearchData, 2026. DOI: 10.4121/0c3fcef0-5b63-480c-ae40-3ff726c657e9.

[16] J. R. Wright and J. E. Cooper. *Introduction to aircraft aeroelasticity and loads*. Wiley, Dec. 2015. ISBN: 9781118700440. DOI: 10.1002/9781118700440.

[17] Baudismodel.com. *Diana 2 (scale 1/3) - Baudismodel*. 2018. URL: https://www.baudismodel.com/en/production/k2408-actual-production/3-diana-2-scale-1-3.html.

[18] Micro-Measurements. *Precision Strain Gages and Sensors*. Feb. 2016. URL: http://www.vishaypg.com/docs/50003/precsg.pdf.

[19] R. Calmer, G. Roberts and J. Preissler. “3D Wind Vector Measurements using a 5-hole Probe with Remotely Piloted Aircraft”. In: *Atmospheric Measurement Techniques Discussions* (July 2017), pp. 1–33. DOI: 10.5194/amt-2017-233.

[20] T. Skopinski, W. Aiken and W. Huston. *Calibration of Strain-gage Installations in Aircraft Structures for the Measurement of Flight Loads*. NACA R-1178. National Advisory Committee for Aeronautics, 1953, pp. 1–29.

[21] ZONA Technology Inc. *ZAERO Theoretical Manual, Version 9.0*. Scottsdale, Arizona, 2014.

2.A. AEROELASTIC SIMULATION MODEL OVERVIEW

An aeroelastic flight dynamics model of the scaled Diana 2 glider was developed using ZAERO software (ZONA Technology) [21] to support comparison with the flight test measurements. The model consists of a structural representation based on a NASTRAN finite element model, as illustrated in Fig. 2.30 and an aerodynamic model based on lifting surface panels, as illustrated in Fig. 2.31.

The structural model is composed of beam elements and was tuned using ground vibration test results from Chapter 3 to accurately capture the aircraft's modal characteristics. The resulting model includes the six rigid-body degrees of freedom together with the first eight structural modes.

Unsteady aerodynamic effects are represented using a rational function approximation of the aerodynamic forces, enabling a time-domain state-space formulation of the aeroelastic system. The model is driven by control surface inputs and includes virtual sensors for rigid-body states, structural responses, and loads at selected locations. The model is used in this work to generate open-loop response predictions for comparison with the flight test measurements.

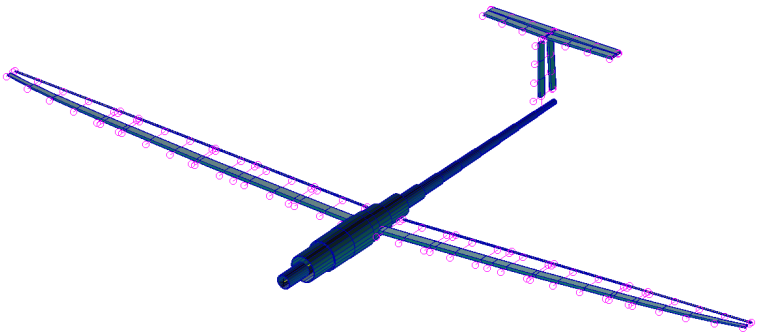

Figure 2.30: Structural beam model for scaled Diana 2 glider.

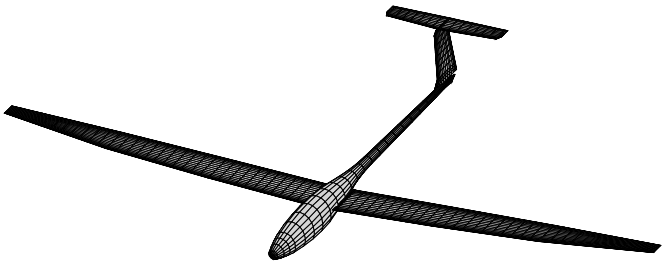

Figure 2.31: ZAERO model for scaled Diana 2 glider.

3

GROUND VIBRATION TESTING OF THE SCALED DIANA 2 UAV

The dynamic response of an aeroelastic aircraft is governed by the interaction between aerodynamic forces and the structural dynamics of the airframe. Ground vibration testing (GVT) provides an experimental approach to estimating the modal parameters that characterise an aircraft's structural behaviour. This chapter presents the GVT results for the scaled Diana 2 glider UAV, obtained using integrated accelerometers, gyroscopes, and strain gauges. By comparing these results with those from an external reference system, the accuracy and sensitivity of the custom data acquisition system was evaluated and validated.

This chapter is based on the following article: Jürisson, A., Eussen, B. J. G., de Visser, C. C., & De Breuker, R., "Combined Estimation of Structural Displacement, Rotation and Strain Modes on a Scaled Glider" in *MDPI Applied Sciences*, 2026

3.1. INTRODUCTION

In the development and certification process of a new aircraft, Ground Vibration Testing (GVT) is an essential step in updating and validating the mathematical models of the aircraft. These models are then used to predict flutter and show that the aircraft is safe to fly within the operating conditions [1, 2]. During the GVT, the aircraft structure is excited with a modal hammer or shakers and the excitation force is measured together with the structure's response. The excitation and response measurements are then used to derive frequency response functions (FRFs) from which modal parameters such as natural frequencies, damping and mode shapes are extracted [3]. In the traditional experimental modal analysis (EMA), the responses are measured using motion sensors such as piezoelectric accelerometers or laser vibrometers. Therefore, the resulting mode shapes correspond to displacement mode shapes. Accelerometers, in particular, have been the standard choice for aircraft GVTs for decades and have been used extensively across many GVT programs [1, 2, 4, 5].

An alternative but a less common approach is to measure the aircraft responses using strain sensors such as strain gauges or fiber Bragg grating sensors. Then, strain frequency response functions (SFRFs) are derived instead, and the resulting mode shapes correspond to strain mode shapes. This allows to directly investigate the strain distribution for different vibration modes in the structure in an experimental manner. The small size and low weight of strain gauges make them especially suitable for testing structures sensitive to the sensors' added mass, such as helicopter or turbine blades [6–9]. In such applications even the small added weight of the accelerometers can result in a shift in modal frequencies and change the mode shapes. Fiber optic strain sensors offer additional benefits, including high sensitivity, immunity to electromagnetic interference, and the possibility of having multiple sensors along a single fiber. These sensors are already being implemented in aircraft and rotorcraft for real-time structural health monitoring for damage or wing shape sensing [10–15]. However, the main drawback of using strain sensors is the need for careful installation to ensure a good quality bond between the strain gauge and the test structure. Moreover, interpreting the strain mode shapes on their own can be challenging as it can be unclear which displacement mode shape they correspond to. Therefore, a GVT using both strain gauges and accelerometers simultaneously is recommended instead by dos Santos and Peeters [7]. This allowed them to obtain a better understanding between the displacement modes and corresponding strains when testing the wings of the F-16 aircraft.

Another relatively unexplored option in aerospace is to measure the response of the aircraft structure using gyroscopes. This allows to use the measured rotational rates to directly estimate the rotational modes instead of indirectly deriving them from the displacement modes. Using gyroscopes for vibration testing has been explored in civil engineering, where it showed improved sensitivity to damage localization when testing concrete beams [16]. The addition of gyroscopes could also bring further advantages to aircraft vibration testing, where improvements to reduce testing time, setup effort, and overall costs are

continuously being explored [1, 5]. For example, to capture the twisting motion of the aircraft wing, the accelerometers are usually placed in pairs along the wing's span. Instead of instrumenting two locations with accelerometers, only one location with a combination of accelerometer and gyro would need to be installed to capture the same information. For a GVT program of an Airbus A380, where around 850 sensors were used [2] or Airbus A350 with more than 500 accelerometers [5], this would reduce the number of sensor locations and could lead to significant time savings during the test preparation. Furthermore, the gyroscope measurements and rotational mode shapes can also be used in flight for improved tracking of the structural modes or wing shape sensing [17].

As different types of sensors each have their own advantages, a combination of different sensor types could lead to further improvements when estimating the aircraft modal parameters during a GVT or in flight. Both 3-axis accelerometers and gyros can be commonly found in inertial measurement units (IMUs). Microelectromechanical system (MEMS) IMUs have become only a few millimetres in size, are very lightweight and low in cost, and can be found in many consumer electronics products like smartphones and smartwatches. One advantage of MEMS IMUs over piezoelectric accelerometers is their ability to capture static and very low-frequency responses, which is particularly beneficial when testing large or highly flexible aircraft with low-frequency structural modes. These characteristics make MEMS sensors an appealing candidate for in-flight structural monitoring and vibration testing, although their performance in GVT environments remains largely unexplored.

This chapter evaluates the feasibility and accuracy of using MEMS accelerometers and gyroscopes in combination with strain gauges for aircraft ground vibration testing and demonstrates simultaneous estimation of displacement, rotation, and strain modes. For this purpose, a GVT was conducted on a 1:3 scaled Diana 2 glider model instrumented with IMUs and strain gauges across its structure for aeroelastic flight testing. The modal parameter estimates obtained using MEMS IMUs and strain gauges were then compared with traditional piezoelectric accelerometer results and a Finite Element Method (FEM) model.

The remainder of this chapter is organised as follows. Section 3.2 presents an overview of the modal analysis theory. Section 3.3 describes the test aircraft and the experimental setup, while Section 3.4 outlines the FEM model updating procedure based on the GVT and load-displacement test data. Section 3.5 evaluates the GVT results obtained using different sensor sets by comparing the estimated modal frequencies, damping ratios, and mode shapes. Finally, Section 3.6 summarises the main findings and conclusions.

3.2. Modal analysis theoretical background

This section gives a brief overview of the equations governing modal analysis, while a more extensive derivation is presented by Silva [18]. The motion of a continuous structure can be approximated as a system of masses, springs, and dampeners. Such a system with an external force excitation can be described as

in Eq. (3.1).

$$\mathbf{M}\ddot{\mathbf{x}}(t) + \mathbf{C}\dot{\mathbf{x}}(t) + \mathbf{K}\mathbf{x}(t) = \mathbf{f}(t) \tag{3.1}$$

where $\mathbf{M}$, $\mathbf{C}$, and $\mathbf{K}$ are the mass, damping, and stiffness matrices, respectively. The column vector $\mathbf{x}(t)$ contains the mass displacements, and $\mathbf{f}(t)$ contains the time-varying excitation forces. When looking at the steady state response in the frequency-domain and using the system modal parameters, it can be represented as in Eq. (3.2).

$$\mathbf{X}(\omega) = \mathbf{\Phi}[\omega_n^2 - \omega^2 + i2\zeta_n\omega_n^2]^{-1}\mathbf{\Phi}^T\mathbf{F}(\omega) = \mathbf{H}(\omega)\mathbf{F}(\omega) \tag{3.2}$$

where ω is the oscillation frequency and $\mathbf{\Phi}$, ω_n and ζ_n are the mode shape matrix, nth natural frequency and nth damping ratio respectively. These parameters are part of the FRF matrix $\mathbf{H}(\omega)$. During the EMA, the goal is to extract these parameters from the test data.

$$\mathbf{H}(\omega) = \sum_{n=1}^{N} \frac{\mathbf{\Phi}_n\mathbf{\Phi}_n^T}{\omega_n^2 - \omega^2 + i2\zeta_n\omega_n^2} \tag{3.3}$$

According to the modal theory, it is then possible to approximate the structural response as a summation of N modal contributions:

$$\mathbf{x}(t) \approx \sum_{n=1}^{N} \mathbf{\Phi}_n\eta_n(t) \tag{3.4}$$

where $\eta_n(t)$ is the generalised modal coordinate of mode n.

These FRFs are traditionally determined from the displacement, velocity, or acceleration responses measured during the vibration testing. However, this formulation is also valid when gyroscopes are used to measure the rotational rate responses. Then, the degrees of freedom in $\mathbf{x}(t)$ correspond to displacement in rotation instead of translation, and the resulting mode shapes are rotational mode shapes rather than displacement mode shapes. When strain responses of the structure are measured, it is possible to relate the strains to modal coordinates as shown in Eq. (3.5) [8, 18].

$$x_\varepsilon(t) = \mathbf{D}\mathbf{x}(t) = \mathbf{D}\mathbf{\Phi}\eta(t) \tag{3.5}$$

$$\mathbf{\Psi} = \mathbf{D}\mathbf{\Phi} \tag{3.6}$$

where x_ε corresponds to measured strains, and $\mathbf{D}$ is a differential operator matrix, which gives the strain mode shapes $\mathbf{\Psi}$ when applied to the displacement mode shape. Transforming the displacement responses in Eq. (3.2) to strain responses, one can obtain the strain frequency response functions $\mathbf{H}^\varepsilon(\omega)$.

$$\mathbf{X}^\varepsilon(\omega) = \mathbf{D}\mathbf{X}(\omega) = \mathbf{\Psi}[\omega_n^2 - \omega^2 + i2\zeta_n\omega_n^2]^{-1}\mathbf{\Phi}^T\mathbf{F}(\omega) = \mathbf{H}^\varepsilon(\omega)\mathbf{F}(\omega) \tag{3.7}$$

$$\mathbf{H}^\varepsilon(\omega) = \sum_{n=1}^{N} \frac{\mathbf{\Psi}_n\mathbf{\Phi}_n^T}{\omega_n^2 - \omega^2 + i2\zeta_n\omega_n^2} \tag{3.8}$$

As the form for both FRFs and SFRFs is similar, it is possible to apply the same modal parameter estimation tools for both cases.

3.3. TEST AIRCRAFT AND SETUP OVERVIEW

The experiments were conducted on a 1:3 scaled Diana 2 glider model. This model was manufactured by Baudismodel [19] and was subsequently instrumented to serve as a test platform for aeroelastic flight testing and flexible aircraft system identification. This composite glider model has a wingspan of 5 m at a weight of 10.7 kg. An overview of the main technical parameters for the model are presented in Table 3.1 together with a picture of the glider shown in Fig. 3.1.

Table 3.1: Diana 2 model technical parameters.

Property	Value	Units
Aspect ratio	24.3	-
Mean chord	0.206	m
Weight	10.7	kg
Wing area	1.03	m^2
Wingspan	5.0	m

Figure 3.1: Diana 2 1:3 scaled glider.

The model was instrumented with IMUs, strain gauges, and other sensors, as presented in Chapter 2. For the IMUs, the ICM20948 MEMS sensors were used, while the strain gauge voltages were measured using ADS1115 16-bit analog to digital converters. External PCB 356A33 and PCB 352C22 piezoelectric accelerometers were used during the GVT to validate the integrated sensor results. In Fig. 3.2, the integrated sensor locations are presented, while Fig. 3.3 shows the placement of the external accelerometers. There are 12 IMUs, all measuring acceleration and rotational rate along three axes. The external accelerometers consist of 5 triaxial and 30 single-axis sensors connected to a SCADAS acquisition system and Siemens Testlab. As can be seen, the reference accelerometers on the wings are placed in pairs of two to capture the wing torsion.

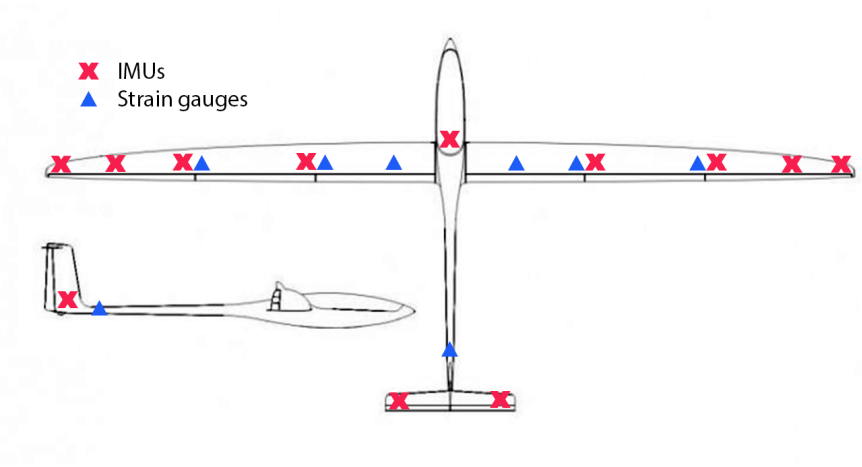

Figure 3.2: Integrated IMU and strain gauge locations.

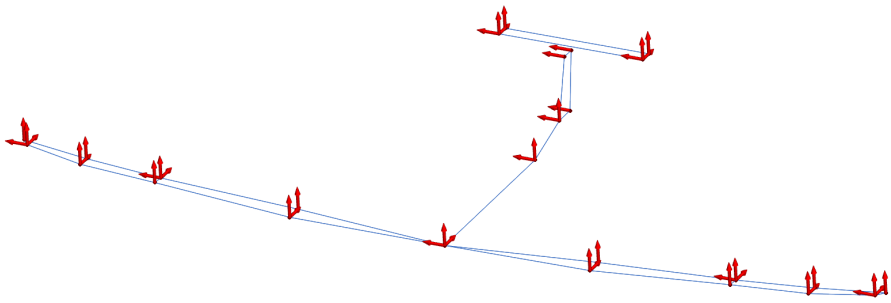

Figure 3.3: Reference accelerometer locations.

Strain gauges are installed at three locations along the span of the wings. Each location has one strain gauge for bending in full bridge configuration and two strain gauges for shear, as seen in Fig. 3.4. At the tail, there are two bending and one shear gauge in full bridge configuration. The strain gauge used for bending is the EA-06-250PD-350, while the CEA-06-250US-350 was used for shear. In total, 21 strain responses are measured.

Figure 3.4: Strain gauge placement on the wings.

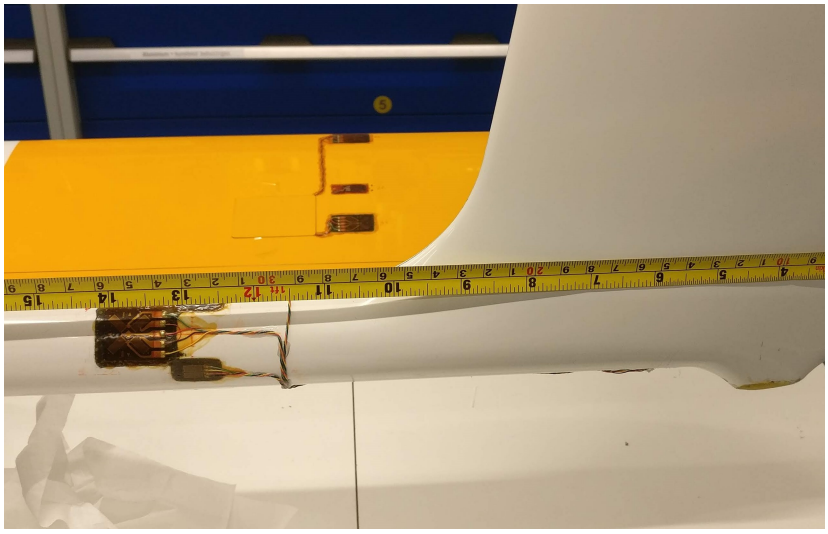

Figure 3.5: Strain gauge placement at the tail.

During the test, the aircraft was suspended with elastic bands and excited with a modal hammer at multiple locations. This test setup can be seen in Fig.3.6.

Figure 3.6: Ground vibration testing setup.

As the structural responses were collected using two different systems (internal and external), it was necessary to synchronize both systems to ensure the correct calculation of the frequency response functions. The modal hammer output was split into two and connected to both systems to achieve this. This allowed the time signals for a given test point and direction to be recorded in a single, long measurement that covered all hammer hits. The peaks corresponding to the hammer impacts were determined, and the time shift between the two systems was calculated for each hit. The time shifts were then averaged to obtain the final time offset applied to the internal system data. The overall magnitude of this offset was in the order of a few seconds, as the data recordings were started at slightly different times. The variations in the time offsets determined between the different hammer hit peaks were less than the sampling time of the

system. At each test location, seven hits were performed to better estimate the average time shift and improve the averaged FRFs for the internal sensors. The custom-built data acquisition system inside the glider does not enforce a fixed sampling time. Therefore, after determining the time shift between the systems, the measurements were also interpolated to match them to the fixed 512 Hz sampling time of the reference system. During the GVT, the objective was to capture structural modes up to approximately 50 Hz. To reduce the influence of high-frequency noise, a low-pass filter with a 100 Hz cutoff was also applied to the data.

3.4. DIANA 2 GLIDER FEM MODEL UPDATING

A FEM model of the glider was created and updated using the GVT test responses. This was required to be able to directly evaluate the rotational mode shape estimates obtained using the gyroscopes as opposed to indirectly deriving them from the displacement shapes.

The outer geometry of the scaled glider was used to create an initial NASTRAN model that consists of 48 beam elements. These beam elements contain parameters like material properties, cross-sectional area, moment of inertia and mass which can then be adjusted and connected with other beams to represent the structural behaviour of the aircraft. As there was limited information available about the structural properties, this model also allowed to evaluate different sensor layout options for the GVT. In Fig. 3.7, the outer geometry and the beam model are presented.

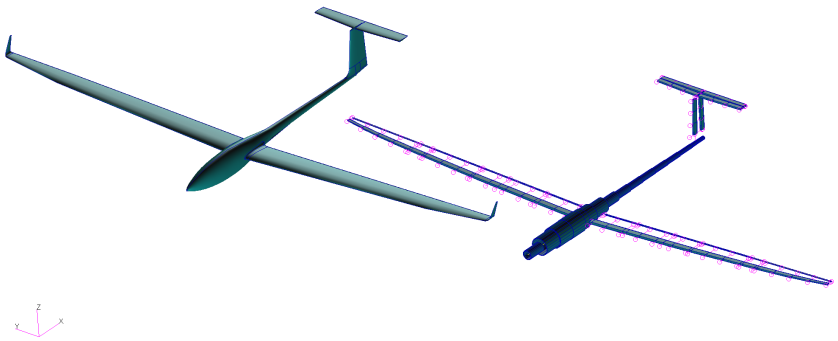

Figure 3.7: Diana 2 model outline and NASTRAN model.

The FEM model structural parameters were updated using the modal frequencies and mode shapes obtained from the GVT tests. However, also additional measurements about the aircraft structure were conducted to provide extra constraints for the updating procedure.

3.4.1. Component Weight and Centre of Gravity Measurement

The mass and centre of gravity of the wing and the aircraft were measured. The weight of the individual wings was measured to be 1.95 kg with a centre of gravity located 0.975 m from the aircraft axis of symmetry. The weight of the fuselage and the tail was 6.8 kg, resulting in a total weight of 10.7 kg for the aircraft, with a centre of gravity 0.74 m from the nose.

3.4.2. Wing Load-Displacement Test

A load-displacement test was conducted to gather information about the stiffness of the wings. During the testing, the wing tips were first loaded with lead weights, and then additional loads were applied 1 m from the wing tip. The displacements at 4 points on both wings were recorded for each load case, as shown in Fig. 3.8. These measurement points are indicated as distance y from the centre of the fuselage.

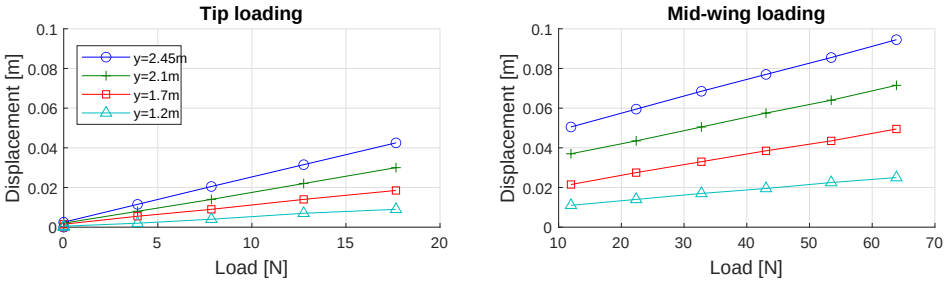

Figure 3.8: Diana 2 wing displacement responses for varying tip and mid-wing loads.

3.4.3. Estimating the Aircraft Moments of Inertia

Knowing the moments of inertia of an aircraft is not only important for evaluating the FEM model but are essential for understanding moments that are applied on the aircraft. The moments of inertia of the Diana 2 were estimated using an experimental swing setup and using the GVT measurements. During the swing tests, the aircraft is suspended with cables and made to oscillate around the axis of interest with a small amplitude. The oscillation period is then measured and averaged over multiple oscillations to find the moment of inertia.

First, the aircraft pitch moment of inertia I_y was determined. The test setup is presented in Fig. 3.9 where the aircraft is suspended from two points with four cables and oscillated in a back and forth motion. The oscillations were then recorded using an IMU attached to the aircraft. Tests were conducted at two different swing lengths and repeated twice. The oscillation frequencies for each

test were found by determining the spectral density of the responses which are presented in Fig. 3.10.

Figure 3.9: Pitch inertia setup.

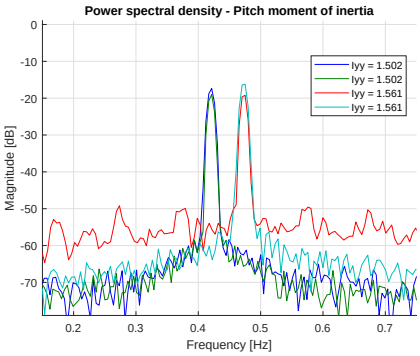

Figure 3.10: Pitch response frequencies.

With the measured oscillation period it is then possible to estimate the pitch moment of inertia using Eq.(3.9) [20].

$$I_y = mgl\left(\frac{\tau}{2\pi}\right)^2 - ml^2 \tag{3.9}$$

where m is the mass of the model, l is the distance from the axis of rotation to the centre of gravity, g is the gravitational acceleration and τ is the measured oscillation period.

Next, the yaw and roll moments of inertia were determined. Figure 3.11 and 3.12 present the setup for these experiments. Here the aircraft is suspended from two points with two cables and then oscillated in a rotational motion. Again the measured oscillation frequencies are presented in Fig. 3.13 and 3.14.

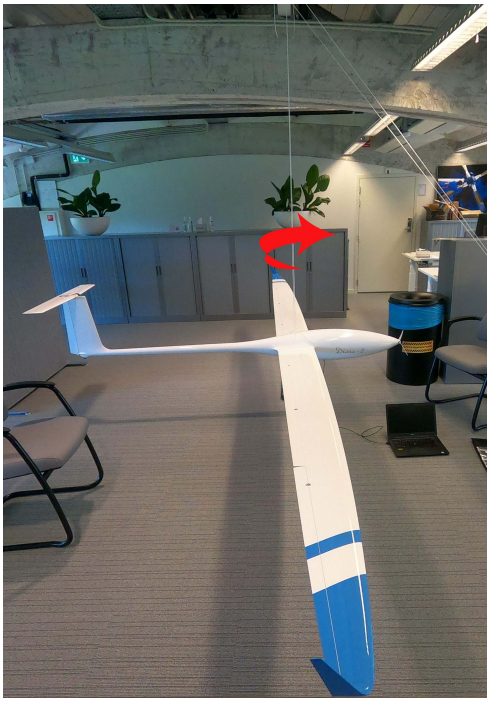

Figure 3.11: Yaw inertia setup.

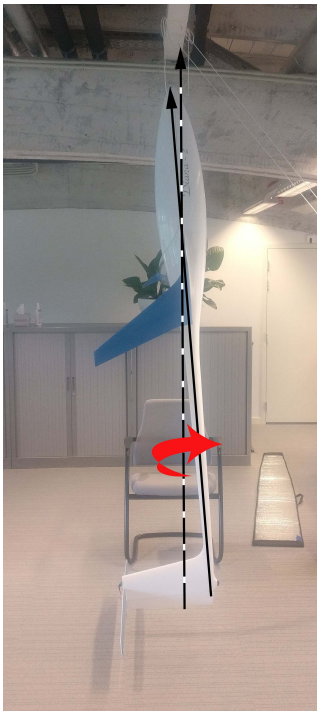

Figure 3.12: Roll inertia setup.

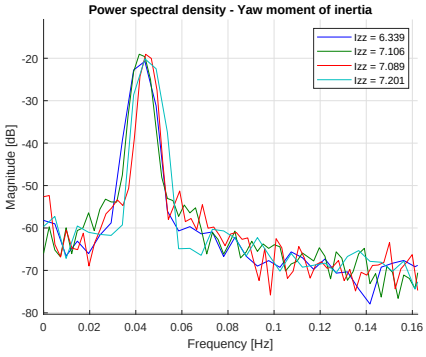

Figure 3.13: Yaw response frequencies.

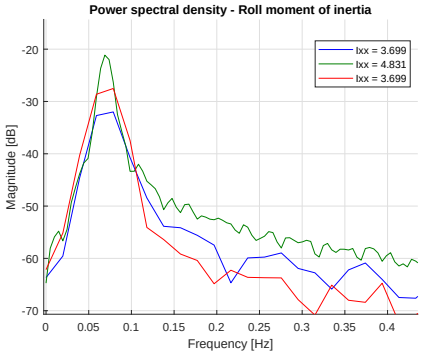

Figure 3.14: Roll response frequencies.

With the measured oscillation period it is then possible to estimate the yaw and

roll moments of inertia using Eq. (3.10) for the rotational pendulums [20].

$$I = \frac{mgd^2}{4l}\left(\frac{\tau}{2\pi}\right)^2 \tag{3.10}$$

where d is the distance between the two suspension points.

However, as can be seen from Fig. 3.12, the aircraft body axis in the roll test is at an angle to the axis of rotation. Therefore, a correction transformation was applied to the measured moment of inertia to rotate it to the aircraft body axis. The angle between the aircraft body axis and the measured rotation axis was measured to be -5 deg. The applied transformation is presented in Eq. (3.11). As can be seen, this transformation also gives a product of inertia I_{xz} component.

$$\begin{bmatrix} 0 & 0 & I_{xz} \\ 0 & 0 & 0 \\ I_{xz} & 0 & I_z \end{bmatrix} = \begin{bmatrix} \cos\theta & 0 & \sin\theta \\ 0 & 1 & 0 \\ -\sin\theta & 0 & \cos\theta \end{bmatrix} \begin{bmatrix} 0 & 0 & 0 \\ 0 & 0 & 0 \\ 0 & 0 & I'_z \end{bmatrix} \begin{bmatrix} \cos\theta & 0 & \sin\theta \\ 0 & 1 & 0 \\ -\sin\theta & 0 & \cos\theta \end{bmatrix}^T \tag{3.11}$$

In Table 3.2, the averaged oscillation periods and moments of inertia are presented. The weight of the aircraft during the swing tests was measured 8.65 kg as it was conducted without installing batteries. The inertia estimates obtained from GVT measurements are also presented. As can be seen, a close agreement is observed between the results of both experiments.

Table 3.2: Moments of inertia estimates for the scaled Diana 2 glider.

Inertia	$\tau_{avg}[s]$	l [m]	d [m]	Swing $[kg \cdot m^2]$	GVT $[kg \cdot m^2]$
I_x	13.61	0.966	0.203	4.246	4.445
I_y	2.37	1.262	-	1.531	1.642
I_z	23.05	2.100	0.219	6.881	6.897
I_{xz}				-0.602	-0.332

3.4.4. FEM MODEL TUNING

With all the tests completed, it was possible to perform FEM model updating. For this purpose, FEMtools 4.1 software was used, where all the individual responses can be collected, and automated parameter updating can be performed. First, only the parameters related to wing stiffness were updated based on the load-displacement responses. After that, the entire glider model could be updated using the mass, centre of gravity, and GVT measurements, including the estimated modal frequencies and the displacement and rotational mode shapes. Both of the wings were constrained to have identical structural properties. During the updating, the model parameters are optimized by minimizing a cost function based on the differences between the responses predicted by the FEM model and the experimental measurements. The model updating iterations were then

performed until convergence was reached, where additional iterations did not improve the model fit further. With the updated FEM model, it was now possible to have an extra point of reference when evaluating the modal estimation results.

3.5. Results and Discussion

Once the vibration testing was completed and the raw time signals were resampled and filtered, it was possible to determine the FRFs of the internal and external sensors using a H_1 estimator as in Eq. (3.12).

$$H_1(\omega) = \frac{\hat{S}_{yu}(\omega)}{\hat{S}_{uu}(\omega)} \tag{3.12}$$

Here $\hat{S}_{yu}(\omega)$ is the cross-spectrum estimate between the acceleration, rotational rate, or strain output and force input while $\hat{S}_{uu}(\omega)$ is the estimate of the input power spectrum. These FRFs were then imported to Siemens Testlab, where the natural frequencies, modal damping, and mode shapes were estimated using the PolyMAX method [21].

First, the quality of the FRFs was assessed. Fig. 3.15 and Fig. 3.16 show the FRFs for the external reference and internal accelerometers. These correspond to the accelerations measured at the elevator's right tip when the excitation impact was given to the side of the vertical tail. These are indicated as points 23 and 29 in the legend, respectively. The FRFs were calculated from the response measurements covering seven hammer hits at this location. As can be seen, the resonance peaks and phase signals are well captured for both cases and have similar quality.

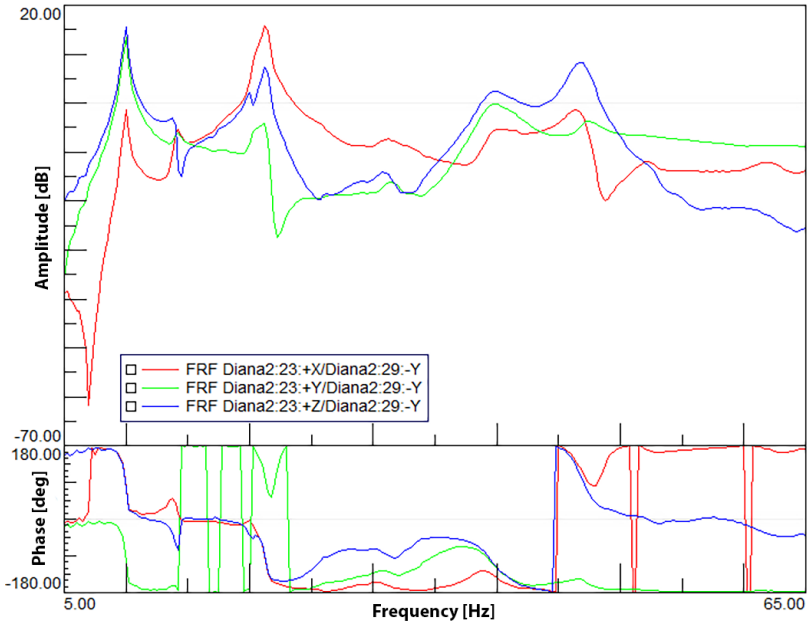

Figure 3.15: Right elevator tip reference accelerometer FRFs - vertical tail excitation.

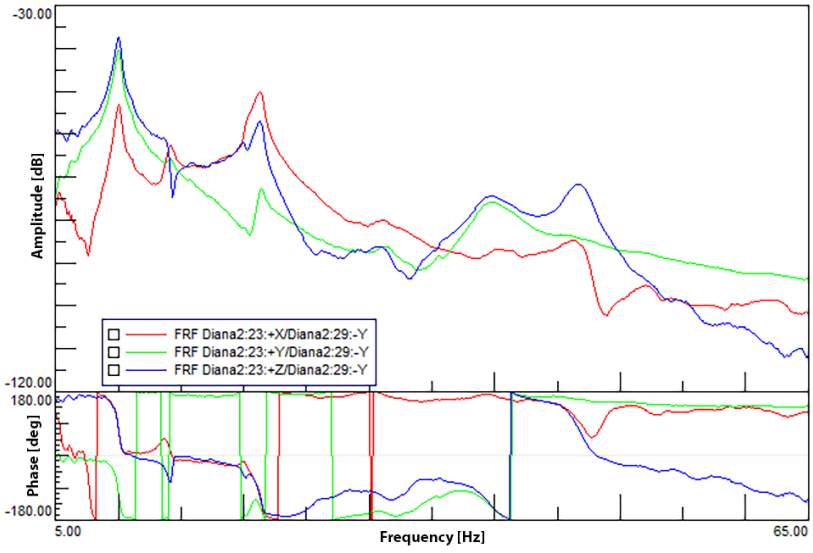

Figure 3.16: Right elevator tip internal accelerometer FRFs - vertical tail excitation.

Fig. 3.17 and Fig. 3.18 also present the FRFs for the gyroscopes and strain gauges corresponding to the same test point. Both gyroscopes and strain gauges are able to capture the resonance peaks seen in the accelerometer responses. A slight increase in noise for the FRF amplitude and phase can be seen for the gyroscopes, whereas the strain gauge responses present a much larger noise level. This was expected, as the strain gauge responses are measured using low-cost analog to digital converters that are limited by their sensitivity and noise. However, despite the sensor limitations, the resonance peaks can still be clearly distinguished.

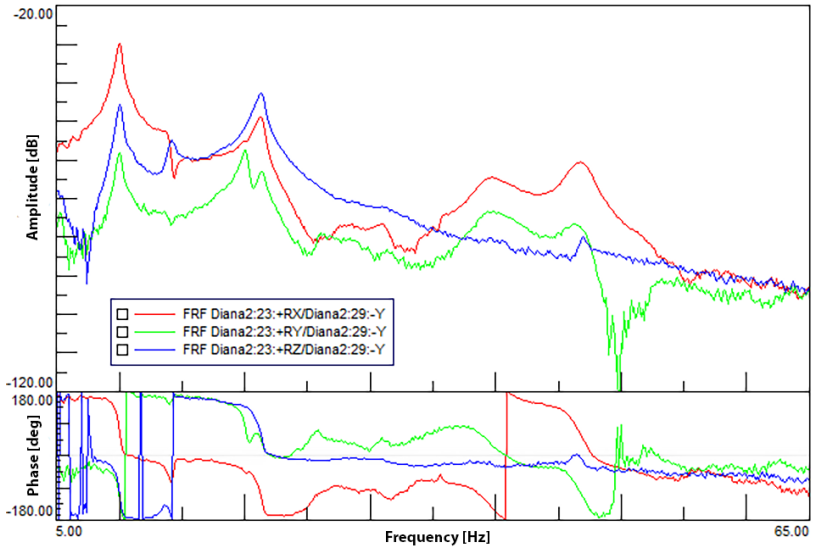

Figure 3.17: Right elevator tip gyroscope FRFs - vertical tail excitation.

Next, the modal parameters were estimated for all the sensor types separately, together with a single combined estimation where the internal accelerometers, gyros, and strain gauges were used simultaneously. The estimations were based on the FRFs from all test points, which were processed together in a single evaluation. First, in Table 3.3, a description of the estimated modes is presented.

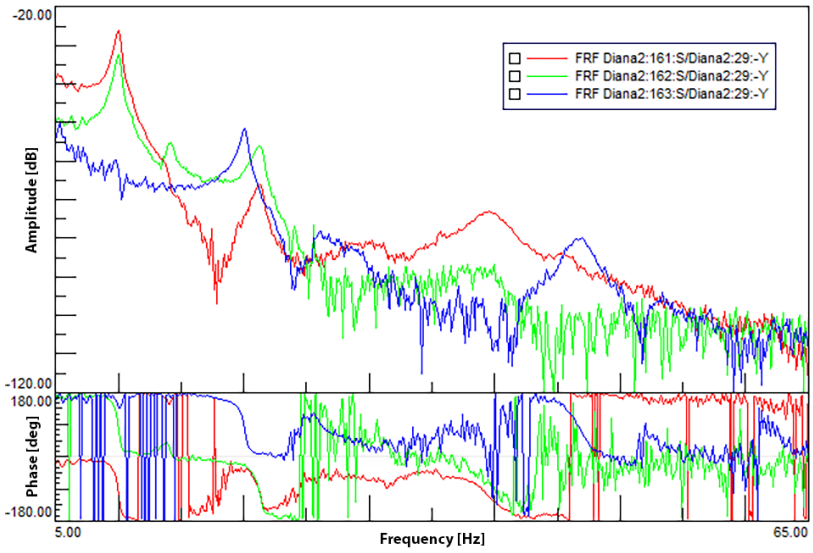

Figure 3.18: Tail strain FRFs for vertical tail excitation - torsion (red), side force (green), lift (blue).

Table 3.3: Identified mode descriptions

Mode	Description
1	1st sym. wing bending
2	1st asym. inplane wing bending, tail roll
3	Vertical tail torsion, horizontal tail 1st asym. inplane bending
4	2nd asym. wing bending, horizontal stabilizer in phase roll
5	1st inplane wing bending, fuselage bending in sym. plane
6	1st asym. inplane wing bending, fuselage bending out of sym. plane, vertical tail torsion
7	2nd sym. wing bending, 1st sym. inplane bending, fuselage bending in sym. plane
8	2nd sym. wing bending, fuselage bending in sym. plane
9	3rd asym. wing bending, fuselage bending out of sym. plane, horizontal tail out of phase roll
10	3rd asym. wing bending
11	1st sym. bending of horizontal tail
12	3rd sym. wing bending, sym. wing twist, 1st sym. bending of horizontal tail, fuselage 2nd bending in sym. plane

In Table 3.4, a comparison with respect to the reference accelerometers in terms of the natural frequencies is presented. As can be seen, the mode frequency estimates are very close to each other in all cases, with mostly less than 1% difference from the external accelerometer reference case and the largest estimate difference being 3.55%.

Table 3.4: Estimated modal frequency [Hz] comparison between FEM model, reference external accelerometers and internal sensors individually and combined.

Mode	FEM	Ref.	Accel.	Diff.	Gyro.	Diff.	Strain	Diff.	Comb.	Diff.
1	7.65	7.53	7.53	-0.02%	7.57	0.48%	7.60	0.88%	7.42	-1.44%
2	9.50	9.94	9.97	0.21%	9.96	0.19%	9.95	0.10%	9.94	-0.07%
3	14.28	14.18	13.88	-2.13%	13.90	-1.97%	13.91	-1.86%	13.82	-2.55%
4	17.34	17.34	17.31	-0.19%	17.31	-0.18%	17.31	-0.21%	17.31	-0.20%
5	20.97	20.13	20.14	0.05%	20.02	-0.54%	20.06	-0.32%	20.01	-0.60%
6	21.15	21.18	21.17	-0.07%	21.16	-0.11%	21.20	0.07%	21.19	0.03%
7	23.50	23.42	23.76	1.44%	23.45	0.13%	23.41	-0.05%	23.14	-1.20%
8	25.94	27.01	26.05	-3.55%	26.76	-0.95%	26.75	-0.98%	26.60	-1.52%
9	41.13	39.81	39.70	-0.29%	39.49	-0.81%	39.49	-0.80%	39.53	-0.71%
10	45.81	45.00	45.14	0.31%	45.12	0.26%	44.91	-0.19%	44.94	-0.12%
11	46.06	47.14	46.99	-0.34%	46.97	-0.38%	46.71	-0.92%	46.91	-0.49%
12	53.15	53.25	53.06	-0.37%	53.23	-0.04%	53.07	-0.35%	53.15	-0.20%

A similar comparison is made for the damping estimates in Table 3.5. A larger variation in the estimated values can be observed for damping, but generally, a close match is still achieved for all sensor types. Furthermore, most of the damping values are close to the $1-2\%$ that is traditionally assumed for structural damping when developing FEM models. For modes 8 and 9, there is a larger difference between the estimates where one estimate resulted in around 1% damping, but other cases have estimates around $5-6\%$ and $3-4\%$, respectively.

Table 3.5: Estimated modal damping [%] results for reference external accelerometers and internal sensors individually and combined.

Mode	Ref.	Accel.	Gyro	Strain	Comb.
1	2.37	1.53	2.73	1.25	2.88
2	1.90	2.14	2.02	1.31	2.18
3	1.85	2.86	2.73	1.38	2.72
4	0.93	1.03	1.19	1.03	1.10
5	0.94	1.25	0.92	0.91	0.75
6	2.81	2.98	2.51	1.75	2.47
7	3.80	3.17	4.44	3.38	3.56
8	6.74	1.76	6.63	5.78	6.46
9	1.09	4.24	4.23	3.93	4.10
10	2.25	1.98	2.08	1.88	1.76
11	1.82	1.49	1.63	1.44	1.60
12	1.76	1.97	1.96	1.86	1.98

Next, the corresponding mode shapes were evaluated. In Figures 3.19 to 3.24, the first mode shapes are presented that were obtained using all internal sensors simultaneously. In these figures, the aircraft displacement corresponds to the displacement mode shapes. The arrows correspond to the rotational mode

shapes, point in the resultant vector direction, and follow the right-hand rule. Finally, the colours correspond to the strain mode shapes, with blue indicating compression and red tension.

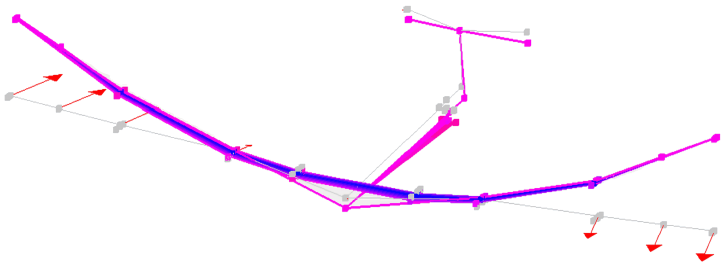

Figure 3.19: Mode 1.

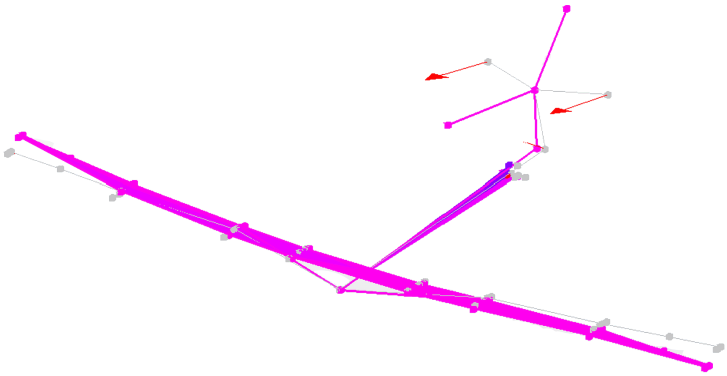

Figure 3.20: Mode 2.

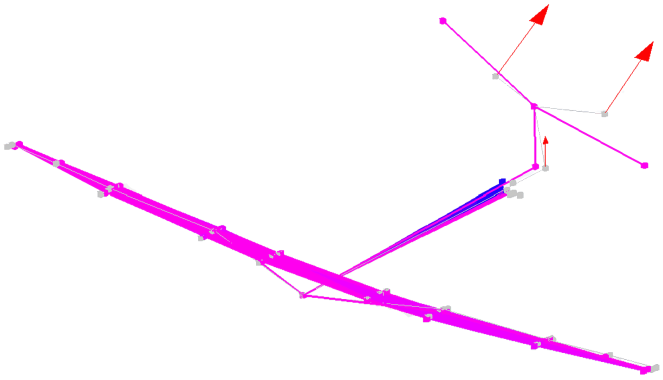

Figure 3.21: Mode 3.

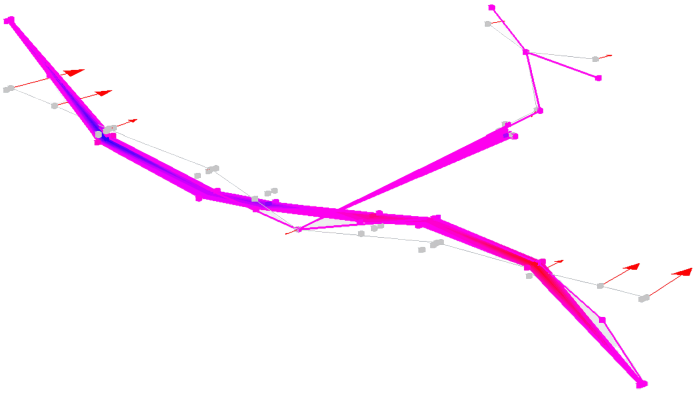

Figure 3.22: Mode 4.

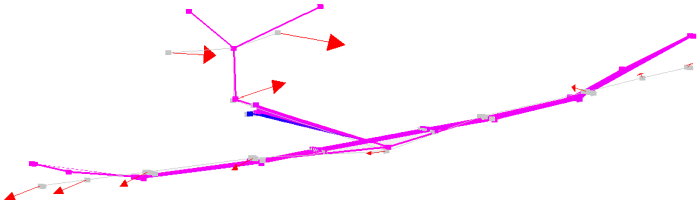

Figure 3.23: Mode 5.

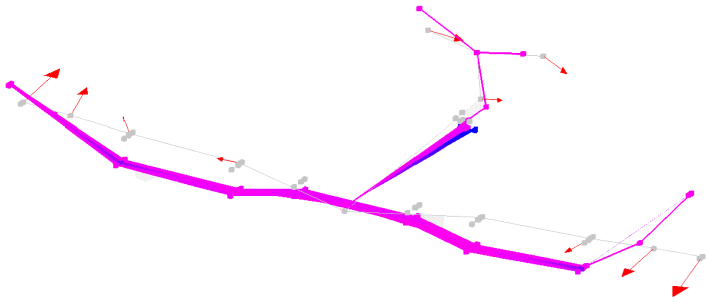

Figure 3.24: Mode 7.

The estimated mode shapes were then compared to the external accelerometer reference and FEM model shapes using the Modal Assurance Criterion (MAC) [22] as shown in Eq. (3.13).

$$MAC(\boldsymbol{\Phi_1}, \boldsymbol{\Phi_2}) = \frac{\left\|\boldsymbol{\Phi_1}^T \boldsymbol{\Phi_2}\right\|^2}{(\boldsymbol{\Phi_1}^T \boldsymbol{\Phi_1})(\boldsymbol{\Phi_2}^T \boldsymbol{\Phi_2})} \tag{3.13}$$

where $\boldsymbol{\Phi_1}$ and $\boldsymbol{\Phi_2}$ are the mode shape vectors being compared. The closer the MAC value is to one, the more similar the mode shapes are.

Table 3.6 presents the computed MAC values for the displacement and rotational mode shapes. The MAC values for the internal MEMS and reference accelerometer mode shapes are calculated in the second column. As can be seen, the displacement mode shapes estimated using the internal MEMS sensors match the reference accelerometer mode shapes very closely, with MAC values close to or well over 0.9 for most modes. Mode 5 was the only outlier with a MAC value of 0.737. The main reason for this appeared to be the wingtip nodes moving out of phase with the rest of the wing during the inplane bending in the reference accelerometer mode. Columns 4 and 5 show the comparison between the displacement and rotational mode shapes estimated using the internal sensors and the FEM model. It can be seen that the FEM model mode shapes were fitted well during the model updating process as, again, most modes achieve a MAC value close to or over 0.9. Both displacement and rotational shapes in the FEM model show similar fitting performance. Only outliers can be seen for modes 9, 10 and 12, where the MAC values remain around 0.7 for either the displacement or rotational shapes. Finally, in column 3, the comparison between the reference accelerometer and FEM model displacement mode shapes is presented. In this case, it was also possible to include the additional measurement points used for capturing the torsion of the wings and horizontal stabilizer. Here again, a similar trend can be seen with most MAC values above 0.9 and a few around 0.65-0.75, matching the other columns. Overall, all the comparisons showed excellent matches in mode shapes with only a few outlier modes with MAC values around 0.7, which can still be considered a good match.

Table 3.6: Mode shape comparison between FEM, reference, and internal sensors for displacement and rotational shapes.

Mode	Ref./MEMS	Ref./FEM	MEMS/FEM	MEMS/FEM rot.
1	0.984	0.981	0.997	0.966
2	0.994	0.970	0.973	0.968
3	0.985	0.890	0.930	0.924
4	0.978	0.971	0.986	0.977
5	0.737	0.644	0.912	0.911
6	0.986	0.881	0.912	0.817
7	0.935	0.757	0.883	0.884
8	0.880	0.880	0.957	0.931
9	0.969	0.766	0.699	0.883
10	0.872	0.888	0.837	0.746
11	0.981	0.952	0.935	0.904
12	0.905	0.895	0.923	0.715

In Table 3.7 the MAC values are determined between the individual mode shapes estimated using the accelerometers, gyroscopes and strain gauges simultaneously. This allows to check how similar the mode shapes are to each other. As can be seen, the largest similarities are between modes 1, 7, and 8, which cover the first and second symmetric wing bending motion, and modes 4 and 10, which cover the second and third asymmetric wing bending motion.

Table 3.7: AutoMAC results for mode shapes estimated using combined accelerometer, gyroscope, and strain gauge responses.

Mode	1	2	3	4	5	6	7	8	9	10	11	12
1	100.0	0.0	0.0	0.3	2.8	0.0	35.2	46.4	0.1	1.0	1.6	13.7
2	0.0	100.0	34.8	0.8	0.1	28.6	0.0	0.0	17.8	0.0	0.0	0.1
3	0.0	34.8	100.0	1.3	0.0	3.7	0.1	0.2	21.8	0.6	0.0	0.0
4	0.3	0.8	1.3	100.0	0.9	0.7	1.3	1.5	0.7	60.0	0.5	3.5
5	2.8	0.1	0.0	0.9	100.0	0.3	39.7	1.6	0.6	0.3	4.6	10.3
6	0.0	28.6	3.7	0.7	0.3	100.0	0.0	0.0	7.0	0.0	0.0	0.1
7	35.2	0.0	0.1	1.3	39.7	0.0	100.0	20.5	0.6	1.7	0.1	33.4
8	46.4	0.0	0.2	1.5	1.6	0.0	20.5	100.0	0.0	2.6	5.6	18.3
9	0.1	17.8	21.8	0.7	0.6	7.0	0.6	0.0	100.0	1.8	0.0	0.5
10	1.0	0.0	0.6	60.0	0.3	0.0	1.7	2.6	1.8	100.0	0.8	4.1
11	1.6	0.0	0.0	0.5	4.6	0.0	0.1	5.6	0.0	0.8	100.0	11.3
12	13.7	0.1	0.0	3.5	10.3	0.1	33.4	18.3	0.5	4.1	11.3	100.0

A well-tuned FEM model was essential to be able to directly compare the rotational mode shapes obtained from the gyroscope measurements. This is opposed to indirectly deriving them from the displacement mode shapes, as is typically required when only accelerometer measurements are available. However, such a derivative-based approach can now be used to evaluate the strain mode shapes. To illustrate this, the mode shapes for the glider main wing are presented in Fig. 3.25 to 3.28 for modes 1, 4, 7, and 10. These

correspond to the first symmetric bending, second asymmetric bending, second symmetric bending, and third asymmetric bending modes. First, the normalized displacement modes in the z-direction are shown, which were all directly obtained from the experiments or the FEM model. Next, a polynomial fitting was performed on the reference accelerometer results, which are also presented. Using the fitted polynomial, it was possible to obtain the corresponding rotational mode shape by differentiation. This is then presented together with directly obtained gyroscope and FEM model results. Other numerical differentiation methods can also be used, as polynomials were used here for simplistic illustration purposes.

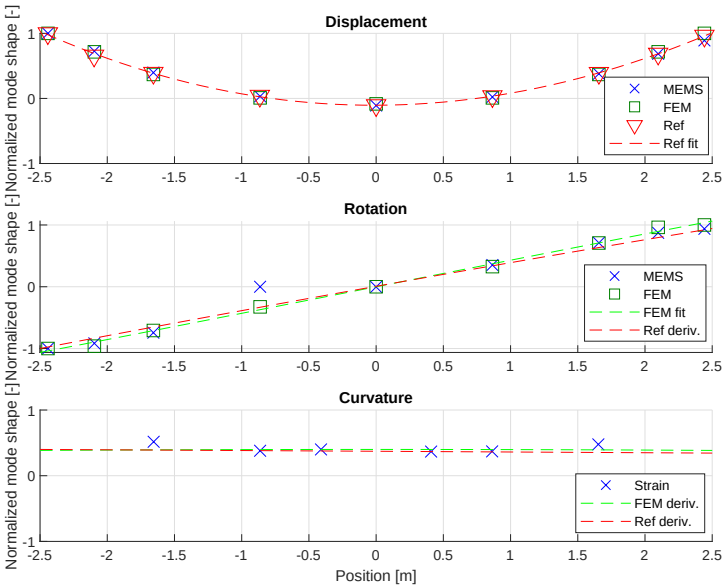

Figure 3.25: Mode 1 - 1st symmetric wing bending mode shape comparison.

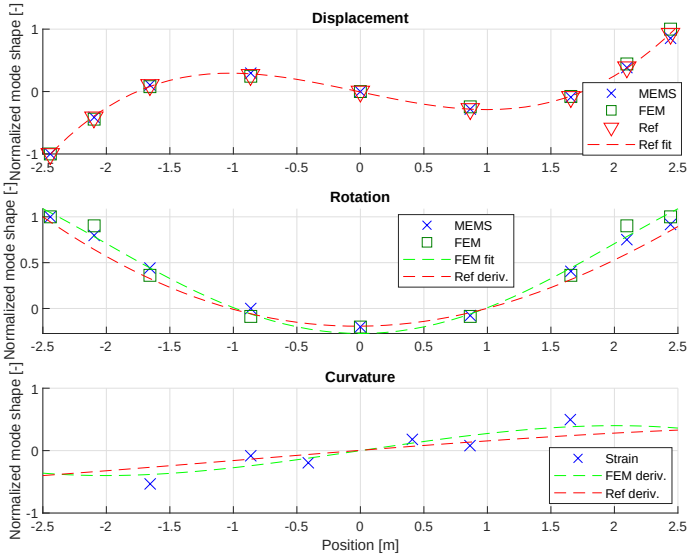

Figure 3.26: Mode 4 - 2nd asymmetric wing bending mode shape comparison.

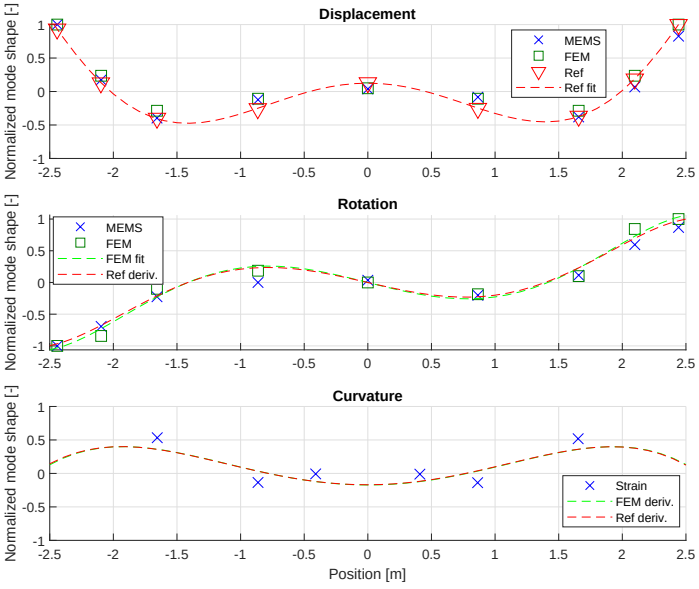

Figure 3.27: Mode 7 - 2nd symmetric wing bending mode shape comparison.

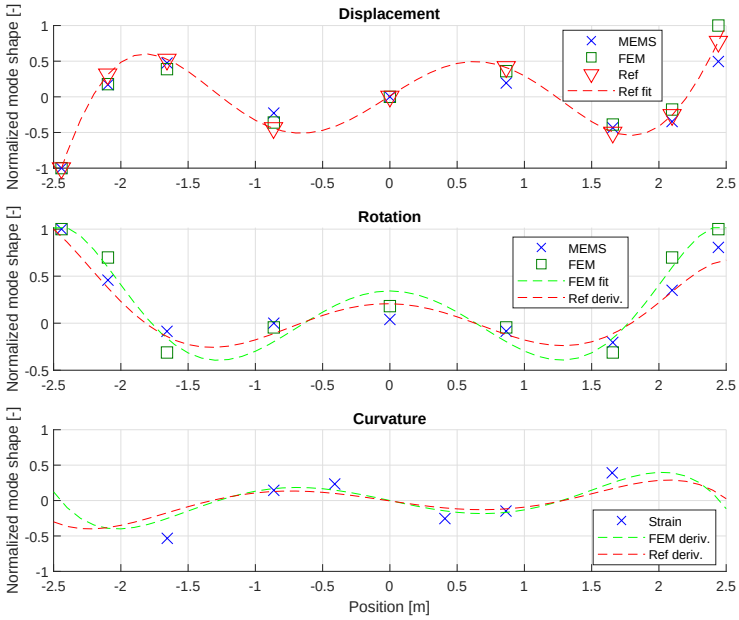

Figure 3.28: Mode 10 - 3rd asymmetric wing bending mode shape comparison.

When considering the main wing as a beam, it is also possible to evaluate the measured strain shapes by comparing them with the wing curvature. This is due to the relation between the curvature and strain at the beam surface shown in Eq. (3.14) [16]:

$$\kappa = \frac{d\vartheta}{dx} = \frac{d^2 w}{dx^2} \approx \pm \frac{2\varepsilon_{max}}{h} \tag{3.14}$$

Here, w is the out-of-plane displacement of the beam, ϑ is the slope of that displacement corresponding to the rotation, and κ is the curvature which is related to the maximum strain ε_{max} on the beam surface through the height of the beam h.

Therefore, in Fig. 3.25 to 3.28, the wing's curvature is estimated by taking a second derivative of the polynomial fit for the reference accelerometers. Similarly, for the FEM model, a polynomial fitting for the rotational shapes is performed that is then differentiated and used to estimate the curvature. Both of these indirect results are then compared to the measured strain results. While the results in Table 3.6 showed good agreement for the displacement and rotational modes, it was now possible to determine that the bending strain modes on the main wings are consistent with the curvature estimates obtained through differentiation.

However, the indirect estimation of mode shapes is very sensitive to errors in the initial displacement shapes, as the minor differences can become significant

differences for the rotational and curvature shapes due to differentiation. In this case, it was possible to evaluate the fit accuracy by comparing it with the experimental data and adjusting the polynomial order when necessary. However, in most cases, this would not be possible due to the lack of experimental data, making this process much more difficult. For this reason, using gyroscopes and strain gauges during the GVT has the advantage of obtaining those results directly. Such additional insight into the measured structure can then be used, for example, as additional higher-order constraints during FEM model fitting.

Overall, the results show that it is possible to obtain modal parameter estimates using MEMS IMUs and strain gauges that closely match those obtained using piezoelectric accelerometers. While the objective was not to surpass the traditional approach, the use of different sensor types can provide unique advantages and support new applications such as tracking structural dynamics in flight. A key benefit is the complementary sensitivity of accelerometers, gyroscopes, and strain gauges. At a location where one type of sensor might only show a weak response, another can have a much stronger signal. Gyroscopes and the resulting rotational mode shapes are particularly effective at revealing where twisting and rotational motion occurs, without the need to place accelerometers in pairs along the wings and tail. As a result, their use could reduce the time required to instrument aircraft for future GVTs. The combined estimation approach using IMUs and strain gauges provided greater insight into the structural dynamics than accelerometers alone, offering a much clearer picture of where displacements, rotations, and strains occur. Importantly, using IMUs and strain gauges does not impose limitations on the GVT procedure, as the same excitation methods can be applied. The estimated modal parameters for both the reference and internal sensors have been published and are available in the 4TU.ResearchData repository [23].

3.6. CONCLUSION

In this chapter, experimental modal analysis was performed on a scaled Diana 2 glider using MEMS-based IMUs and strain gauges to estimate displacement, rotation, and strain modes. The estimated modal parameters were compared with results obtained using traditional piezoelectric accelerometers and FEM model predictions. This allowed to evaluate the accuracy of the MEMS IMU sensors and explore the feasibility of using gyroscopes for aircraft ground vibration testing.

For this purpose, ground vibration testing was carried out on the scaled Diana 2 glider model using a modal hammer to excite the structure. From the testing, natural frequencies, damping, and mode shapes of the structure were estimated for all different sensor types. A comparison of the experimental results showed that the natural frequency estimates of the structure were within 1% for all the sensors in most cases, with 3.55% being the largest difference. While more variation in the structural damping estimates was observed, a close match with the reference sensor values was still obtained, with most estimates resulting in around $1-2\%$ damping. Finally, the mode shapes were compared, where MAC

values well above 0.9 were achieved for most modes.

The rotational and strain modes obtained directly using the internal sensors were compared to results obtained indirectly by differentiating the external accelerometer displacement modes. The results showed that getting a good approximation of the rotational shapes is possible through displacement shape differentiation. However, as these results are sensitive to errors in the displacement shapes, rotational shapes obtained directly with gyroscopes would be preferred instead.

In conclusion, the estimated modal parameters obtained using the MEMS IMUs and strain gauges integrated into the scaled Diana 2 glider closely aligned with the results obtained using the reference piezoelectric accelerometers. Furthermore, using accelerometers, gyroscopes, and strain gauges simultaneously during the modal analysis allowed a more comprehensive overview of the vibration modes to be established. More specifically, it allows for a better interpretation of strains resulting from corresponding displacements, and gyroscopes help to capture twisting motions without the need for additional accelerometers. These derived displacement, rotation, and strain mode shapes have potential applications in improving in-flight structural dynamics tracking or acting as additional constraints during FEM model updating.

REFERENCES

[1] B. Peeters, W. Hendricx, J. Debille and H. Climent. “Modern solutions for ground vibration testing of large aircraft”. In: *Sound and vibration* 43.1 (2009), p. 8.

[2] S. Giclais, P. Lubrina and C. Stephan. “Aircraft Ground Vibration Testing at ONERA”. In: *AerospaceLab Journal* 12 (2016). DOI: 10.12762/2016.AL12-05.

[3] D. J. Ewins. *Modal testing: theory, practice and application*. eng. 2. ed. Mechanical engineering research studies engineering dynamics series 10. Baldock: Research Studies Press, 2000. ISBN: 978-0-86380-218-8.

[4] D. Göge, M. Böswald, U. Füllekrug and P. Lubrina. “Ground Vibration Testing of Large Aircraft - State-of-the-Art and Future Perspectives”. In: *Proceedings of the 25th International Modal Analysis Conference (IMAC XXV)*. 258. 2007. URL: https://elib.dlr.de/48110/.

[5] P. Lubrina, S. Giclais, C. Stephan, M. Boeswald, Y. Govers and N. Botargues. “AIRBUS A350 XWB GVT: State-of-the-Art Techniques to Perform a Faster and Better GVT Campaign”. In: *Topics in Modal Analysis II, Volume 8*. Ed. by R. Allemang. Cham: Springer International Publishing, 2014, pp. 243–256. ISBN: 978-3-319-04774-4.

[6] B. Peeters, F. L. M. dos Santos, A. Pereira and F. Araujo. “On the use of optical fiber Bragg grating (FBG) sensor technology for strain modal analysis”. In: *AIP Conference Proceedings*. Vol. 1600. 1. May 2014, pp. 39–49. DOI: 10.1063/1.4879567.

[7] F. L. M. dos Santos and B. Peeters. “On the use of strain sensor technologies for strain modal analysis: Case studies in aeronautical applications”. In: *Review of Scientific Instruments* 87 (10 Oct. 2016), p. 102506. ISSN: 0034-6748. DOI: 10.1063/1.4965814.

[8] T. Kranjc, J. Slavič and M. Boltežar. “A comparison of strain and classic experimental modal analysis”. In: *Journal of Vibration and Control* 22 (2 Feb. 2016), pp. 371–381. ISSN: 1077-5463. DOI: 10.1177/1077546314533137.

[9] S. Weber, T. Kissinger, E. Chehura, S. Staines, J. Barrington, K. Mullaney, L. Z. Fragonara, I. Petrunin, S. James, M. Lone and R. Tatam. “Application of fibre optic sensing systems to measure rotor blade structural dynamics”. en. In: *Mechanical Systems and Signal Processing* 158 (Sept. 2021), p. 107758. ISSN: 08883270. DOI: 10.1016/j.ymssp.2021.107758.

[10] Z. Ma, X. Chen, Z. Ma and X. Chen. “Fiber Bragg Gratings Sensors for Aircraft Wing Shape Measurement: Recent Applications and Technical Analysis”. en. In: *Sensors* 19.1 (Dec. 2018). ISSN: 1424-8220. DOI: 10.3390/s19010055.

[11] F. Terroba, M. Frövel and R. Atienza. “Structural health and usage monitoring of an unmanned turbojet target drone”. en. In: *Structural Health Monitoring* 18.2 (Mar. 2019), pp. 635–650. ISSN: 1475-9217, 1741-3168. DOI: 10.1177/1475921718764082.

[12] J. Alvarez-Montoya, A. Carvajal-Castrillón and J. Sierra-Pérez. “In-flight and wireless damage detection in a UAV composite wing using fiber optic sensors and strain field pattern recognition”. In: *Mechanical Systems and Signal Processing* 136 (Feb. 2020), p. 106526. ISSN: 0888-3270. DOI: 10.1016/j.ymssp.2019.106526.

[13] M. Murthy N and P. D. Kakade. “Review on Strain Monitoring of Aircraft Using Optical Fibre Sensor”. en. In: *International Journal of Electronics and Telecommunications* (Sept. 2022), pp. 625–634. ISSN: 2300-1933. DOI: 10.24425/ijet.2022.141282.

[14] S. W. James, T. Kissinger, S. Weber, K. Mullaney, E. Chehura, H. H. Pekmezci, J. H. Barrington, S. E Staines, T. O. H. Charrett, N. J. Lawson, M. Lone, R. Atack and R. P. Tatam. “Fibre-optic measurement of strain and shape on a helicopter rotor blade during a ground run: 1. Measurement of strain”. en. In: *Smart Materials and Structures* 31.7 (July 2022), p. 075014. ISSN: 0964-1726, 1361-665X. DOI: 10.1088/1361-665X/ac736d.

[15] H. Zhang, Z. Wang, F. Teng and P. Xia. “Dynamic Strain Measurement of Rotor Blades in Helicopter Flight Using Fiber Bragg Grating Sensor”. en. In: *Sensors* 23.15 (July 2023), p. 6692. ISSN: 1424-8220. DOI: 10.3390/s23156692.

[16] P. A. Bońkowski, P. Bobra, Z. Zembaty and B. Jędraszak. “Application of rotation rate sensors in modal and vibration analyses of reinforced concrete beams”. In: *Sensors (Switzerland)* 20 (17 Sept. 2020), pp. 1–18. ISSN: 14248220. DOI: 10.3390/s20174711.

[17] L. R. Lustosa, I. Kolmanovsky, C. E. S. Cesnik and F. Vetrano. “Aided Inertial Estimation of Wing Shape”. In: *Journal of Guidance, Control, and Dynamics* 44.2 (2 Feb. 2021), pp. 210–219. ISSN: 1533-3884. DOI: 10.2514/1.G005368.

[18] J. M. M. E Silva. “An Overview of the Fundamentals of Modal Analysis”. In: *Modal Analysis and Testing*. Dordrecht: Springer Netherlands, 1999, pp. 1–34. ISBN: 978-94-011-4503-9. DOI: 10.1007/978-94-011-4503-9_1.

[19] Baudismodel.com. *Diana 2 (scale 1/3) - Baudismodel*. 2018. URL: https://www.baudismodel.com/en/production/k2408-actual-production/3-diana-2-scale-1-3.html.

[20] G. Genta and C. Delprete. “Some considerations on the experimental determination of moments of inertia”. In: *Meccanica* 29.2 (June jun 1994), pp. 125–141. ISSN: 00256455. DOI: 10.1007/BF01007497.

[21] B. Peeters, H. Van der Auweraer, P. Guillaume and J. Leuridan. “The PolyMAX frequency-domain method: A new standard for modal parameter estimation?” In: *Shock Vib.* 11.3-4 (2004), pp. 395–409.

[22] R. J. Allemang. “The Modal Assurance Criterion - Twenty Years of Use and Abuse”. In: *Sound and Vibration* (2003), pp. 14–21.

[23] A. Jürisson, B. Eussen, C. C. de Visser and R. De Breuker. *Flexible Diana 2 Scaled Glider UAV - Ground Vibration Test Results*. Dataset. 4TU.ResearchData, 2026. DOI: 10.4121/2c7ef9a5-d749-4b82-a63e-bde7d15d213e.

4

FLIGHT DATA FILTERING FOR AEROELASTIC AIRCRAFT STATE ESTIMATION

Accurate estimation of aircraft's states and structural responses from flight test data is essential for analysing its aeroelastic behaviour and validating flight dynamics and loads models. However, raw flight measurements are often affected by noise, biases, and unmeasured disturbances, requiring filtering techniques to estimate the aircraft states and ensure consistency of the dataset. This chapter presents a Kalman filter based approach for estimating both rigid-body states and structural modal responses of a flexible aircraft using measurements from accelerometers, gyroscopes, and strain gauges. This approach is based on kinematic equations of a flexible aircraft and does not require an aeroelastic flight dynamics model of the aircraft. The method is evaluated through simulations and using flight test measurements of the scaled Diana 2 glider UAV.

This chapter is based on the following article: Jürisson, A., Eussen, B., de Visser, C. C., & De Breuker, R., "Flight path reconstruction filter extension for flexible aircraft state estimation" in *Journal of Aircraft (submitted)*, 2026

4.1. INTRODUCTION

Flight testing is a core part of the development process of any new aircraft. As part of the testing, the aircraft responses during various manoeuvres are recorded, from which aircraft stability coefficients describing its characteristics can be determined. These estimates can then be used to validate or update existing numerical models. However, the measured responses are noisy, biased, and possibly sampled at different rates, which can lead to inaccuracies in the models. For this reason, flight path reconstruction (FPR) [1, 2] is often the first step in filtering and checking the consistency of gathered flight test data before estimating these stability coefficients. FPR is a filtering technique where the time history of the aircraft's state is reconstructed by combining aircraft kinematic equations with the response measurements. In these equations, the aircraft is represented as a point mass translating and rotating through the air. However, aircraft structures are becoming lighter and more flexible to become more fuel efficient. This, in turn, results in the structural dynamics of the aircraft having a more considerable interaction with the aircraft flight dynamic response. Therefore, to model this interaction correctly, it is necessary to reconstruct the structural dynamics together with the rigid body states.

In addition to aeroelastic modelling, tracking the aircraft's structural deformation is important for applications such as structural health monitoring and active control for load and gust alleviation, drag reduction, or flutter suppression [3–5]. For this reason, in literature, many approaches have been explored to track the aircraft wing deflections, shape, or the state of the whole structure. Solutions based on different sensors and sensor combinations have been proposed. One approach is to use only strain measurements either from strain gauges or fiber Bragg grating sensors. These can be either directly integrated into a displacement estimate, converted into modal amplitudes using strain modes, or combined with a Finite Element Method (FEM) model to obtain a fit of the wing shape [6–9]. These strain sensors need to be integrated into the structure, and many measurement points or an accurate FEM model are required to achieve good tracking [3]. A nonintrusive alternative is to use camera-based solutions that estimate deformations by tracking markers placed on the wings [10–12]. However, when using only cameras, the tracking accuracy can be significantly influenced by lighting and visibility conditions, and obtaining high sampling rates is challenging. For this reason, recent studies have also explored using a combination of different sensors such as accelerometers+cameras [13], gyroscopes+cameras [14], accelerometers+gyroscopes [15] or accelerometers+strain gauges [3] to reconstruct the structural deformations.

However, it is desirable for aeroelastic modelling to simultaneously reconstruct the structural dynamics and the states related to the aircraft's rigid body motion. The main contribution of this study is an extension to the FPR filter equations that allow estimation of the modal amplitude and velocity responses of the aircraft structure in addition to the aircraft's rigid body states. The proposed method uses additional accelerometer, gyroscope, and strain gauge measurements collected from across the aircraft to achieve this. The proposed method is based on

aircraft kinematic equations, and therefore, a flight dynamics model of the aircraft is not required to perform the filtering. This way, minimal previous knowledge about the aircraft is needed. Only the mode shapes of interest for the sensor locations must be provided.

The chapter is organized as follows. In Sec. 4.2, the FPR filter equations are extended to incorporate the tracking of modal amplitude and velocity using additional sensors. Then, in Sec. 4.3, the scaled glider model is presented that is used as a reference model for the simulation study and flight testing. A simulation study of the filter performance is presented in Sec. 4.4 followed by flight testing results in Sec. 4.5. Finally, Sec. 4.6 summarises the main findings of the chapter.

4.2. THEORETICAL BACKGROUND

The proposed filter uses an Extended Kalman filter together with a kinematics model for flexible aircraft according to the mean-axis formulation [16, 17] and is an extension of the flight path reconstruction filters [1]. This approach uses additional accelerometers, gyroscopes, and strain gauges distributed along the flexible aircraft structure to estimate the states related to the aircraft rigid body responses together with the modal amplitude and modal velocities.

A core part of the Kalman filter is a model of the system's dynamics that describes the evolution of that system and is used to predict and correct the system responses. For a nonlinear system and Kalman filter, the system is represented in the following format:

$$\dot{\mathbf{X}} = f(\mathbf{X}, \mathbf{U}) + \mathbf{w} \tag{4.1}$$

$$\mathbf{Y} = h(\mathbf{X}) + \mathbf{v} \tag{4.2}$$

Here, $\mathbf{X}$ is a vector for system states, $\mathbf{U}$ represents the system inputs, $\mathbf{Y}$ system outputs, and $\mathbf{w}$ and $\mathbf{v}$ are for process and measurement noise, respectively. The evolution of the system state is represented by nonlinear function f, and output is determined by nonlinear function h.

In the case of the extension to the flight path reconstruction filter presented in this chapter, these equations represent the kinematics of a flexible aircraft. Therefore, the states that are being estimated using the filter are as follows:

$$\mathbf{X} = [x\ y\ z\ u\ v\ w\ \phi\ \theta\ \psi\ p\ q\ r\ \dot{\boldsymbol{\eta}}\ \boldsymbol{\eta}\ \boldsymbol{\lambda}]^T \tag{4.3}$$

The variables $x,\ y,\ z$ represent the aircraft position in the Earth fixed reference frame, $u,\ v,\ w$ are the velocity components in the Body reference frame and $\phi,\ \theta,\ \psi$ are the roll, pitch, and yaw angles, $p,\ q,\ r$ are the aircraft centre of gravity rotational rates, $\dot{\boldsymbol{\eta}},\ \boldsymbol{\eta}$ are vectors containing the modal velocities and amplitudes, which are proposed as additions to the FPR filter in this chapter. Finally, $\boldsymbol{\lambda}$ is a vector containing all the unknown biases that are estimated as part of the filtering process:

$$\boldsymbol{\lambda} = [\lambda_{A_x}\ \lambda_{A_y}\ \lambda_{A_z}\ \lambda_p\ \lambda_q\ \lambda_r\ \lambda_\alpha\ \lambda_\beta\ ] \tag{4.4}$$

Here λ_{A_x} λ_{A_y} λ_{A_z} are the centre of gravity accelerometer sensor biases, λ_p, λ_q, λ_r are the biases for the centre of gravity gyroscope and λ_α, λ_β are biases for aerodynamic angle measurements. While the filter uses extra accelerometers and gyros placed across the aircraft structure, additional biases related to these sensors were not added to the filter to ensure the system remains observable.

Traditionally, wind is also added to the filter as a constant bias term or a Markov process [1]. However, this was not suitable as the flight testing was conducted at a low altitude with rapidly changing wind speed and direction. Fortunately, it was possible to estimate the wind speed by determining the difference between the aircraft velocity measured in the Earth frame by the GPS and the airspeed measured by the aeroprobe, which was converted to the Earth frame using aerodynamic angle and attitude measurements.

$$\boldsymbol{W^E} = \boldsymbol{T_{Eb}}\ \boldsymbol{T_{ba}}\ \boldsymbol{V^a_{probe}} - \boldsymbol{V^E_{GPS}} \tag{4.5}$$

where $\boldsymbol{W^E}$ is a wind speed vector in the Earth frame, $\boldsymbol{V^a_{probe}}$ is the airspeed by the aeroprobe, and $\boldsymbol{V^E_{GPS}}$ is the aircraft velocity given by the GPS. The transformation matrix from the body-fixed frame to the Earth frame is given by Eq. (4.6), and transformation from the aerodynamic frame to aircraft body-fixed is given by Eq. (4.7).

$$\boldsymbol{T_{Eb}}(\phi,\theta,\psi) = \begin{bmatrix} \cos\theta\cos\psi & \sin\phi\sin\theta\cos\psi - \cos\phi\sin\psi & \cos\phi\sin\theta\cos\psi + \sin\phi\sin\psi \\ \cos\theta\sin\psi & \sin\phi\sin\theta\sin\psi + \cos\phi\cos\psi & \cos\phi\sin\theta\sin\psi - \sin\phi\cos\psi \\ -\sin\theta & \sin\phi\cos\theta & \cos\phi\cos\theta \end{bmatrix} \tag{4.6}$$

$$\boldsymbol{T_{ba}}(\alpha,\beta) = \begin{bmatrix} \cos\beta\cos\alpha & -\sin\beta\cos\alpha & -\sin\alpha \\ \sin\beta & \cos\beta & 0 \\ \cos\beta\sin\alpha & -\sin\beta\sin\alpha & \cos\alpha \end{bmatrix} \tag{4.7}$$

This allowed to provide the wind speed as an input to the filter together with all the accelerations $\boldsymbol{A_N}$ and rotational accelerations $\boldsymbol{\dot{\omega}_N}$ measured by in total N sensors placed across the aircraft structure. The rotational accelerations were obtained through numerical differentiation of the gyroscope measurements. The complete input vector is then as follows:

$$\boldsymbol{U} = [\boldsymbol{W^E}\ \boldsymbol{A_N}\ \dot{\boldsymbol{\omega}}_{\boldsymbol{N}}]^T \tag{4.8}$$

Next, the system state equations are determined. In a flexible aircraft, the accelerations measured across the structure include the acceleration of the aircraft's centre of gravity but also effects due to the structural dynamics and effects of the aircraft rotation. The acceleration measured by sensor k on the flexible aircraft can be found using Eq. (4.9) [17].

$$\boldsymbol{A_k} = \boldsymbol{A_{cg}} + \dot{\boldsymbol{\omega}}_{\boldsymbol{cg}} \times (\boldsymbol{r} + \boldsymbol{\Phi_k\eta}) + \boldsymbol{\omega_{cg}} \times [\boldsymbol{\omega_{cg}} \times (\boldsymbol{r} + \boldsymbol{\Phi_k\eta})] + \boldsymbol{\Phi_k}\ddot{\boldsymbol{\eta}} + (2\boldsymbol{\omega_{cg}} \times \boldsymbol{\Phi_k}\dot{\boldsymbol{\eta}}) \tag{4.9}$$

Here $\boldsymbol{A_{cg}}$ and $\boldsymbol{\omega_{cg}}$ correspond to the acceleration and rotational rate of the aircraft's centre of gravity. The modal acceleration vector is $\ddot{\boldsymbol{\eta}}$ while $\boldsymbol{\Phi_k}$ is the structural mode shape matrix corresponding to the sensor location, and $\boldsymbol{r}$ is the sensor distance to the aircraft centre of gravity. Similarly, the structural dynamics influence the rotational accelerations measured across the aircraft structure. The rotational acceleration measured by gyroscope sensor k can be found using Eq. (4.10) [17].

$$\dot{\boldsymbol{\omega}}_{\boldsymbol{k}} = \dot{\boldsymbol{\omega}}_{\boldsymbol{cg}} + \boldsymbol{H_k}\ddot{\boldsymbol{\eta}} \tag{4.10}$$

Here, $\boldsymbol{H_k}$ is the rotational mode shape matrix corresponding to the sensor location. Combining and rearranging these two equations, it is possible to arrive at the following matrix multiplication:

$$\begin{bmatrix} \boldsymbol{A_k} - \boldsymbol{\omega_{cg}} \times [\boldsymbol{\omega_{cg}} \times (\boldsymbol{r_k} + \boldsymbol{\Phi_k}\boldsymbol{\eta})] - (2\boldsymbol{\omega_{cg}} \times \boldsymbol{\Phi_k}\dot{\boldsymbol{\eta}}) \\ \dot{\boldsymbol{\omega}}_{\boldsymbol{k}} \end{bmatrix} = \underbrace{\begin{bmatrix} \boldsymbol{I} & \boldsymbol{R} & \boldsymbol{\Phi_k} \\ 0 & \boldsymbol{I} & \boldsymbol{H_k} \end{bmatrix}}_{\boldsymbol{G_k}} \begin{bmatrix} \boldsymbol{A_{cg}} \\ \dot{\boldsymbol{\omega}}_{\boldsymbol{cg}} \\ \ddot{\boldsymbol{\eta}} \end{bmatrix} \tag{4.11}$$

Here, $\boldsymbol{R}$ is the skew-symmetric matrix to represent the $\dot{\boldsymbol{\omega}}_{\boldsymbol{cg}} \times (\boldsymbol{r} + \boldsymbol{\Phi_k}\boldsymbol{\eta})$ cross product as a matrix multiplication, and $\boldsymbol{I}$ is the identity matrix. When the amplitude of the deformations is small, the $\boldsymbol{\Phi_k}\boldsymbol{\eta}$ and $\boldsymbol{\Phi_k}\dot{\boldsymbol{\eta}}$ terms can be assumed to be zero. This equation can then be repeated for all accelerometer and gyroscope sensors, each with mode shapes corresponding to their location, as shown in Eq. (4.12).

$$\begin{bmatrix} \boldsymbol{A_1} - \boldsymbol{\omega_{cg}} \times [\boldsymbol{\omega_{cg}} \times (\boldsymbol{r_1} + \boldsymbol{\Phi_1}\boldsymbol{\eta})] - (2\boldsymbol{\omega_{cg}} \times \boldsymbol{\Phi_1}\dot{\boldsymbol{\eta}}) \\ \dot{\boldsymbol{\omega}}_{\boldsymbol{1}} \\ \vdots \\ \boldsymbol{A_N} - \boldsymbol{\omega_{cg}} \times [\boldsymbol{\omega_{cg}} \times (\boldsymbol{r_N} + \boldsymbol{\Phi_N}\boldsymbol{\eta})] - (2\boldsymbol{\omega_{cg}} \times \boldsymbol{\Phi_N}\dot{\boldsymbol{\eta}}) \\ \dot{\boldsymbol{\omega}}_{\boldsymbol{N}} \end{bmatrix} = \begin{bmatrix} \boldsymbol{G_1} \\ \vdots \\ \boldsymbol{G_N} \end{bmatrix} \begin{bmatrix} \boldsymbol{A_{cg}} \\ \dot{\boldsymbol{\omega}}_{\boldsymbol{cg}} \\ \ddot{\boldsymbol{\eta}} \end{bmatrix} \tag{4.12}$$

The aircraft's centre of gravity translation, rotation, and modal accelerations can then be estimated using the least squares fit of the combined mode shape matrix by taking the pseudoinverse (†) of the matrix.

$$\begin{bmatrix} \tilde{\boldsymbol{A}}_{\boldsymbol{cg}} \\ \tilde{\dot{\boldsymbol{\omega}}}_{\boldsymbol{cg}} \\ \tilde{\ddot{\boldsymbol{\eta}}} \end{bmatrix} = \begin{bmatrix} \boldsymbol{G_1} \\ \vdots \\ \boldsymbol{G_N} \end{bmatrix}^{\dagger} \begin{bmatrix} \boldsymbol{A_1} - \boldsymbol{\omega_{cg}} \times [\boldsymbol{\omega_{cg}} \times (\boldsymbol{r_1} + \boldsymbol{\Phi_1}\boldsymbol{\eta})] - (2\boldsymbol{\omega_{cg}} \times \boldsymbol{\Phi_1}\dot{\boldsymbol{\eta}}) \\ \dot{\boldsymbol{\omega}}_{\boldsymbol{1}} \\ \vdots \\ \boldsymbol{A_N} - \boldsymbol{\omega_{cg}} \times [\boldsymbol{\omega_{cg}} \times (\boldsymbol{r_N} + \boldsymbol{\Phi_N}\boldsymbol{\eta})] - (2\boldsymbol{\omega_{cg}} \times \boldsymbol{\Phi_N}\dot{\boldsymbol{\eta}}) \\ \dot{\boldsymbol{\omega}}_{\boldsymbol{N}} \end{bmatrix} \tag{4.13}$$

However, when the aircraft's centre of gravity accelerations are measured directly and have little influence from structural dynamics, the approach for estimating modal acceleration can be further simplified. Then, instead of estimating the centre of gravity accelerations they can directly be subtracted from the sensor

measurements, leading to Eq. (4.14).

$$\begin{bmatrix}\boldsymbol{\Phi_k}\\ \boldsymbol{H_k}\end{bmatrix}\ddot{\boldsymbol{\eta}} = \begin{bmatrix}\boldsymbol{A_k} - \boldsymbol{A_{cg}} - \dot{\boldsymbol{\omega}}_{\boldsymbol{cg}} \times (\boldsymbol{r_k} + \boldsymbol{\Phi_k\eta}) - \boldsymbol{\omega_{cg}} \times [\boldsymbol{\omega_{cg}} \times (\boldsymbol{r_k} + \boldsymbol{\Phi_k\eta})] - (2\boldsymbol{\omega_{cg}} \times \boldsymbol{\Phi_k}\dot{\boldsymbol{\eta}})\\ \dot{\boldsymbol{\omega}}_{\boldsymbol{k}} - \dot{\boldsymbol{\omega}}_{\boldsymbol{cg}}\end{bmatrix} \tag{4.14}$$

By again combining measurements from all the accelerometers and gyroscopes, the modal acceleration can be estimated by taking the pseudoinverse of the mode shape matrix.

$$\ddot{\boldsymbol{\eta}} = \begin{bmatrix}\boldsymbol{\Phi_1}\\ \boldsymbol{H_1}\\ \vdots\\ \boldsymbol{\Phi_N}\\ \boldsymbol{H_N}\end{bmatrix}^{\dagger} \begin{bmatrix}\boldsymbol{A_1} - \boldsymbol{A_{cg}} - \dot{\boldsymbol{\omega}}_{\boldsymbol{cg}} \times (\boldsymbol{r_1} + \boldsymbol{\Phi_1\eta}) - \boldsymbol{\omega_{cg}} \times [\boldsymbol{\omega_{cg}} \times (\boldsymbol{r_1} + \boldsymbol{\Phi_1\eta})] - (2\boldsymbol{\omega_{cg}} \times \boldsymbol{\Phi_1}\dot{\boldsymbol{\eta}})\\ \dot{\boldsymbol{\omega}}_{\boldsymbol{1}} - \dot{\boldsymbol{\omega}}_{\boldsymbol{cg}}\\ \vdots\\ \boldsymbol{A_N} - \boldsymbol{A_{cg}} - \dot{\boldsymbol{\omega}}_{\boldsymbol{cg}} \times (\boldsymbol{r_N} + \boldsymbol{\Phi_N\eta}) - \boldsymbol{\omega_{cg}} \times [\boldsymbol{\omega_{cg}} \times (\boldsymbol{r_N} + \boldsymbol{\Phi_N\eta})] - (2\boldsymbol{\omega_{cg}} \times \boldsymbol{\Phi_N}\dot{\boldsymbol{\eta}})\\ \dot{\boldsymbol{\omega}}_{\boldsymbol{N}} - \dot{\boldsymbol{\omega}}_{\boldsymbol{cg}}\end{bmatrix} \tag{4.15}$$

With the estimates for the centre of gravity and modal accelerations, it is now possible to combine them with the rigid aircraft kinematic equations to extend the flight path reconstruction filter for a flexible aircraft case. The time derivatives for all of the filter states presented in Eq. (4.3) are as follows, with $\tilde{\boldsymbol{A}}_{\boldsymbol{cg}}, \tilde{\dot{\boldsymbol{\omega}}}_{\boldsymbol{cg}}, \tilde{\ddot{\boldsymbol{\eta}}}$ found using Eq. (4.13) or Eq. (4.15):

$$\begin{bmatrix}\dot{x}\\ \dot{y}\\ \dot{z}\end{bmatrix} = \boldsymbol{T_{Eb}}\begin{bmatrix}u\\ v\\ w\end{bmatrix} + \boldsymbol{W^E} \tag{4.16}$$

$$\begin{bmatrix}\dot{u}\\ \dot{v}\\ \dot{w}\end{bmatrix} = \tilde{\boldsymbol{A}}_{\boldsymbol{cg}} + \begin{bmatrix}0 & -w & v\\ w & 0 & -u\\ -v & u & 0\end{bmatrix}\begin{bmatrix}p\\ q\\ r\end{bmatrix} + \boldsymbol{T_{bE}}\begin{bmatrix}0\\ 0\\ g\end{bmatrix} \tag{4.17}$$

$$\begin{bmatrix}\dot{\phi}\\ \dot{\theta}\\ \dot{\psi}\end{bmatrix} = \begin{bmatrix}1 & \sin\phi\tan\theta & \cos\phi\tan\theta\\ 0 & \cos\phi & -\sin\phi\\ 0 & \frac{\sin\phi}{\cos\theta} & \frac{\cos\phi}{\cos\theta}\end{bmatrix}\begin{bmatrix}p\\ q\\ r\end{bmatrix} \tag{4.18}$$

$$\begin{bmatrix}\dot{p}\\ \dot{q}\\ \dot{r}\end{bmatrix} = \tilde{\dot{\boldsymbol{\omega}}}_{\boldsymbol{cg}} \tag{4.19}$$

$$\begin{bmatrix}\ddot{\boldsymbol{\eta}}\\ \dot{\boldsymbol{\eta}}\end{bmatrix} = \begin{bmatrix}0 & 0\\ \boldsymbol{I} & 0\end{bmatrix}\begin{bmatrix}\dot{\boldsymbol{\eta}}\\ \boldsymbol{\eta}\end{bmatrix} + \begin{bmatrix}\boldsymbol{I}\\ 0\end{bmatrix}\tilde{\ddot{\boldsymbol{\eta}}} \tag{4.20}$$

$$\begin{bmatrix}\dot{\boldsymbol{\lambda}}\end{bmatrix} = 0 \tag{4.21}$$

Next, the filter output equations are determined. Again, first, the standard FPR output equations are presented with aircraft position, attitude, velocity, aerodynamic angle measurements, and GPS velocities [1] where v_* represents

white noise on the measurement.

$$\boldsymbol{Y} = \begin{bmatrix} x \\ y \\ z \\ \phi \\ \theta \\ \psi \\ V_{probe} \\ \alpha \\ \beta \\ V_{GPS_x} \\ V_{GPS_y} \\ V_{GPS_z} \end{bmatrix}_m = \begin{bmatrix} x \\ y \\ z \\ \phi \\ \theta \\ \psi \\ \sqrt{u^2+v^2+w^2} \\ \tan^{-1}(\frac{w}{u}) + \lambda_\alpha \\ \tan^{-1}(\frac{v}{u}) + \lambda_\beta \\ \boldsymbol{T_{Eb}} \begin{bmatrix} u \\ v \\ w \end{bmatrix} + \boldsymbol{W^E} \end{bmatrix} + \begin{bmatrix} \nu_x \\ \nu_y \\ \nu_z \\ \nu_\phi \\ \nu_\theta \\ \nu_\psi \\ \nu_V \\ \nu_\alpha \\ \nu_\beta \\ \nu_{Vx} \\ \nu_{Vy} \\ \nu_{Vz} \end{bmatrix} \tag{4.22}$$

For the flexible aircraft, additional output equations are required to correct the modal velocity and amplitude estimates. Strain gauge measurements collected across the aircraft structure can be used to aid in tracking the modal amplitudes and are therefore added to the system output vector $\boldsymbol{Y}$. The measured strains can be approximated as a summation of strain modes scaled by the modal amplitudes as shown in Eq. (4.23).

$$\epsilon_k = \boldsymbol{\Psi_k \eta} + \nu_\epsilon \tag{4.23}$$

Here, ϵ_k is the measured strain, $\boldsymbol{\Psi_k}$ is the strain mode shape matrix corresponding to that sensor, and ν_ϵ is noise. Furthermore, the rotational rates collected across the flexible aircraft structure using gyroscopes are also added. The measured rotational rates include the rotational rate of the aircraft's rigid body and are influenced by the structural modal velocities as shown in Eq. (4.24). These measurements are also added to the system output vector $\boldsymbol{Y}$ to improve the tracking of the modal velocities.

$$\boldsymbol{\omega_k} = \boldsymbol{\omega_{cg}} + \boldsymbol{H_k \dot{\eta}} + \boldsymbol{\nu_\omega} \tag{4.24}$$

Here, $\boldsymbol{\omega_k}$ is the measured rotational rate, and $\boldsymbol{H_k}$ is the rotational mode shape matrix corresponding to that sensor.

While the states, equations and outputs related to the aircraft rigid body states are according to the FPR filter which are shown to be observable [1], it is important to choose the amount and location of the additional accelerometers, gyros and strain sensors such that they provide sufficient information about the modes selected for reconstruction. When focusing on the state and output equations related to the structural modes in Eq. (4.25) and (4.26), it can be seen that the observability of the modal states is directly related to the sensor mode shapes. To improve system observability, gyro and strain sensors can be added, thereby increasing the number of rows in the $\boldsymbol{C}$ matrix until the observability matrix is full rank.

$$\begin{bmatrix} \ddot{\boldsymbol{\eta}} \\ \dot{\boldsymbol{\eta}} \end{bmatrix} = \underbrace{\begin{bmatrix} 0 & 0 \\ \boldsymbol{I} & 0 \end{bmatrix}}_{\boldsymbol{A}} \begin{bmatrix} \dot{\boldsymbol{\eta}} \\ \boldsymbol{\eta} \end{bmatrix} + \begin{bmatrix} \boldsymbol{I} \\ 0 \end{bmatrix} \tilde{\ddot{\boldsymbol{\eta}}} \tag{4.25}$$

$$\begin{bmatrix} \omega_k \\ \epsilon_k \end{bmatrix} = \underbrace{\begin{bmatrix} \boldsymbol{H_k} & 0 \\ 0 & \boldsymbol{\Psi_k} \end{bmatrix}}_{\boldsymbol{C}} \begin{bmatrix} \dot{\boldsymbol{\eta}} \\ \boldsymbol{\eta} \end{bmatrix} + \begin{bmatrix} \boldsymbol{\omega_{cg}} \\ 0 \end{bmatrix} + \begin{bmatrix} 1 & 0 \\ 0 & 1 \end{bmatrix} \begin{bmatrix} v_\omega \\ v_\epsilon \end{bmatrix} \tag{4.26}$$

Not all sensors provide the same amount of information about the structural modes. To evaluate a set of sensors and mode shapes or assist with sensor placement, the condition number of the mode shape matrix can be used as shown in Eq. (4.27). A condition number close to 1 indicates that the matrix is well-conditioned, meaning its inverse can be computed accurately. As a result, the projection of sensor measurements into modal coordinates will also be accurate.

$$\kappa(\boldsymbol{\Phi}) = \|\boldsymbol{\Phi}\| \left\|\boldsymbol{\Phi}^{\dagger}\right\| \tag{4.27}$$

As an example, Table 4.1 shows the condition number computed for varying numbers of modes N and sensor types using the mode shapes of the aircraft used in this study. As can be seen, the condition number increases as more modes are included. A larger increase occurs with mode 7 (second symmetric wing bending) as it is similar in shape to mode 1 (first symmetric wing bending). Larger condition values can also be seen for strain mode shapes, as there were fewer strain sensors compared to accelerometers or gyroscopes.

Table 4.1: Mode shape condition number for varying number of modes.

N	Acc. $\boldsymbol{\Phi_k}$	Rot. $\boldsymbol{H_k}$	Strain $\boldsymbol{\Psi_k}$	Comb. $\boldsymbol{G_k}$
1	1.00	1.00	1.00	2.61
2	1.25	1.43	1.24	2.62
3	1.63	2.52	2.47	2.94
4	1.68	2.58	2.47	3.23
5	5.30	5.75	4.71	6.48
6	5.80	8.00	52.49	6.70
7	17.55	33.87	56.00	29.05
8	17.69	37.89	99.71	33.50
9	18.25	41.59	100.26	34.51
10	18.55	44.05	300.63	37.63
11	20.94	55.52	301.40	44.00
12	27.55	59.84	304.87	47.28

Some flight test segments used in this analysis were relatively short and contained only a few excitation manoeuvres. To ensure that the estimated states from both the initial and final portions of these segments could be later used

for modelling, the Kalman filter was applied both forward and backward in time. In the beginning of the forward pass, the filter is still converging and the state estimates can be less accurate. The final estimated state and covariance from the forward pass are therefore used as the initial conditions for the backward pass, ensuring converged estimates also for the beginning of the segment. The results from the two passes were then combined to obtain a smoothed state estimate. The Fraser-Potter smoothing method computes the smoothed solution at each time step as a weighted combination of the forward and backward filtered estimates, using the respective covariance matrices as weights. The smoothed covariance and state estimates are given by [18, 19]:

$$\boldsymbol{P_S} = [\boldsymbol{P_f}^{-1} + \boldsymbol{P_b}^{-1}]^{-1} \tag{4.28}$$

$$\hat{\boldsymbol{X}} = \boldsymbol{P_S}[\boldsymbol{P_f}^{-1}\hat{\boldsymbol{X}}_f + \boldsymbol{P_b}^{-1}\hat{\boldsymbol{X}}_b] \tag{4.29}$$

where $\boldsymbol{P_S}$ is the smoothed covariance estimate, and $\hat{\boldsymbol{X}}$ is the smoothed state estimate, $\boldsymbol{P_f}$ and $\boldsymbol{P_b}$ are the covariance estimates from the forward and backward filter, respectively, and $\hat{\boldsymbol{X}}_f$ and $\hat{\boldsymbol{X}}_b$ are the state estimates from the forward and backward filter.

4.3. REFERENCE MODEL

A 1:3 scaled Diana 2 glider is used as a test aircraft to validate the working principle of the filter with flight data. A numerical model of this glider is also built for a simulation study. The glider is instrumented for flight testing with numerous sensors placed across the entire aircraft. These included inertial measurement units (IMUs), strain gauges, a GPS sensor, a 5-hole aeroprobe, and other sensors as presented in Chapter 2. An overview of the sensors used by the filter and their locations are presented in Fig. 4.1. At each IMU location, the accelerations and rotational rates on all 3-axis are measured using ICM-20948 sensors at a sampling rate of around 400 Hz. At each strain gauge location, both shear and bending strain responses are measured at a sampling rate of around 200 Hz. In total, 36 accelerations and rotational rates and 21 strains are measured. All measurements were resampled to 200 Hz, and a low-pass filter with a 60 Hz cutoff was applied before using the Kalman filter.

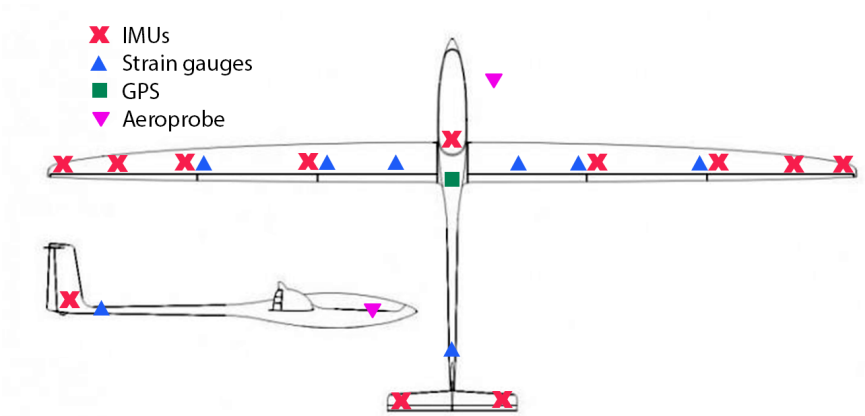

Figure 4.1: Diana 2 sensor placement overview.

The main technical parameters of the scaled glider are presented in Table 4.2 while an image of the glider is presented in Fig. 4.2.

Table 4.2: Diana 2 model technical parameters.

Property	Value	Units
Aspect ratio	24.3	-
Mean chord	0.206	m
Weight	10.7	kg
Wing area	1.03	m^2
Wingspan	5.0	m

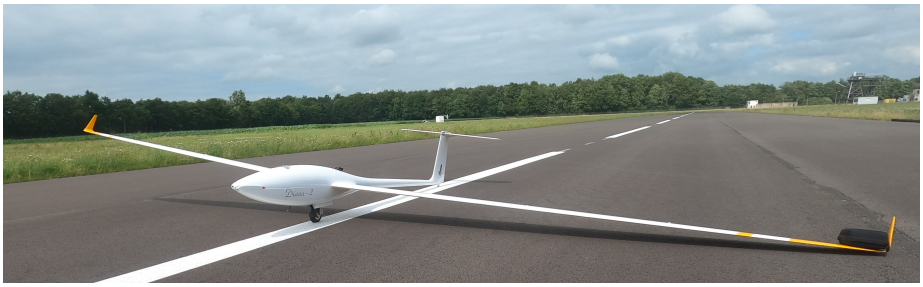

Figure 4.2: Diana 2 1:3 scaled glider.

A flight dynamics simulation model was also created to simulate and generate response measurements for an aeroelastic aircraft. This allows to evaluate the

filter's performance as the system's true states are known. First, a Finite Element Method (FEM) model of this scaled glider was created and updated using ground vibration test measurements as presented in Chapter 3. Using the FEM model together with aerodynamic panels created based on an outline scan of the glider, it was possible to create an aeroservoelastic model of the aircraft using ZAERO software [20]. This model was then implemented in Simulink to be able to fly reference manoeuvres in real time.

The implemented flight dynamics model is based on the mean-axis formulation [16, 17]. An overview of the equations governing the aircraft centre of gravity movement and the structural dynamics are presented in Eq. (4.30) to (4.36).

$$\bar{q}SC_X = m\dot{u} + m(qw - rv) + mg\sin\theta \tag{4.30}$$
$$\bar{q}SC_Y = m\dot{v} + m(ru - pw) - mg\cos\theta\sin\phi \tag{4.31}$$
$$\bar{q}SC_Z = m\dot{w} + m(pv - qu) - mg\cos\theta\cos\phi \tag{4.32}$$

$$\frac{\bar{q}Sb}{I_x}C_l = \dot{p} - \frac{I_{xz}}{I_x}\dot{r} + \frac{I_z - I_y}{I_x}qr - \frac{I_{xz}}{I_x}qp \tag{4.33}$$
$$\frac{\bar{q}S\bar{c}}{I_y}C_m = \dot{q} - \frac{I_x - I_z}{I_y}pr + \frac{I_{xz}}{I_y}(p^2 - r^2) \tag{4.34}$$
$$\frac{\bar{q}Sb}{I_z}C_n = \dot{r} - \frac{I_{xz}}{I_z}\dot{p} + \frac{I_y - I_x}{I_z}pq + \frac{I_{xz}}{I_z}qr \tag{4.35}$$

$$\frac{\bar{q}S\bar{c}}{m_i}C_{Q_i} = \ddot{\eta}_i + 2\zeta_i\omega_i\dot{\eta}_i + \omega_i^2\eta_i \tag{4.36}$$

The aerodynamic force coefficients C_X, C_Y, C_Z and moment coefficients C_l, C_m, C_n are obtained from ZAERO together with the generalised force coefficients C_{Q_i}. The state η_i represents the i-th modal amplitude, and m_i is the corresponding generalised mass. The corresponding natural frequency ω_i and damping ζ_i were determined during the ground vibration testing. The dynamic pressure $\bar{q}$ corresponds to the simulation airspeed and wing area S, and moment of inertias I_* are properties of the aircraft.

The first 12 structural modes were included in the aeroelastic model, which covers a frequency range of up to 60 Hz. In addition to the traditional displacement mode shapes, the rotational and strain modes also need to be determined during the vibration testing as they are required by the filter. In Fig. 4.3 to 4.8, six structural modes of the scaled Diana 2 glider are presented. In these figures, the displacement corresponds to displacement mode shapes, arrows correspond to rotational mode shapes, and blue/red colours show compression and tension of the strain shapes.

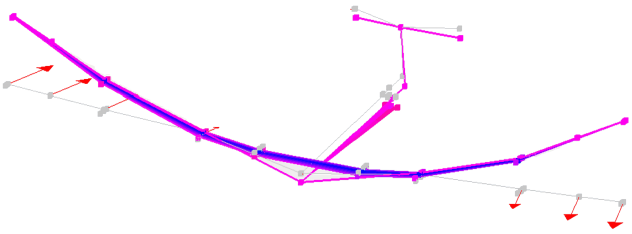

Figure 4.3: Mode 1 - 1st sym. wing bending.

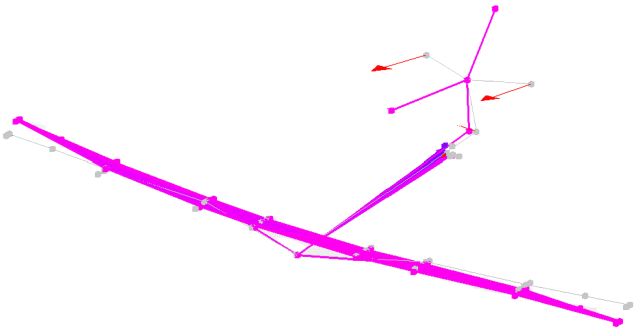

Figure 4.4: Mode 2 - horizontal tail roll.

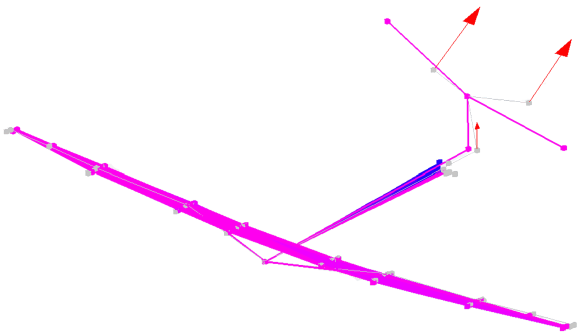

Figure 4.5: Mode 3 - vertical tail torsion.

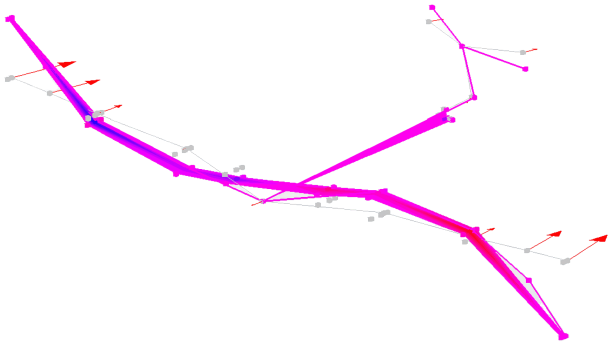

Figure 4.6: Mode 4 - 2nd asym. wing bending.

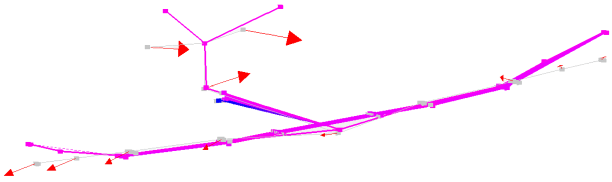

Figure 4.7: Mode 5 - fuselage bending in sym. plane.

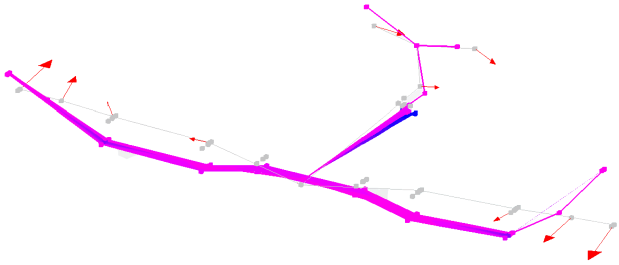

Figure 4.8: Mode 7 - 2nd sym. wing bending.

4.4. SIMULATION STUDY

In this section, the performance of the developed filter is first assessed through a simulation study, where the true system responses are known. Additionally, the filter's robustness is evaluated with respect to variations in the number of modes included in the filter and potential errors in the provided mode shapes.

4.4.1. Reference Signal Generation

With the flight dynamics simulator of the flexible aircraft implemented, it was possible to generate reference responses for the filter. Sine sweeps on the ailerons, elevator, and rudder were chosen for the control surface inputs as they can excite both the aircraft's rigid body dynamics and a range of structural modes. To evaluate the performance of the filter, zero mean white noise was added to the simulated response signals before applying the filter. Table 4.3 presents an overview of the used noise standard deviations. The chosen values are similar to or even more conservative than the sensor values used during the flight tests.

Table 4.3: Noise standard deviations for simulation study.

Signal	Noise std.	Units
Acceleration	0.05	m/s^2
AoA, AoS	0.2	deg
Attitude	1.5	deg
Position XY	1.3	m
Position Z	0.3	m
Rotational rates	0.3	deg/s
Strain	1.0	microstrain
V_{GPS}	1.0	m/s
V_{probe}	0.5	m/s
Wind	2.0	m/s

4.4.2. Filter Performance

After adding zero mean white noise to the simulation responses, the filter was applied. First, the states and measurements related to the rigid body motion were assessed. In Fig. 4.9, the aircraft attitude tracking and aerodynamic angles are presented for a time window corresponding to an elevator sine sweep. As can be seen, the filter is able to accurately reconstruct the aircraft's rigid body signals from the noisy measurements with less than 0.1 deg root mean squared error for the attitude and aerodynamic angles.

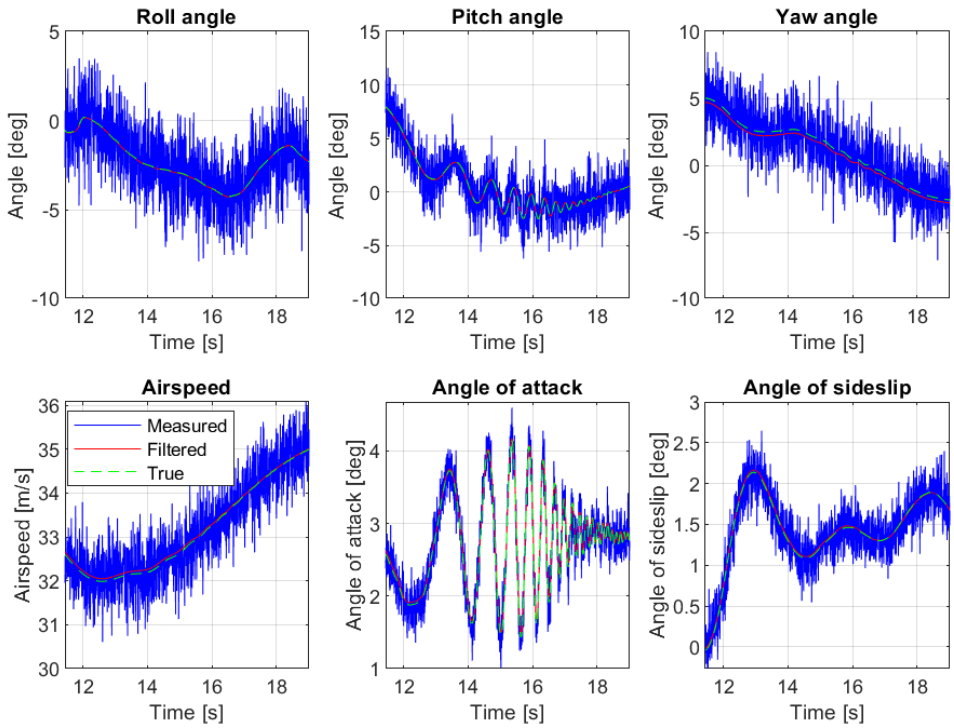

Figure 4.9: Aircraft attitude and aerodynamic angle signal tracking, simulation study.

Next, the modal tracking is explored. In addition to tuning the noise parameters for each signal, it is necessary to provide the mode shapes of modes that are to be reconstructed. To evaluate the tracking performance sensitivity to the number of modes used in the filter, reconstruction was performed while adding higher order modes one by one. In Fig. 4.10 and Fig. 4.11, the amplitude and velocity tracking for mode 1 and mode 3 are presented for varying numbers of total modes N included in the filter. These modes were selected as they were well excited by the elevator sweep manoeuvre.

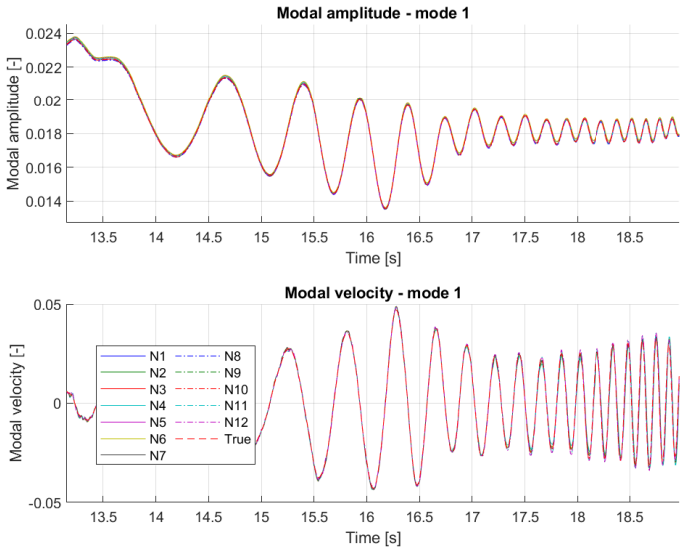

Figure 4.10: Mode 1 amplitude and velocity tracking for varying number (N) of modes included in the filter.

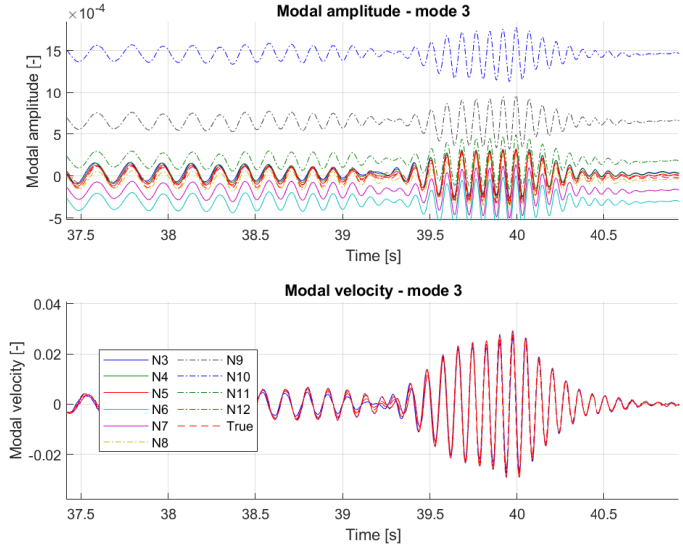

Figure 4.11: Mode 3 amplitude and velocity tracking for varying number (N) of modes included in the filter.

As can be seen, both modal amplitude and velocity have been accurately reconstructed, and the tracking results remain consistent when higher order modes are added to the filter. However, in some cases, an offset in the modal amplitude responses can be observed, as shown in Fig. 4.11. As more modes get added, a better fit of the responses can be achieved by readjusting the existing mode amplitudes. Therefore, different constant offsets for the modal amplitudes can be observed, but the dynamics of the mode are still well captured. This can be seen in Fig. 4.12 where the relative root mean square (RMS) error is found for each mode as shown in Eq. (4.37). The $\hat{\eta}$ represents the true modal amplitude, and η is the filtered. This was repeated also for the modal velocities.

$$RMS_{rel} = \frac{\sqrt{\frac{1}{N}\sum_{k=1}^{N}(\hat{\eta}_i(k) - \eta_i(k))^2}}{|max(\hat{\eta}_i) - min(\hat{\eta}_i))|} \tag{4.37}$$

In this case, the constant offset in the modal amplitudes was removed beforehand to compare the reconstructed signal dynamics. The tracking errors for each mode remain close to constant values as additional modes are added. Only for mode 7 was a significant drop in the modal amplitude error seen after adding mode 8. This is due to both of the modes being second symmetric bending modes very similar in shape. This requires both of them to be present in the filter to correctly reconstruct their contributions. While adding more modes leads to a better overall fit, there is a limit where the higher order modes can no longer be correctly distinguished from the sensor noise. This can be seen for modes 9 and 11, which show large errors for modal amplitude reconstruction. In a simulation setting where the true modal signals are known, this would be an indication to remove these modes from the filter. However, with real-world measurements, this would not be possible. Nevertheless, the key takeaway is that adding these modes to the filter does not degrade the reconstruction of the other modes.

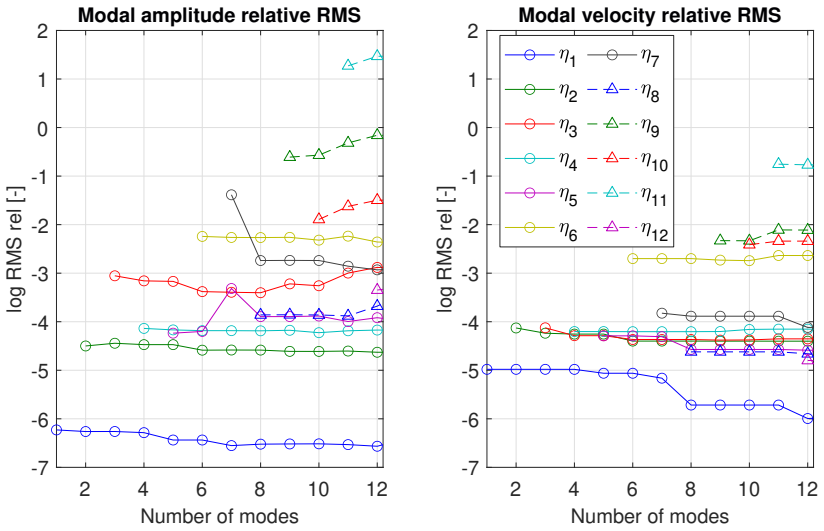

Figure 4.12: Modal amplitude and velocity tracking relative RMS error for varying modes included in the filter.

Until now, the mode shapes in the simulation model used to create the reference responses and the filter have been identical. However, in the real world, this is very unlikely. Therefore, to check the filter sensitivity for mismatches and errors in the mode shapes all the mode shape entries were randomly varied by up to ±15%. This was implemented by multiplying the values with a random gain matrix with a 5% standard deviation. In total 250 separate runs with random mode shape variations were performed. In Fig. 4.13 and Fig. 4.14 again the modal amplitude and velocity reconstruction for modes 1 and 3 are shown. Here the true modal response is shown together with the mean response across all the runs and the area covering two standard deviations of the variations in the responses. As can be seen, even with the perturbations applied on the mode shapes the filter is able to closely reconstruct the modal responses.

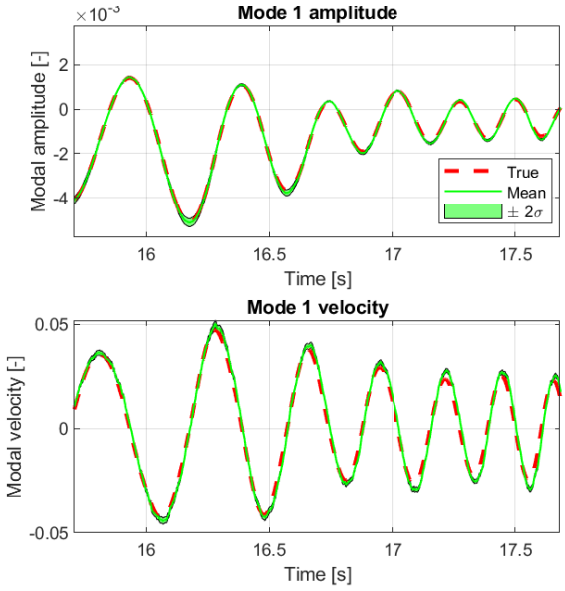

Figure 4.13: Mode 1 amplitude and velocity tracking with mode shape perturbations.

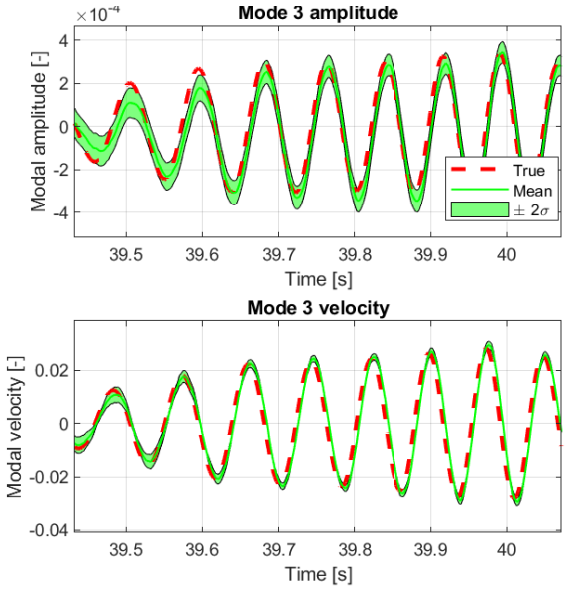

Figure 4.14: Mode 3 amplitude and velocity tracking with mode shape perturbations.

4.5. FLIGHT TEST RESULTS

After evaluating the filter performance using simulated responses, it was now possible to apply it to measurements collected during flight testing. The flight tests were conducted by piloting the aircraft remotely by line of sight using an RC radio transmitter. The aircraft was flown to an altitude of around 150-200 metres, after which the engine was turned off, and excitation manoeuvres were conducted during the gliding part of the flight to collect measurements for aeroelastic model identification. The filter was applied to the measurements collected during the gliding part of the flight to exclude segments with higher levels of noise introduced by the engine and only focus on segments including excitation manoeuvres. In total, 9 test flights were conducted, of which 145 different excitation manoeuvres were selected and analysed using the filter. In Table 4.4 the sensor noise standard deviations are presented that were used for filtering the flight test measurements.

Table 4.4: Noise standard deviations for flight test analysis.

Signal	Noise std.	Units
Acceleration	0.07	m/s^2
AoA, AoS	0.03	deg
Attitude	0.2	deg
Position XY	1.2	m
Position Z	0.3	m
Rotational acceleration	24.3	deg/s^2
Rotational rates	0.4	deg/s
Strain	0.87	microstrain
V_{GPS}	1.0	m/s
V_{probe}	0.05	m/s
Wind	2.0	m/s

First, the filter's convergence was assessed by monitoring the state estimate covariance matrix entries, as shown in Fig. 4.15. The results indicate that the covariances for all model states rapidly converge from their initial values and remain stable. The modal state covariances exhibit particularly fast convergence, possibly due to persistent excitation during the flight due to manoeuvres and atmospheric disturbances that provide sufficient information for accurate estimation. Some covariances associated with rigid body responses continue to approach their final values beyond the 500 samples presented.

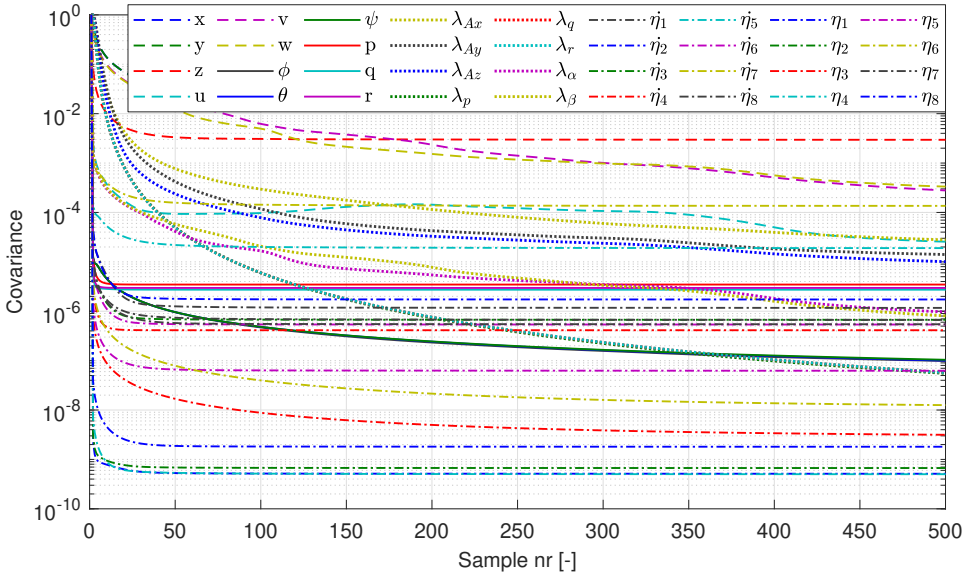

Figure 4.15: Kalman filter state estimate covariance matrix convergence.

In Fig. 4.16, the states related to the rigid body motion are presented for a flight segment that covers manually executed elevator sine sweeps. The aircraft attitude, airspeed and aerodynamic angle response measurements are presented together with filter estimates. With flight data, the true system states are unknown, which is why the filter is applied in the first place. However, the estimated states can be compared to those obtained using the FPR filter applied to the same manoeuvres. Therefore, in the following results, the measured responses are presented alongside the estimates obtained from the filter developed in this study, as well as those from the FPR filter.

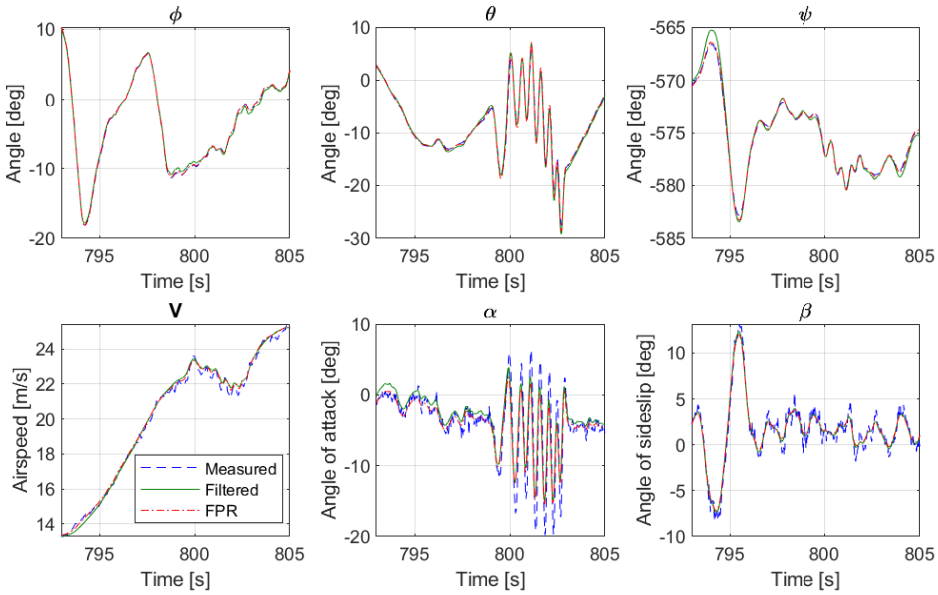

Figure 4.16: Aircraft rigid body state estimates - elevator sweep excitation.

It can be seen that the estimated states from both filters are able to closely follow the test measurements. Across all flight test segments, an average RMSE of 0.38 deg and 0.29 deg for the angle of attack and sideslip and 0.52 deg for attitude angles were observed compared to the FPR estimates. Therefore, even with all the additions to the filter, the rigid body signal reconstruction remains close to the traditional FPR results. The average RMSE between the measured responses and filter estimates was 0.73 deg for attitude angles and 1.25 deg and 0.92 deg for angle of attack and sideslip, respectively. To determine the errors, the flight segments with excitation manoeuvres were used, which contain the most dynamic responses. In Fig. 4.16, it can be seen that both filters seem to underestimate the peaks in the angle of attack responses, which was also observed during other excitations. Possible causes for this could be due to disturbed airflow from the fuselage or flexibility and deformation of the L-shaped aeroprobe under inertial loads.

Another way to check the consistency of the filter is by looking at the estimated biases. In Fig. 4.17, the mean offset biases for the angle of attack and sideslip are presented for all analysed flight test manoeuvres. As can be seen, an average offset of around -5.1 deg and 1.5 deg is found for the angle of attack and angle of sideslip, respectively. Furthermore, the biases determined across different flights and manoeuvres are consistent and grouped together. Some outliers that are further away from the mean biases were also found like the set

of negative sideslip angle bias values. However, these all corresponded to a single flight test, which could indicate a deviation in the aeroprobe installation.

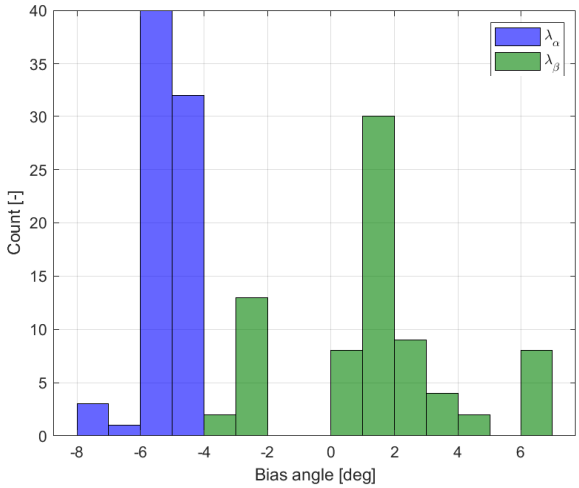

Figure 4.17: Distribution of estimated aerodynamic angle biases across different flight test segments.

Next, the modal amplitude and velocity estimates corresponding to the elevator sweep excitation are presented. Fig. 4.18 and 4.19 show the estimates for modes 1 and 7 corresponding to the first and second symmetric bending modes. The filtering was performed for varying number of modes N included in the filter.

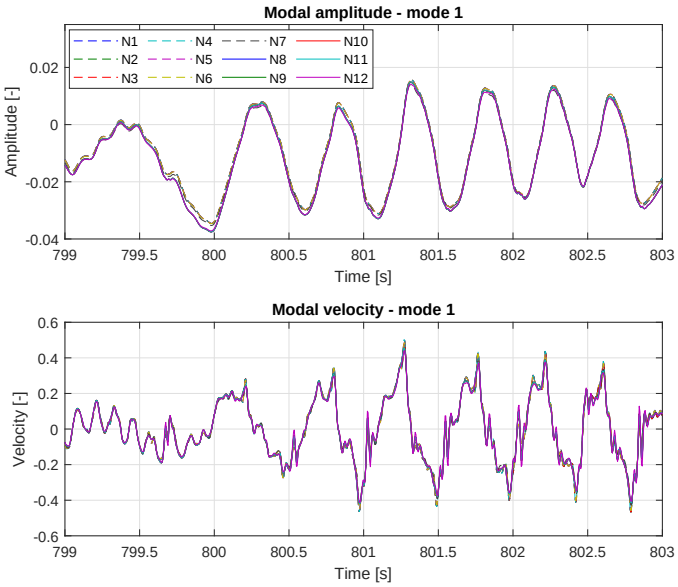

Figure 4.18: Mode 1 amplitude and velocity estimates - elevator sweep excitation.

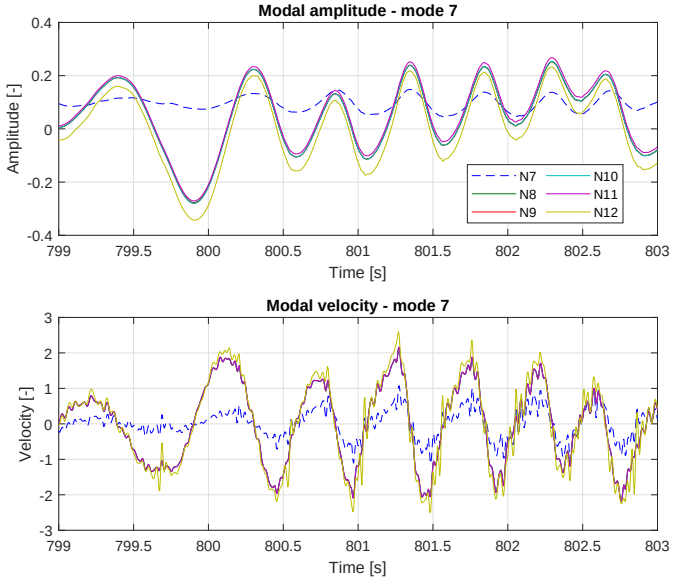

Figure 4.19: Mode 7 amplitude and velocity estimates - elevator sweep excitation.

As can be seen, the modal amplitude and velocity estimates are consistent and the addition of extra modes in the filter does not have a significant effect on the estimates. However, there is a large difference in mode 7 estimates between the case where $N = 7$ modes are included and 8 or more modes are included. This is because the mode shapes for both mode 7 and 8 both include second symmetric wing bending but mode 7 also includes first inplane wing bending while mode 8 includes fuselage bending in the symmetry plane. Therefore, once both of these modes are included in the estimation, the measured responses can be separated, which also changes the state estimates.

In Fig. 4.20, the average RMSE for rotational rate and strain responses are presented for varying number of modes included in the filter. These errors between the measured and reconstructed responses were averaged across all flight manoeuvres and included all rotational rate and strain sensors. As can be seen, the addition of modes steadily decreases the overall error in rotational rate and strain responses collected across the aircraft structure. While a large part of the responses can already be predicted with just the first mode, incremental improvements are obtained until the addition of modes 7 and 8. After mode 8, no significant improvements are obtained for the strain responses and the rotational rate response error starts to increase even. With the higher-order modes, the response amplitudes are also expected to become very small and have much less contribution to the overall response measurements. For comparison, also the RMSE for aerodynamic angle estimates is presented which shows that the estimates related to the rigid body motion are not influenced by the number of modes included in the filter.

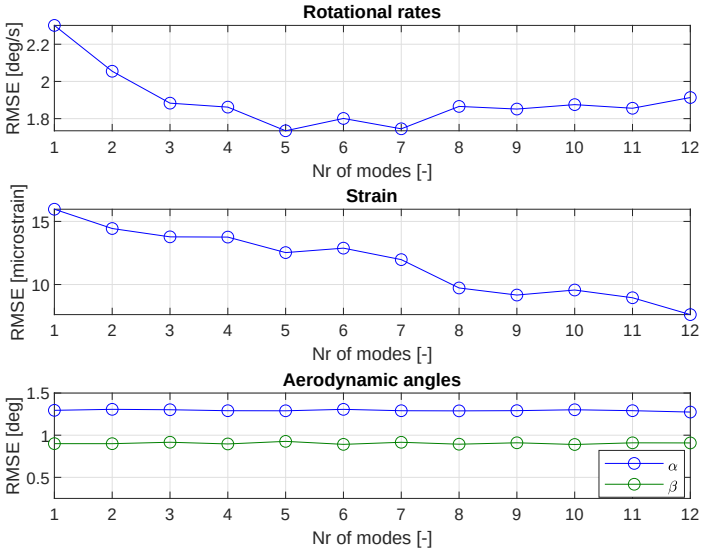

Figure 4.20: Average strain and rotational rate measurement error for varying number of modes.

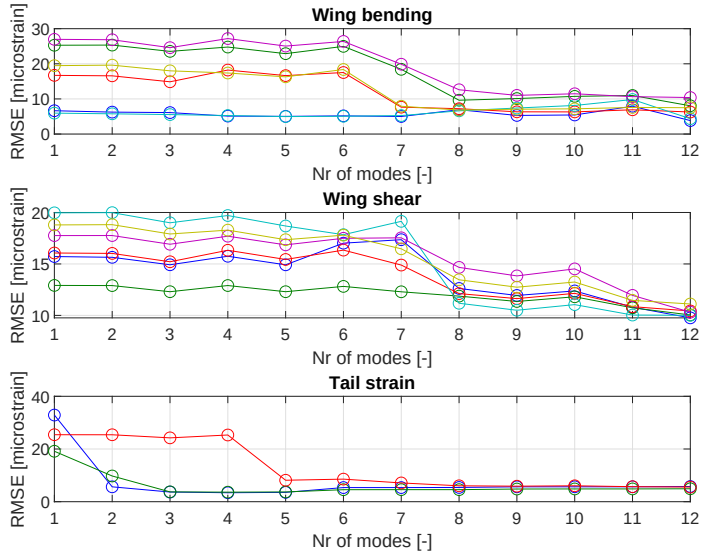

Figure 4.21: Individual strain gauge response error for varying number of modes.

Figure 4.21 presents the RMSE for individual wing bending, wing shear, and tail strain responses. The results demonstrate that modes associated with tail motion, such as modes 2, 3, and 5, lead to improvements in tail strain responses, while wing-related modes, such as modes 7 and 8, improve wing strain responses. Additionally, mode 4, corresponding to the second asymmetric wing bending mode, shows minimal improvement, likely due to insufficient excitation during the flight tests. The results also show that modes 7 and 8 should be included together in the filter to avoid an increase in wing shear strain error. In Fig. 4.22, the bending strain and yaw rate measurements collected at the aircraft tail are presented together with filter predictions for the elevator sine sweep excitation. For the yaw rate, the rigid body response is subtracted from the measurements to be able to emphasise the responses related to the structural modes. This illustrates how the addition of modes allows to better fit the filter predictions to the measured strain and rotational rate responses.

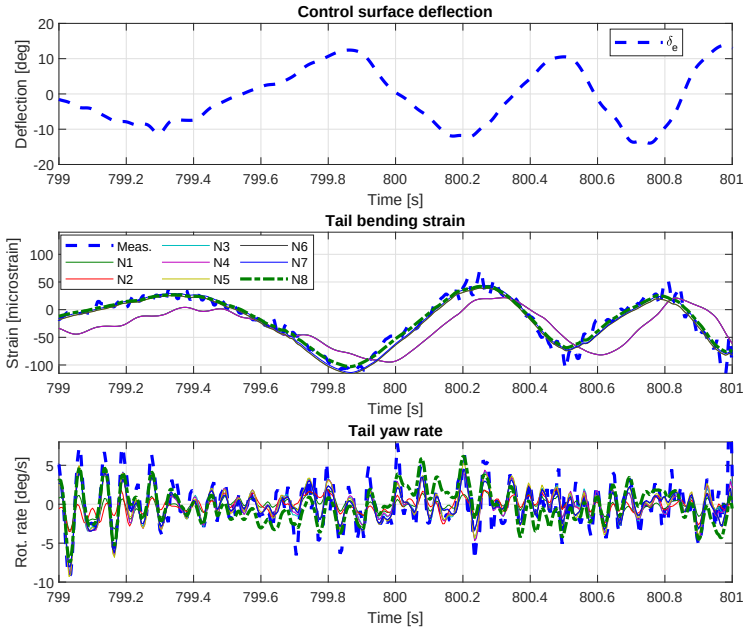

Figure 4.22: Tail bending strain and yaw rate estimates - elevator sweep excitations.

Next, the filtering results are presented for a flight segment where a series of rudder excitations were conducted. In Fig. 4.23, the state estimates related to the rigid body responses are presented again together with FPR estimates. Also for this case, the larger sideslip angle peaks were underestimated by both of

the filters but less than observed for angle of attack estimates during elevator excitations.

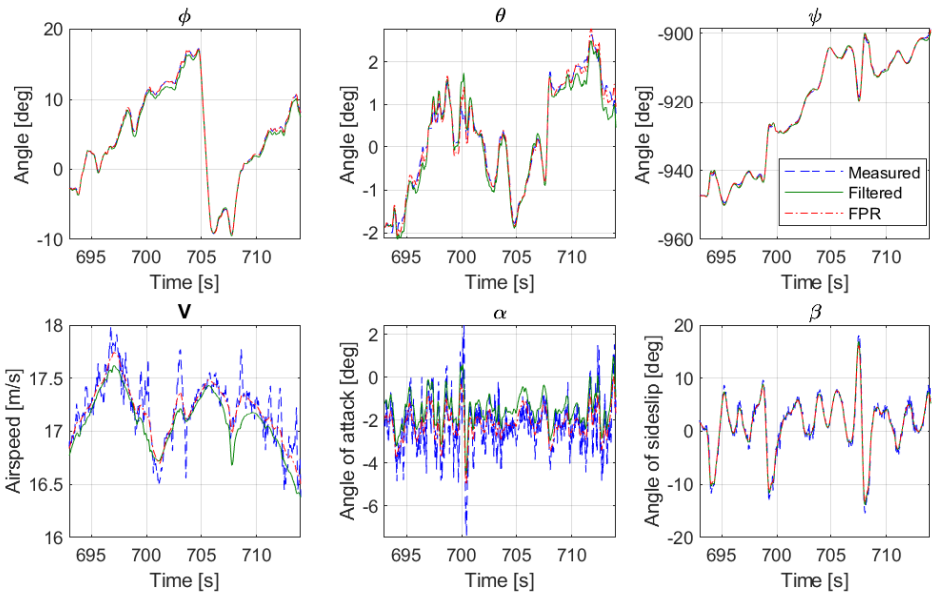

Figure 4.23: Aircraft rigid body state estimates - rudder excitations.

In Fig. 4.24 and 4.25, the modal amplitude and velocity estimates are presented for modes 2 and 6 for the rudder excitations. These modes represent the aircraft tail roll and torsion of the vertical tail, respectively. Again it can be seen that the modal estimates are consistent and do not change with the introduction of additional modes in the filter. However, there is a shift in the modal amplitude estimates as the number of modes is varied, and the weights to fit the responses using different mode shapes are readjusted.

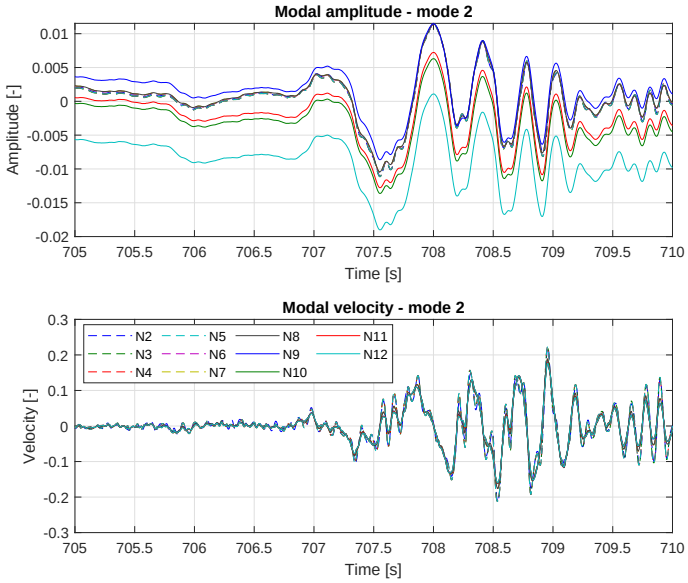

Figure 4.24: Mode 2 amplitude and velocity estimates - rudder excitations.

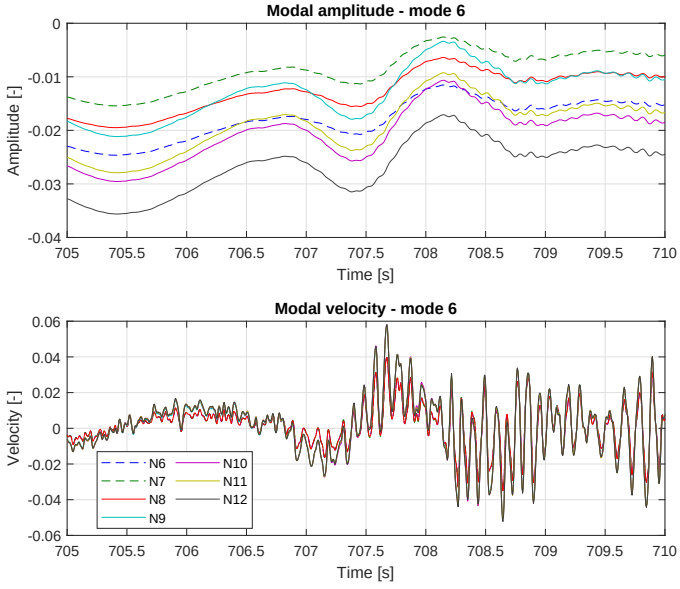

Figure 4.25: Mode 6 amplitude and velocity estimates - rudder excitations.

In Fig. 4.26, the tail shear strain and roll rate response measurements and filter predictions are presented for the rudder excitations. As there is no contribution to the tail shear strain in the first mode shape, there is also no predicted strain response for $N = 1$. However, after the addition of the tail mode, the tail shear strain responses are closely matched.

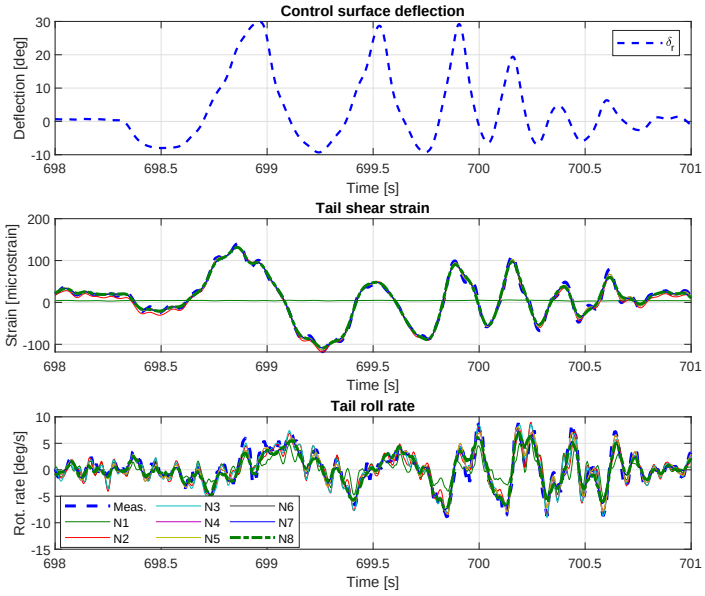

Figure 4.26: Tail shear strain and roll rate estimates - rudder excitations.

Finally, the filtering results are presented for an aileron excitation manoeuvre. In Fig. 4.27, the rigid body response measurements and filter estimates are presented once more. Also in this case, an undershoot for the larger angle of attack and sideslip peaks can be seen. While good tracking of the airspeed is obtained, a small offset can be seen in the filtered pitch attitude estimates. By lowering the noise parameters related to the attitude measurements further, a lower estimation error could be obtained but with an increase in errors for aerodynamic angle estimates.

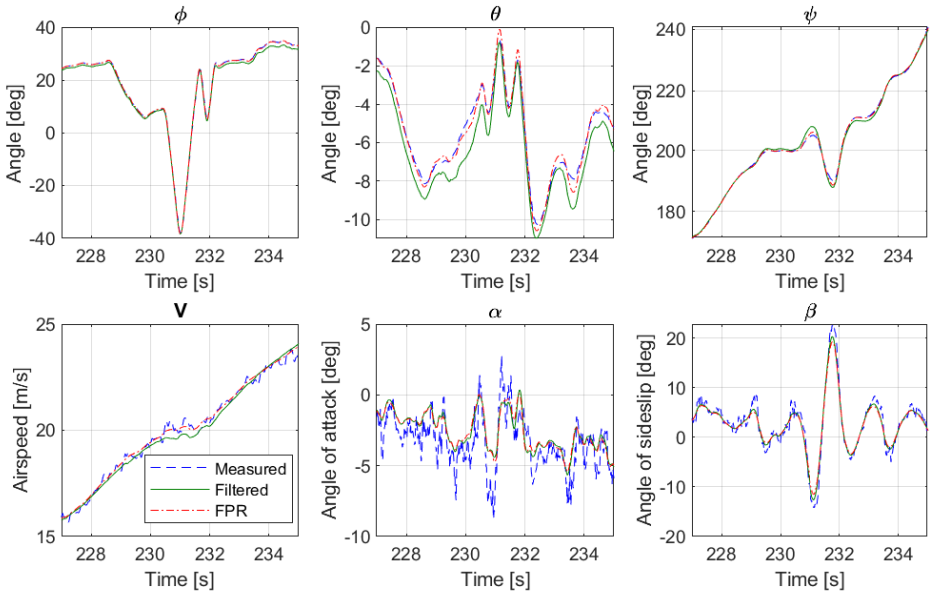

Figure 4.27: Aircraft rigid body state estimates - aileron excitations.

In Fig. 4.28, the shear strain and pitch rate response measurements for the aircraft wing are presented for the aileron excitations. Here a limitation with the approach of using only vibration test mode shapes was identified. Namely, these global vibration mode shapes are not able to fit the local effects caused by control surface movements even if all modes are included in the filter. As can be seen in Fig. 4.28, the deflection of ailerons results in shear strain due to the torsion of the wings. However, these local torsion and pitching responses cannot be matched by the filter as there are no suitable mode shapes to fit the response with. Therefore, to be able to capture these local effects, additional localised mode shapes could be considered.

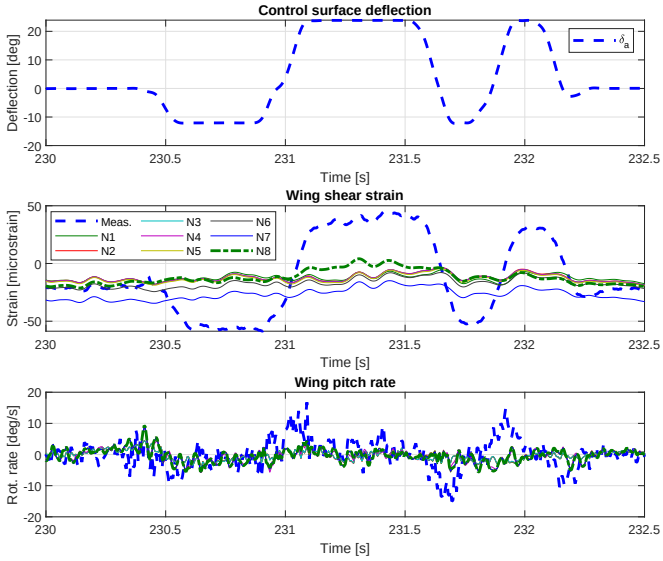

Figure 4.28: Wing shear strain and pitch rate estimates - aileron excitations.

The measured responses and state estimates for all the manoeuvres and flight tests have been published and can be found in the 4TU.ResearchData repository [21].

4.6. CONCLUSION

In this chapter, an extension to the flight path reconstruction filter was developed that is also able to estimate the aircraft modal amplitude and velocity states related to the aircraft's structural dynamic responses. This is achieved using additional measurements collected using accelerometers, gyroscopes, and strain gauges placed across the aircraft structure. The developed filter is based on flexible aircraft kinematic equations which eliminates the need for a flight dynamics model and ensures a broad applicability to different aircraft platforms. However, it is necessary to provide the displacement, rotation, and strain mode shapes corresponding to the structural modes of interest.

The performance of the proposed filter was evaluated using a scaled Diana 2 glider as a reference aircraft. The filter was first evaluated using simulated responses from an aeroelastic flight dynamics model. In this case, both the aircraft's rigid body states and the modal amplitude and velocity were accurately estimated from the noisy measurements. Furthermore, they showed to be insensitive to the number of modes used for the filter and inaccuracies in their shapes. The filter was also applied to flight test measurements during which

various excitation manoeuvres were conducted. The results showed that the rigid body state estimates closely matched the results obtained using a traditional flight path reconstruction filter with the estimated states being on average within 0.3 deg of the measured attitude responses and within 1.5 deg of aerodynamic angle measurements. Additionally, the filter was able to identify and account for constant offset biases in the aeroprobe measurements. The modal amplitude and velocity state estimates were consistent and insensitive to the number of modes included in the filter. Increasing the number of modes improved rotational rate and strain response estimates across the aircraft structure. However, limitations were observed when using aircraft vibration mode shapes to estimate responses related to local wing torsion deformations by aileron deflections.

REFERENCES

[1] J. A. Mulder, Q. P. Chu, J. K. Sridhar, J. H. Breeman and M. Laban. “Non-linear aircraft flight path reconstruction review and new advances”. In: *Progress in Aerospace Sciences* 35.7 (7 Oct. 1999), pp. 673–726. ISSN: 03760421. DOI: 10.1016/s0376-0421(99)00005-6.

[2] B. O. S. Teixeira, L. A. B. Tôrres, P. Iscold and L. A. Aguirre. “Flight path reconstruction – A comparison of nonlinear Kalman filter and smoother algorithms”. In: *Aerospace Science and Technology* 15.1 (Jan. 2011), pp. 60–71. DOI: 10.1016/j.ast.2010.07.005.

[3] P. Suh. “Robust Modal Filtering For Control Of Flexible Aircraft”. PhD thesis. Georgia Institute of Technology, 2014, p. 337.

[4] E. Livne. “Aircraft Active Flutter Suppression: State of the Art and Technology Maturation Needs”. In: *Journal of Aircraft* 55.1 (Jan. 2018), pp. 410–452. ISSN: 0021-8669. DOI: 10.2514/1.C034442.

[5] B. Z. Hadlaczky, N. Friedman, B. Takarics and B. Vanek. “Wing shape estimation with Extended Kalman filtering and KalmanNet neural network of a flexible wing aircraft”. In: *5th Annual Conference on Learning for Dynamics and Control*. PMLR. 2023, pp. 1429–1440.

[6] C. Pak. “Wing Shape Sensing from Measured Strain”. en. In: *AIAA Journal* 54.3 (Mar. 2016), pp. 1068–1077. ISSN: 0001-1452, 1533-385X. DOI: 10.2514/1.J053986.

[7] M. Gherlone, P. Cerracchio and M. Mattone. “Shape sensing methods: Review and experimental comparison on a wing-shaped plate”. In: *Progress in Aerospace Sciences* 99 (Dec. 2018), pp. 14–26. DOI: 10.1016/j.paerosci.2018.04.001.

[8] A. Derkevorkian, S. F. Masri, J. Alvarenga, H. Boussalis, J. Bakalyar and W. L. Richards. “Strain-based deformation shape-estimation algorithm for control and monitoring applications”. In: *AIAA Journal* 51.9 (2013), pp. 2231–2240. DOI: 10.2514/1.j052215.

[9] Z. Ma and X. Chen. “Fiber Bragg gratings sensors for Aircraft Wing Shape Measurement: Recent applications and technical analysis”. In: *Sensors* 19.1 (2018), p. 55. DOI: 10.3390/s19010055.

[10] A. W. Burner and T. Liu. “Videogrammetric model deformation measurement technique”. en. In: *Journal of Aircraft* 38.4 (July 2001), pp. 745–754. DOI: 10.2514/2.2826.

[11] A. W. Burner, W. A. Lokos and D. A. Barrows. *Aeroelastic Deformation: Adaptation of Wind Tunnel Measurement Concepts to Full-Scale Vehicle Flight Testing*. TM-2005-213790. NASA Langley Research Center, Jan. 2005, pp. 1–17.

[12] T. Mkhoyan, C. C. de Visser and R. De Breuker. "Adaptive real-time clustering method for dynamic visual tracking of very flexible wings". en. In: *Journal of Aerospace Information Systems* 18.2 (Feb. 2021), pp. 58–79. DOI: 10.2514/1.I010860.

[13] A. Kotikalpudi, D. K. Schmidt, C. D. Regan and P. J. Seiler. "Real-time shape estimation for flexible unmanned air vehicle via Kalman filtering". In: *AIAA Scitech 2020 Forum*. Orlando, FL: American Institute of Aeronautics and Astronautics, Jan. 2020. DOI: 10.2514/6.2020-1267.

[14] L. R. Lustosa, I. Kolmanovsky, C. E. S. Cesnik and F. Vetrano. "Aided Inertial Estimation of Wing Shape". In: *Journal of Guidance, Control, and Dynamics* 44.2 (2 Feb. 2021), pp. 210–219. ISSN: 1533-3884. DOI: 10.2514/1.G005368.

[15] G. Schirmer, J. E. Steck and A. Chakravarthy. "Design, implementation and experimental testing of an inertial sensor system to quantify wing deflection". In: *AIAA Scitech 2019 Forum*. San Diego, California: American Institute of Aeronautics and Astronautics, Jan. 2019. DOI: 10.2514/6.2019-1539.

[16] M. R. Waszak and D. K. Schmidt. "Flight dynamics of aeroelastic vehicles". In: *Journal of Aircraft* 25.6 (1988), pp. 563–571. ISSN: 0021-8669. DOI: 10.2514/3.45623.

[17] J. A. Grauer and M. J. Boucher. *Output Measurement Equations for Flexible Aircraft Flight Dynamics*. TM–2018–220102. NASA Langley Research Center, 2018, pp. 1–36.

[18] C. Karlgaard, P. Tartabini, R. Blanchard, M. Kirsch and M. Toniolo. "Hyper-X Post-Flight Trajectory Reconstruction". In: *AIAA Atmospheric Flight Mechanics Conference and Exhibit*. American Institute of Aeronautics and Astronautics, Aug. 2004. DOI: 10.2514/6.2004-4829.

[19] D. Fraser and J. Potter. "The optimum linear smoother as a combination of two optimum linear filters". In: *IEEE Transactions on Automatic Control* 14.4 (Aug. 1969), pp. 387–390.

[20] ZONA Technology Inc. *ZAERO Theoretical Manual, Version 9.0*. Scottsdale, Arizona, 2014.

[21] A. Jürisson, B. Eussen, C. C. de Visser and R. De Breuker. *Flexible Diana 2 Scaled Glider UAV - State Estimation Results*. Dataset. 4TU.ResearchData, 2026. DOI: 10.4121/ba9d8ff9-98aa-40bc-b0db-3b5f406c21f1.

5

FLIGHT DYNAMICS AND LOADS MODEL IDENTIFICATION

The main challenge in incorporating unsteady aerodynamic effects into the flexible aircraft model identification was finding a method to estimate the states that characterise these effects from the aircraft response measurements collected during flight. This chapter introduces a methodology for estimating aerodynamic lag poles and reconstructing the aerodynamic lag states from flight test measurements.

The reconstructed aerodynamic lag states are then used, alongside the aircraft states estimated in the previous chapter, to identify models for the aerodynamic force and moment coefficients, generalised force coefficients for the structural modes, and wing root and tail load coefficients. Finally, the identified models are validated through an open-loop simulation, where their predictions are compared with the responses measured during flight tests.

This chapter is based on the following article: Jürisson, A., Eussen, B., de Visser, C. C., & De Breuker, R., ”Flexible aircraft model identification from flight tests including unsteady aerodynamic effects” in *Journal of Aircraft (submitted)*, 2026

5.1. Introduction

In order to increase aircraft performance and reduce fuel consumption, modern aircraft designs are incorporating lighter materials and slender, high-aspect-ratio wings. While these innovations improve performance and reduce fuel consumption, they also increase structural flexibility that affects flight dynamics. The reduced frequency separation between rigid-body and structural dynamics leads to increased coupling between aeroelastic effects and conventional flight dynamics. Accurately capturing these interactions is not only essential for ensuring flight safety, but also for control system design and developing high-fidelity flight simulators.

System identification methods provide a way to obtain models that capture these effects from flight test measurements. Well-established techniques exist for rigid aircraft but these do not capture the interactions with the flexible structure. System identification for flexible aircraft remains an area of active research, particularly when using flight test data. Grauer [1] highlights several challenges in this domain, including the complexity of larger models, the requirement to excite a broad frequency range during flight tests, the need for extensive sensor instrumentation, the indirect observability of modal states, and the reliance on nonlinear optimisation methods requiring accurate initial parameter estimates.

Several identification methods have been applied to flexible aircraft in prior research. Grauer and Boucher [1, 2] employed equation-error and output-error methods in the frequency-domain to identify the longitudinal dynamics of the X-56A aircraft. Danowsky et al. [3] used time-domain prediction-error methods to identify a scaled X-56A model by first estimating the rigid-body coefficients before incorporating the structural modes to the model. Similarly, Silva [4] applied an output-error method in the time-domain to identify the SB10 glider model by also increasing the model size incrementally with added structural modes. Viana [5] extended that approach by identifying local aerodynamic loads alongside flight dynamics and structural responses on the Discus-2c glider, integrating six structural modes into a comprehensive model.

The Waszak and Schmidt [6] mean-axis formulation was used by these existing methods to describe the equations of motion for flexible aircraft. However, it assumes quasi-steady aerodynamics, grouping all unsteady aerodynamic effects into aeroelastic stability derivatives [1]. Consequently, this approach may not fully capture response amplitude variations and phase shifts due to unsteady aerodynamic effects as described by Theodorsen [7], particularly when operating in unsteady aerodynamic conditions.

This chapter presents a methodology for identifying flight dynamics models of flexible aircraft while considering unsteady aerodynamic effects. A key component of this approach is the identification of aerodynamic lag poles and the reconstruction of aerodynamic lag states from flight test measurements, which are critical for capturing unsteady flow effects. The methodology is applied to a scaled Diana 2 glider unmanned aerial vehicle (UAV), for which both flight dynamics and loads models are identified. For this purpose, the Two-Step Method (TSM) [8, 9] is employed, in which the flexible aircraft states are first

estimated before an ordinary least squares estimation is used to identify model parameters. This circumvents challenges associated with nonconvex optimisation and dependence on the availability of good initial parameter values. The resulting grey-box model provides physically interpretable parameters, offering insights into the coupled flight dynamics and aeroelastic behaviour of the aircraft.

The remainder of this chapter is structured as follows. Section 5.2 presents an overview of aeroelastic aircraft modelling with unsteady aerodynamics and details the proposed method for reconstructing aerodynamic lag states from flight test measurements. Section 5.3 introduces the test aircraft and provides an overview of the conducted flight tests. In Sec. 5.4 aerodynamic lag poles are estimated from flight test measurements and flexible aircraft states are estimated. Section 5.5 presents the identified flight dynamics and loads models and in Sec. 5.6 the models are validated in open-loop simulations. Finally, the conclusions of the chapter are provided in Sec. 5.7.

5.2. THEORETICAL BACKGROUND

This section provides a brief overview of aeroelastic aircraft modelling and unsteady aerodynamics, along with a method for reconstructing aerodynamic lag states from flight test response measurements. To illustrate the proposed approach, a typical section model is used for simplicity. A typical section represents an aeroelastic model of a symmetric airfoil with heave (h) and pitch (θ) degrees of freedom (DOF). According to Theodorsen [7], the aerodynamic force and moment about the airfoil's elastic axis can be expressed as the sum of circulatory and non-circulatory components. The circulatory terms are frequency-dependent and correspond to the vorticity in the airflow. The Theodorsen function describes the amplitude and phase variations in unsteady aerodynamic forces relative to quasi-steady forces across different reduced frequencies. The reduced frequency, denoted as k, is defined in Eq. (5.1), where ω is the oscillation frequency, $\bar{b}$ is the half-chord length, and V is the airspeed.

$$k = \frac{\omega \bar{b}}{V} \tag{5.1}$$

Figure 5.1 illustrates the Theodorsen function evaluated across different reduced frequencies, highlighting the variations in amplitude and phase. Notably, the largest phase differences between unsteady and quasi-steady forces are experienced within the reduced frequency range of approximately 0.15 to 0.3.

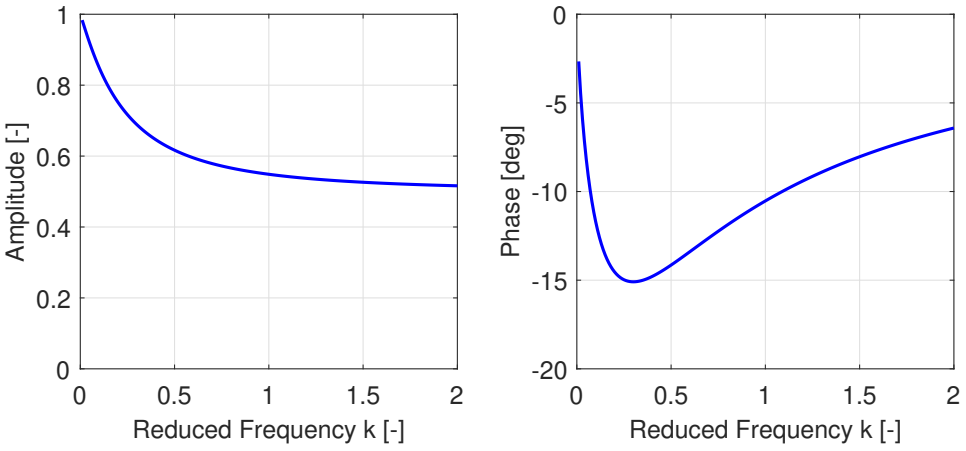

Figure 5.1: Theodorsen function amplitude and phase lag effects [10].

While the Theodorsen function describes the unsteady aerodynamic response in the frequency-domain, Wagner's function is its time-domain counterpart, which characterises the lift response of a typical section to a step change in angle of attack. Then, Jones's approximation [11] provides an analytical expression for Wagner's function, as shown in Eq. (5.2), where $\psi_1 = 0.165, \psi_2 = 0.335$ and $p_1 = -0.0455, p_2 = -0.3$.

$$\phi(t) = 1 - \psi_1 e^{p_1 \frac{V}{b} t} - \psi_2 e^{p_2 \frac{V}{b} t} \tag{5.2}$$

However, for state-space models, the aerodynamics lag states, as shown in Eq. (5.3), are more commonly used to represent the unsteady aerodynamic responses.

$$\dot{x}_{lag} = p_i \frac{V}{b} x_{lag} + u_i \tag{5.3}$$

Here u_i corresponds to the model DOF and x_{lag} is the corresponding state with delayed responses. Figure 5.2 illustrates the impact of different pole values on step responses, using the Diana 2 glider's chord length and an airspeed of 20 m/s. As shown, more negative pole values result in shorter response delays.

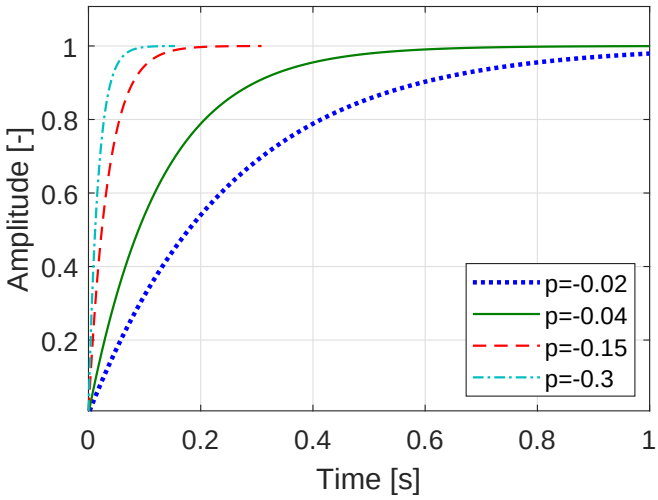

Figure 5.2: Lag pole effect on the lag state response.

In aeroelastic analysis, the generalised aerodynamic forces $\boldsymbol{Q}$ acting on the system are computed for different reduced frequencies. A time-domain approximation of these frequency-domain solutions can be achieved using the rational function approximation (RFA) method. This approach utilises aerodynamic matrices $\boldsymbol{A_i}$ along with the aerodynamic lag states, as shown in Eq. (5.4), to accurately fit the frequency-domain data.

$$\boldsymbol{Q} \approx \bar{q}(\boldsymbol{A_2}\ddot{\boldsymbol{x}} + \boldsymbol{A_1}\dot{\boldsymbol{x}} + \boldsymbol{A_0}\boldsymbol{x} + \sum_{i=1}^{N_{lag}} \boldsymbol{A_{(2+i)}} x_{lag}^{i}) \tag{5.4}$$

where $\bar{q}$ is the dynamic pressure and $\boldsymbol{x}$ is the vector with system DOF, which for a typical section include the pitch and plunge DOF. N_{lag} represents the number of aerodynamic lag states used for the fitting.

While the lag poles p_i for the 2-DOF typical section are well established and can be derived from Jones's approximation, they become additional fitting parameters in the RFA procedure when approximating frequency-domain solutions. In this process, the number of aerodynamic lag states N_{lag} is incrementally increased until the time-domain model achieves a satisfactory fit with the frequency-domain data. However, such a solution is not available when using flight test response measurements and measuring the lag states directly is also not possible. Thus, an alternative approach is required to determine both the lag poles and reconstruct the lag states.

In this chapter, a method is proposed to estimate the lag pole values and reconstruct the lag states, which is first demonstrated using a 2-DOF typical section model. Following the derivation by Boutet and Dimitriadis [12], a state-space representation of the typical section is obtained, as shown in Eq.(5.5),

where the aerodynamic forces described by Eq.(5.4) are coupled with a structural model, with $\boldsymbol{M_s}$ and $\boldsymbol{K_s}$ representing the structural mass and stiffness matrices, respectively.

$$\boldsymbol{M_s}\ddot{\boldsymbol{x}} + \boldsymbol{K_s}\boldsymbol{x} = \bar{q}(\boldsymbol{A_2}\ddot{\boldsymbol{x}} + \boldsymbol{A_1}\dot{\boldsymbol{x}} + \boldsymbol{A_0}\boldsymbol{x} + \boldsymbol{A_{lag}}\boldsymbol{x_{lag}}) \tag{5.5}$$

Using this model, responses to different initial conditions were simulated and the pitch (θ) and plunge (h) states together with lift force (C_L) and pitch moment (C_m) coefficients were recorded as shown in Fig. 5.3. From these responses, the goal is to estimate the lag poles and reconstruct the lag states.

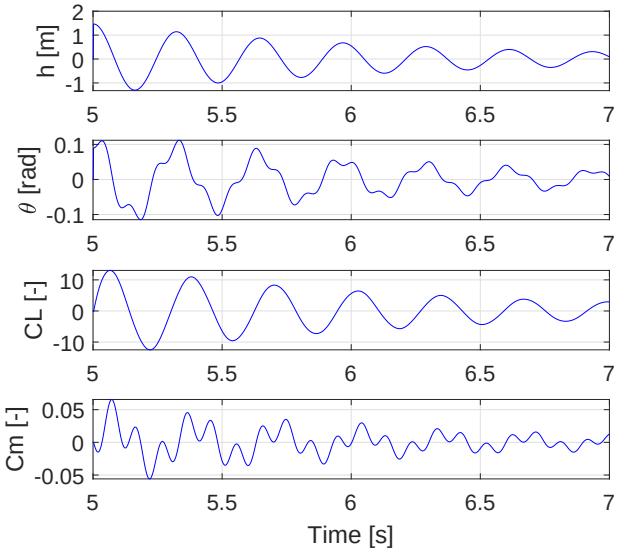

Figure 5.3: Typical section response to an initial condition.

In the case of the typical section, the aerodynamic lag states are driven by the pitch angle and plunge states. Therefore, as long as the aerodynamic lag state inputs are measured, it is possible to reconstruct the lag state using Eq. (5.6).

$$x_{lag}(t_{k+1}) = \left(1 + p_i \frac{V(t_k)}{\bar{b}} \Delta t\right) x_{lag}(t_k) + \Delta t \cdot u_i(t_k) \tag{5.6}$$

where Δt is the sampling time of the response measurements and t_k is the sample at time t. In the case of flight test measurements, where the airspeed is changing, it needs to be measured and accounted for by using the current airspeed $V(t_k)$ when reconstructing the lag states.

Next, a set of different aerodynamic lag states are reconstructed by varying pole values from poles corresponding to long delays $p_i = -0.01$ to short delays $p_i < -0.3$. Each reconstructed lag state is then cross-correlated with an

aerodynamic force and/or moment coefficient and the resulting correlation values are plotted for each pole value as presented in Fig. 5.4.

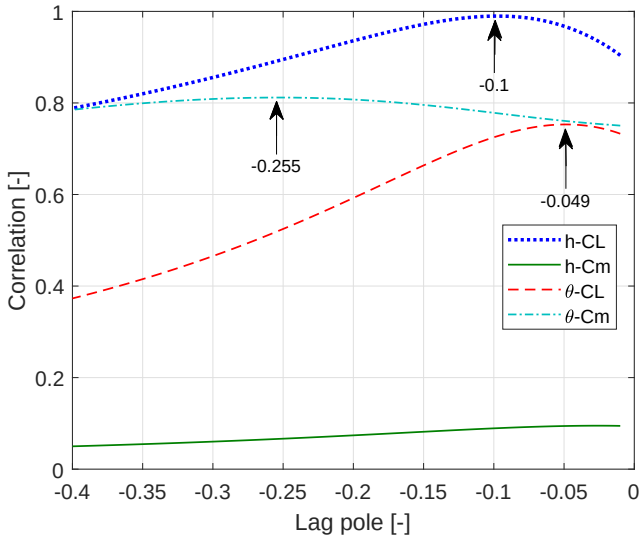

Figure 5.4: Lag state correlation with response signals for varying lag pole values.

The results in Fig. 5.4 show that, as the lag poles are varied between -0.01 and -0.4, certain input-response combinations display distinct peaks in correlation, which are highlighted in the figure. Table 5.1 lists the pole values corresponding to these peaks. As shown, the method successfully identifies estimates that are close to the true pole values of -0.0455 and -0.3. Additionally, a peak corresponding to a pole value of -0.1 is observed, which was not present in the typical section model. As a result, all these candidate lag states must be evaluated during the modelling process to determine which ones improve modelling accuracy and should be included in the final model. For the $h - C_m$ combination, no pole value was selected, as the overall correlation remained low and no distinct peak was observed in the correlation results. A minimum correlation threshold can be applied during the selection process to ensure that selected pole values exhibit a strong correlation with the measured force and moment coefficients.

Table 5.1: Lag pole estimates determined from typical section responses.

Input	Response	Pole
h	C_L	-0.1
θ	C_L	-0.049
θ	C_m	-0.255

The proposed approach can be seen as a cross-correlation analysis. However, since the delay between input states and response coefficients is airspeed dependent, the lag states must first be reconstructed while accounting for the current airspeed measurements. This allows to identify the delay that maximises correlation and determine the corresponding pole value. To summarise the method, the following algorithm overview is presented:

Algorithm 1 Aerodynamic lag state pole estimation procedure

1. Select a response and an input for evaluation.
2. Assume a pole value, p_i.
3. Reconstruct the lag state using Eq. (5.6), initializing $x_{\text{lag}}(t_0) = 0$.
4. Compute the correlation between the response and the lag state.
5. Repeat steps 2–4 for varying pole values, p_i, resulting in plots as shown in Fig. 5.4.
6. Search for a peak in correlation value that exceeds a predefined minimum threshold.
7. Select the corresponding pole value as the lag state pole.

Repeat the procedure for different response and input combinations.

5.3. Test aircraft and flight testing

For this research, flight response measurements were gathered using a 1:3 scale model of the Diana 2 glider as the test platform. This unmanned aerial vehicle (UAV) has a weight of 10.7 kg and high aspect ratio wings with a 5-metre wingspan. The aircraft is equipped with two ailerons and a flap on each wing, along with two elevator control surfaces and a single rudder in a T-tail configuration. Additionally, an electric propulsion system with folding propellers is integrated into the nose of the aircraft. The key technical specifications of the scaled glider are summarised in Table 5.2, while an image of the aircraft is provided in Fig. 5.5.

Table 5.2: Diana 2 model technical parameters.

Property	Value	Units
Aspect ratio	24.3	-
Mean chord	0.206	m
Weight	10.7	kg
Wing area	1.03	m^2
Wingspan	5.0	m

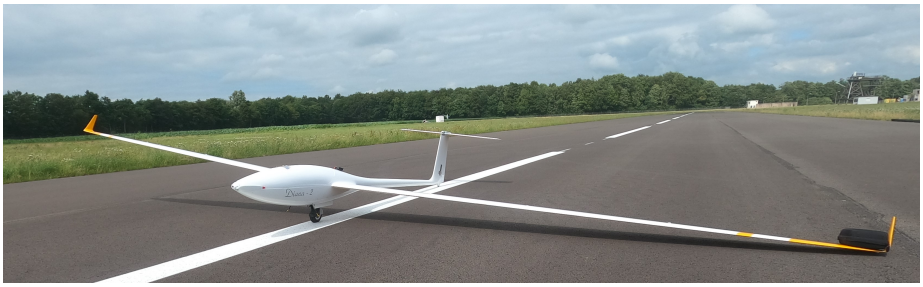

Figure 5.5: Diana 2 scaled glider.

5.3.1. Instrumentation of the scaled Diana 2 glider

To capture both the aircraft's dynamic responses and structural behaviour, the glider is equipped with numerous sensors distributed across its structure. A total of 36 acceleration and rotational rate measurements are recorded using 3-axis ICM-20948 inertial measurement units (IMUs). Additionally, shear and bending strain gauges are used to monitor structural deformations and loads acting on the aircraft, providing 21 strain measurements - nine from each wing and three from the tail. A 5-hole aeroprobe is used to measure airspeed, angle of attack, and angle of sideslip. The aircraft's position is determined using an RTK-GPS system, while magnetic rotary encoders record control surface deflections. A more detailed description of the data acquisition system and calibration procedures, including load-strain calibration, is provided in Chapter 2. Figure 5.6 illustrates the sensor locations across the aircraft. For clarity, only the locations of the IMUs and rotary encoders are shown on the left wing, and the strain gauges on the right wing. In the aircraft, the instrumentation is identical on both wings.

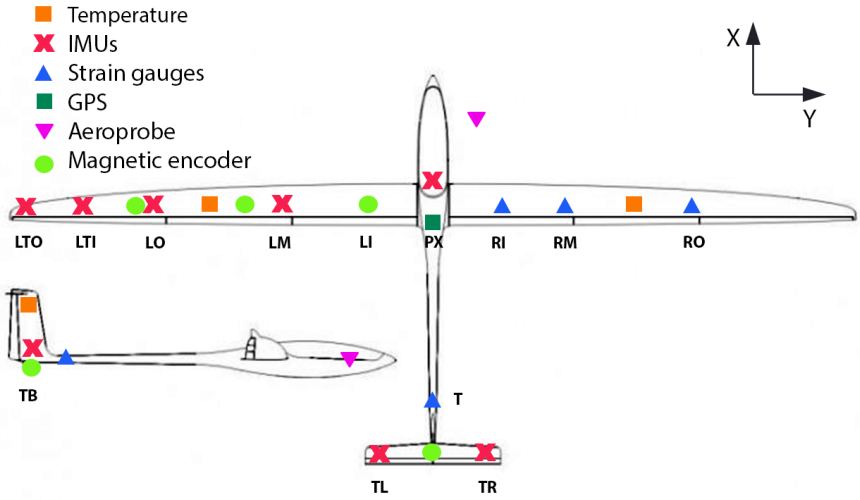

Figure 5.6: Diana 2 sensor placement overview.

To control the aircraft, a differential aileron mixing law was implemented based on manufacturer recommendations. This mixing law restricts the maximum upward deflection to 100% for the outer ailerons and 70% for the middle ailerons, while limiting downward deflection to 60% and 50% for the outer and middle ailerons, respectively. As a result, the movements of the outer and middle ailerons remained linked throughout flight testing. Rather than using individual control surface measurements for modelling, the deflection measurements from the right wing outer (RO) and left wing outer (LO) ailerons are combined into a single aileron and flap setting signals, as shown in Eq. (5.8) and Eq. (5.7). The same approach was applied to the middle ailerons and flaps.

$$\delta_{ao} = \frac{1}{2}\left(\delta_a^{RO} - \delta_a^{LO}\right) \tag{5.7}$$

$$\delta_{fo} = \frac{1}{2}\left(\delta_a^{RO} + \delta_a^{LO}\right) \tag{5.8}$$

This representation avoids collinearity, which arises because the linked ailerons do not move independently, making it difficult to capture their individual effects during parameter estimation [13].

5.3.2. Structural properties of the test aircraft

A ground vibration test (GVT) was performed using the integrated sensors to determine the modal parameters of the aircraft structure. This test also allowed to validate the accuracy and sensitivity of the sensors in capturing structural

modes. An overview of the first six structural modes is presented in Table 5.3, with detailed results available in Chapter 3.

Table 5.3: Overview of scaled Diana 2 structural modes.

Mode	Frequency [Hz]	Damping [-]	Description
1	7.42	2.88%	1st sym. wing bending
2	9.94	2.18%	Tail roll
3	13.82	2.72%	Vertical tail torsion
4	17.31	1.10%	2nd asym. wing bending
5	20.01	0.75%	1st inplane wing bending
6	21.19	2.47%	Fuselage bending out of sym. plane

The mode shapes for the first four structural modes are illustrated in Figs.5.7 to 5.10. The GVT was performed using accelerometers, gyroscopes, and strain gauges, which resulted in displacement, rotational, and strain mode shapes. In these figures, displacement mode shapes are represented by structural deformation. Arrows indicate rotational mode shapes, pointing in the direction of the resultant vector. The strain mode shapes are represented by colour, with blue for compression and red indicating tension.

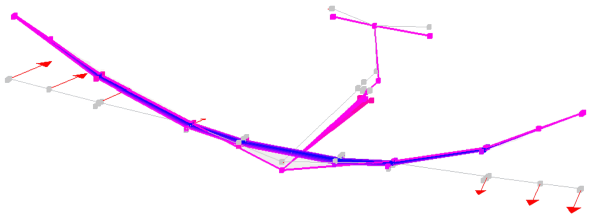

Figure 5.7: Mode 1 - 1st sym. wing bending.

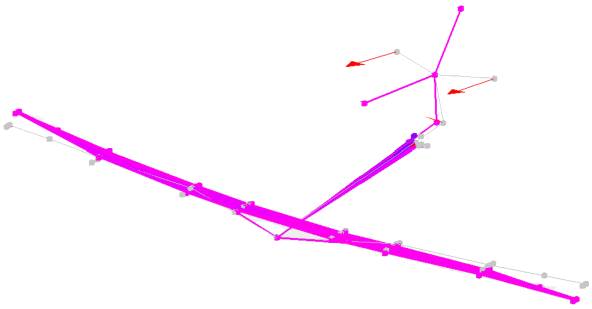

Figure 5.8: Mode 2 - horizontal tail roll.

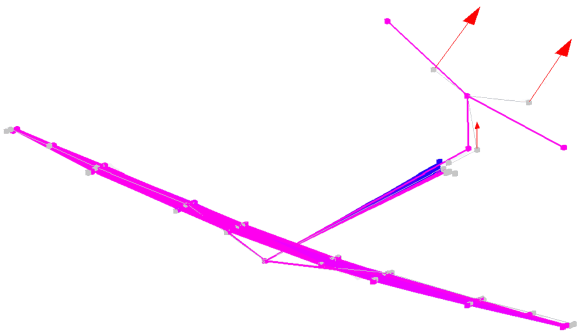

Figure 5.9: Mode 3 - vertical tail torsion.

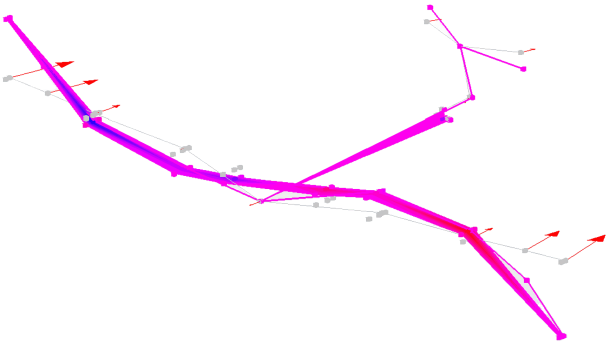

Figure 5.10: Mode 4 - 2nd asym. wing bending.

During the GVT, the moment of inertia of the aircraft was also estimated, which is presented in Table 5.4.

Table 5.4: Moment of inertia of scaled Diana 2 glider.

Inertia	I_x	I_y	I_z	I_{xz}
Value $[kg \cdot m^2]$	4.445	1.642	6.897	0.332

5.3.3. Flight test manoeuvres

The flight test campaign was conducted at the airfield of the Royal Netherlands Aerospace Centre in Marknesse, The Netherlands. A total of nine successful flight tests were carried out over four separate test days. The aircraft was remotely piloted via line-of-sight using an RC radio transmitter. At the start and

end of each flight, the aircraft was kept steady and level on the ground for roughly one minute to also record measurements for potential sensor bias corrections. Each flight began with a climb to a target altitude of approximately 150-200 metres using the electric motor. Once at altitude, the motor was switched off, and excitation manoeuvres were performed during the gliding phase. These manoeuvres were initiated from straight and level flight conditions at an airspeed of 20-25 m/s. As shown in Fig. 5.11, this airspeed range places the first structural mode and control surfaces within a target reduced frequency range of 0.15-0.3. In this range, the phase shift between quasi-steady and unsteady aerodynamic forces is the largest, as illustrated in Fig. 5.1.

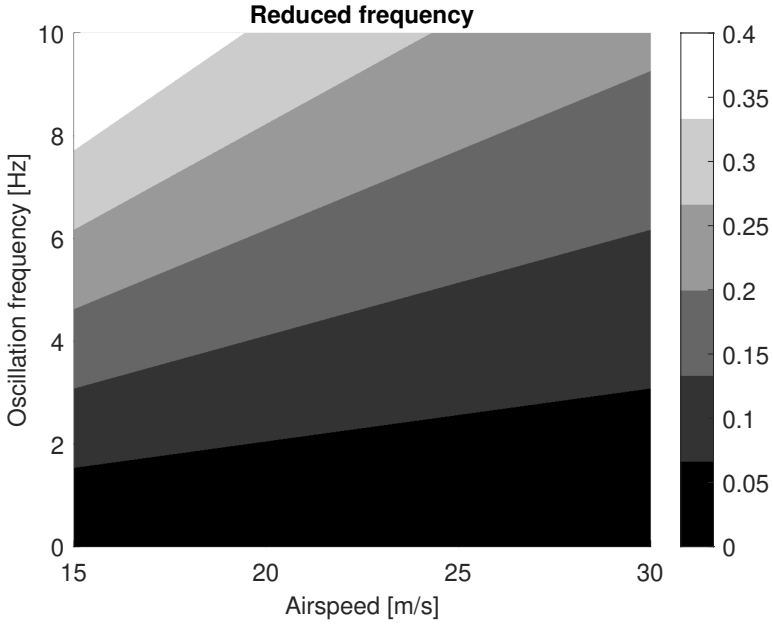

Figure 5.11: Reduced frequency for varying airspeeds and oscillation frequencies for the scaled Diana 2 glider.

Table 5.5 provides a summary of the flight test manoeuvres conducted in this study, detailing the type of excitation performed, the corresponding control surface, and the number of repetitions. As the manoeuvres were executed manually by the pilot, variations in excitation amplitudes and frequency contents were present between repetitions.

A total of 145 manoeuvres were performed, covering various excitation types. Impulse inputs consisted of short, abrupt control surface deflections followed by an immediate return to neutral, while doublet manoeuvres involved a quick deflection in one direction, immediately followed by an equal deflection in the opposite direction. Frequency sweeps were performed by applying a continuous oscillatory input to a control surface, with the input frequency gradually increasing

over time. The 3211 manoeuvres consisted of pulses with different lengths alternating between positive and negative deflections.

Additionally, angle of attack sweeps were executed by gradually increasing the aircraft's pitch attitude while maintaining airspeed, whereas sideslip sweeps were performed by adjusting the rudder to vary the sideslip angle while keeping the wings level. Phugoid oscillations were induced by a small pitch disturbance, leading to alternating climbs and descents. Some test segments also involved combined manoeuvres, where multiple control surfaces were excited simultaneously, as well as standard flight manoeuvres such as turns. For system identification, the test segments were randomly divided into fitting and validation datasets, as shown in Table 5.5. The fitting dataset was used to estimate model parameters, while the validation dataset was only used to evaluate fitting results.

Table 5.5: Overview of conducted flight test manoeuvres.

Manoeuvre	Control surface				Data partitioning	
	Aileron	Elevator	Rudder	Combined	Fitting	Validation
AoA, AoS sweep	-	4	4	-	5	3
Phugoid	-	4	-	-	3	1
Impulse	4	5	6	-	9	6
Doublet	13	15	8	-	14	22
3211	9	11	15	-	20	15
Freq. sweep	4	6	7	-	6	11
Combined	-	-	-	30	11	19
Total:	30	45	40	30	68	77

In total, the dataset includes over 18 min of excitation manoeuvres, ranging from short manoeuvres lasting 1-2 seconds to the longest spanning 62 seconds, with an average duration of 7.5 seconds. Although a larger number of test manoeuvres were performed, some had to be excluded during post-processing due to missing sensor data in certain segments. Once all excitation responses were collected, they were resampled to a uniform sampling rate of 200 Hz. To reduce high-frequency noise, a low-pass filter with a 60 Hz cutoff frequency was then applied, which is just above the highest mode frequency considered in the analysis. The dataset containing the flight test response measurements used in this study is publicly available in the 4TU.ResearchData repository [14].

5.4. State estimation and aerodynamic lag reconstruction

The identification of the flexible aircraft model was performed using the Two-Step Method [8, 9], which separates the nonlinear aerodynamic model identification into separate state estimation and parameter estimation steps. In this section, the aircraft's rigid-body and modal states are estimated from the measured flight test responses. Using these estimated states, the aerodynamic force and

moment coefficients, as well as the generalised force coefficients associated with structural modes, are computed. Additionally, force and moment coefficients related to wing root and tail loads are determined. The parameter estimation step, described in Section 5.5, involves identifying models to predict these coefficients. Finally, the aerodynamic lag states are reconstructed by first estimating the aerodynamic lag poles based on the calculated aerodynamic force and moment coefficient responses.

5.4.1. Flexible Aircraft State Estimation

The states of the flexible aircraft were estimated using the Extended Kalman Filter based flight path reconstruction approach [9]. The Kalman filter combines measured responses with predictions from an internal model to estimate system states. For a nonlinear system, the system model is represented in the following format:

$$\dot{\mathbf{X}} = f(\mathbf{X}, \mathbf{U}) + \mathbf{w} \tag{5.9}$$

$$\mathbf{Y} = h(\mathbf{X}) + \mathbf{v} \tag{5.10}$$

where, $\mathbf{X}$ is a vector for system states, $\mathbf{U}$ contains the system inputs and $\mathbf{Y}$ system outputs. The process and measurement noise are represented by $\mathbf{w}$ and $\mathbf{v}$, respectively. The evolution of the system state is represented by nonlinear function f, and output is determined by nonlinear function h.

For flight path reconstruction, the internal model represents the kinematic equations of the aircraft. The mean-axis formulation [2, 6] was used to extend these equations to account for structural dynamics, making it suitable for flexible aircraft modelling. This approach enabled the estimation of modal amplitude and velocity states by integrating additional sensor data from accelerometers, gyroscopes, and strain gauges distributed across the aircraft together with structural mode shapes obtained during the GVT. As a result, the estimates to the following states were obtained:

$$\mathbf{X} = [x\ y\ z\ u\ v\ w\ \phi\ \theta\ \psi\ p\ q\ r\ \dot{\boldsymbol{\eta}}\ \boldsymbol{\eta}\ \boldsymbol{\lambda}]^T \tag{5.11}$$

The states $x,\ y,\ z$ represent the aircraft position in the Earth fixed reference frame, $u,\ v,\ w$ are the velocity components in the Body reference frame and $\phi,\ \theta,\ \psi$ are the roll, pitch, and yaw angles, $p,\ q,\ r$ are the aircraft centre of gravity rotational rates, $\dot{\boldsymbol{\eta}},\ \boldsymbol{\eta}$ are vectors containing the modal velocities and amplitudes and $\boldsymbol{\lambda}$ is a vector containing all the unknown sensor biases.

5.4.2. Derivation of Aerodynamic Coefficients

Using the estimated aircraft states, the aerodynamic force and moment coefficients were calculated. The equations of motion for an elastic aircraft, formulated using the mean-axis approach, closely resemble conventional flight dynamics equations [2, 6].

The translational motion of the aircraft's centre of mass is described by Eqs. (5.12) to (5.14).

$$\bar{q}SC_X = mA_x = m\dot{u} + m(qw - rv) + mg\sin\theta \tag{5.12}$$
$$\bar{q}SC_Y = mA_y = m\dot{v} + m(ru - pw) - mg\cos\theta\sin\phi \tag{5.13}$$
$$\bar{q}SC_Z = mA_z = m\dot{w} + m(pv - qu) - mg\cos\theta\cos\phi \tag{5.14}$$

The force coefficients C_X, C_Y, C_Z are determined from the measured accelerations A_x, A_y, A_z using the aircraft mass m, wing area S, and dynamic pressure $\bar{q}$. By applying an axis transformation using the angle of attack α, the lift C_L and drag C_D coefficients can be derived.

$$C_L = C_X\sin\alpha - C_Z\cos\alpha \tag{5.15}$$
$$C_D = -C_X\cos\alpha - C_Z\sin\alpha \tag{5.16}$$

5

The rotation of the aircraft's mean-axis frame relative to the inertial frame is described by Eqs. (5.17) to (5.19). Similarly, the moment coefficients C_l, C_m, C_n are computed using the angular rates and angular accelerations $\dot{p}, \dot{q}, \dot{r}$, along with the aircraft's mass moment of inertia, wingspan, and mean chord [15]. The angular accelerations were obtained through smoothed numerical differentiation of the angular rates.

$$\frac{\bar{q}Sb}{I_x}C_l^{CG} = \dot{p} - \frac{I_{xz}}{I_x}\dot{r} + \frac{I_z - I_y}{I_x}qr - \frac{I_{xz}}{I_x}qp \tag{5.17}$$
$$\frac{\bar{q}S\bar{c}}{I_y}C_m^{CG} = \dot{q} - \frac{I_x - I_z}{I_y}pr + \frac{I_{xz}}{I_y}(p^2 - r^2) \tag{5.18}$$
$$\frac{\bar{q}Sb}{I_z}C_n^{CG} = \dot{r} - \frac{I_{xz}}{I_z}\dot{p} + \frac{I_y - I_x}{I_z}pq + \frac{I_{xz}}{I_z}qr \tag{5.19}$$

The moment coefficients about the aerodynamic centre reference point are determined using Eqs. (5.20) to (5.22), where $\Delta X_{CG}, \Delta Y_{CG}, \Delta Z_{CG}$ represent the distances from the aircraft's centre of gravity to the aerodynamic centre [15].

$$C_l^{AC} = C_l^{CG} - C_Z\frac{\Delta Y_{CG}}{b} + C_Y\frac{\Delta Z_{CG}}{b} \tag{5.20}$$
$$C_m^{AC} = C_m^{CG} - C_X\frac{\Delta Z_{CG}}{\bar{c}} + C_Z\frac{\Delta X_{CG}}{\bar{c}} \tag{5.21}$$
$$C_n^{AC} = C_n^{CG} - C_Y\frac{\Delta X_{CG}}{b} + C_X\frac{\Delta Y_{CG}}{b} \tag{5.22}$$

The structural deformations of the flexible aircraft are expressed as linear combinations of vibration modes, such as those presented in Sec. 5.3.2. The

dynamics of each structural vibration mode are described by Eq. (5.23), where η_i represents the modal amplitude, m_i the modal mass, ω_i the modal frequency, and ζ_i the damping ratio, while C_{Q_i} denotes the generalised force coefficient. The modal mass, frequency, and damping parameters were estimated during the GVT, while the modal accelerations $\ddot{\eta}_i$ were obtained by numerical differentiation of the modal velocities $\dot{\eta}_i$ obtained from state estimation.

$$\frac{\bar{q}S\bar{c}}{m_i}C_{Q_i} = \ddot{\eta}_i + 2\zeta_i\omega_i\dot{\eta}_i + \omega_i^2\eta_i \tag{5.23}$$

Additionally, the forces and moments acting on the wings and tail were determined from flight test measurements. These loads were computed from strain response measurements combined with calibration coefficients obtained from static load tests. The load coefficients for the right wing root bending (RWB) and left wing root bending (LWB) were then calculated by scaling the moment measurements with the dynamic pressure, wing area, and chord length.

$$C_M^{RWB} = \frac{M_{RWB}}{\bar{q}S\bar{c}} \tag{5.24}$$

Similarly, the load coefficients were also determined for the right and left wing root torsion (RWT, LWT) moments C_M^{RWT}, C_M^{LWT}, tail torsion (TT) moment C_M^{TT} and tail side (TS) and lift (TL) force C_F^{TS}, C_F^{TL} which were scaled by the dynamic pressure and wing area.

$$C_F^{TS} = \frac{F_{TS}}{\bar{q}S} \tag{5.25}$$

5.4.3. Aerodynamic Lag State Reconstruction and Pole Estimation

The aerodynamic lag states account for the delays and amplitude reductions in the aircraft's responses due to unsteady aerodynamic effects. Unlike steady aerodynamic models, where forces and moments respond instantaneously to changes, unsteady aerodynamics introduce a time-dependent response.

These lag states are driven by changes in the aircraft's attitude, control surface deflection, or structural deformations. The duration of the response delay is dependent on the airspeed and determined by the aerodynamic lag pole. To estimate these lag poles, the procedure outlined for the typical section in Sec. 5.2 was applied to all individual flight test manoeuvres. This involved using changes in the aircraft states as input signals, reconstructing the corresponding aerodynamic lag states for different pole values and cross-correlating them with the aerodynamic coefficient responses. The reconstructed lag state and the accompanying pole value that would result in a peak in the correlation above a specified threshold are then stored. In this case, a threshold of 0.4 was used which ensured that only peaks with strong correlation would be included. By

repeating this estimation process for each flight test manoeuvre, a distribution of estimated lag poles was obtained, as shown in Fig. 5.12.

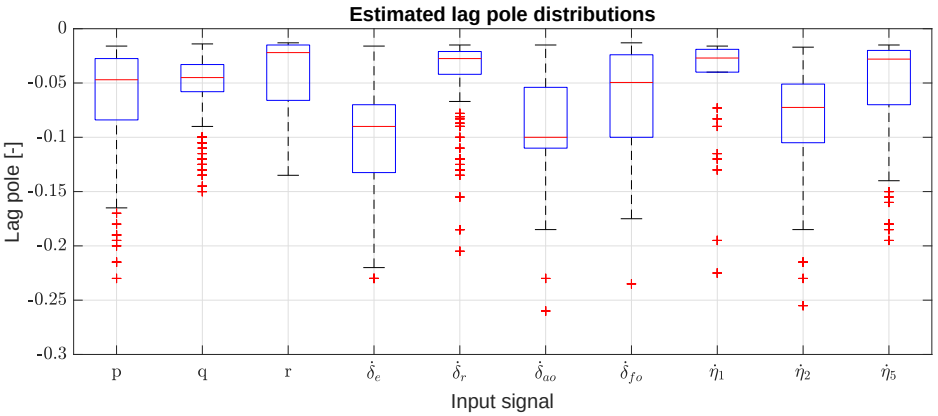

Figure 5.12: Estimated lag pole distributions for Diana 2.

In these box plots, the red lines indicate the median values of the estimated lag poles, which are also summarised in Table 5.6. The edges of the boxes represent the 25^{th} and 75^{th} percentiles. As can be seen, most of the estimated lag poles are distributed close to -0.0455, which aligns with Jones's approximation for a 2D wing. This suggests that the high aspect ratio wings of the glider closely follow 2D aerodynamic behaviour. The estimated lag pole for the elevator δ_e is -0.09. Considering that the horizontal tail's chord length is approximately half that of the main wing, this value scales to an equivalent of about -0.045, again closely matching Jones's approximation. The lag poles for the aileron δ_{ao} and flap deflections δ_{fo} are -0.1 and -0.049, respectively.

In Fig. 5.12, red $'+'$ markers denote outliers that deviate significantly from the median values. Some of these outliers may also correspond to faster poles, such as the -0.3 pole in Jones's approximation. However, detecting such a pole in the Diana 2 glider is challenging due to the minimal delay. For reference, at a flight speed of 20 m/s, lag poles of -0.0455 and -0.3 correspond to response delays of approximately 0.5 s and 0.07 s, respectively.

Table 5.6: Aerodynamic lag states and pole estimates.

Lag state	x^{p}_{lag}	x^{q}_{lag}	x^{r}_{lag}	$x^{\delta_e}_{lag}$	$x^{\delta_r}_{lag}$	$x^{\delta_{ao}}_{lag}$	$x^{\delta_{fo}}_{lag}$	$x^{\eta_1}_{lag}$	$x^{\eta_2}_{lag}$	$x^{\eta_5}_{lag}$
Input	p	q	r	$\dot{\delta}_e$	$\dot{\delta}_r$	$\dot{\delta}_{ao}$	$\dot{\delta}_{fo}$	$\dot{\eta}_1$	$\dot{\eta}_2$	$\dot{\eta}_5$
Pole (p_i)	-0.047	-0.045	-0.022	-0.090	-0.028	-0.100	-0.049	-0.027	-0.073	-0.028

With the lag state poles estimated, it was possible to reconstruct the lag states

using the input signals and the measured airspeed according to Eq. (5.6) and use these states for model identification.

5.5. IDENTIFIED FLIGHT DYNAMICS AND LOADS MODELS

After obtaining estimates for the aircraft rigid body states, structural modes and aerodynamic lag states, it was now possible to identify the flight dynamics and loads models for the scaled Diana 2 glider. In this section, the methodology used for identifying these models is outlined, the model parameters are estimated and the fitting results are evaluated.

5.5.1. PARAMETER ESTIMATION

In the previous section, the first step of the Two-Step Method was carried out which consisted of a non-linear state estimation process. As a result, it is now possible to apply linear regression techniques for the parameter estimation step [9]. This approach contrasts with the output-error parameter estimation method, which estimates model parameters through a single non-linear optimisation process, which requires an initial guess for all parameters and does not guarantee convergence to a globally optimal solution.

To model the previously derived aerodynamic force and moment coefficients, Ordinary Least Squares (OLS) regression is applied. These coefficients serve as the dependent variables in the estimation process and are assumed to have measurement errors that are zero-mean with constant covariance, as shown in Eq. (5.26).

$$\mathbf{z} = \mathbf{y} + \mathbf{v} \tag{5.26}$$

$$E[\mathbf{v}] = 0, \quad E[\mathbf{v}\mathbf{v}^T] = \sigma^2 \mathbf{I} \tag{5.27}$$

where $\mathbf{z}$ represents the measurement vector, $\mathbf{y}$ denotes the true value of the dependent variable, and $\mathbf{v}$ accounts for measurement errors.

The dependent variable is then modelled as a linear combination of independent variables, as formulated in Eq. (5.28).

$$\hat{\mathbf{y}} = \mathbf{X_{reg}}\boldsymbol{\theta} \tag{5.28}$$

where $\hat{\mathbf{y}}$ is the vector of predicted responses, $\mathbf{X_{reg}}$ is the regression matrix containing the independent variables and $\boldsymbol{\theta}$ is the parameter vector to be estimated. The optimal parameter estimate is obtained by minimising the OLS cost function, given in Eq. (5.29).

$$J = \frac{1}{2}[\mathbf{z} - \mathbf{X_{reg}}\boldsymbol{\theta}]^T[\mathbf{z} - \mathbf{X_{reg}}\boldsymbol{\theta}], \quad \hat{\boldsymbol{\theta}} = (\mathbf{X_{reg}^T}\mathbf{X_{reg}})^{-1}\mathbf{X_{reg}^T}\mathbf{z} \tag{5.29}$$

The covariance matrix of the parameter estimate $\hat{\boldsymbol{\theta}}$ is obtained using Eq. (5.30) [13].

$$Cov(\hat{\boldsymbol{\theta}}) = E[(\hat{\boldsymbol{\theta}} - \boldsymbol{\theta})(\hat{\boldsymbol{\theta}} - \boldsymbol{\theta})^T] = \sigma^2(\mathbf{X_{reg}^T}\mathbf{X_{reg}})^{-1} \tag{5.30}$$

where σ^2 can be independently estimated using Eq. (5.31) [13].

$$\hat{\sigma}^2 = \frac{\sum_{i=1}^{N}[\boldsymbol{z}(i) - \hat{\boldsymbol{y}}(i)]^2}{N - n_p} \tag{5.31}$$

where N is the number of measurements and n_p is the number of parameters in the model.

To assess the model accuracy and evaluate different model structures, multiple statistical metrics were used.

1. Coefficient of Determination (R^2) - Measures the proportion of variance in the dependent variable explained by the independent variables. Higher values indicate better model fit.

$$R^2 = 1 - \frac{\sum_{k=1}^{N}(\boldsymbol{z}(k) - \hat{\boldsymbol{y}}(k))^2}{\sum_{k=1}^{N}(\boldsymbol{z}(k) - \bar{\boldsymbol{z}}(k))^2} \tag{5.32}$$

2. Relative Root Mean Square Error (RMS_{rel}) - Represents the RMS error normalised by the variable's range, where a lower value indicates a better fit.

$$RMS_{rel} = \frac{\sqrt{\frac{1}{N}\sum_{k=1}^{N}(\boldsymbol{z}(k) - \hat{\boldsymbol{y}}(k))^2}}{|max(\boldsymbol{z}) - min(\boldsymbol{z})|} \tag{5.33}$$

3. Theil's Inequality Coefficient (TIC) - Evaluates the correlation between predicted and measured time-series data. Values closer to 0 indicate a better fit, while values near 1 signify poor agreement. A TIC value below 0.3 generally indicates a good match [15].

$$TIC = \frac{\sqrt{\frac{1}{N}\sum_{k=1}^{N}(\boldsymbol{z}(k) - \hat{\boldsymbol{y}}(k))^2}}{\sqrt{\frac{1}{N}\sum_{k=1}^{N}\boldsymbol{z}(k)^2} + \sqrt{\frac{1}{N}\sum_{k=1}^{N}\hat{\boldsymbol{y}}(k)^2}} \tag{5.34}$$

5.5.2. Model structure selection

By collecting all the estimated states, the overall regression matrix can be constructed with all the independent variables that are available for model fitting.

$$\mathbf{X_{reg}} = [1, \alpha, \alpha^2, \beta, u, v, w, \frac{pb}{2V}, \frac{q\bar{b}}{V}, \frac{rb}{2V}, \phi, \theta, \delta_{ao}, \delta_{fo}, \delta_e, \delta_r, \boldsymbol{\eta}, \frac{\dot{\boldsymbol{\eta}}\bar{b}}{V}, \boldsymbol{x_{lag}}] \tag{5.35}$$

However, not all independent variables should be included in the aerodynamic coefficient models, as some may not be relevant. Therefore, selecting an optimal model structure is necessary.

In this study, a relatively brute-force approach was employed due to the low computational cost of OLS regression. Each aerodynamic coefficient was first fitted using a single independent variable, and those that improved the model fit

were used as potential candidates. The final model structure was determined by systematically evaluating all possible regressor combinations for varying model sizes and selecting the best-performing structure based on predictions on the validation dataset while the fitting was performed using the training dataset. This approach allowed to automatically evaluate a large set of potential model structures and choose the best-performing one in a short amount of time. Alternatively, methods like stepwise regression could also be used to determine the model structure [16].

An example of the results of this procedure is shown in Table 5.7, where the optimal model structure for the C_Y coefficient is presented for varying numbers of included parameters, N. The final models were selected at a point where adding more parameters provided little or no improvements. This also allowed to evaluate the increase in model fit accuracy by the inclusion of additional parameters. Model structure evaluation results for all coefficients are detailed in Appendix 5.A.1.

Table 5.7: C_Y coefficient model structure evaluation for varying model sizes.

	C_Y - flex model		C_Y - rigid model	
N	Parameters	R^2[%]	Parameters	R^2[%]
1	η_2,	71.6	β,	66.2
2	β, η_2,	87.6	β, δ_r,	78.8
3	β, η_2, η_5,	89.6	$\beta, \delta_r, \delta_{ao}$,	81.5
4	$\beta, x^r_{lag}, \eta_2, \eta_5$,	91.3	$\boldsymbol{\beta, q, r, \delta_r, \delta_{ao}}$,	84.3
5	$\boldsymbol{\beta, x^r_{lag}, x^{\delta_r}_{lag}, \eta_2, \eta_5}$,	91.9	$\beta, q, r, \delta_r, \delta_{ao}$,	84.3
6	$\beta, x^q_{lag}, x^r_{lag}, x^{\delta_r}_{lag}, \eta_2, \eta_5$,	92.3	$\alpha^2, \beta, q, r, \delta_r, \delta_{ao}$,	84.6

Two different models were identified for the scaled Diana 2 glider. A ”rigid” aircraft model, which includes only regressors related to rigid-body responses and control surface deflections, and a ”flexible” model that also includes the structural states and aerodynamic lags. This allowed to evaluate the improvements in model accuracy resulting from the inclusion of structural and aerodynamic lag states.

AERODYNAMIC FORCE AND MOMENT COEFFICIENTS

The model structures that were selected for the aerodynamic force and moment coefficients for the rigid and flexible model are as follows:

$$C_D^{rigid} = C_{D_0} + C_{D_\alpha}\alpha + C_{D_{\alpha^2}}\alpha^2 \tag{5.36}$$

$$C_D^{flex} = C_{D_0} + C_{D_\alpha}\alpha + C_{D_{\alpha^2}}\alpha^2 \tag{5.37}$$

$$C_Y^{rigid} = C_{Y_0} + C_{Y_\beta}\beta + +C_{Y_q}\frac{q\bar{b}}{V} + C_{Y_r}\frac{rb}{2V} + C_{Y_{\delta_r}}\delta_r + C_{Y_{\delta_{ao}}}\delta_{ao} \tag{5.38}$$

$$C_Y^{flex} = C_{Y_0} + C_{Y_\beta}\beta + C_{Y_{x^r_{lag}}}x^r_{lag} + C_{Y_{x^{\delta_r}_{lag}}}x^{\delta_r}_{lag} + C_{Y_{\eta_2}}\eta_2 + C_{Y_{\eta_5}}\eta_5 \tag{5.39}$$

$$C_L^{rigid} = C_{L_0} + C_{L_\alpha}\alpha + C_{L_\beta}\beta + C_{L_q}\frac{q\bar{b}}{V} + C_{L_{\delta_e}}\delta_e + C_{L_{\delta_{fo}}}\delta_{fo} \tag{5.40}$$

$$C_L^{flex} = C_{L_0} + C_{L_\alpha}\alpha + C_{L_{\delta_e}}\delta_e + C_{L_{x^{\delta_e}_{lag}}}x^{\delta_e}_{lag} + C_{L_{\eta_1}}\eta_1 + C_{L_{\eta_5}}\eta_5 \tag{5.41}$$

$$C_l^{rigid} = C_{l_0} + C_{l_\beta}\beta + C_{l_p}\frac{pb}{2V} + C_{l_q}\frac{q\bar{b}}{V} + C_{l_r}\frac{rb}{2V} + C_{l_{\delta_r}}\delta_r + C_{l_{\delta_{ao}}}\delta_{ao} \tag{5.42}$$

$$C_l^{flex} = C_{l_0} + C_{l_r}\frac{rb}{2V} + C_{l_{x^p_{lag}}}x^p_{lag} + C_{l_{\delta_{ao}}}\delta_{ao} + C_{l_{x^{\delta_{ao}}_{lag}}}x^{\delta_{ao}}_{lag} \tag{5.43}$$

$$C_m^{rigid} = C_{m_0} + C_{m_\alpha}\alpha + C_{m_\beta}\beta + C_{m_q}\frac{q\bar{b}}{V} + C_{m_{\delta_e}}\delta_e \tag{5.44}$$

$$C_m^{flex} = C_{m_0} + C_{m_\alpha}\alpha + C_{m_{x^q_{lag}}}x^q_{lag} + C_{m_{\delta_e}}\delta_e + C_{m_{x^{\delta_e}_{lag}}}x^{\delta_e}_{lag} \tag{5.45}$$

$$C_n^{rigid} = C_{n_0} + C_{n_\beta}\beta + C_{n_p}\frac{pb}{2V} + C_{n_r}\frac{rb}{2V} + C_{n_{\delta_r}}\delta_r + C_{n_{\delta_{ao}}}\delta_{ao} \tag{5.46}$$

$$C_n^{flex} = C_{n_0} + C_{n_\beta}\beta + C_{n_p}\frac{pb}{2V} + C_{n_{\delta_r}}\delta_r + C_{n_{x^r_{lag}}}x^r_{lag} + \\ + C_{n_{x^{\delta_r}_{lag}}}x^{\delta_r}_{lag} + C_{n_{\eta_2}}\eta_2 \tag{5.47}$$

Table 5.8 presents the corresponding fitting results for the aircraft aerodynamic force and moment coefficients. The individual values estimated for each parameter are presented in Appendix 5.A.2 in Table 5.20 for the flexible model and in Table 5.21 for the rigid model. In addition, also the relative standard deviations for each parameter are presented, where the standard deviations are divided by the parameter values.

The results show that including structural modes and aerodynamic lag states in the flexible aircraft model improved the fitting results. The only exception was

the drag coefficient C_D, where additional parameters did not lead to significant improvements and the same model structure for both rigid and flexible models was used. The most significant improvement was seen for the aircraft rolling moment coefficient C_l. With the rigid model, only a 53.4% R^2 fit was achieved, while the flexible model achieved close to 82.0% R^2 fit while using fewer parameters in the model. The majority of the nearly 29% improvement in the accuracy was due to aerodynamic lag state related to the aileron input, which emphasised the importance of including aerodynamic lag states in the model. Increases of $6-10\%$ in the R^2 fitting were also obtained for the side force C_Y, pitching moment C_m, and yaw moment C_n coefficients, while lift C_L coefficient improved less than 2%. Overall, the rigid model achieved an average R^2 fit of 76.98% while the flexible model achieved 86.09%.

In many cases, there were large similarities or overlaps between the rigid and flexible model parameters as would be expected. For example, the dynamic roll, pitch and yaw damping terms in the rigid model ($C_{l_p}, C_{m_q}, C_{n_r}$), were replaced by their aerodynamic lag counterparts in the flexible model ($C_{l_{x_{lag}}^p}, C_{m_{x_{lag}}^q}, C_{n_{x_{lag}}^r}$).

As the aerodynamic lag terms related to control surfaces are driven by changes in control surface deflections and not by the deflection angle, they were added to the model together with the deflection angle terms even if the optimal model structure did not include it. Otherwise, the control surfaces could be deflected at a constant offset and over time, the lag state would go to zero, and there would not be any force or moment contribution from the deflected surface in the model.

In addition to the aerodynamic lag states, also the first, second, and fifth structural modes (η_1, η_2, η_5) were included in the flexible model. The first symmetric wing bending and inplane bending modes had an influence on the lift coefficient, while tail rotation mode contributed to the side force and yaw moment coefficients.

Table 5.8: Flight dynamics coefficient fitting results.

Coefficient	Model	$R^2[\%]$	$TIC[-]$	$RMS_{rel}[\%]$
C_D	Rigid	84.71	0.139	2.09
	Flexible	84.71	0.139	2.09
C_Y	Rigid	84.33	0.180	2.33
	Flexible	91.90	0.126	1.68
C_L	Rigid	89.73	0.071	2.69
	Flexible	91.34	0.065	2.47
C_l	Rigid	53.38	0.431	3.34
	Flexible	81.95	0.225	2.08
C_m	Rigid	79.31	0.157	2.56
	Flexible	85.91	0.127	2.11
C_n	Rigid	70.45	0.304	3.73
	Flexible	80.72	0.232	3.01

To illustrate the differences between the rigid and flexible models, fitting results

are presented for three validation manoeuvres in which all control surfaces were simultaneously excited. This allows to observe the responses and fitting performance across all axes at once. Figure 5.13 shows the control surface inputs alongside the measured aerodynamic force and moment responses, compared with predictions from both the rigid and flexible models.

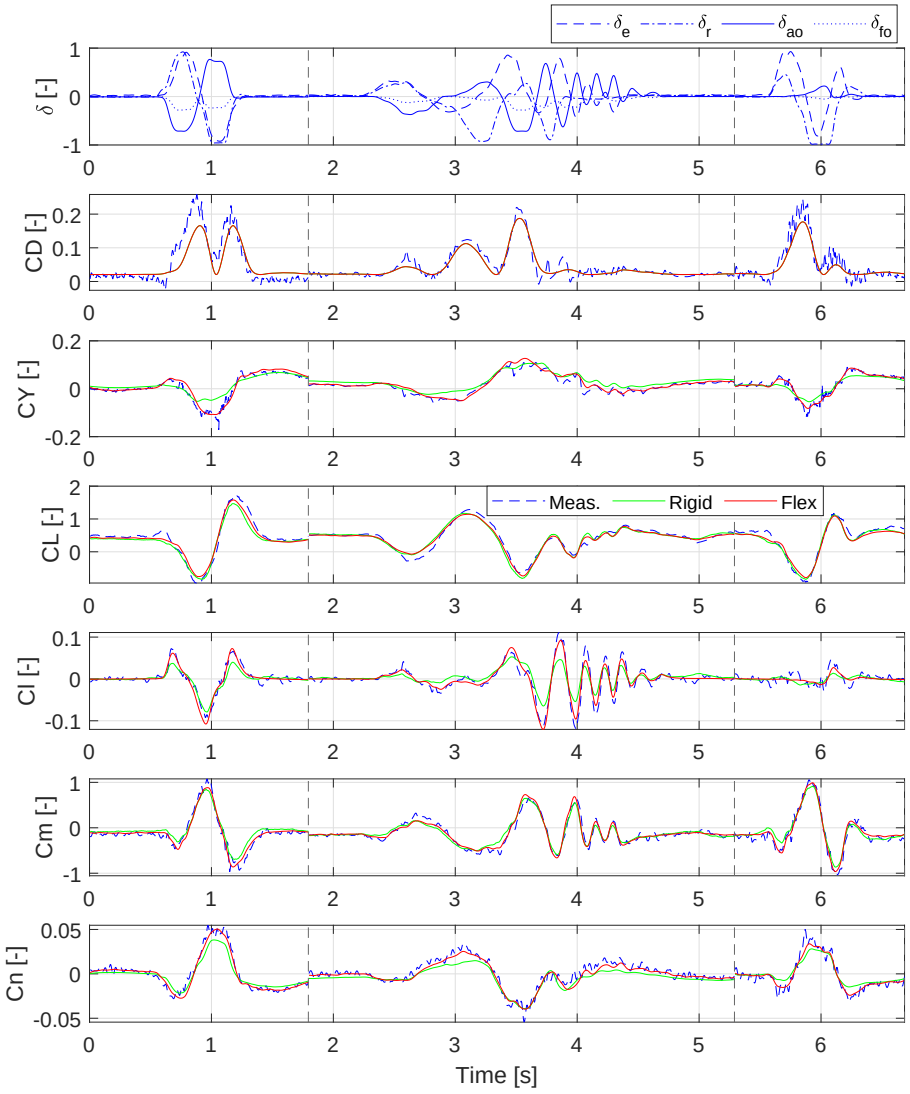

Figure 5.13: Aerodynamic force and moment coefficient fitting comparison.

Both the rigid and flexible models accurately capture the dynamic responses of the scaled Diana 2 glider, with the flexible model providing more precise predictions. The differences in fitting accuracy for the rolling coefficient can be seen, where the rigid model underestimates the response amplitudes.

GENERALISED FORCE COEFFICIENTS

Modes η_1, η_2, and η_5 were included to model the aerodynamic force and moment coefficients of the Diana 2 glider. To be able to simulate the dynamic responses of these modes correctly, it is also necessary to model their generalised force coefficients. However, when identifying these generalised forces, it was found that additional factors need to be considered when including modal states in the model. The coefficients were determined according to Eq. (5.48) as described before.

$$\frac{\bar{q}S\bar{c}}{m_i}C_{Q_i} = \ddot{\eta}_i + 2\zeta_i\omega_i\dot{\eta}_i + \omega_i^2\eta_i \tag{5.48}$$

This makes the modal amplitude and velocity signals strongly correlated with the force coefficient due to the structural stiffness and damping terms. Therefore, when considering aerodynamic stiffness $C_{Q_{\eta_i}}$ and damping $C_{Q_{\dot{\eta}_i}}$ terms for the generalised force coefficient fitting, as shown in Eq. (5.49), a good model fit can be obtained, but it might not correctly predict the simulation responses and even lead to an unstable model.

$$C_{Q_i} = C_{Q_{\eta_i}}\eta_i + C_{Q_{\dot{\eta}_i}}\frac{\dot{\eta}_i\bar{b}}{V} \tag{5.49}$$

To ensure that the identified structural model is not self-exciting, constraints must be added to the fitting procedure. When combining Eq. (5.48) and (5.49), a state-space model can be obtained as shown in Eq. (5.50).

$$\begin{bmatrix}\ddot{\eta}_i \\ \dot{\eta}_i\end{bmatrix} = \begin{bmatrix}-2\omega_i\zeta_i + \frac{\bar{q}S\bar{c}}{m_i}\frac{\bar{b}}{V}C_{Q_{\dot{\eta}_i}} & -\omega_i^2 + \frac{\bar{q}S\bar{c}}{m_i}C_{Q_{\eta_i}} \\ 1 & 0\end{bmatrix}\begin{bmatrix}\dot{\eta}_i \\ \eta_i\end{bmatrix} \tag{5.50}$$

From the state-space model, the constraints for $C_{Q_{\eta_i}}$ and $C_{Q_{\dot{\eta}_i}}$ coefficients can be determined to ensure that the system dynamics are stable.

$$C_{Q_{\eta_i}} < \omega_i^2\frac{m_i}{\bar{q}S\bar{c}},\ C_{Q_{\dot{\eta}_i}} < 2\omega_i\zeta_i\frac{m_i}{\bar{q}S\bar{c}}\frac{V}{\bar{b}} \tag{5.51}$$

After incorporating these constraints using Matlab's *lsqlin* solver, the same procedure was followed to determine the optimal model structure for fitting the generalised force coefficients corresponding to modes η_1, η_2, and η_5. The following models were obtained:

$$C_{Q1} = C_{Q1_0} + C_{Q1_\alpha}\alpha + C_{Q1_u}u + C_{Q1_\phi}\phi + C_{Q1_{\delta_{fo}}}\delta_{fo} + C_{Q1_{\eta_1}}\eta_1 + \\ + C_{Q1_{\dot{\eta}_1}}\frac{\dot{\eta}_1\bar{b}}{V} \tag{5.52}$$

$$C_{Q2} = C_{Q2_0} + C_{Q2_v}v + C_{Q2_{\delta_r}}\delta_r + C_{Q2_{\delta_{ao}}}\delta_{ao} + C_{Q2_{x^r_{lag}}}x^r_{lag} + \\ + C_{Q2_{x^{\delta_r}_{lag}}}x^{\delta_r}_{lag} + C_{Q2_{\eta_2}}\eta_2 + C_{Q2_{\dot{\eta}_2}}\frac{\dot{\eta}_2\bar{b}}{V} \tag{5.53}$$

$$C_{Q5} = C_{Q5_0} + C_{Q5_\alpha}\alpha + C_{Q5_\phi}\phi + C_{Q5_{\delta_e}}\delta_e + C_{Q5_{\eta_5}}\eta_5 + C_{Q5_{\dot{\eta}_5}}\frac{\dot{\eta}_5\bar{b}}{V} \tag{5.54}$$

All generalised force models included modal amplitude and velocity terms to ensure model stability. Additionally, the aircraft roll angle ϕ appeared as a significant factor in all models, which is likely due to the direction of gravity loading on the aircraft structure. Table 5.9 presents the fitting results for the generalised force coefficients. The estimated parameter values are presented in Table 5.22 in Appendix 5.A.2.

Table 5.9: Generalised force coefficient fitting results.

Coefficient	Model	$R^2[\%]$	$TIC[-]$	$RMS_{rel}[\%]$
C_{Q1}	Flexible	85.75	0.065	3.23
C_{Q2}	Flexible	84.98	0.204	3.37
C_{Q5}	Flexible	79.73	0.166	4.89

As can be seen, around 85.0% R^2 fit was obtained for the first and second mode, while for the fifth mode a 79.7% fit was obtained. Higher-order structural modes exhibit lower response amplitudes at increased frequencies and are, therefore, more difficult to capture and excite. However, based on the TIC metric, the generalised force model for the fifth mode is able to capture the response dynamics well, and the lower performance in terms of R^2 and RMS_{rel} metrics seems to be mainly due to offsets in the predictions. This can be observed in Fig. 5.14, where the generalised force coefficient fitting is presented for the same three manoeuvres as for aerodynamic force and moment coefficients.

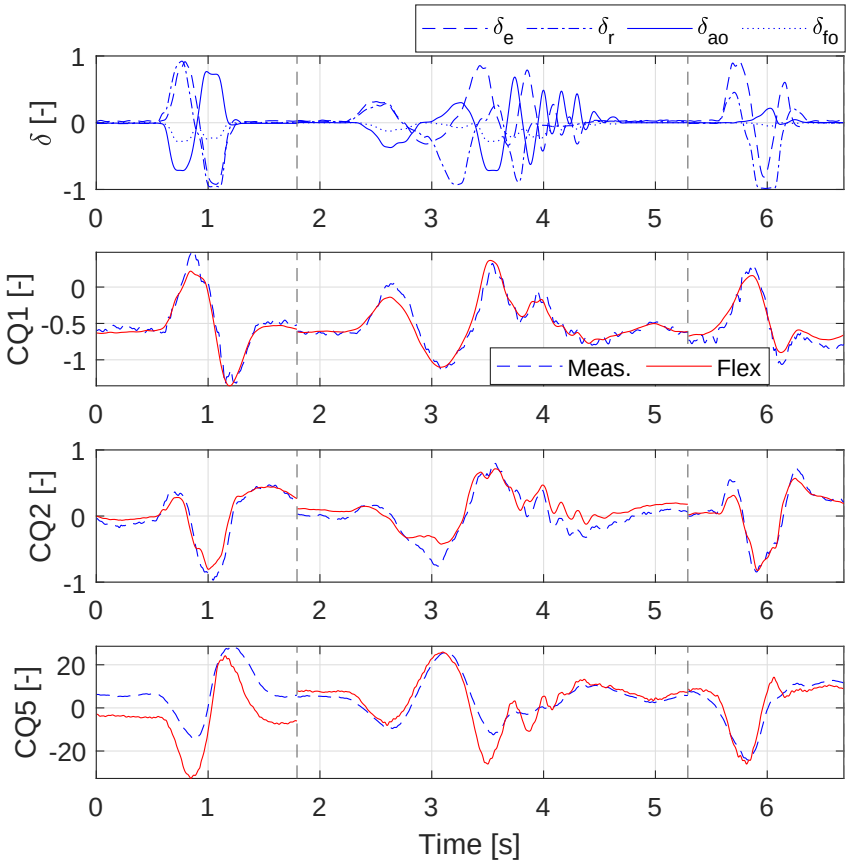

Figure 5.14: Generalised force coefficient fitting for flight manoeuvres.

WING AND TAIL LOAD COEFFICIENTS

Finally, the force and moment coefficients experienced by the wings and tail were modelled. These included the root bending C_M^{WB} and torsion moments C_M^{WT} for the right and left wing. For the tail, the lift force C_F^{TL}, side force C_F^{TS} and torsion moment C_M^{TT} were modelled. Again a similar approach as before was followed when determining an optimal model structure. Only for wing bending and torsion, both wings were constrained to have the same structure. Similar to the aerodynamic force and moment models, both a rigid and a flexible model were identified. The following model structures were determined:

$$C_M^{WB_{rigid}} = C_{M_0}^{WB} + C_{M_\alpha}^{WB}\alpha + C_{M_u}^{WB}u + C_{M_w}^{WB}w + C_{M_q}^{WB}\frac{q\bar{b}}{V} + C_{M_{\delta e}}^{WB}\delta_e + C_{M_{\delta_{fo}}}^{WB}\delta_{fo} \tag{5.55}$$

$$C_M^{WB_{flex}} = C_{M_0}^{WB} + C_{M_\alpha}^{WB}\alpha + C_{M_u}^{WB}u + C_{M_w}^{WB}w + C_{M_{x_{lag}}^{q}}^{WB}x_{lag}^{q} + C_{M_{\eta_1}}^{WB}\eta_1 + C_{M_{\eta_5}}^{WB}\eta_5 \tag{5.56}$$

$$C_M^{WT_{rigid}} = C_{M_0}^{WT} + C_{M_\alpha}^{WT}\alpha + C_{M_u}^{WT}u + C_{M_p}^{WT}\frac{pb}{2V} + C_{M_{\delta ao}}^{WT}\delta_{ao} + C_{M_{\delta_{fo}}}^{WT}\delta_{fo} \tag{5.57}$$

$$C_M^{WT_{flex}} = C_{M_0}^{WT} + C_{M_\alpha}^{WT}\alpha + C_{M_u}^{WT}u + C_{M_{\delta ao}}^{WT}\delta_{ao} + C_{M_{\delta_{fo}}}^{WT}\delta_{fo} + C_{M_{x_{lag}}^{\delta ao}}^{WT}x_{lag}^{\delta_{ao}} \tag{5.58}$$

$$C_F^{TL_{rigid}} = C_{F_0}^{TL} + C_{F_\alpha}^{TL}\alpha + C_{F_u}^{TL}u + C_{F_{\delta e}}^{TL}\delta_e + C_{F_{\delta_{fo}}}^{TL}\delta_{fo} \tag{5.59}$$

$$C_F^{TL_{flex}} = C_{F_0}^{TL} + C_{F_\alpha}^{TL}\alpha + C_{F_u}^{TL}u + C_{F_{\delta e}}^{TL}\delta_e + C_{TL_{x_{lag}^{\delta e}}}x_{lag}^{\delta_e} + C_{F_{\eta_1}}^{TL}\eta_1 \tag{5.60}$$

$$C_F^{TS_{flex}} = C_{F_0}^{TS} + C_{F_\beta}^{TS}\beta + C_{M_r}^{TS}\frac{rb}{2V} + C_{F_{\delta_r}}^{TS}\delta_r + C_{F_{\delta ao}}^{TS}\delta_{ao} \tag{5.61}$$

$$C_F^{TS_{flex}} = C_{F_0}^{TS} + C_{F_\beta}^{TS}\beta + C_{F_v}^{TS}v + C_{F_{\delta_r}}^{TS}\delta_r + C_{F_{\delta ao}}^{TS}\delta_{ao} + C_{F_{\eta_2}}^{TS}\eta_2 \tag{5.62}$$

$$C_M^{TT_{rigid}} = C_{M_0}^{TT} + C_{TT_\alpha}\alpha + C_{M_\beta}^{TT}\beta + C_{M_{\delta_r}}^{TT}\delta_r + C_{M_{\delta ao}}^{TT}\delta_{ao} \tag{5.63}$$

$$C_M^{TT_{flex}} = C_{M_0}^{TT} + C_{TT_\alpha}\alpha + C_{M_\beta}^{TT}\beta + C_{M_v}^{TT}v + C_{M_{\eta_2}}^{TT}\eta_2 \tag{5.64}$$

Again, large similarities and overlaps between the rigid and flexible models can be seen as expected. As can be seen, structural modes had an influence on all flexible load models except wing torsion while aerodynamic lag states were included for both wing bending and torsion models as well as tail lift force. Table 5.10 presents the fitting results for the load models while the estimated parameter values are presented in Table 5.23 and 5.24.

Table 5.10: Load model fitting results.

Coefficient	Model	$R^2[\%]$	$TIC[-]$	$RMS_{rel}[\%]$
Right wing root bending [RWB]	Rigid	82.25	0.094	3.39
	Flexible	93.02	0.058	2.12
Left wing root bending [LWB]	Rigid	84.86	0.093	3.11
	Flexible	93.27	0.060	2.07
Right wing root torsion [RWT]	Rigid	79.11	0.215	4.02
	Flexible	86.33	0.172	3.25
Left wing root torsions [LWT]	Rigid	75.99	0.252	4.58
	Flexible	81.25	0.222	4.05
Tail lift force [TL]	Rigid	79.39	0.071	3.35
	Flexible	81.24	0.067	3.20
Tail side force [TS]	Rigid	73.12	0.289	3.58
	Flexible	88.38	0.172	2.35
Tail torsion [TT]	Rigid	73.55	0.255	4.14
	Flexible	91.86	0.129	2.30

Results show that the addition of structural modes and aerodynamic lag states to the wing and tail load models leads to improvements in the fitting accuracy. An R^2 fit above 80% was achieved for all flexible models with wing bending and torsion even reaching above 90% together with the tail torsion model. Over 15% increase in the tail side force and torsion responses were obtained when compared to the rigid model by the inclusion of the tail roll mode η_2 in the model. Overall, the rigid model achieved an average R^2 fit of 78.32% while the flexible model achieved 87.91%. In Fig. 5.15 and 5.16, the wing load and tail load response predictions are presented for the three manoeuvres as before.

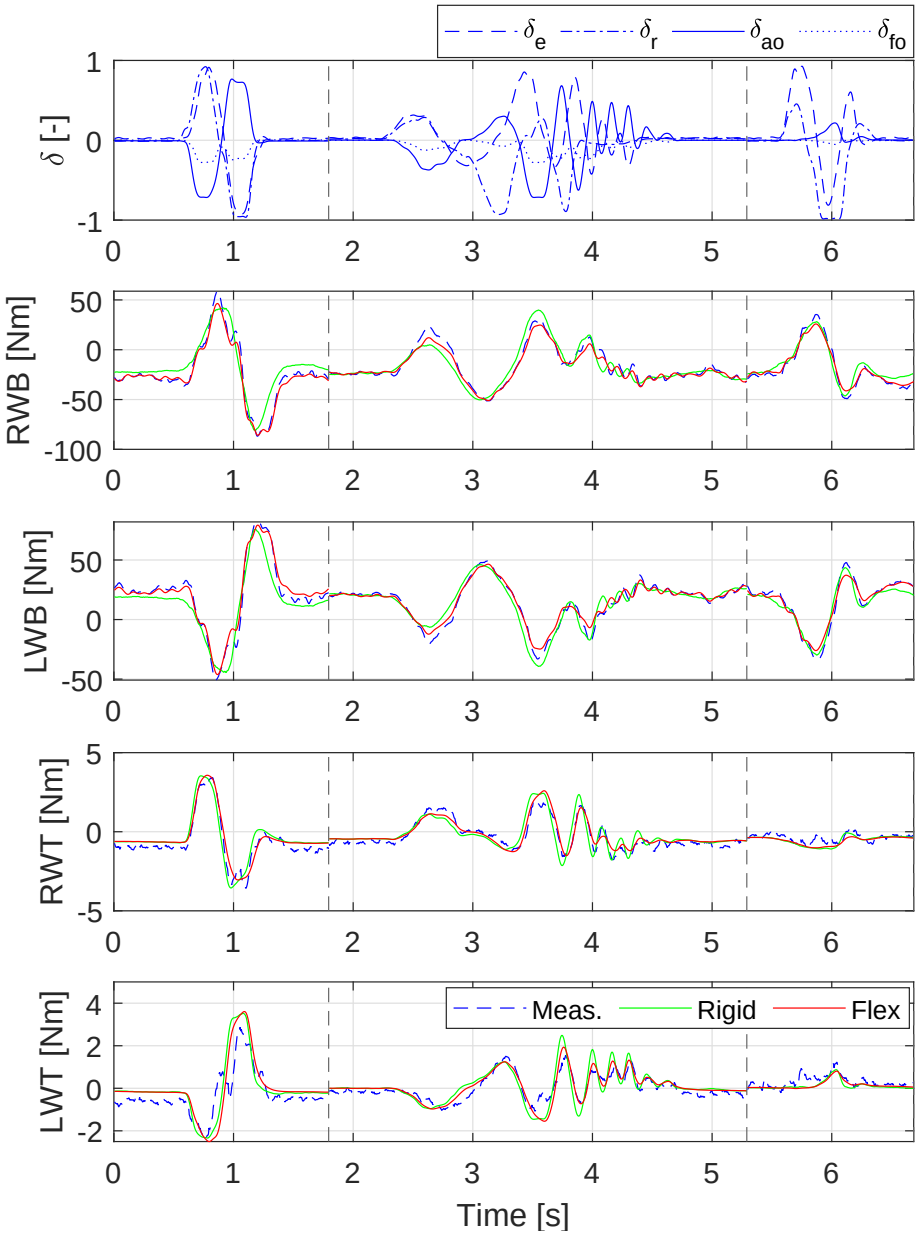

Figure 5.15: Wing load fitting comparison.

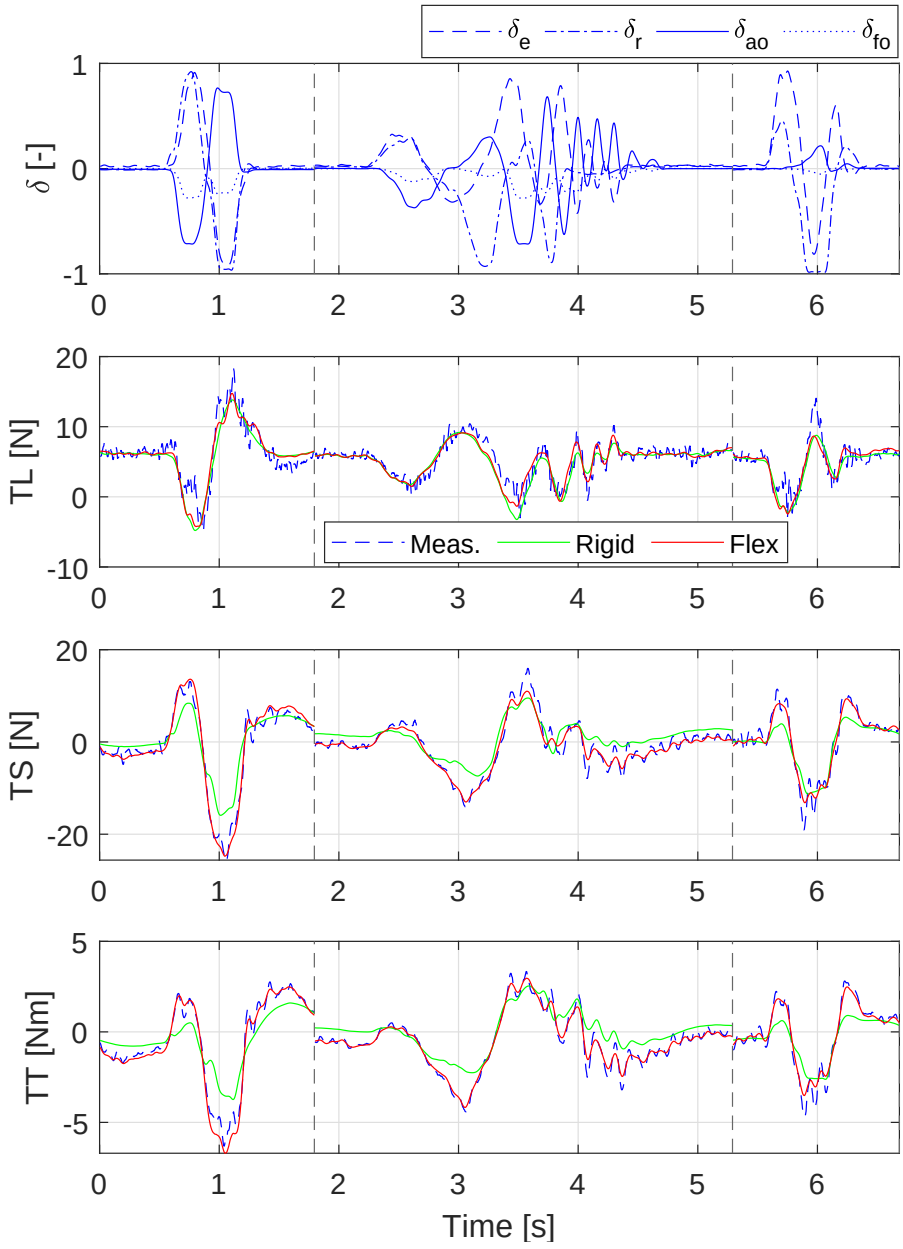

Figure 5.16: Tail load fitting comparison.

The identified models together with fitting and validation set evaluations can

again be found in the published dataset [14].

5.6. Model validation simulation

Identifying flight dynamics and loads models for flexible aircraft is relevant to be able to analyse the aircraft behaviour and optimise resulting structural loads during aircraft operations, which allows to increase the aircraft's lifespan and monitor its health. Furthermore, having such models is also necessary to develop and evaluate control systems for aircraft load alleviation. In these cases, the identified models should not only fit the measured data well but also be able to accurately simulate the responses. For this purpose, the models were initialised at a measured initial condition and the responses were simulated in open-loop by applying the measured control surface deflections. The simulated responses from the rigid and flexible models were then compared with flight test measurements. As an additional comparison, also simulated responses of an aeroelastic reference model were included. This model was built using ZAERO software based on potential flow aerodynamics and a NASTRAN structural model. More details about the reference model are presented in Appendix 5.A.3.

Performing open-loop simulation error analysis can be challenging as even small errors are integrated, which causes the responses to diverge over time. Particularly because disturbances such as atmospheric turbulence are not included in the simulation responses, but they were present during flight testing. This effect was most prevalent in the simulated sideslip angle and yaw rate responses as the flight tests were conducted in windy conditions that were mainly in the aircraft's body plane. Still, such simulations can provide insight into the model simulation performance. To balance the simulation model and prevent divergence in the aircraft attitude, constant trim offsets were applied to the control surface inputs, along with initial pitch and roll angle offsets. These offsets were determined through an optimisation routine that minimised the differences between measured and simulated responses and were constrained to within 10% of the control surface range or 6 deg for the attitude angles.

In Fig. 5.17 to 5.19, the most dominant responses are presented for the doublet, 3211, and sweep excitations performed with the elevator, ailerons, and rudder, respectively. In each figure, the control surface input is presented together with the aerodynamic angle, rotational rate and load responses. For the flexible aircraft model and reference ZAERO model, the modal amplitude response is also presented. This way all the identified model components are represented. A more detailed overview with all response signals for these manoeuvres can be found in Appendix 5.A.4. All presented manoeuvres were selected from the validation set.

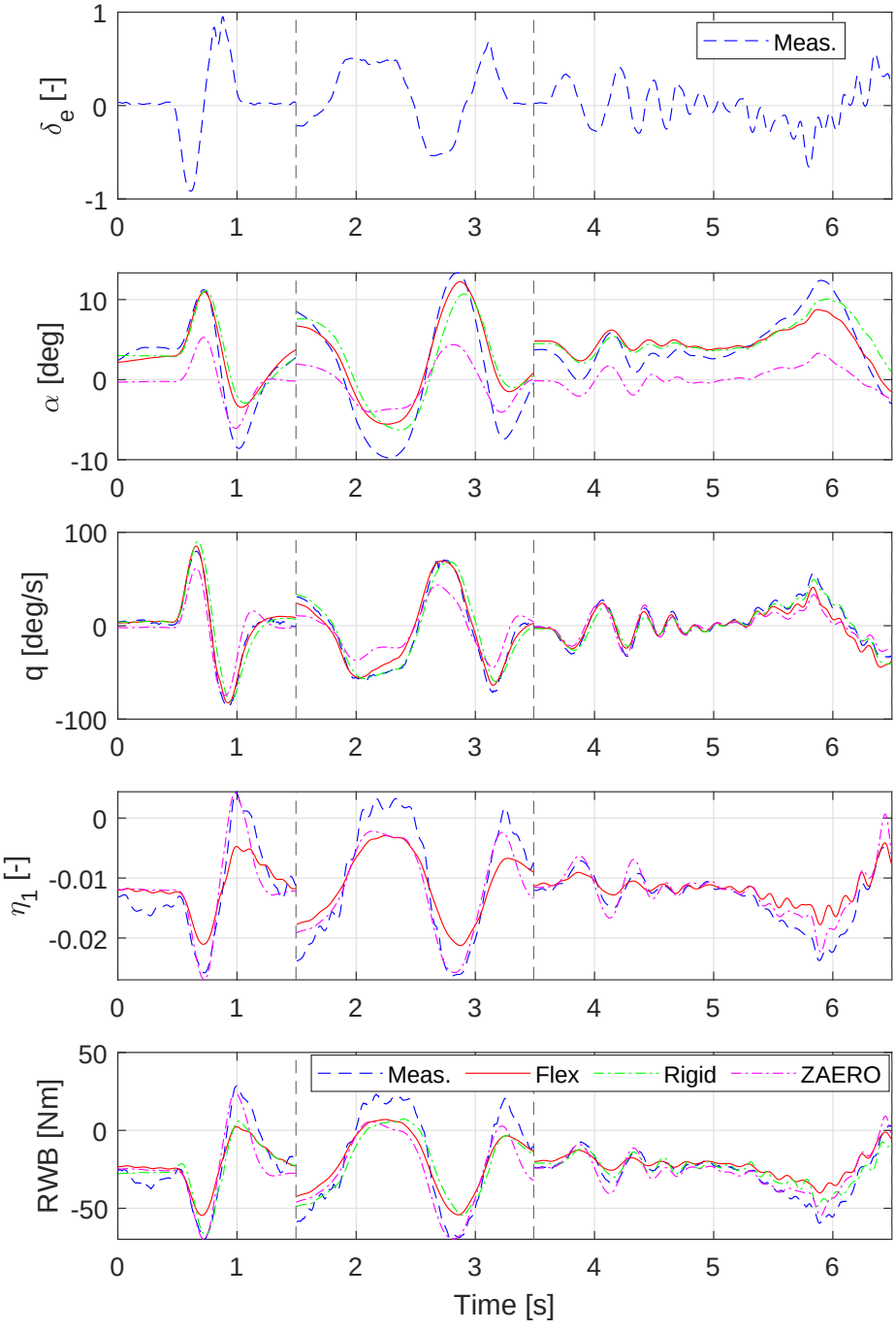

Figure 5.17: Elevator excitation response simulations.

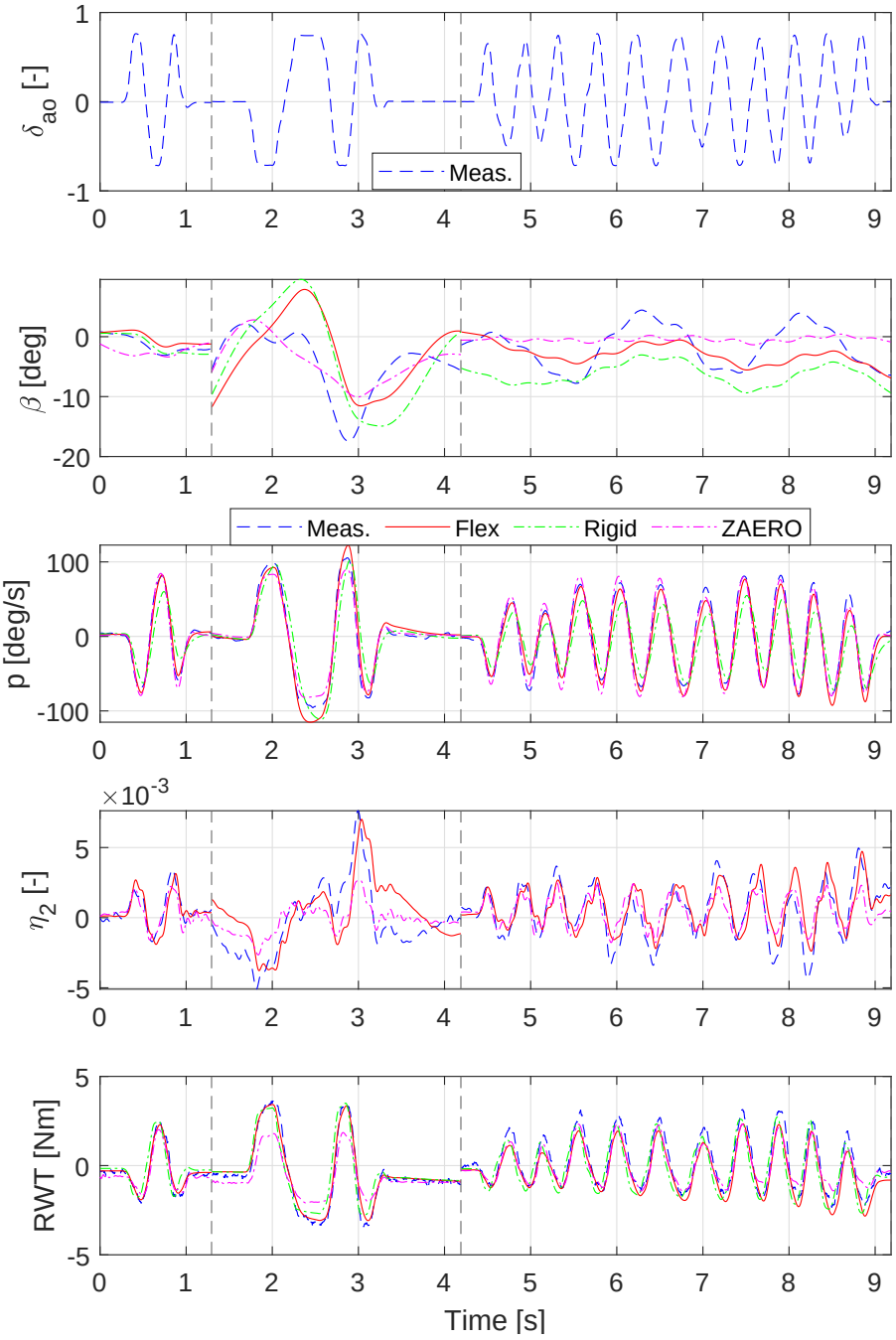

Figure 5.18: Aileron excitation response simulations.

From Fig. 5.17, it can be seen that all models capture the pitch rate responses well during elevator excitations. The models are also able to track the angle of attack responses, but tend to underestimate the peak values. As a result, the flexible model also underestimates the peak amplitudes of the first mode, which leads to similar discrepancies in the predicted wing bending loads. This highlights the importance of accurately modelling both the rigid body dynamics and structural dynamics to reliably simulate the responses of a flexible aircraft. The simulated responses of the reference ZAERO model also show lower amplitudes for the angle of attack responses, which then causes differences in the pitch rate responses. However, the first mode amplitude and wing bending load responses can closely capture the measured behaviour.

During aileron and rudder excitations, all models struggle to accurately match the measured sideslip angle, likely due to wind effects during flight testing. This is supported by the good agreement in sideslip angle predictions among the rigid, flexible, and ZAERO models seen for the rudder excitations, none of which include wind effects. This way, the ZAERO model could also serve as an indicator of possible external disturbances not included in the simulated responses.

The roll rate responses resulting from aileron excitations are well captured by both the flexible model and the ZAERO model. Divergences in the flexible model's roll rate predictions appear primarily in regions where larger differences in sideslip angle occur. In contrast, the rigid model tends to underestimate the roll rate responses, particularly during the sweep manoeuvre, and exhibits a phase shift compared to the measurements.

Although the yaw rate responses during rudder excitations were able to track the measured responses, some deviations were present. As noted earlier, these discrepancies likely resulted from sideslip variations induced by wind disturbances during flight testing.

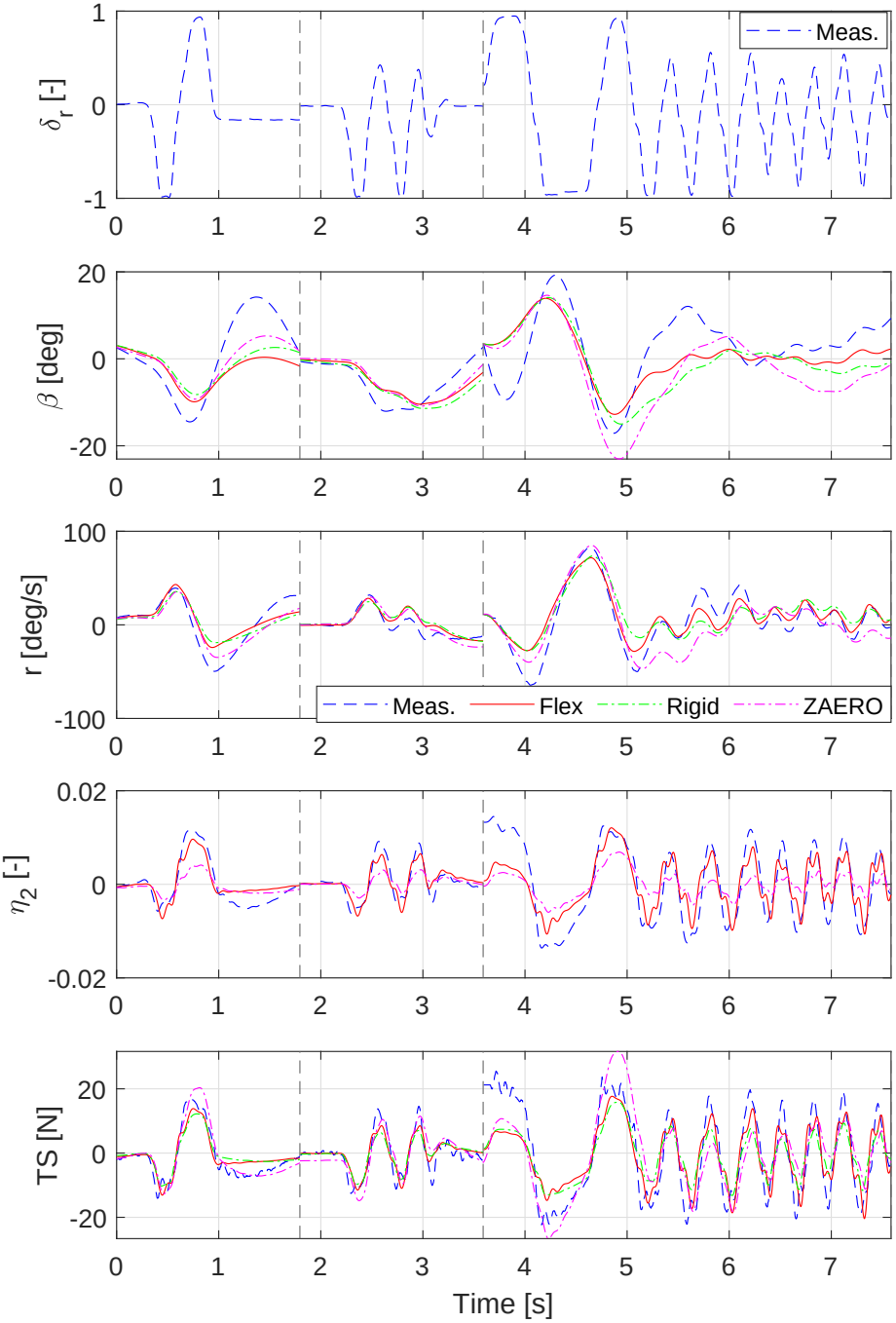

Figure 5.19: Rudder excitation response simulations.

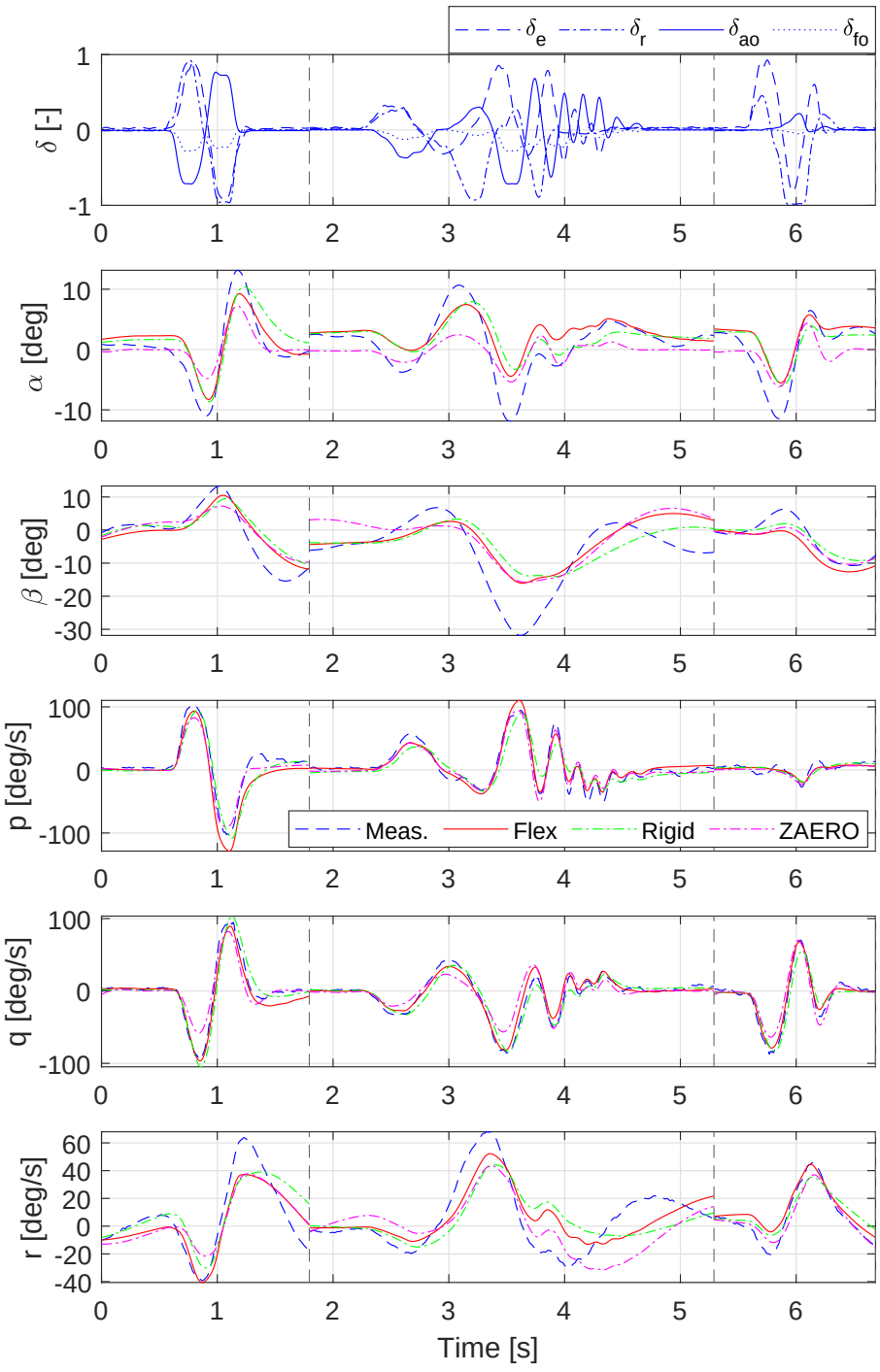

Figure 5.20: Multiple control surface excitation simulations - rigid body responses.

For both the aileron and rudder excitations, the flexible model was able to accurately simulate the second mode amplitude responses, as well as wing torsion and tail side force loads. The strong agreement in modal amplitude responses between the numerical ZAERO model and flight test measurements further validates that the identification procedure is capable of accurately measuring and modelling modal states from flight data.

In Fig. 5.20 to 5.22, simulated responses are shown for three manoeuvres in which all control surfaces were excited simultaneously - these same manoeuvres were previously used to illustrate fitting accuracy. This allows to evaluate the identified models under conditions where responses are not confined to a single axis and potential cross-coupling effects may be present. First, the rigid-body responses are presented, followed by the modal responses, and finally the load responses.

Overall, all models were able to replicate the aircraft's rotational rate responses, even during manoeuvres involving multiple control surface excitations. Again, the identified models and ZAERO model show similar differences in angle of attack and sideslip responses from measured responses, suggesting that external wind disturbances were influencing the responses during flight testing. By underestimating the peak responses in angle of attack, the pitch rate responses for the ZAERO model are also underestimated. For the sideslip angle and yaw rate, the first and third manoeuvre responses closely match the measurements across all models. However, the second manoeuvre shows the largest deviations in sideslip angle, which in turn causes greater divergence in the yaw rate predictions.

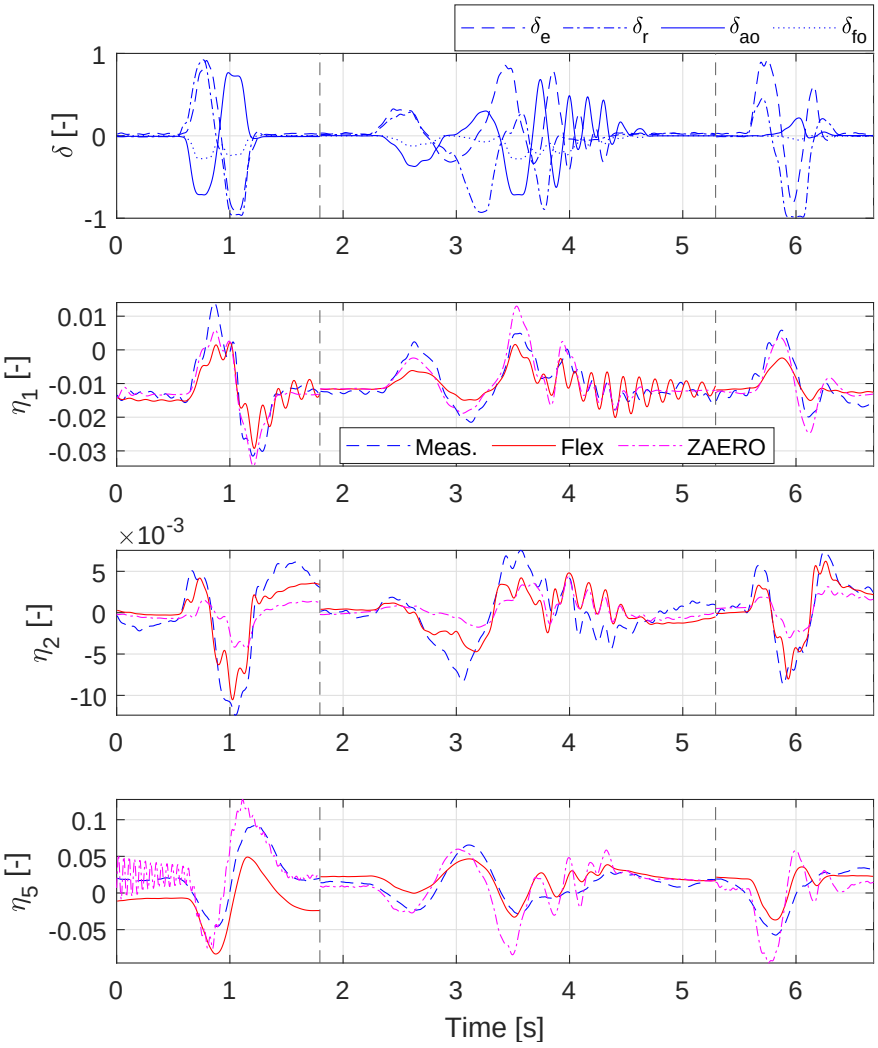

Figure 5.21: Multiple control surface excitation simulations - modal responses.

In Fig. 5.21 the modal responses to the same manoeuvres are presented. It can be seen that the structural mode responses are well captured by both the flexible model and ZAERO model simulations. This again indicates that the state estimation process was able to accurately extract the structural modal behaviour from the flight test measurements and that the model identification step successfully captured the corresponding dynamics.

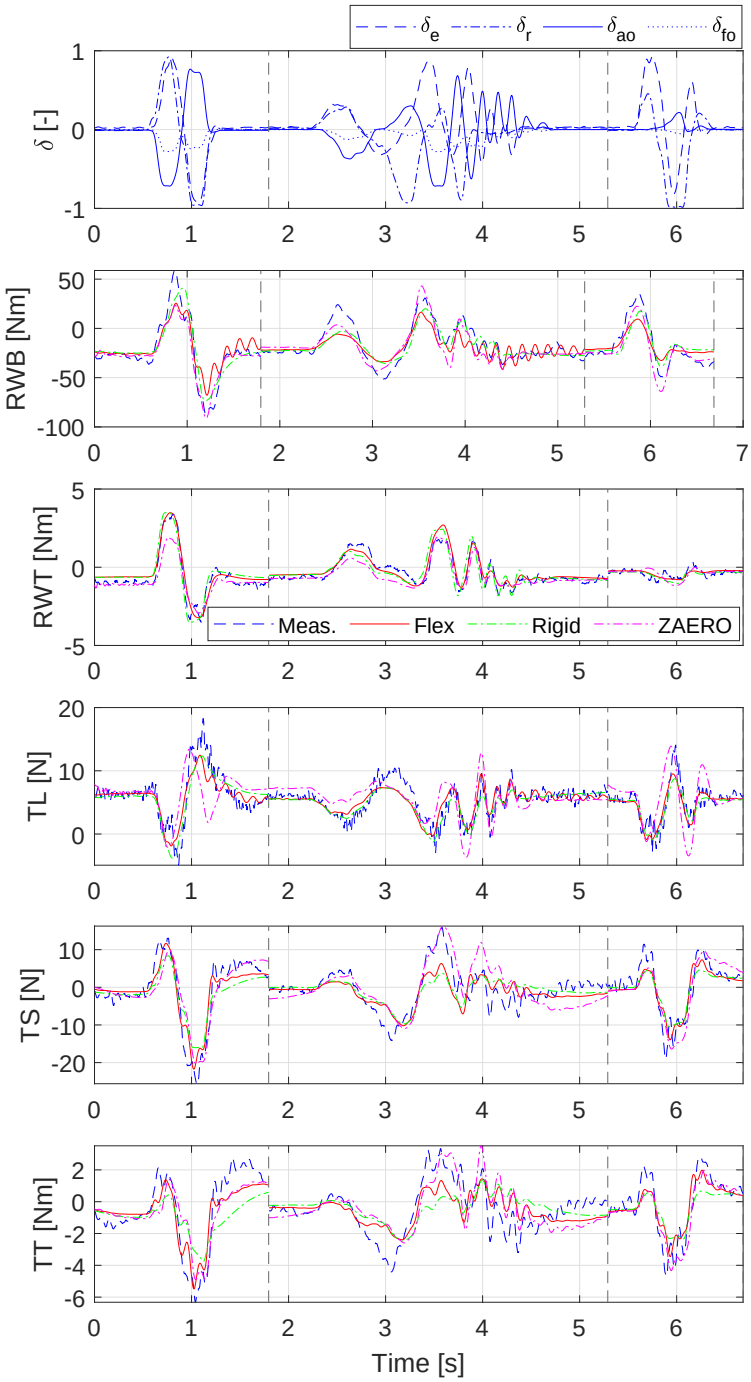

Figure 5.22: Multiple control surface excitation simulations - load responses.

In Fig. 5.22, the simulated wing and tail load responses corresponding to the manoeuvres are presented. Overall, all models successfully capture the dominant dynamics of the load responses, although some discrepancies remain, primarily due to previously discussed differences in angle of attack and sideslip behaviour.

In general, while the flexible model achieves higher accuracy in fitting, it is also more sensitive to modelling inaccuracies. Since it incorporates an internal structural dynamic loop, its overall performance depends on the accurate simulation of both rigid-body dynamics and structural dynamics. Consequently, in the presence of external or unmodelled disturbances, errors in one component of the model can propagate, reducing overall simulation accuracy. In most cases, the rigid model performs comparably to the flexible model. However, in the case of aileron excitations, the rigid model does underperform as it showed to be crucial to add the aerodynamic lag term related to the aileron motion. Similarly, the inclusion of the tail mode does lead to improved load response simulation accuracy in the flexible model. Ultimately, the selection of a model and the specific elements to include depend on the intended application and purpose of the simulation.

5.7. Conclusion

This chapter presented the identification of flight dynamics and load models for a scaled Diana 2 glider, which included the effects of its structural modes and delays related to unsteady aerodynamics. To account for unsteady aerodynamics, aerodynamic lag states were introduced, requiring the estimation of aerodynamic lag poles that characterise response delays. A correlation-based approach was developed to estimate these poles from flight test data and reconstruct the aerodynamic lag states for modelling. The estimated aerodynamic lag poles closely aligned with predictions from aeroelastic numerical theory.

By first reconstructing the aerodynamic lag states and performing state estimation to determine modal amplitude and velocity responses from flight test measurements, it was possible to estimate model parameters using ordinary least squares parameter estimation. In addition to the aerodynamic force and moment coefficients, the generalised force coefficients of the included structural modes were also identified together with load models for the wing root bending and torque moments, as well as tail loads.

Two models were identified for the scaled Diana 2 glider - a ”rigid” model for which only parameters related to the aircraft’s rigid-body responses and control surfaces were considered and a ”flexible” model for which the aerodynamic lag states and structural modes were also considered. On average, around 10% improvement in the fitting results was obtained by including the structural modes and aerodynamic lag states in the model, with the most significant improvement of 29% observed in the roll moment coefficient by incorporating aerodynamic lag states related to aileron deflections. More than 15% improvement in the tail side force and torsion responses was achieved compared to the rigid model by including the structural mode related to tail roll motion.

Finally, the identified models were validated by performing an open-loop simulation and comparing the simulation responses to the flight test measurements. The results showed that the simulated responses by the identified models are able to accurately predict the rigid body, modal and load responses when compared to flight test measurements and reference aeroelastic simulation model predictions.

REFERENCES

[1] J. A. Grauer and M. J. Boucher. “Real-time parameter estimation for flexible aircraft”. In: *2018 Atmospheric Flight Mechanics Conference*. Atlanta, Georgia: American Institute of Aeronautics and Astronautics, June 2018. DOI: 10.2514/6.2018-3155.

[2] J. A. Grauer and M. J. Boucher. *Output Measurement Equations for Flexible Aircraft Flight Dynamics*. TM–2018–220102. NASA Langley Research Center, 2018, pp. 1–36.

[3] B. P. Danowsky, D. K. Schmidt and H. Pfifer. “Control-Oriented System and Parameter Identification of a Small Flexible Flying-Wing Aircraft”. In: *AIAA Atmospheric Flight Mechanics Conference*. American Institute of Aeronautics and Astronautics, Jan. 2017, p. 25. ISBN: 978-1-62410-448-0. DOI: 10.2514/6.2017-1394.

[4] B. G. de Oliveira Silva. “System Identification of Flexible Aircraft in Time Domain”. PhD thesis. Technical University of Braunschweig, Aug. 2018, p. 225.

[5] M. V. Preisighe Viana. “Time-Domain System Identification of Rigid-Body Multipoint Loads Model”. PhD thesis. Technical University of Braunschweig, June 2016, p. 385. DOI: 10.2514/6.2016-3706.

[6] M. R. Waszak and D. K. Schmidt. “Flight dynamics of aeroelastic vehicles”. In: *Journal of Aircraft* 25.6 (1988), pp. 563–571. ISSN: 0021-8669. DOI: 10.2514/3.45623.

[7] T. Theodorsen. *General Theory of Aerodynamic Instability and the Mechanism of Flutter*. Tech. rep. TR-496. NACA, 1935.

[8] Q. P. Chu, J. A. Mulder and J. K. Sridhar. “Decomposition of Aircraft State and Parameter Estimation Problems”. In: *Proceedings of the 10th IFAC Symposium on System Identification*. 1994, pp. 61–66.

[9] J. A. Mulder, Q. P. Chu, J. K. Sridhar, J. H. Breeman and M. Laban. “Non-linear aircraft flight path reconstruction review and new advances”. In: *Progress in Aerospace Sciences* 35.7 (7 Oct. 1999), pp. 673–726. ISSN: 03760421. DOI: 10.1016/s0376-0421(99)00005-6.

[10] J. R. Wright and J. E. Cooper. *Introduction to Aircraft Aeroelasticity and Loads*. Wiley, Dec. 2014. ISBN: 9781118700440. DOI: 10.1002/9781118700440.

[11] R. T. Jones. *Operational Treatment of the Nonuniform-Lift Theory in Airplane Dynamics*. Tech. rep. NACA TN 667. NACA, 1938.

[12] J. Boutet and G. Dimitriadis. “Unsteady lifting line theory using thewagner function for the aerodynamic and aeroelastic modeling of 3D wings”. In: *Aerospace* 5 (3 Sept. 2018), p. 92. ISSN: 22264310. DOI: 10.3390/aerospace5030092.

[13] E. A. Morelli and V. Klein. *Aircraft system identification: Theory and Practice*. en. AIAA Education Series. Reston, VA: American Institute of Aeronautics & Astronautics, Aug. 2006.

[14] A. Jürisson, B. Eussen, C. C. de Visser and R. De Breuker. *Flexible Diana 2 Scaled Glider UAV - Flight Dynamics and Loads Model Identification Results*. Dataset. 4TU.ResearchData, 2026. DOI: 10.4121/5e5ee442-12d3-4947-8ed0-46e93ba700f1.

[15] R. V. Jategaonkar. *Flight Vehicle System Identification: A Time Domain Methodology*. Vol. 216. Progress in Astronautics and Aeronautics. AIAA, Aug. 2006. ISBN: 1563478366.

[16] V. Klein, J. G. Batterson and P. C. Murphy. “Airplane model structure determination from Flight Data”. In: *Journal of Aircraft* 20.5 (May 1983), pp. 469–474. DOI: 10.2514/3.44895.

[17] ZONA Technology Inc. *ZAERO Theoretical Manual, Version 9.0*. Scottsdale, Arizona, 2014.

5.A. APPENDIX

5.A.1. MODEL STRUCTURE EVALUATION RESULTS

Table 5.11: Model structure evaluation for aerodynamic forces - flexible model.

C_D		C_Y		C_L	
Parameters	R^2[%]	Parameters	R^2[%]	Parameters	R^2[%]
α^2,	83.1	η_2,	71.6	α,	83.9
α, α^2,	84.7	β, η_2,	87.6	α, η_1,	89.9
$\alpha, \alpha^2, \delta_{fo}$,	85.4	β, η_2, η_5,	89.6	$\alpha, x_{lag}^{\delta_e}, \eta_1$,	90.5
$\alpha, \alpha^2, \beta, \delta_{fo}$,	85.8	$\beta, x_{lag}^{r}, \eta_2, \eta_5$,	91.3	$\alpha, \delta_e, x_{lag}^{\delta_e}, \eta_1$,	91.0
		$\beta, x_{lag}^{r}, x_{lag}^{\delta_r}, \eta_2, \eta_5$,	91.9	$\alpha, \delta_e, x_{lag}^{\delta_e}, \eta_1, \eta_5$,	91.3
		$\beta, x_{lag}^{q}, x_{lag}^{r}, x_{lag}^{\delta_r}, \eta_2, \eta_5$,	92.3	$\alpha, \alpha^2, \delta_e, x_{lag}^{\delta_e}, \eta_1, \eta_5$,	91.6

Table 5.12: Model structure evaluation for aerodynamic forces - rigid model.

C_D		C_Y		C_L	
Parameters	R^2[%]	Parameters	R^2[%]	Parameters	R^2[%]
α^2,	83.1	β,	66.2	α,	83.9
α, α^2,	84.7	β, δ_r,	78.8	α, q,	86.7
$\alpha, \alpha^2, \delta_{fo}$,	85.4	$\beta, \delta_r, \delta_{ao}$,	81.5	α, β, q,	88.2
$\alpha, \alpha^2, \beta, \delta_{fo}$,	85.8	$\beta, r, \delta_r, \delta_{ao}$,	83.4	$\alpha, \beta, q, \delta_e$,	89.2
		$\beta, q, r, \delta_r, \delta_{ao}$,	84.3	$\alpha, \beta, q, \delta_e, \delta_{fo}$,	89.7
		$\alpha^2, \beta, q, r, \delta_r, \delta_{ao}$,	84.6	$\alpha, \alpha^2, \beta, q, \delta_e, \delta_{fo}$,	90.0

Table 5.13: Model structure evaluation for aerodynamic moments - flexible model.

C_l		C_m		C_n	
Parameters	R^2[%]	Parameters	R^2[%]	Parameters	R^2[%]
$x_{lag}^{\delta_{ao}}$,	81.4	$x_{lag}^{\delta_e}$,	57.0	η_2,	60.6
$r, x_{lag}^{\delta_{ao}}$,	81.8	$\alpha, x_{lag}^{\delta_e}$,	84.2	p, η_2,	72.5
$r, x_{lag}^{p}, x_{lag}^{\delta_{ao}}$,	82.0	$\alpha, x_{lag}^{q}, x_{lag}^{\delta_e}$,	85.8	$p, x_{lag}^{\delta_r}, \eta_2$,	76.2
$r, \delta_{ao}, x_{lag}^{p}, x_{lag}^{\delta_{ao}}$,	82.0	$\alpha, q, x_{lag}^{q}, x_{lag}^{\delta_e}$,	86.0	$p, x_{lag}^{r}, x_{lag}^{\delta_r}, \eta_2$,	78.9
$r, \delta_{ao}, x_{lag}^{p}, x_{lag}^{\delta_e}, x_{lag}^{\delta_{ao}}$,	82.0	$\alpha, q, x_{lag}^{q}, x_{lag}^{\delta_e}, \eta_1$,	86.0	$\beta, p, \delta_r, x_{lag}^{r}, \eta_2$,	79.4
$r, \delta_{ao}, x_{lag}^{p}, x_{lag}^{\delta_e}, x_{lag}^{\delta_{ao}}, x_{lag}^{\delta_{fo}}$	82.1	$\alpha, q, x_{lag}^{q}, x_{lag}^{\delta_e}, \eta_1, \eta_5$,	86.1	$\beta, p, \delta_r, x_{lag}^{r}, x_{lag}^{\delta_r}, \eta_2$,	80.7

Table 5.14: Model structure evaluation for aerodynamic moments - rigid model.

C_l		C_m		C_n	
Parameters	R^2[%]	Parameters	R^2[%]	Parameters	R^2[%]
δ_{ao},	13.4	α,	46.6	β,	28.6
p, δ_{ao},	41.2	α, δ_e,	60.3	β, δ_r,	64.2
β, p, δ_{ao},	49.0	α, q, δ_e,	77.7	β, r, δ_r,	68.1
β, p, r, δ_{ao},	52.8	$\alpha, \beta, q, \delta_e$,	79.3	β, p, r, δ_r,	70.5
$\beta, p, r, \delta_r, \delta_{ao}$,	53.4	$\alpha, \beta, q, \delta_e, \delta_{fo}$,	79.6	$\beta, p, r, \delta_r, \delta_{fo}$,	70.6
$\beta, p, q, r, \delta_e, \delta_{ao}$,	53.7	$\alpha, \beta, q, r, \delta_e, \delta_{fo}$,	79.7	$\alpha^2, \beta, p, r, \delta_r, \delta_{fo}$,	70.6

Table 5.15: Model structure evaluation for generalised forces - flexible model.

C_{Q1}		C_{Q2}		C_{Q5}	
Parameters	R^2[%]	Parameters	R^2[%]	Parameters	R^2[%]
$\eta_1, \dot{\eta_1}$	12.4	$\eta_2, \dot{\eta_2}$	17.1	$\eta_5, \dot{\eta_5}$	18.3
$\eta_1, \dot{\eta_1}, \alpha$	77.1	$\eta_2, \dot{\eta_2}, x^{\delta_r}_{lag}$	51.8	$\eta_5, \dot{\eta_5}, \alpha$	67.5
$\eta_1, \dot{\eta_1}, \alpha, u$,	82.6	$\eta_2, \dot{\eta_2}, \beta, \delta_r$	76.6	$\eta_5, \dot{\eta_5}, \alpha, \phi$	76.7
$\eta_1, \dot{\eta_1}, \alpha, u, \delta_{fo}$	84.5	$\eta_2, \dot{\eta_2}, \beta, \delta_r, \delta_{ao}$	80.9	$\eta_5, \dot{\eta_5}, \alpha, \phi, \delta_e$	79.7
$\eta_1, \dot{\eta_1}, \alpha, \phi, u, \delta_{fo}$	85.7	$\eta_2, \dot{\eta_2}, \beta, \delta_r, \delta_{ao}, x^{\delta_r}_{lag}$	83.8	$\eta_5, \dot{\eta_5}, \alpha, \phi, x^q_{lag}, x^{\delta_e}_{lag}$	79.8
$\eta_1, \dot{\eta_1}, \alpha, \phi, u, \delta_{fo}, x^q_{lag}$	86.9	$\eta_2, \dot{\eta_2}, \nu, , \delta_r, \delta_{ao}, x^r_{lag}, x^{\delta_r}_{lag}$	85.0	$\eta_5, \dot{\eta_5}, \alpha, q, \phi, \delta_e, x^q_{lag}$	80.4
$\eta_1, \dot{\eta_1}, \alpha, \phi, u, \delta_e, \delta_{fo}, x^{\delta_e}_{lag}$	87.1	$\eta_2, \dot{\eta_2}, \beta, \nu, \delta_r, \delta_{ao}, x^r_{lag}, x^{\delta_r}_{lag}$	85.3	$\eta_5, \dot{\eta_5}, q, \phi, u, w, \delta_e, x^q_{lag}$	81.6

Table 5.16: Model structure evaluation for wing loads - flexible model.

Wing bending			Wing torsion		
Parameters	RWB R^2[%]	LWB R^2[%]	Parameters	RWT R^2[%]	LWT R^2[%]
w,	74.6	77.7	δ_{ao},	61.6	62.4
α, η_1,	82.5	85.6	$\delta_{ao}, x^{\delta_{ao}}_{lag}$,	71.6	69.5
α, u, η_1,	88.3	89.7	$u, \delta_{ao}, x^{\delta_{ao}}_{lag}$,	72.4	76.8
α, ϕ, u, η_1,	89.8	91.1	$\alpha, u, \delta_{ao}, x^{\delta_{ao}}_{lag}$,	80.9	77.3
$\alpha, u, w, \eta_1, \eta_5$,	91.4	91.8	$\alpha, u, \delta_{ao}, \delta_{fo}, x^{\delta_{ao}}_{lag}$,	86.3	81.2
$\alpha, u, w, x^q_{lag}, \eta_1, \eta_5$,	93.0	93.3	$\alpha, u, \delta_{ao}, \delta_{fo}, x^{\delta_{ao}}_{lag}, \eta_2$,	86.5	82.4

Table 5.17: Model structure evaluation for wing loads - rigid model.

Wing bending			Wing torsion		
Parameters	RWB R^2[%]	LWB R^2[%]	Parameters	RWT R^2[%]	LWT R^2[%]
w,	74.6	77.7	δ_{ao},	61.5	62.4
w, δ_{fo},	78.2	81.2	u, δ_{ao},	62.4	69.6
α, w, δ_{fo},	80.0	82.4	α, u, δ_{ao},	71.7	70.0
$\alpha, q, \delta_e, \delta_{fo}$,	81.3	84.0	$\alpha, u, \delta_{ao}, \delta_{fo}$,	76.7	73.9
$\alpha, q, w, \delta_e, \delta_{fo}$,	81.6	84.6	$\alpha, p, u, \delta_{ao}, \delta_{fo}$,	79.1	76.0
$\alpha, q, u, w, \delta_e, \delta_{fo}$,	82.3	84.9	$\alpha, \beta, p, u, \delta_{ao}, \delta_{fo}$,	80.1	78.2

Table 5.18: Model structure evaluation for tail loads - flexible model.

Tail lift force		Tail side force		Tail torsion	
Parameters	R^2[%]	Parameters	R^2[%]	Parameters	R^2[%]
α,	54.8	η_2,	75.3	η_2,	88.5
α, δ_e,	72.2	δ_r, η_2,	84.0	β, η_2,	90.1
u, δ_e, η_1,	79.2	$\delta_r, x_{lag}^{\delta_r}, \eta_2$,	86.2	β, v, η_2,	91.3
$\alpha, u, \delta_e, \eta_1$,	80.2	$\beta, v, \delta_r, \eta_2$,	87.5	α, β, v, η_2,	91.9
$\alpha, u, \delta_e, x_{lag}^{\delta_e}, \eta_1$,	81.2	$\beta, v, \delta_r, \delta_{ao}, \eta_2$,	88.4	$\alpha, \beta, v, x_{lag}^{\delta_r}, \eta_2$,	92.1
$\alpha, q, u, \delta_e, \delta_{fo}, \eta_1$,	82.2	$\beta, v, \delta_r, \delta_{ao}, x_{lag}^{\delta_r}, \eta_2$,	89.0	$\alpha, \beta, v, w, x_{lag}^{\delta_r}, \eta_2$,	92.2

Table 5.19: Model structure evaluation for tail loads - rigid model.

Tail lift force		Tail side force		Tail torsion	
Parameters	R^2[%]	Parameters	R^2[%]	Parameters	R^2[%]
α,	54.8	δ_r,	26.7	β,	40.9
α, δ_e,	72.2	β, δ_r,	71.2	β, δ_r,	68.6
u, w, δ_e,	77.8	β, δ_r, r,	72.2	$\beta, \delta_{ao}, \delta_r$,	72.3
$\alpha, u, \delta_e, \delta_{fo}$,	79.4	$\beta, \delta_r, \delta_{ao}, r$,	73.1	$\alpha, \beta, \delta_{ao}, \delta_r$,	73.5
$q, u, w, \delta_e, \delta_{fo}$,	80.3	$\beta, \delta_r, \delta_{ao}, p, r$,	73.6	$\alpha, \beta, \delta_{ao}, p, \delta_r$,	74.0
$q, u, w, \delta_e, \delta_{fo}, \delta_r$,	80.5	$\beta, \delta_r, \delta_{ao}, \alpha, p, r$,	73.9	$\alpha, \beta, v, \delta_{ao}, p, \delta_r$,	74.2

5.A.2. IDENTIFIED MODEL PARAMETERS

In this section, the identified parameters are presented. The parameter values are provided together with their relative standard deviations which were determined by dividing the parameter standard deviation estimates obtained from Eq. 5.31 by the parameter estimates. The parameters related to the aerodynamic force and moment coefficients are provided in Table 5.20 for the flexible model and Table 5.21 for the rigid model. In addition, the parameters related to the generalised forces are found in Table 5.22 and load coefficients are in Table 5.23.

Table 5.20: Identified parameters for aerodynamic force and moment coefficients - flexible model.

Param.	Value	± [%]	Param.	Value	± [%]	Param.	Value	± [%]
C_{D_0}	2.17E-02	0.28	C_{Y_0}	6.04E-03	0.63	C_{L_0}	2.43E-01	0.44
C_{D_α}	-1.23E-01	0.69	C_{Y_β}	-1.07E-01	0.20	C_{L_α}	3.10E+00	0.20
$C_{D_{\alpha^2}}$	3.28E+00	0.10	$C_{Y_{\eta_2}}$	6.05E+00	0.32	$C_{L_{\delta_e}}$	-1.83E-01	1.82
			$C_{Y_{\eta_5}}$	1.39E-01	0.67	$C_{L_{\eta_1}}$	-9.91E+00	0.82
			$C_{Y_{x^r_{lag}}}$	3.99E-01	0.82	$C_{L_{\eta_5}}$	7.06E-01	1.94
			$C_{Y_{x^{\delta_r}_{lag}}}$	2.01E-02	1.43	$C_{L_{x^{\delta_e}_{lag}}}$	6.86E-01	0.97
C_{l_0}	7.19E-05	29.25	C_{m_0}	-9.61E-02	0.34	C_{n_0}	4.99E-04	3.04
C_{l_r}	2.09E-02	2.55	C_{m_α}	-1.18E+00	0.36	C_{n_β}	1.55E-02	1.18
$C_{l_{\delta_{ao}}}$	-7.62E-03	3.08	$C_{m_{\delta_e}}$	-1.85E-02	13.96	C_{n_p}	-3.39E-02	0.99
$C_{l_{x^p_{lag}}}$	-3.06E-01	1.80	$C_{m_{x^q_{lag}}}$	-1.45E+02	1.23	$C_{n_{\delta_r}}$	-9.52E-03	0.99
$C_{l_{x^{\delta_{ao}}_{lag}}}$	-1.81E-01	0.29	$C_{m_{x^{\delta_e}_{lag}}}$	-1.25E+00	0.42	$C_{n_{\eta_2}}$	-1.73E+00	0.69
						$C_{n_{x^r_{lag}}}$	-1.48E-01	1.19
						$C_{n_{x^{\delta_r}_{lag}}}$	-9.38E-03	1.85

Table 5.21: Identified parameters for aerodynamic force and moment coefficients - rigid model.

Param.	Value	± [%]	Param.	Value	± [%]	Param.	Value	± [%]
C_{D_0}	2.17E-02	0.28	C_{Y_0}	1.07E-02	0.37	C_{L_0}	3.16E-01	0.14
C_{D_α}	-1.23E-01	0.69	C_{Y_β}	-2.03E-01	0.15	C_{L_α}	4.11E+00	0.13
$C_{D_{\alpha^2}}$	3.28E+00	0.10	C_{Y_q}	1.59E+00	1.40	C_{L_β}	-2.95E-01	0.62
			C_{Y_r}	1.08E-01	0.95	C_{L_q}	5.37E+01	0.57
			$C_{Y_{\delta_r}}$	4.51E-02	0.39	$C_{L_{\delta_e}}$	4.13E-01	0.80
			$C_{Y_{\delta_{ao}}}$	3.25E-02	0.86	$C_{L_{\delta_{fo}}}$	4.59E-01	1.42
C_{l_0}	1.05E-03	3.01	C_{m_0}	-1.73E-02	1.95	C_{n_0}	3.43E-05	51.83
C_{l_β}	-2.71E-02	0.95	C_{m_α}	-2.24E+00	0.18	C_{n_β}	4.77E-02	0.30
C_{l_p}	-2.65E-01	0.45	C_{m_β}	1.51E-01	0.95	C_{n_p}	-1.70E-02	4.01
C_{l_q}	2.58E-02	68.56	C_{m_q}	-6.38E+01	0.37	C_{n_r}	-3.89E-02	1.21
C_{l_r}	7.61E-02	1.09	$C_{m_{\delta_e}}$	-9.45E-01	0.27	$C_{n_{\delta_r}}$	-2.40E-02	0.33
$C_{l_{\delta_r}}$	3.39E-03	4.10				$C_{n_{\delta_{ao}}}$	1.62E-03	14.43
$C_{l_{\delta_{ao}}}$	-1.07E-01	0.39						

Table 5.22: Identified parameters for generalized force coefficients.

Param.	Value	± [%]	Param.	Value	± [%]	Param.	Value	± [%]
C_{Q1_0}	-7.96E-01	0.28	C_{Q2_0}	9.81E-03	2.67	C_{Q5_0}	3.49E+00	0.79
C_{Q1_α}	-3.01E+00	0.25	C_{Q2_v}	-5.20E-02	0.40	C_{Q5_α}	9.71E+01	0.32
C_{Q1_ϕ}	-1.77E-02	1.05	$C_{Q2_{\delta_r}}$	3.31E-01	0.54	C_{Q5_ϕ}	-1.40E+00	0.69
$C_{Q1_{u,}}$	1.98E-02	0.78	$C_{Q2_{\delta_{ao}}}$	3.33E-01	0.63	$C_{Q5_{\delta_e}}$	-1.29E+01	1.13
$C_{Q1_{\delta_{fo}}}$	-8.42E-01	0.84	$C_{Q2_{\eta_2}}$	8.43E+00	2.78	$C_{Q5_{\eta_5}}$	3.38E+01	2.15
$C_{Q1_{\eta_1}}$	4.85E+00	2.22	$C_{Q2_{\dot{\eta}_2}}$	-6.76E+01	3.27	$C_{Q5_{\dot{\eta}_5}}$	-1.38E+03	2.74
$C_{Q1_{\dot{\eta}_1}}$	-1.08E+01	9.18	$C_{Q2_{x^r_{lag}}}$	5.29E+00	0.58			
			$C_{Q2_{x^{\delta_r}_{lag}}}$	4.01E-01	0.77			

Table 5.23: Identified parameters for load coefficients - flexible model.

Param.	Value	± [%]	Param.	Value	± [%]	Param.	Value	± [%]
$C^{RWB}_{M_0}$	-2.53E-02	0.42	$C^{LWB}_{M_0}$	1.95E-02	0.51	$C^{TL}_{F_0}$	4.14E-02	0.27
$C^{RWB}_{M_\alpha}$	-2.21E-01	0.35	$C^{LWB}_{M_\alpha}$	1.81E-01	0.40	$C^{TL}_{F_\alpha}$	4.39E-02	0.94
$C^{RWB}_{M_u}$	1.51E-03	0.42	$C^{LWB}_{M_u}$	-1.23E-03	0.49	$C^{TL}_{F_{u,}}$	-1.32E-03	0.52
$C^{RWB}_{M_w}$	1.35E-02	0.45	$C^{LWB}_{M_w}$	-9.75E-03	0.58	$C^{TL}_{F_{\delta_e}}$	-2.04E-02	0.80
$C^{RWB}_{M_{\eta_1}}$	1.86E+00	0.27	$C^{LWB}_{M_{\eta_1}}$	-1.65E+00	0.29	$C^{TL}_{F_{\eta_1}}$	-7.54E-01	0.67
$C^{RWB}_{M_{\eta_5}}$	-1.23E-01	0.55	$C^{LWB}_{M_{\eta_5}}$	8.95E-02	0.70	$C^{TL}_{F_{x^{\delta_e}_{lag}}}$	-2.73E-02	1.21
$C^{RWB}_{M_{x^q_{lag}}}$	-1.51E+01	0.69	$C^{LWB}_{M_{x^q_{lag}}}$	1.26E+01	0.78			
$C^{RWT}_{M_0}$	8.30E-04	17.26	$C^{LWT}_{M_0}$	2.77E-02	0.47	$C^{TS}_{F_0}$	-1.76E-03	1.07
$C^{RWT}_{M_\alpha}$	6.79E-02	0.52	$C^{LWT}_{M_\alpha}$	1.40E-02	2.27	$C^{TS}_{F_\beta}$	-1.27E-01	0.50
$C^{RWT}_{M_u}$	-7.54E-04	0.98	$C^{LWT}_{M_u}$	-1.56E-03	0.43	$C^{TS}_{F_\gamma}$	7.84E-03	0.52
$C^{RWT}_{M_{\delta_{ao}}}$	-1.08E-01	0.17	$C^{LWT}_{M_{\delta_{ao}}}$	8.93E-02	0.18	$C^{TS}_{F_{\delta_r}}$	1.93E-02	0.61
$C^{RWT}_{M_{\delta_{fo}}}$	-7.70E-02	0.67	$C^{LWT}_{M_{\delta_{fo}}}$	-5.28E-02	0.89	$C^{TS}_{F_{\delta_{ao}}}$	-1.29E-02	1.17
$C^{RWT}_{M_{x^{\delta_{ao}}_{lag}}}$	8.71E-02	0.52	$C^{LWT}_{M_{x^{\delta_{ao}}_{lag}}}$	-6.14E-02	0.67	$C^{TS}_{F_{\eta_2}}$	6.49E+00	0.24
						$C^{TT}_{M_0}$	-1.26E-02	0.23
						$C^{TT}_{M_\alpha}$	-2.85E-02	1.13
						$C^{TT}_{M_\beta}$	-1.52E-01	0.48
						$C^{TT}_{M_\gamma}$	7.96E-03	0.55
						$C^{TT}_{M_{\eta_2}}$	1.00E+01	0.12

Table 5.24: Identified parameters for load coefficients - rigid model.

Param.	Value	± [%]	Param.	Value	± [%]	Param.	Value	± [%]
$C^{RWB}_{M_0}$	-1.84E-02	0.81	$C^{LWB}_{M_0}$	1.40E-02	0.93	$C^{TL}_{F_0}$	3.91E-02	0.26
$C^{RWB}_{M_\alpha}$	-1.21E-01	0.89	$C^{LWB}_{M_\alpha}$	9.87E-02	0.96	$C^{TL}_{F_\alpha}$	6.18E-02	0.47
$C^{RWB}_{M_q}$	-2.53E+00	0.92	$C^{LWB}_{M_q}$	2.38E+00	0.85	$C^{TL}_{F_{u,}}$	-7.06E-04	0.72
$C^{RWB}_{M_u}$	1.73E-04	4.58	$C^{LWB}_{M_u}$	-9.72E-05	7.14	$C^{TL}_{F_{\delta_e}}$	-3.23E-02	0.35
$C^{RWB}_{M_w}$	-2.50E-03	2.67	$C^{LWB}_{M_w}$	3.74E-03	1.56	$C^{TL}_{F_{\delta_{fo}}}$	2.91E-02	1.17
$C^{RWB}_{M_{\delta_e}}$	-1.80E-02	1.19	$C^{LWB}_{M_{\delta_e}}$	2.01E-02	0.93			
$C^{RWB}_{M_{\delta_{fo}}}$	-4.85E-02	0.83	$C^{LWB}_{M_{\delta_{fo}}}$	4.46E-02	0.79			
$C^{RWT}_{M_0}$	1.83E-04	90.29	$C^{LWT}_{M_0}$	2.82E-02	0.49	$C^{TS}_{F_0}$	-9.58E-04	3.17
$C^{RWT}_{M_\alpha}$	7.05E-02	0.58	$C^{LWT}_{M_\alpha}$	1.18E-02	2.90	$C^{TS}_{F_\beta}$	-8.39E-02	0.28
$C^{RWT}_{M_p}$	3.95E-02	2.36	$C^{LWT}_{M_p}$	-5.30E-02	1.48	$C^{TS}_{F_r}$	5.81E-02	1.37
$C^{RWT}_{M_u}$	-7.41E-04	1.15	$C^{LWT}_{M_u}$	-1.56E-03	0.46	$C^{TS}_{F_{\delta_r}}$	5.85E-02	0.23
$C^{RWT}_{M_{\delta_{ao}}}$	-8.38E-02	0.38	$C^{LWT}_{M_{\delta_{ao}}}$	6.50E-02	0.42	$C^{TS}_{F_{\delta_{ao}}}$	1.31E-02	1.68
$C^{RWT}_{M_{\delta_{fo}}}$	-7.57E-02	0.79	$C^{LWT}_{M_{\delta_{fo}}}$	-5.54E-02	0.92			
						$C^{TT}_{M_0}$	-9.71E-03	0.59
						$C^{TT}_{M_\alpha}$	-4.80E-02	1.30
						$C^{TT}_{M_\beta}$	-1.49E-01	0.22
						$C^{TT}_{M_{\delta_r}}$	5.78E-02	0.32
						$C^{TT}_{M_{\delta_{ao}}}$	3.82E-02	0.80

5.A.3. NUMERICAL MODEL OVERVIEW

To be able to compare the identified models to a more traditional numerical analysis approach, a model of the scaled Diana 2 glider was also constructed using ZAERO software by ZONA technologies [17]. This model consists of a Finite Element Method (FEM) NASTRAN model to represent the aircraft structure and an aerodynamic model created using aerodynamic panels as shown in Fig. 5.23. The structural model consists of simple beam elements as shown in Fig. 5.24 that were tuned with ground vibration test (GVT) results carried out on the Diana 2 glider in Chapter 3.

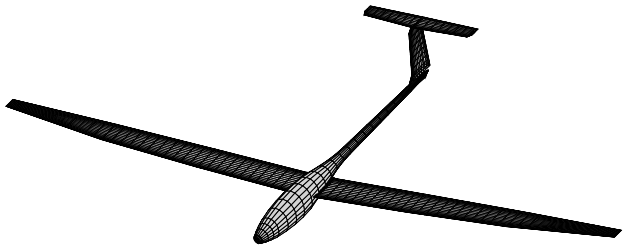

Figure 5.23: ZAERO model for scaled Diana 2 glider.

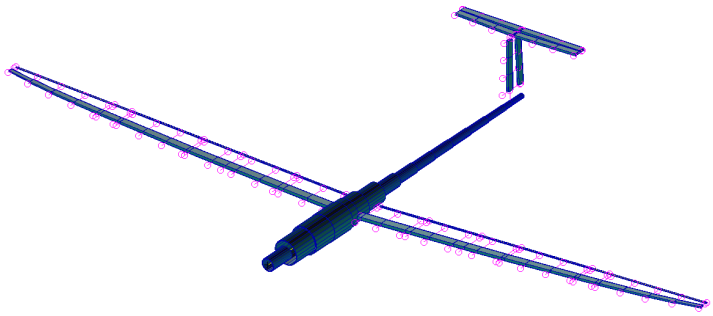

Figure 5.24: ZAERO model for scaled Diana 2 glider.

The model includes all 6-DOF related to the aircraft's rigid body motion and the first 8 structural modes. The frequency-domain solution for the generalised forces was converted to the time-domain using Roger's method for rational function approximation approach where three aerodynamic lag states were used for each rigid body and structural mode. A state-space model was constructed to represent the flight dynamics model of the Diana 2 glider as presented in Eq. 5.65.

$$\begin{bmatrix} \dot{\boldsymbol{\eta}} \\ \ddot{\boldsymbol{\eta}} \\ \dot{\boldsymbol{x}}_{\boldsymbol{lag}} \end{bmatrix} = \begin{bmatrix} 0 & \boldsymbol{I} & 0 \\ -\bar{\boldsymbol{M}}^{-1}[\boldsymbol{K_s} - \bar{q}\boldsymbol{A_0}] & -\bar{\boldsymbol{M}}^{-1}[\boldsymbol{C_s} - \bar{q}\boldsymbol{A_1}] & \bar{q}\bar{\boldsymbol{M}}^{-1}\boldsymbol{A}_{\boldsymbol{lag}} \\ 0 & \boldsymbol{E} & \frac{V}{\bar{b}}\boldsymbol{R} \end{bmatrix} \begin{bmatrix} \boldsymbol{\eta} \\ \dot{\boldsymbol{\eta}} \\ \boldsymbol{x}_{\boldsymbol{lag}} \end{bmatrix} + \tag{5.65}$$

$$+ \begin{bmatrix} 0 & 0 & 0 \\ \bar{\boldsymbol{M}}^{-1}\boldsymbol{A_{c0}} & \bar{\boldsymbol{M}}^{-1}\boldsymbol{A_{c1}} & \bar{\boldsymbol{M}}^{-1}\boldsymbol{A_{c2}} \\ 0 & \boldsymbol{E_c} & 0 \end{bmatrix} \begin{bmatrix} \boldsymbol{\delta} \\ \dot{\boldsymbol{\delta}} \\ \ddot{\boldsymbol{\delta}} \end{bmatrix}$$

$$\bar{\boldsymbol{M}} = \boldsymbol{M_s} - \bar{q}\boldsymbol{A_2} \tag{5.66}$$

The aerodynamic matrices $\boldsymbol{A_0}, \boldsymbol{A_1}, \boldsymbol{A_2}$ were obtained from RFA where $\boldsymbol{A_{c0}}, \boldsymbol{A_{c1}}, \boldsymbol{A_{c2}}$ are the elements related to the control surfaces. The matrices E, E_c assign the correct states as inputs for the aerodynamic lag states while matrix R contains the lag pole values. The inputs to this model are the control surface angles, rotational velocities, and accelerations. The outputs of the model are the aircraft's rigid body responses and modal amplitudes and velocities. In addition, also the loads at the wing and tail root are included.

5.A.4. SIMULATION RESPONSE OVERVIEW

In this section, a more detailed overview with additional response signals is presented for the elevator, aileron, and rudder excitation simulations.

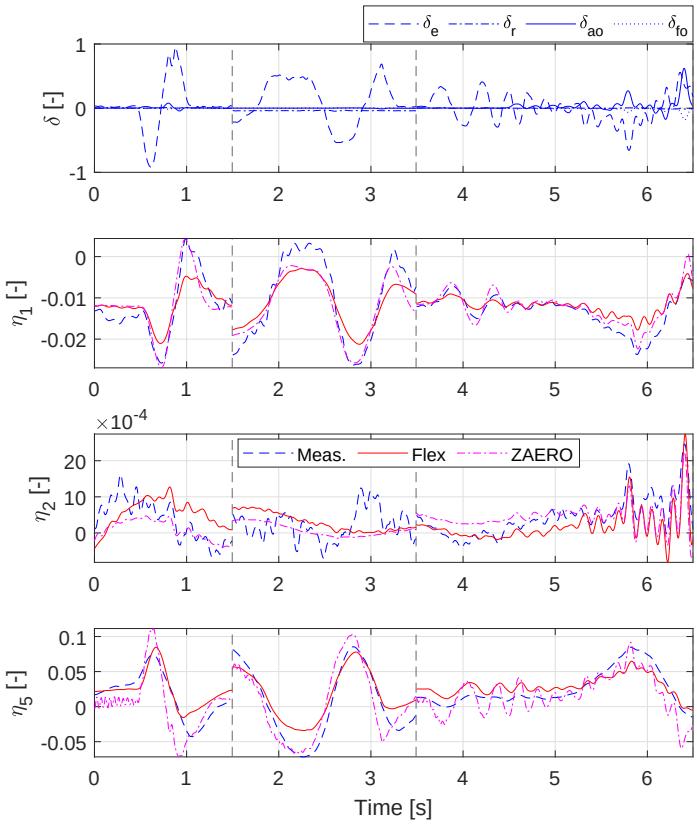

Figure 5.25: Elevator excitation response simulations - modal responses.

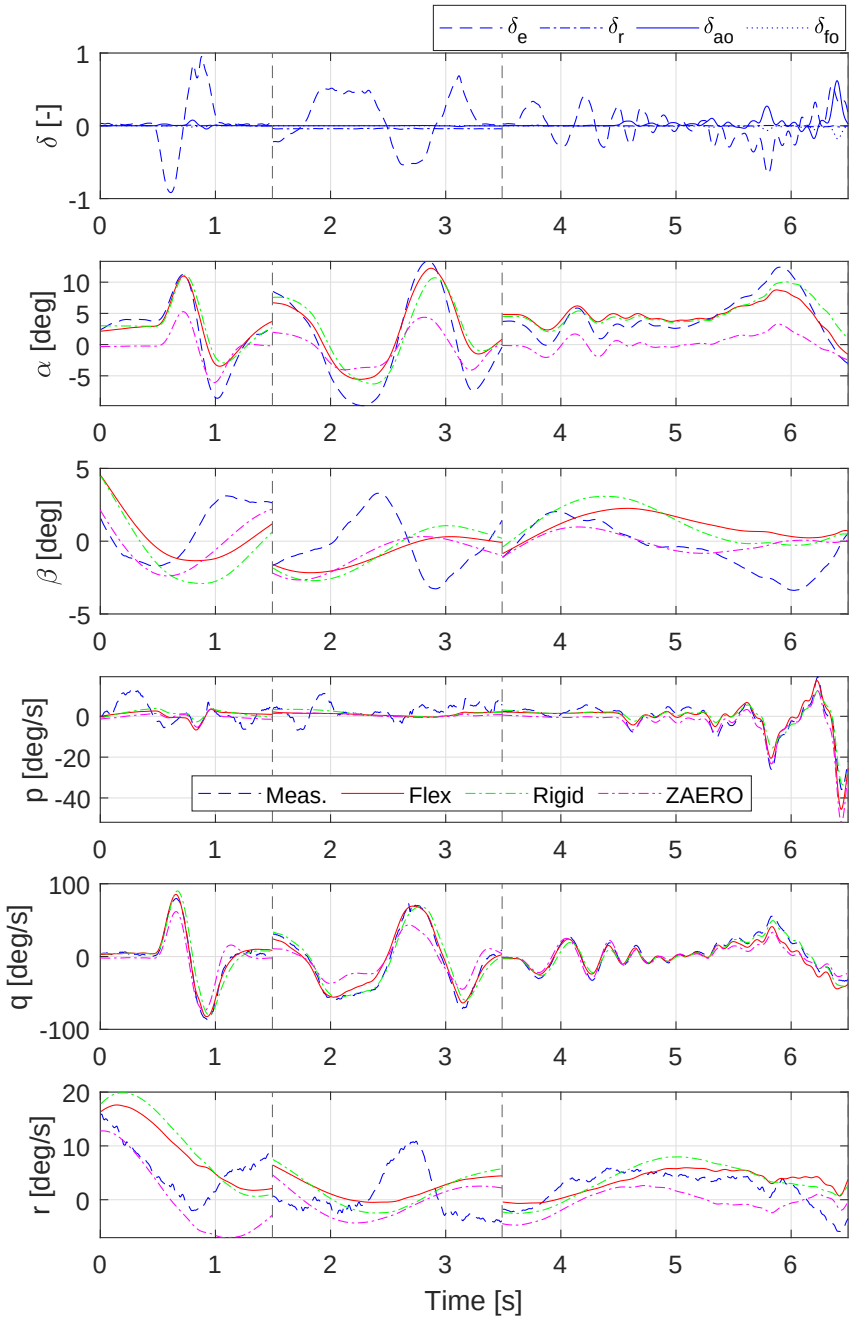

Figure 5.26: Elevator excitation response simulations - rigid body responses.

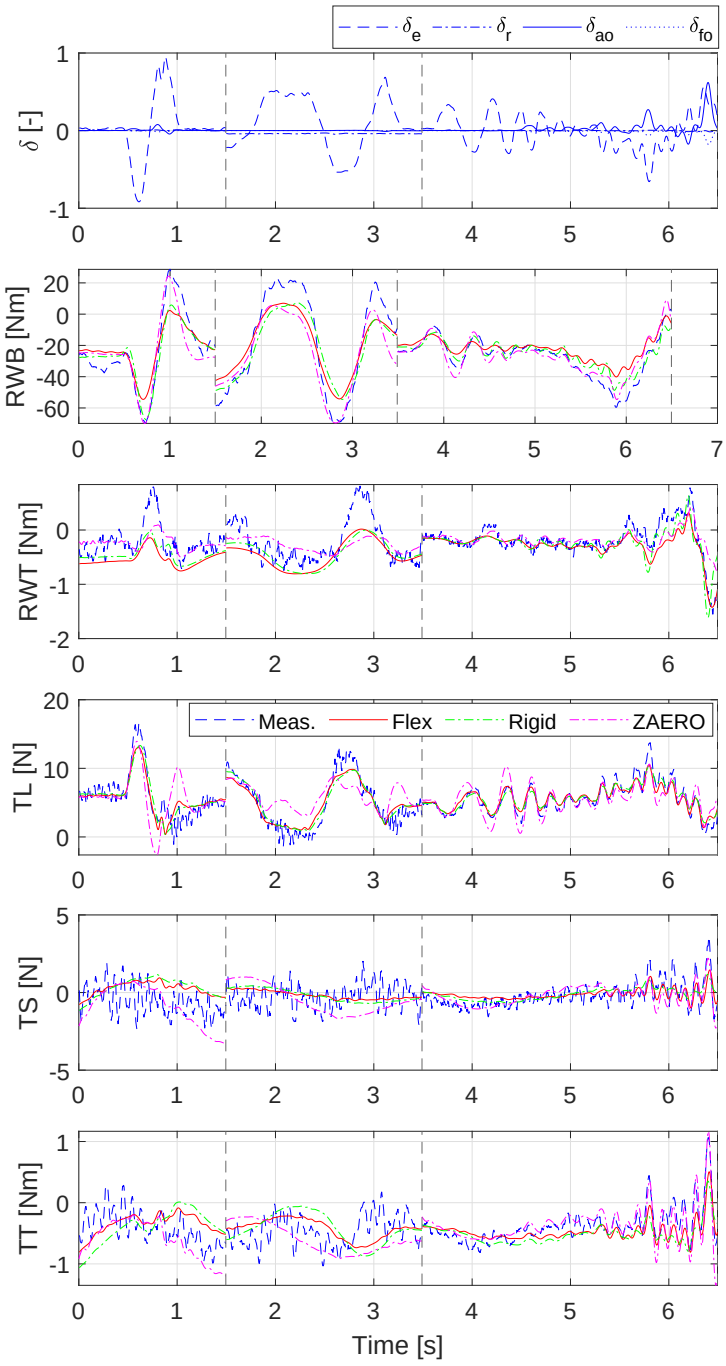

Figure 5.27: Elevator excitation response simulations - load responses.

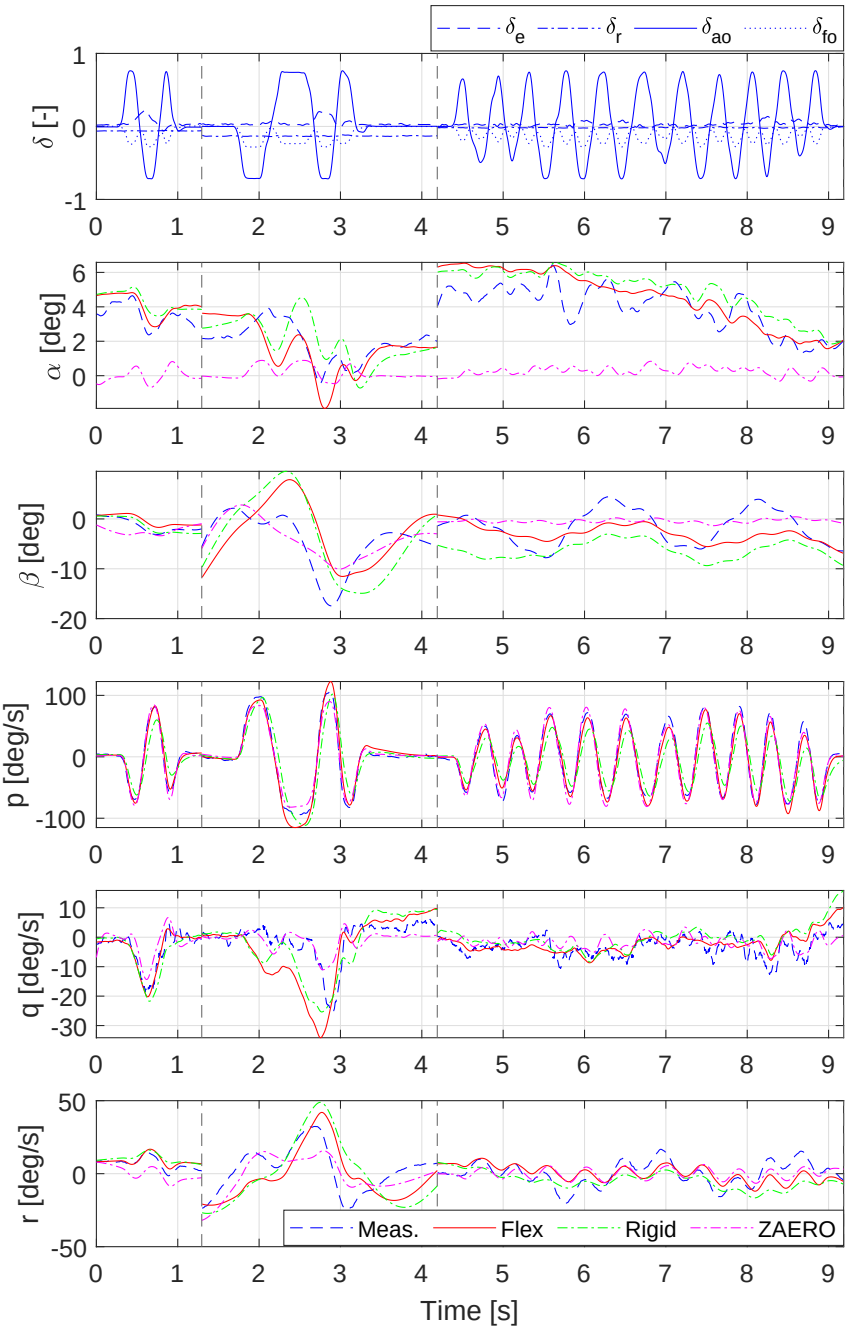

Figure 5.28: Aileron excitation response simulations - rigid body responses.

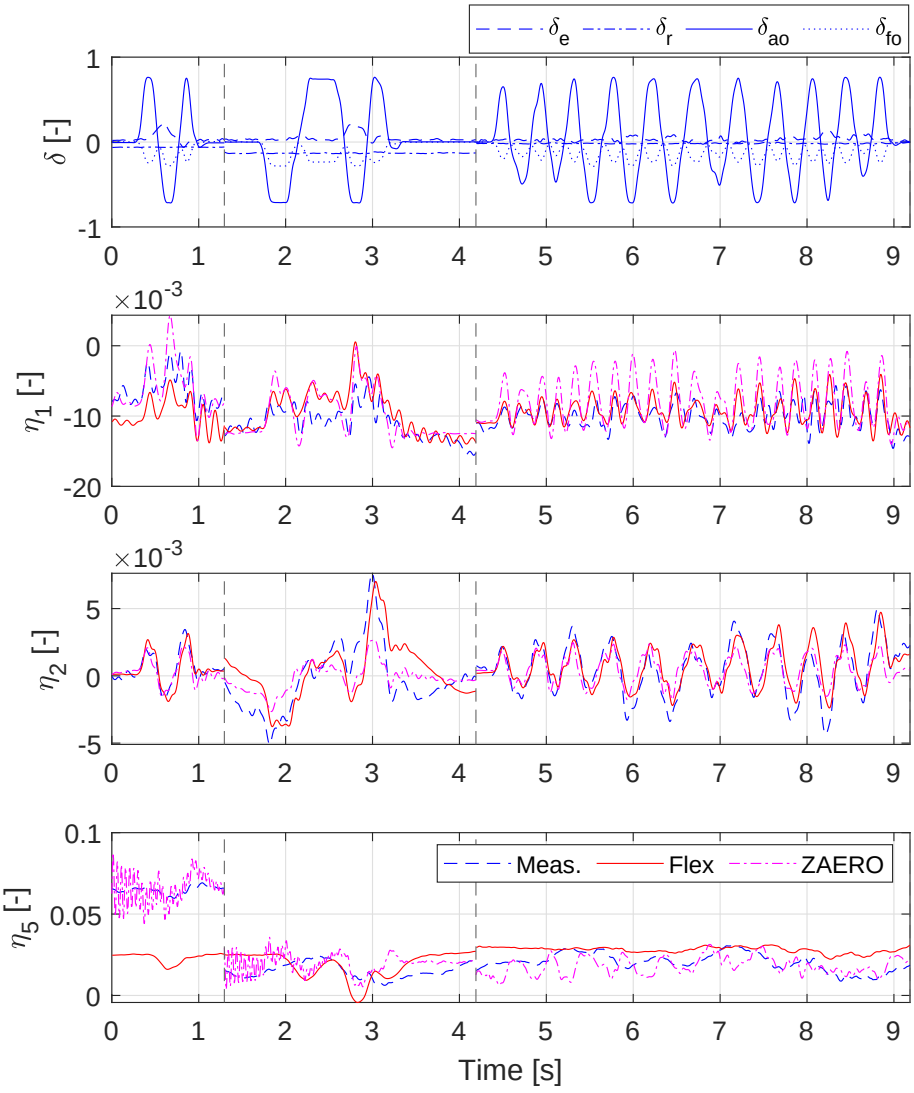

Figure 5.29: Aileron excitation response simulations - modal responses.

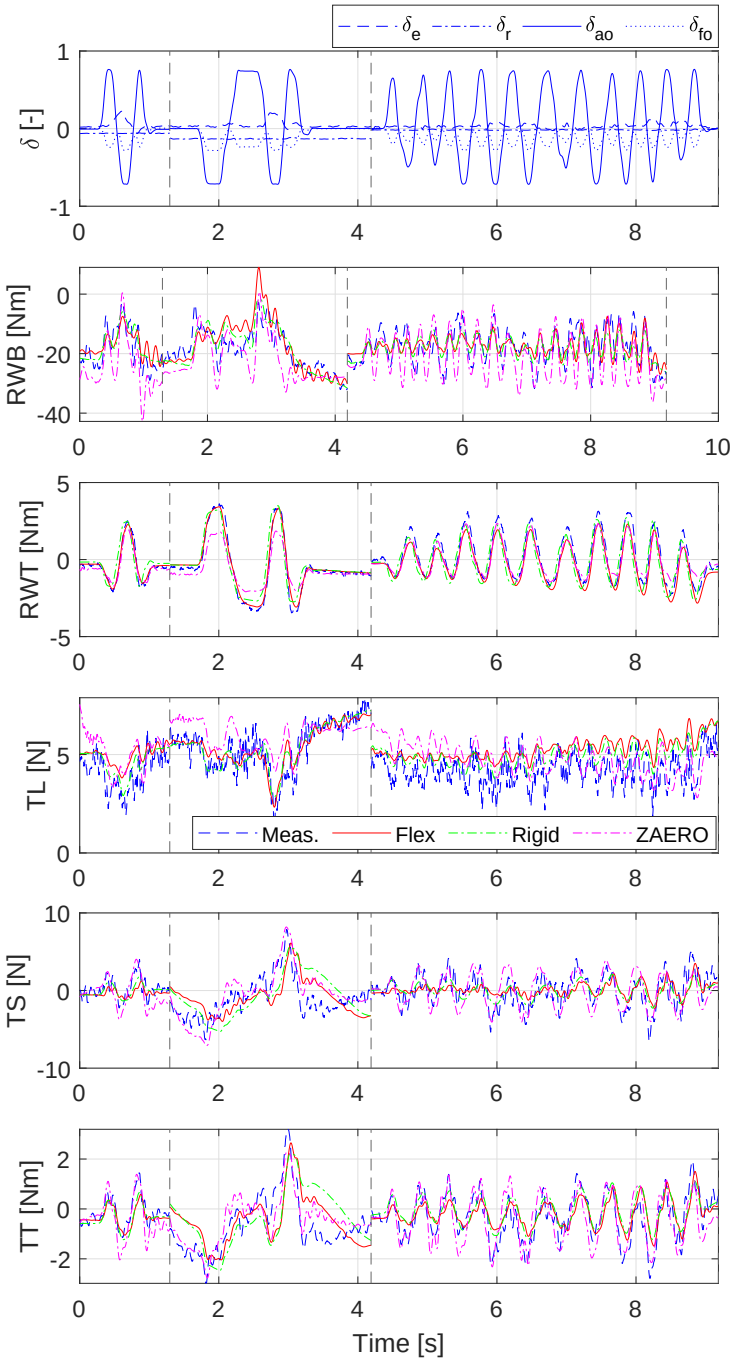

Figure 5.30: Aileron excitation response simulations - load responses.

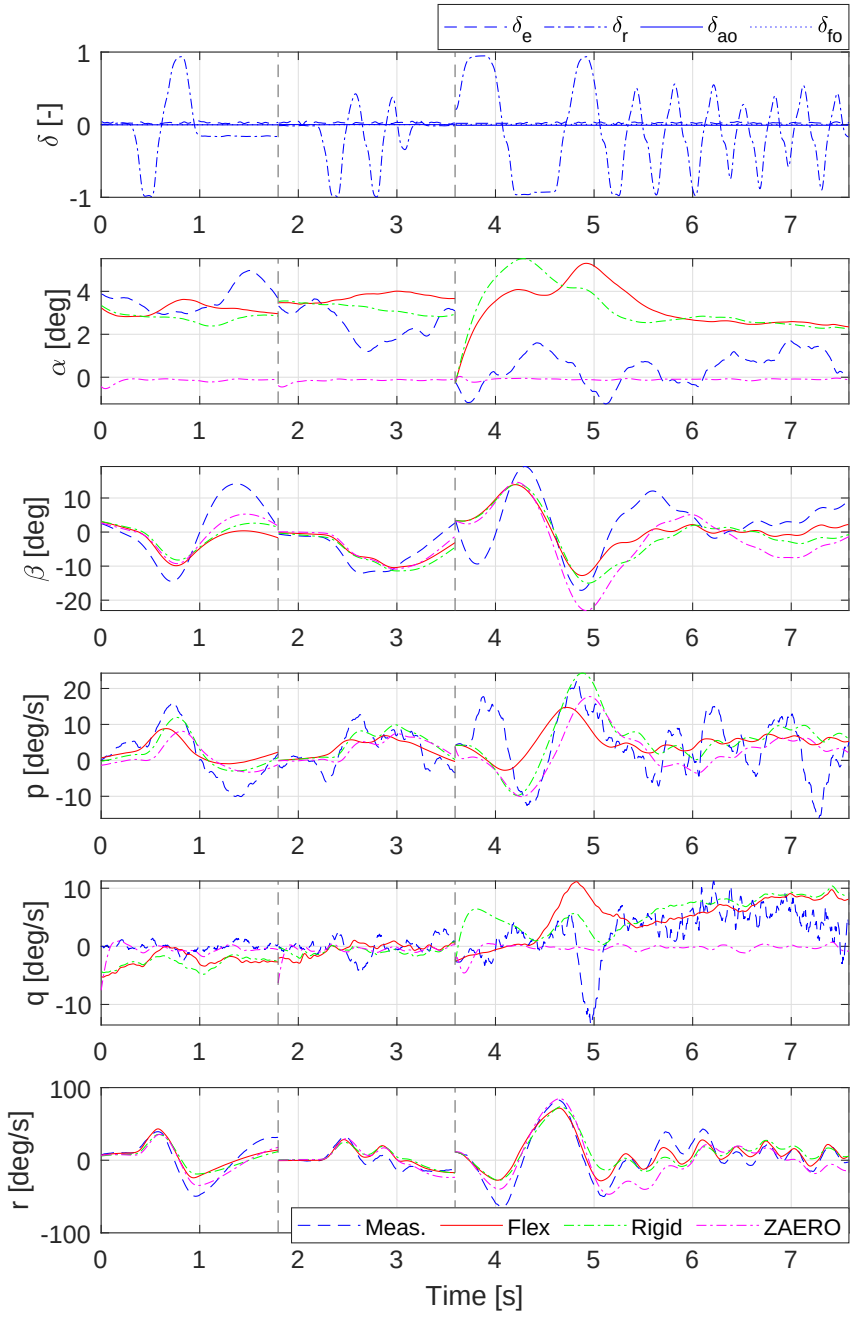

Figure 5.31: Rudder excitation response simulations - rigid body responses.

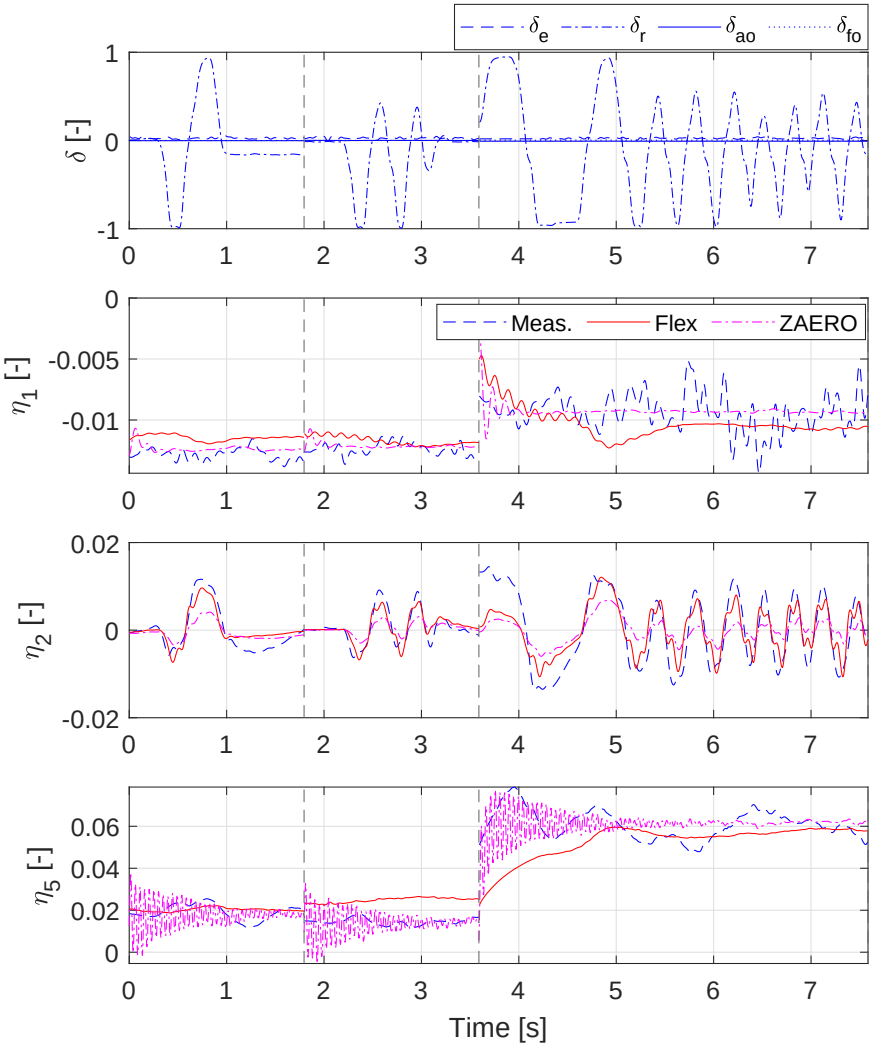

Figure 5.32: Rudder excitation response simulations - modal responses.

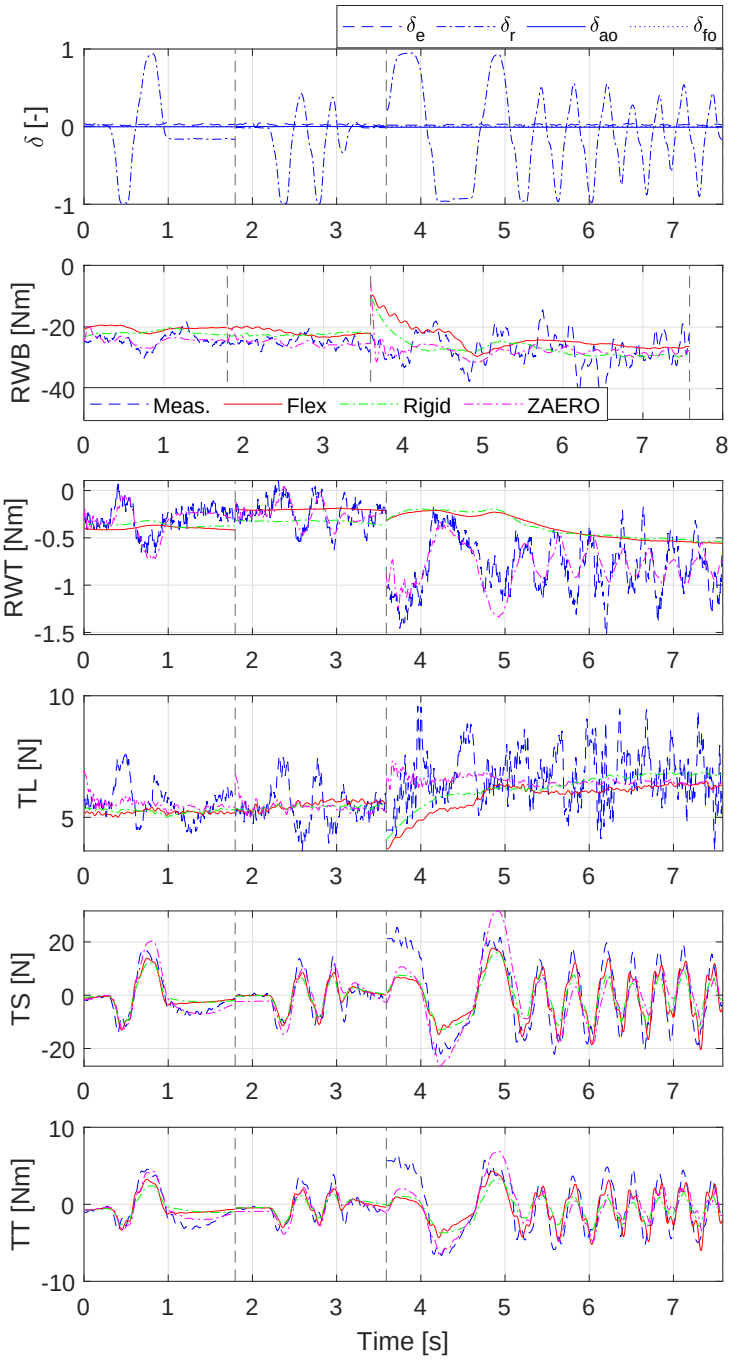

Figure 5.33: Rudder excitation response simulations - load responses.

5.A.5. MODEL PARAMETER CONTRIBUTIONS

In this section, the individual contributions of all flexible model parameters are plotted for three validation manoeuvres in which all control surfaces were excited simultaneously. This provides a clear visualisation of the contribution of each parameter to the overall modelled coefficient.

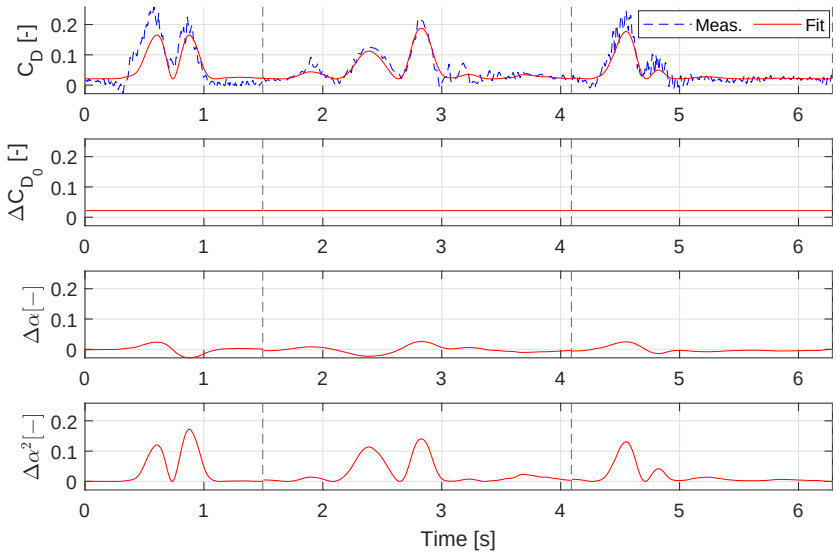

Figure 5.34: Individual parameter contributions to CD coefficient.

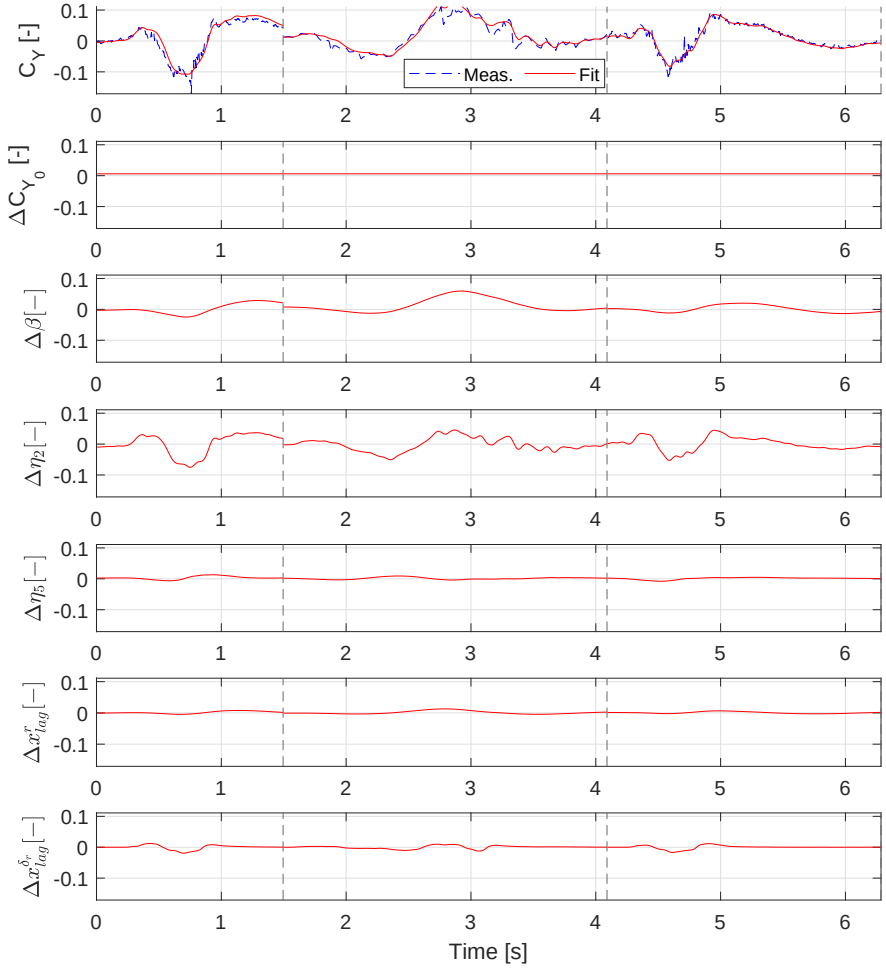

Figure 5.35: Individual parameter contributions to CY coefficient.

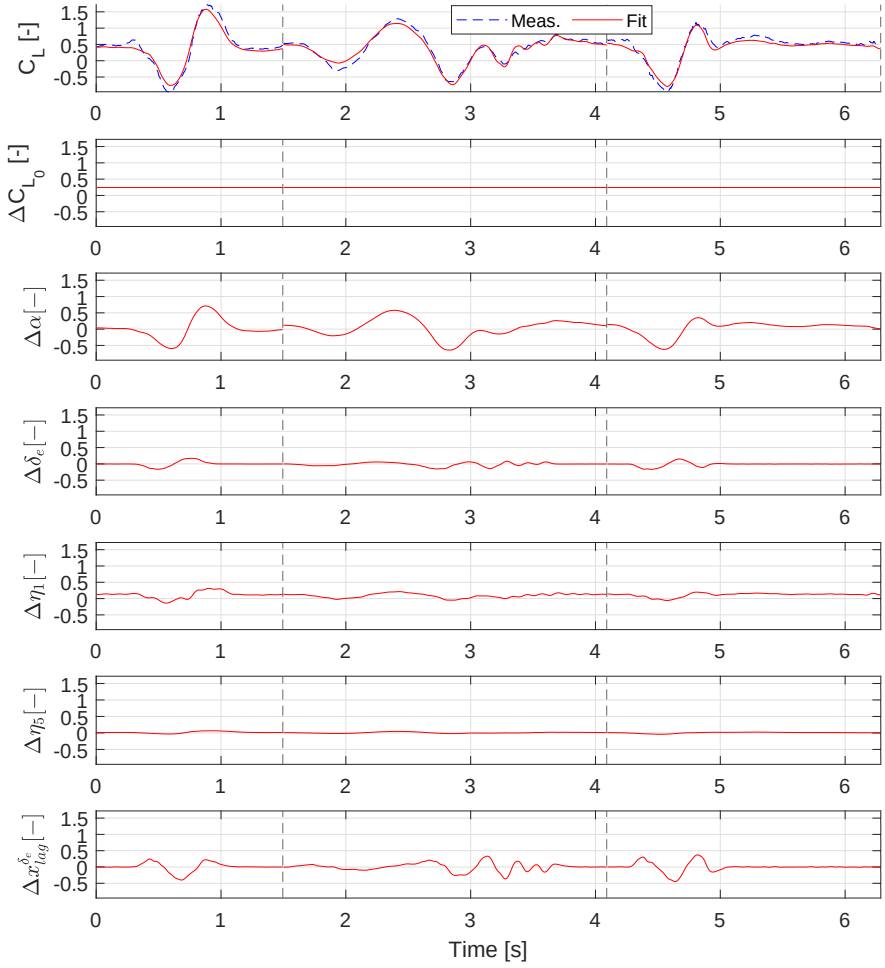

Figure 5.36: Individual parameter contributions to CL coefficient.

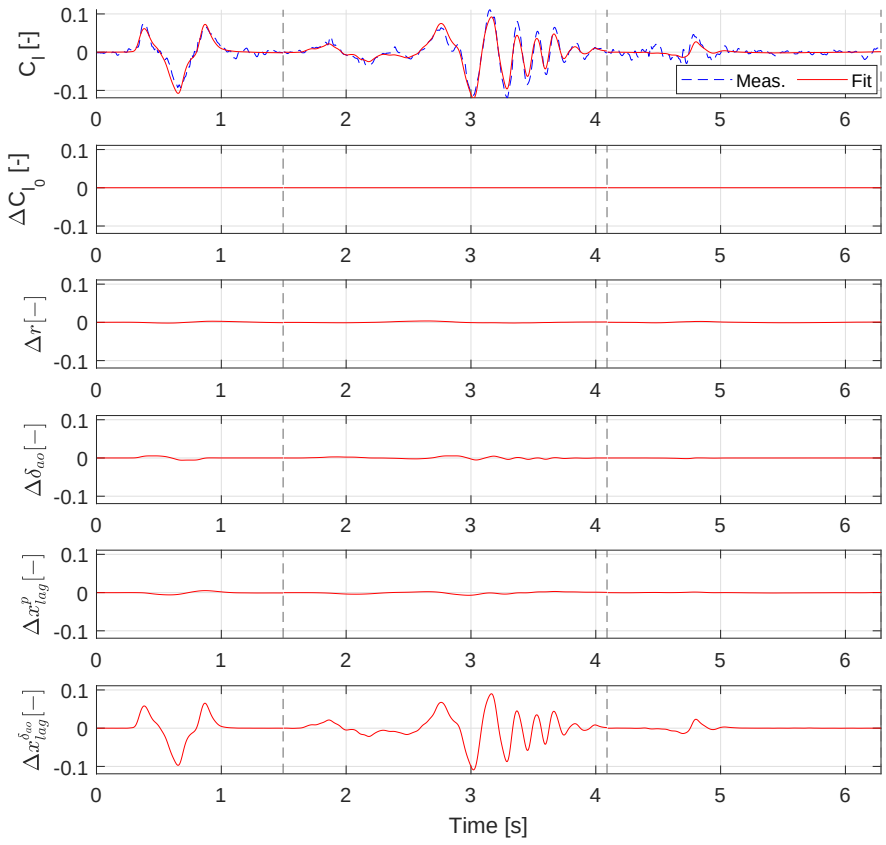

Figure 5.37: Individual parameter contributions to Cl coefficient.

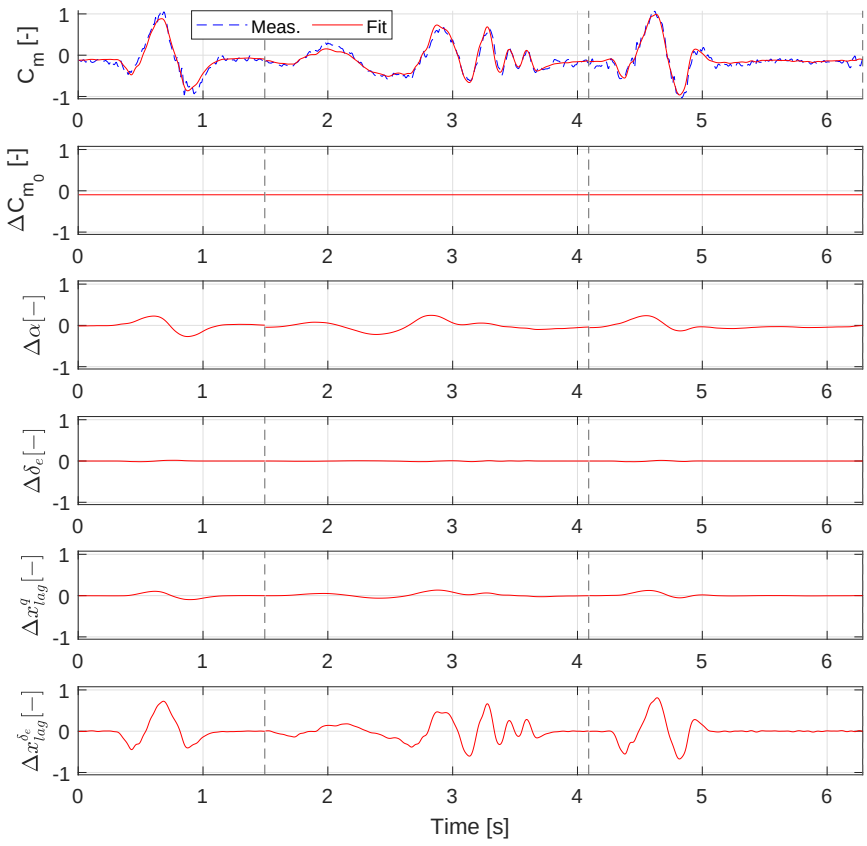

Figure 5.38: Individual parameter contributions to Cm coefficient.

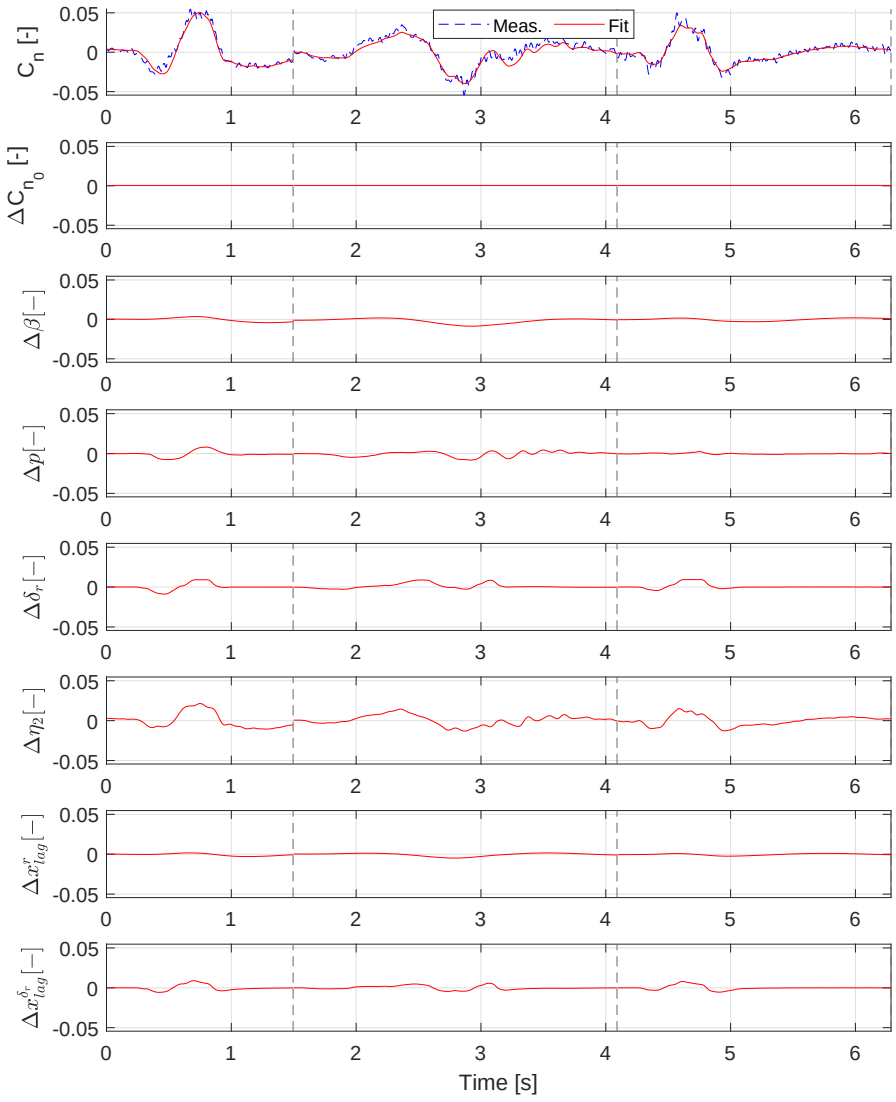

Figure 5.39: Individual parameter contributions to Cn coefficient.

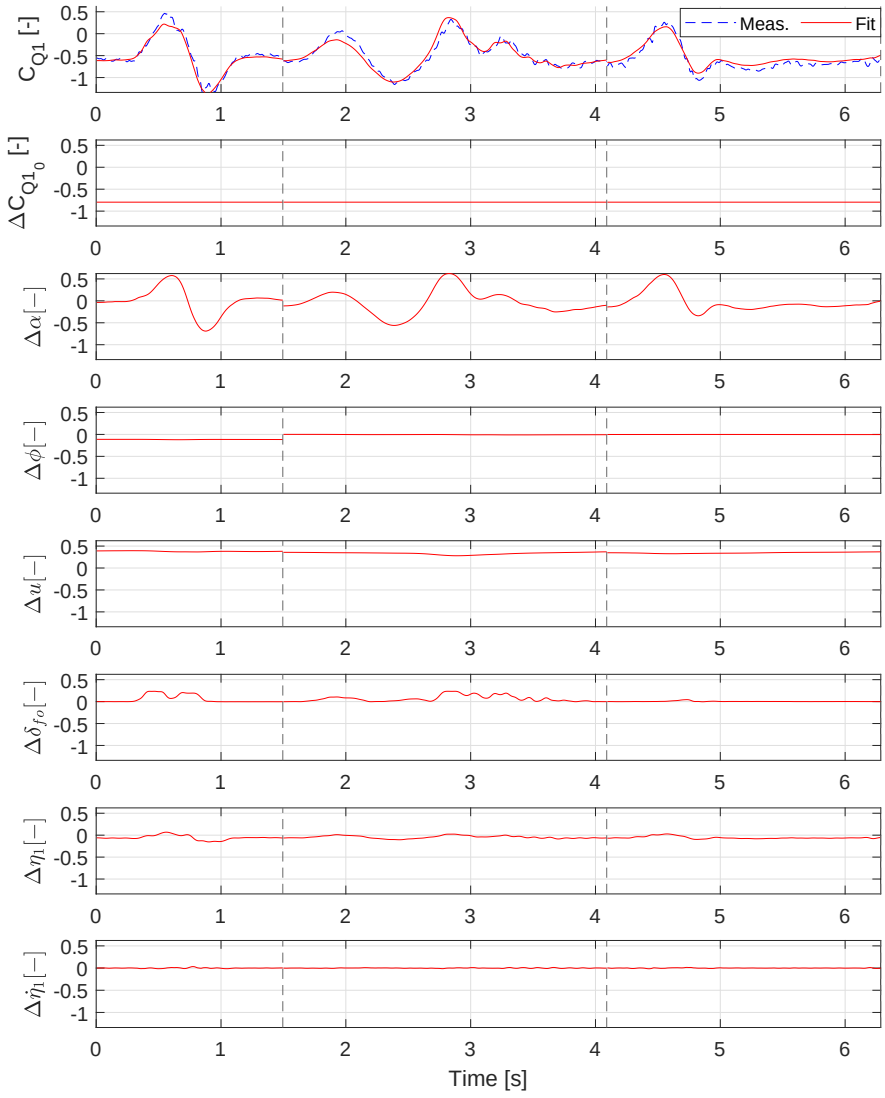

Figure 5.40: Individual parameter contributions to C_{Q1} coefficient.

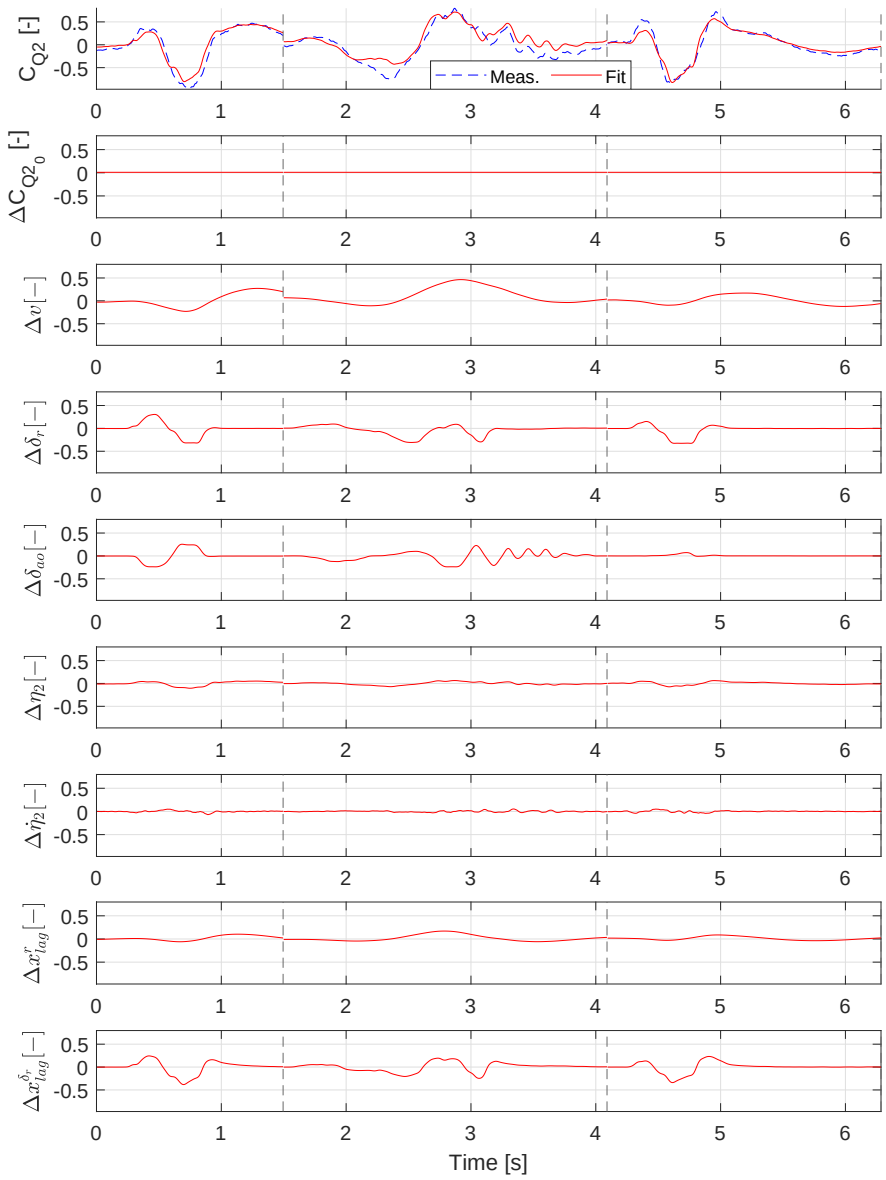

Figure 5.41: Individual parameter contributions to C_{Q2} coefficient.

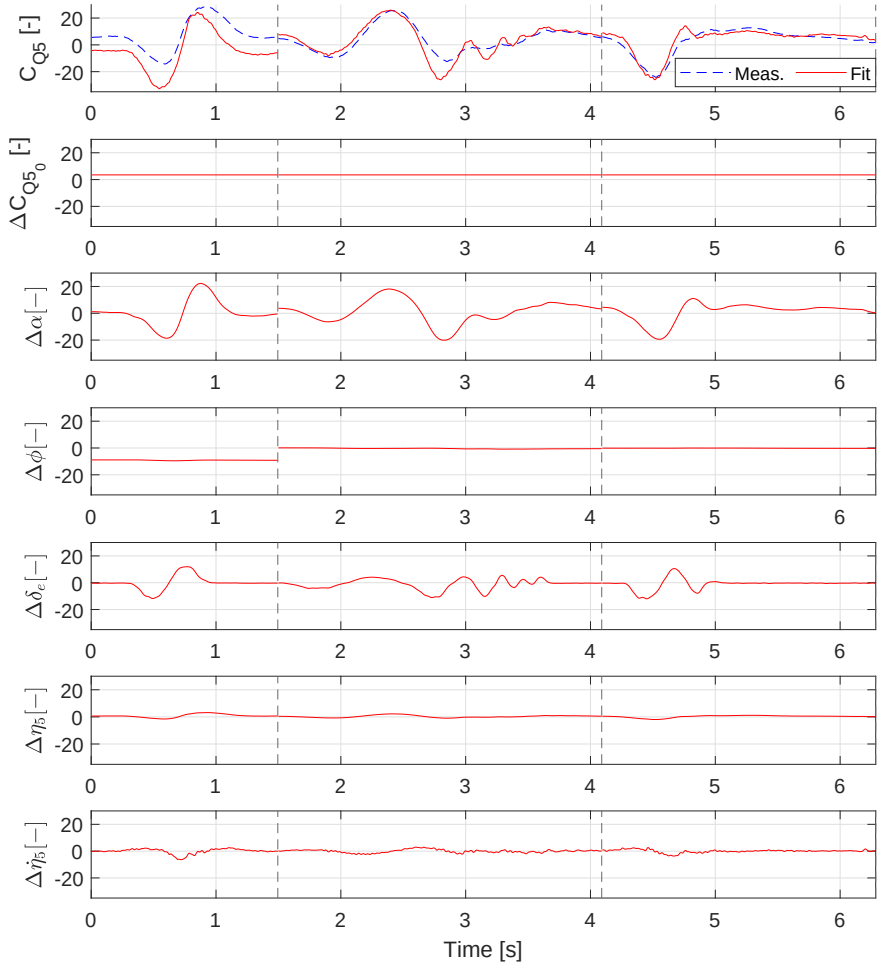

Figure 5.42: Individual parameter contributions to C_{Q5} coefficient.

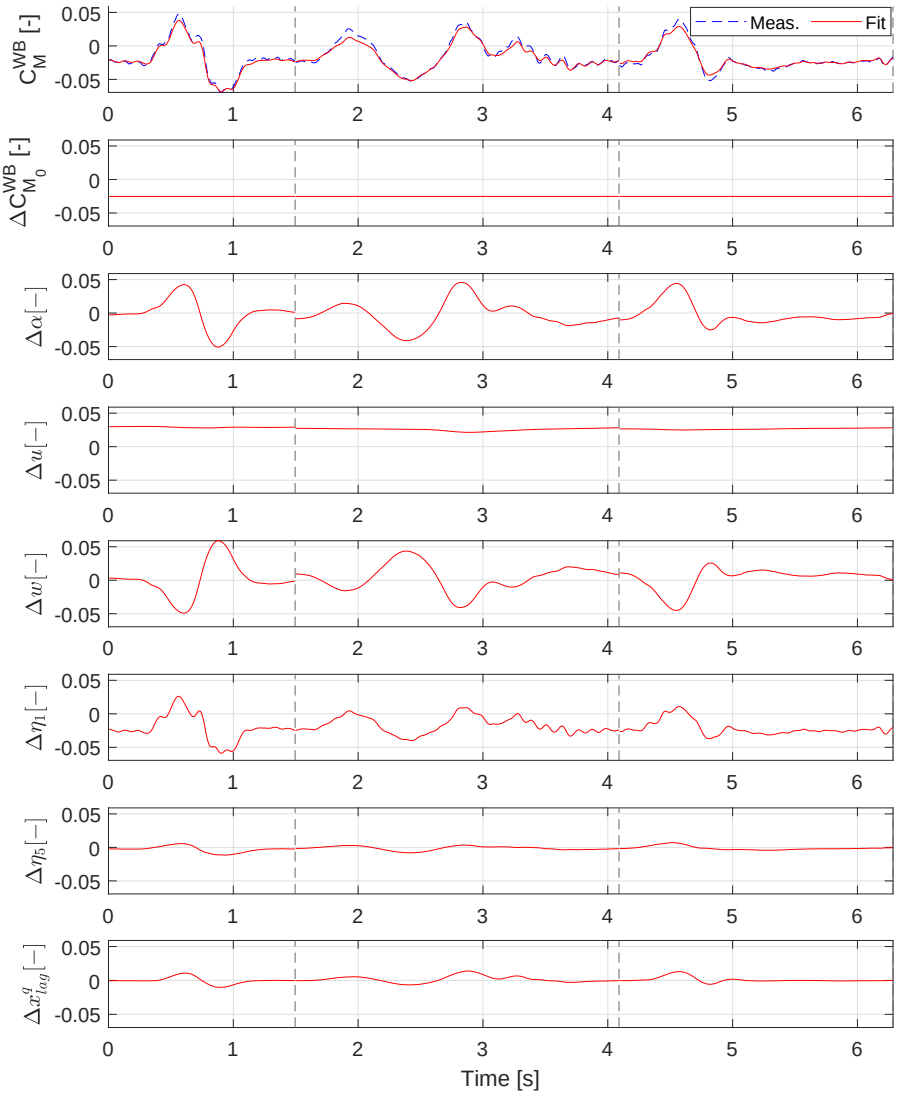

Figure 5.43: Individual parameter contributions to C_M^{WB} coefficient.

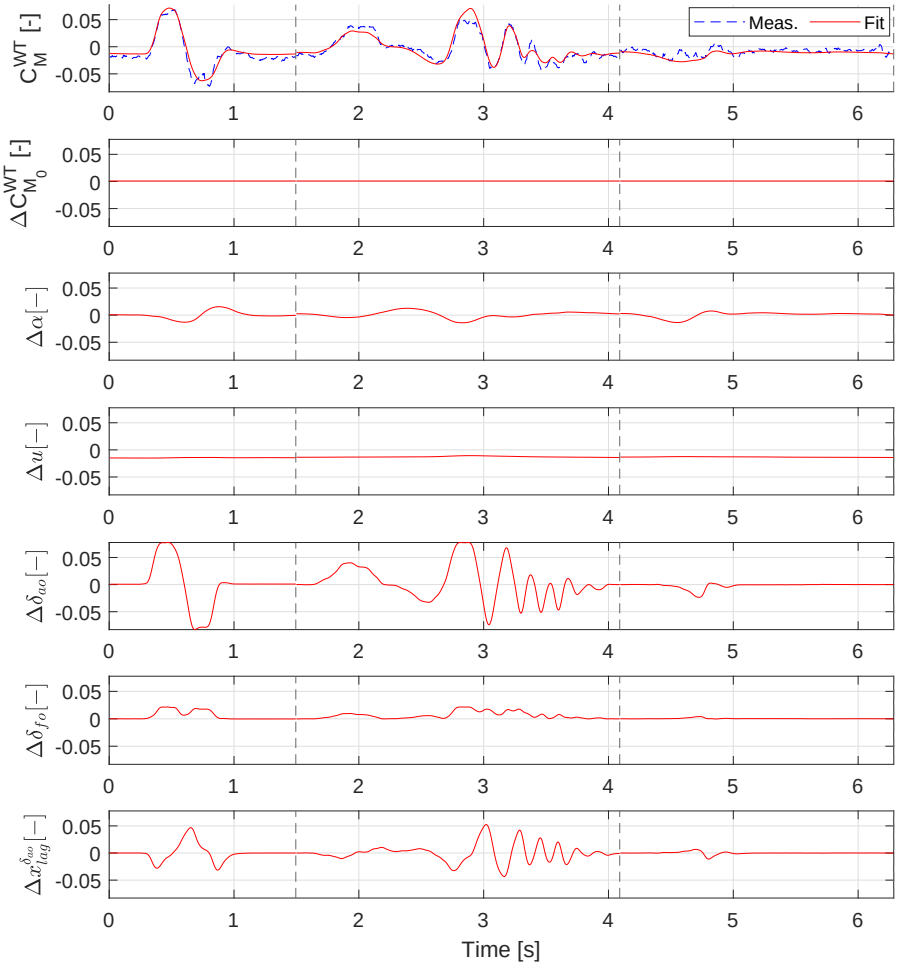

Figure 5.44: Individual parameter contributions to C_M^{WT} coefficient.

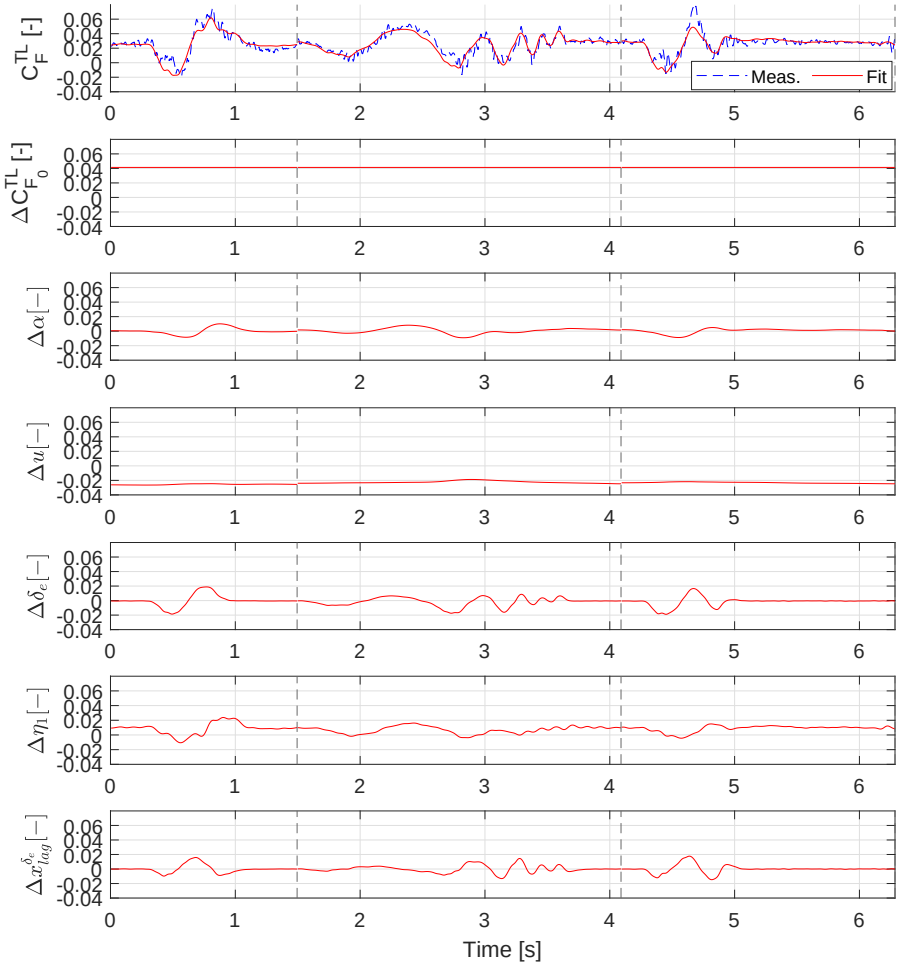

Figure 5.45: Individual parameter contributions to C_F^{TL} coefficient.

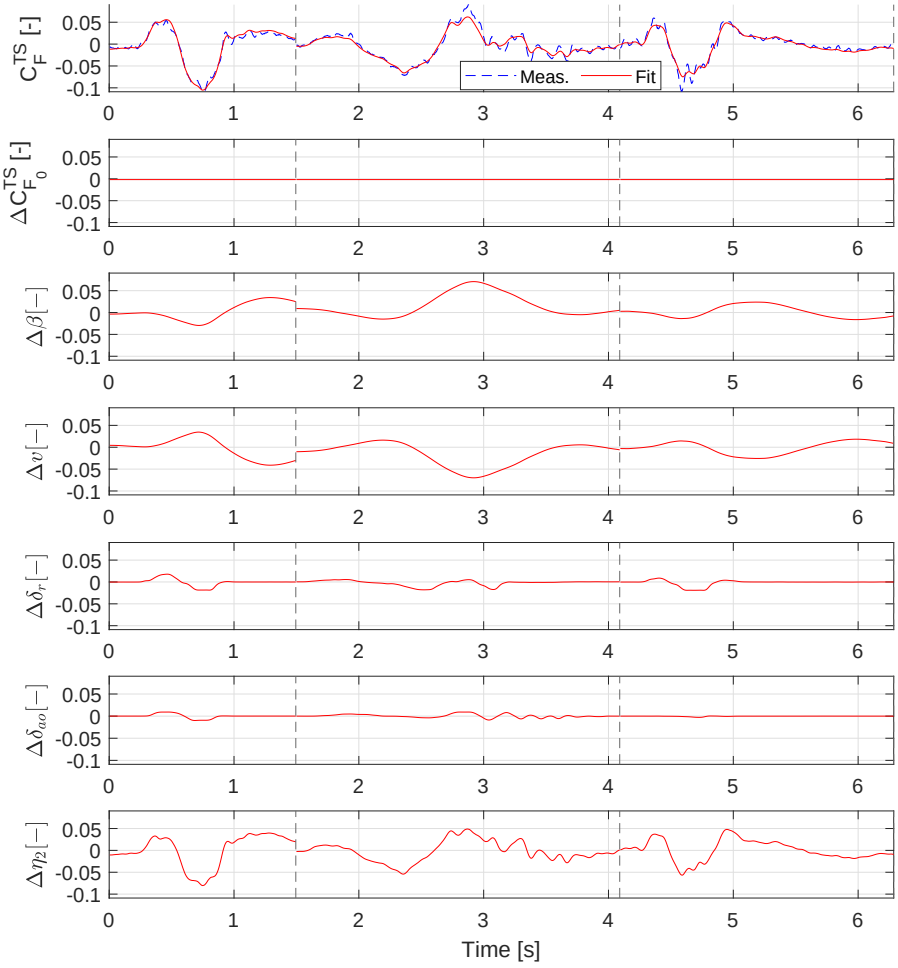

Figure 5.46: Individual parameter contributions to C_F^{TS} coefficient.

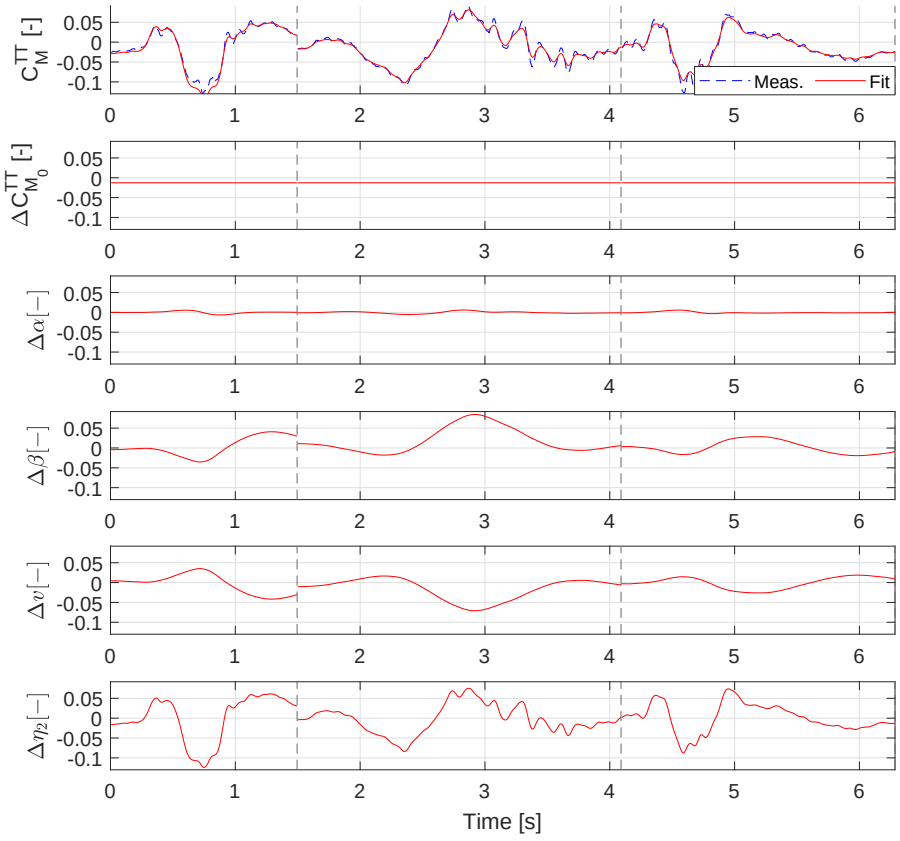

Figure 5.47: Individual parameter contributions to C_M^{TT} coefficient.

6

CONCLUSIONS AND RECOMMENDATIONS

6.1. CONCLUSIONS

This thesis aims at advancing the field of system identification for flexible aircraft by addressing the limitations of existing methodologies in capturing the effects of structural dynamics and unsteady aerodynamics. Traditional approaches assume that the aircraft is rigid and decouple the flight dynamics and the structural dynamics. More recent approaches have explored methods to also include structural dynamics in the identified models. However, these methods assume quasi-steady aerodynamic models which neglect the delays in the aircraft responses caused by unsteady aerodynamics and therefore can result in models with reduced accuracy and predictive capability. To address this research gap, the primary goal of this thesis was defined as follows:

> Develop a methodology for identifying a parametric flight dynamics and loads model from flight test measurements for a flexible aircraft that includes the effects of structural dynamics and unsteady aerodynamics.

The general conclusion of the work in this thesis can be summarised with the following response to the research goal:

> A methodology was successfully developed for identifying flight dynamics and loads models for flexible aircraft. This methodology is able to capture the aerodynamic influences of the aircraft structure as well as delayed effects related to the unsteady aerodynamics. The methodology was successfully demonstrated by identifying the flight dynamics model of a scaled Diana 2 glider unmanned aerial vehicle (UAV) together with a model for wing root and tail loads from collected experimental measurements. Incorporating structural dynamic and unsteady aerodynamic effects into the model resulted in an average

fitting accuracy of 86% for aircraft rigid-body responses and 88% for load responses, compared to 77% and 78%, respectively, for the model without these effects. The largest improvement of 29% was obtained for aircraft roll moment coefficient fitting by incorporating aerodynamic lag states related to aileron deflection. Over 15% improvement was achieved in the tail side force and torsion response predictions by including the structural mode related to tail roll motion.

To achieve this goal, four research questions were formulated in Chapter 1, each representing a specific challenge in the proposed identification approach.

The first research question together with the subquestions addressed the feasibility of using widely available consumer electronic sensors together with open-source software to conduct aeroelastic flight testing and improve the access to and availability of aeroelastic flight test data.

Research question 1:

How feasible is an open-source, low-cost sensor-based flight test system for capturing both rigid body and structural dynamic responses of an aeroelastic aircraft in flight?

Subquestions:

1. What sampling rates can be achieved with such a system?
2. What are the system's measurement capabilities in terms of the number and types of responses captured, as well as its impact on aircraft weight and power consumption?
3. How accurately can the system estimate modal parameters, including natural frequencies, damping ratios, and mode shapes?
4. What are the required sensor accuracy and noise statistics for aeroelastic flight testing?

This research question is addressed in Chapter 2, where a low-cost flight test instrumentation system tailored for aeroelastic research was developed and validated. The system was built using widely available consumer electronics hardware such as Raspberry Pi 4, Pixhawk 4, and Teensy 4 development boards. A wide range of sensors were integrated to the scaled Diana 2 glider test aircraft such as accelerometers, gyroscopes, strain gauges, pressure and temperature sensors and rotary encoders all of which needed to be carefully calibrated to ensure high quality of measurements. The developed flight test system achieved sampling rates exceeding 400 Hz for accelerometers and gyroscopes and over 200 Hz for strain gauges, which is necessary to be able to capture the high frequency oscillations of the structure. The entire DAQ system is very lightweight with the integrated hardware adding only 500 g of additional mass to the aircraft while also having a low power consumption of 16W which makes it suitable for

UAVs. Over 130 different flight parameters were successfully recorded during testing, ranging from aerodynamic angles and structural responses to loads at critical aircraft locations.

The system's capabilities were further validated during ground vibration testing (GVT) of the scaled Diana 2 glider in Chapter 3, where the first 12 structural modes were identified using integrated accelerometer, gyroscope and strain gauge measurements. Natural frequency estimates matched external reference accelerometer and Finite Element Method (FEM) model predictions, with discrepancies within 1%. Damping values also aligned closely, with variations of 1-2%, and mode shape comparisons achieved modal assurance criterion (MAC) values above 0.9 for most cases, demonstrating the system's sensitivity and accuracy. Although the required sensor accuracy depends on the specific test aircraft, the sensors used on the scaled Diana 2 glider were sufficient to capture structural modes up to 60 Hz. The modular system design, implemented via the open-source Robot Operating System (ROS), allowed quick and easy adaptability for different experimental setups such as capturing hammer impacts during the GVT. The combination of high sampling rates, accuracy demonstrated in GVT, low weight and power requirements and modular expandability highlights the feasibility and performance of the developed system for capturing aeroelastic responses. A thorough overview of the system and its capabilities together with published flight test datasets can serve as a reference for developing future aeroelastic flight test platforms and demonstrators.

Research question 2:

How can information from GPS, aeroprobe, accelerometers, gyroscopes and strain gauges be combined to simultaneously estimate the aircraft rigid body states and modal states?

In Chapter 4 an extension to the Flight Path Reconstruction (FPR) filter was developed to simultaneously reconstruct the rigid body states and the structural modal amplitudes and velocities of an aircraft. This approach is based on accelerometer, gyroscope, and strain gauge measurements collected across the aircraft structure, together with the displacement, rotation, and strain mode shapes of the modes to be reconstructed. This filter does not require a pre-existing flight dynamics or FEM model, and is therefore easier to implement as less information about the aircraft is needed beforehand.

The filter was tested using both simulated data and flight test measurements from a scaled Diana 2 glider UAV. Using simulated responses from an aeroelastic flight dynamics model, the filter was able to reconstruct the aircraft attitude and aerodynamic angles with less than 0.1 deg error from the noisy measurements as well as the modal amplitudes and velocities. The modal state estimates also showed to be insensitive to the number of modes included in the filter and to inaccuracies in the provided mode shapes. Larger errors in the reconstructed modes were observed for higher order modes, where the response amplitudes became smaller than the sensor noise. However, adding such modes to the filter

did not degrade the reconstruction of other modes.

When applied to flight test data, the rigid body state estimates were consistent with the results obtained using the standard FPR method. Furthermore, the sensor bias estimates were stable across multiple flight tests, and the modal amplitude and velocity estimates remained consistent while varying the number of included modes. The reconstructed modes were then used for modelling the aircraft aerodynamic forces and moments. The addition of these modes led to improvements in the response fitting accuracy which provided extra confidence that the filter was able to reconstruct meaningful states. Finally, the modal state estimates were further validated in Chapter 5, where good agreement was observed with open-loop simulation responses from a numerical model.

Research question 3:

How to estimate aerodynamic lag poles and reconstruct aerodynamic lag states from flight test response measurements?

Subquestions:

1. Is the first-order lag structure suitable for identifying aerodynamic lag dynamics from flight test data?
2. What adjustments to flight testing are required to estimate the aerodynamic lag states?

In Chapter 5, a novel method was developed to estimate aerodynamic lag poles, which characterise delays and changes in aircraft response amplitudes caused by unsteady aerodynamics, using flight test measurements. The aerodynamic lags were modelled using a first-order lag structure, which was found to be suitable for capturing these unsteady aerodynamic dynamics within the identification framework. By combining the estimated lag poles with the measured aircraft responses, the corresponding aerodynamic lag states could be reconstructed and used for modelling.

The proposed method involved introducing a delay to the measured aircraft state changes and determining the amount of delay that would produce a peak in correlation when compared to the measured force and moment responses, while also accounting for the airspeed dependence of the delay. The pole value corresponding to the delay that resulted in the peak correlation was then selected as the aerodynamic lag pole.

This process was applied on the flight test measurements collected using the scaled Diana 2 glider UAV. The identified lag poles matched the values of Jones's approximation for 2D airfoils. As the high aspect ratio wings of a glider correspond well to a 2D case, this validated the proposed approach and enabled the inclusion of unsteady aerodynamic effects in the modelling process.

During flight testing, the starting airspeed for excitation manoeuvres was chosen to be around 20-25 m/s which would place the first structural mode and control surface motion within the range of targeted reduced frequencies

of 0.15-0.3. At these reduced frequencies, the Theodorsen model shows the largest phase shifts between the quasi-steady and unsteady aerodynamic forces. No specialised excitation manoeuvres were conducted. Instead, the flight test excitations consisted of traditional impulse, doublet, 3211, and frequency sweep manoeuvres.

Research question 4:

How much are the identified model predictions improved by incorporating structural dynamics and unsteady aerodynamic effects in the model?

Subquestions:

1. What is the improvement in aerodynamic force and moment coefficient predictions?
2. What is the improvement in wing root and tail load predictions?

Using the collected flight test response measurements, two models for the flight dynamics and loads were identified for the scaled Diana 2 glider UAV: a ”rigid” model, considering only rigid-body responses and control surface dynamics, and a ”flexible” model, which included the effects of aerodynamic lag states and structural modes.

The model parameters were estimated using ordinary least squares (OLS) regression. This method was chosen for its simplicity, low computational requirements, and ability to be applied without prior knowledge about the aircraft to initialize parameters.

On average, the flexible model achieved around 10% improvement in the fitting results compared to the rigid model by including the structural modes and aerodynamic lag states in the model. The largest improvement of 29% was obtained in the aircraft roll moment coefficient by the addition of the aerodynamic lag state corresponding to the aileron deflections. This highlighted the importance of including unsteady aerodynamics in the model identification procedure. Over 15% improvement in the tail side force and torsion responses was obtained compared to the rigid model by the inclusion of the tail roll structural mode.

Finally, the identified models were validated through open-loop simulations, where the simulated responses were compared with flight test measurements. The identified models successfully captured and predicted the aircraft’s rigid-body motions, structural dynamics, and the loads acting on the wing roots and tail. The flight test measurements and flexible model predictions were also compared with numerical simulation model results. The agreement in the modal amplitude responses demonstrated that the identification process was able to accurately estimate and model the modal states from flight test measurements.

6.2. Recommendations

In this section, the recommendations are presented to continue and further advance the methods and tools presented in this thesis. The limitations of the developed approach are discussed and suggestions are made to generalise the approach further and cover more cases. These recommendations are grouped into three main categories.

First, recommendations for the flight test platform are presented in Section 6.2.1 that focus on enhancing the reliability, automation, and usability of the system to maximize the effectiveness of future testing campaigns. Second, in Section 6.2.2, suggestions for expanding the identification framework are provided to generalise the approach, enabling it to capture a broader range of flight conditions and aircraft configurations while addressing more complex dynamics. Finally, in Section 6.2.3, potential applications of the identified models are outlined, highlighting how the insights and tools developed in this work could be leveraged for structural health monitoring, control law synthesis, and pilot training simulations.

6.2.1. Flight Test Platform

To advance the capabilities of the scaled Diana 2 glider and its flight test system, several improvements can be made to enhance reliability, streamline procedures, and expand the testing capabilities. As pointed out in Chapter 5, the flight test system would occasionally have segments where some sensor measurements were missing. As a result, the corresponding flight manoeuvres could not be used for modelling and additional time might be needed for flight testing. Therefore it is important to determine the root cause of this issue and implement a solution to improve the system reliability and efficiency of the testing procedure.

Currently the flight manoeuvres were constrained to the ones that could be manually executed by the pilot. Consequently, it was not possible to accurately control the excitation frequencies or amplitude. Therefore, it is recommended to implement an automatic flight test excitation system that is capable of performing predefined manoeuvres and excitation sequences, such as sine sweeps and orthogonal multisines. This system would improve test reproducibility and allow to excite a broad range of frequencies or target specific modes and reduced frequencies, potentially enhancing modelling accuracy especially at higher frequencies.

The system could also be extended with additional sensors, such as cameras, allowing to explore alternative approaches like vision-based tracking of structural deformations, which would allow for a direct comparison with the methods and accuracy presented in this work.

To further mature the flight test system, the existing tools for system initialization and data collection can be expanded and refined. By automating tasks such as sensor startup verification, test setup and data acquisition initialization, the system can become easier to use, reducing operator workload and minimizing the potential for human error. Real-time monitoring functionality should also

be incorporated to provide immediate feedback on system performance during flights. This would enable the detection of errors or malfunctions early, preventing unnecessary test flights and wasted resources. In addition, providing clear and comprehensive documentation would allow new users to quickly get familiar with the system and start operating, particularly for users without prior knowledge of ROS.

By implementing these recommendations, the flight test platform can be transformed into a more reliable, automated, and versatile system capable of executing advanced flight test sequences.

6.2.2. Expanding the identification framework

To further develop and generalise the identification approach presented in this thesis, several recommendations are proposed to broaden its applicability to a wider range of flight conditions and aircraft configurations. As discussed in Section 5.5, the identified flight dynamics and loads models included contributions from the structural modes. However, the most significant effects were limited to three structural modes, with minimal interaction between them.

A key recommendation is to test the identification approach on an aircraft that exhibits stronger coupling between rigid body responses and structural dynamics. Specifically, this involves scenarios where the structural modes exhibit larger amplitude responses which would also result in increased influence on the aerodynamic forces and moments. Furthermore, the aim should also be to increase the interaction between structural modes and aerodynamic lag states to have aircraft rigid body responses fully coupled with structural dynamics and unsteady aerodynamics. These conditions would present a more complex and challenging test case for identification, helping to evaluate the robustness and performance of the method. For the scaled Diana 2 glider, these conditions could be achieved by adding mass to the wingtips, which would lower mode frequencies and increase the amplitude of structural responses during excitation manoeuvres. This adjustment would increase the coupling between structural dynamics and rigid body motion, enabling a more comprehensive evaluation of the identification framework.

In Section 5.5, constraints were applied to the generalised forces associated with the structural modes to ensure that the identified model would be stable and the modes would not be self-exciting. However, as the coupling between modes becomes stronger, where the response of one mode influences another, it may become necessary to introduce additional constraints on the associated coefficients. Furthermore, fitting all structural modes simultaneously under these conditions could help ensure the stability of the system as a whole.

The flight tests conducted in this thesis were limited to conditions with constant aircraft mass and inertia at low airspeeds and it was assumed that the structural mode shapes in flight remain close to the GVT mode shapes. To generalise the identification approach further, it should be extended to account for varying aircraft mass, such as changes due to fuel burn, and for a wider range of dynamic pressures. Both factors alter the mode shapes during flight, necessitating

adjustments to the state estimation and model identification procedures. By addressing these variations, a global model could be developed, capable of accurately representing the system across a broader range of aircraft mass configurations and operating conditions.

To address even more complex and nonlinear cases, the identification framework could incorporate scenarios where aircraft inertia is no longer constant during manoeuvres due to significant structural deformations. Nonlinearities such as large structural deflections, stall and transonic aerodynamic effects could also be integrated into the modelling process. These extensions would significantly increase the scope and applicability of the identification approach.

Finally, an uncertainty quantification study should be carried out on the identified models and the identification approach presented in this thesis. Such a study would allow to evaluate how variations in parts of the model, such as the structural modes obtained from GVT, propagate through the identification process and influence the final model predictions.

6.2.3. Applications of identified models

Flight-validated models capable of accurately describing and predicting the responses of a flexible aircraft and the loads acting on its structure have a wide range of practical applications. One potential area for continuing this thesis work is in the field of aircraft Structural Health Monitoring (SHM). SHM involves continuously monitoring an aircraft's structural condition to optimize maintenance schedules, enhance safety and reliability, and extend the aircraft's lifespan. Flight-validated flight dynamics and loads models provide insights into the forces acting on the aircraft during operation, enabling more informed maintenance decisions. By periodically identifying these models for individual aircraft, potential issues can be detected early by observing changes in model parameters.

In the current approach, the aircraft modal parameters were obtained from a GVT. An alternative method is Operational Modal Analysis (OMA), which estimates modal parameters directly from operational data. OMA eliminates the need for costly, separate ground tests by using measurements taken during regular operations which aligns well with SHM. For accurate identification, however, distinguishing structural contributions from aerodynamic effects in the response data remains a challenge. A promising approach could be to use the measurements from aircraft taxiing to perform the OMA [1] [2] as the aerodynamic contributions would then be minimal.

Another key area for continuing research is the development of active load alleviation control laws. These control laws use internal models and sensor measurements to compute control surface commands that would reduce peak

[1] K. I. Soal, Y. Govers, M. Böswald and A. Vollmer. "Taxi vibration testing: A new and time efficient procedure for the identification of modal parameters on aircrafts". In: International Forum on Aeroelasticity and Structural Dynamics 2019, IFASD 2019.

[2] M. Böswald, J. Schwochow, G. Jelicic and Y. Govers. "New Concepts for Ground and Flight Vibration Testing of Aircraft based on Output- Only Modal Analysis". In: 7th International Operational Modal Analysis Conference, IOMAC 2017, pp. 15-34.

structural loads during manoeuvres or gust encounters. They can also improve handling qualities by suppressing structural vibrations, thereby also enhancing passenger comfort. The scaled Diana 2 glider and its identified models could serve as a platform to design and test these control laws in flight, further expanding the capabilities of the flight test system. This would also provide an opportunity to assess the suitability of the identified models for control law synthesis. Moreover, adaptive control laws could be explored, leveraging the least squares fitting approach to continuously tune and update the models in real-time.

Finally, flight simulators can greatly benefit from these identified models. Simulators play a vital role in pilot training by providing a safe environment to practice various scenarios. To ensure training effectiveness, it is crucial that simulators accurately replicate the behaviour of the real aircraft. By incorporating structural dynamics and unsteady aerodynamic effects into the simulator models, the response characteristics of the aircraft can be more accurately represented. These structural dynamics and delays related to unsteady aerodynamics can also result in unfavourable pilot-aircraft interactions that could then be assessed in flight simulator training.

ACKNOWLEDGEMENTS

This PhD has been a long and rewarding journey, carried out over several years within the Flight Physics and Loads department at the Royal Netherlands Aerospace Centre, in close collaboration with the Aerospace Structures and Materials group at Delft University of Technology. Along the way, I had the chance of working with many people, without whom this work would not have been possible.

First and foremost, I would like to thank my promotors, Roeland De Breuker and Coen de Visser. Your expertise in aeroelasticity, system identification, and state estimation has been an excellent resource throughout this research. Your insights and constructive feedback continuously challenged me to improve the quality and rigour of my work. At the same time, I appreciated that our discussions were always held in a relaxed and open atmosphere, where we could talk about anything and there was even room for some of my silly jokes.

I am especially grateful to my daily supervisor, Bart Eussen, for his guidance, patience, and countless discussions. You have taught me that being a great engineer is not about having all the answers, but about asking the right questions. Your extensive experience in aircraft flight testing has been instrumental throughout this project.

I would also like to thank my department managers Onno Bartels and Kees Wijnberg for providing me with the opportunity to pursue this PhD at NLR and for their continued support. Your confidence in me, especially during challenging moments, and your efforts in securing the necessary resources made this work possible.

My workplace was made enjoyable and fun by my dear colleagues - Huub, Jos, Stevie-Ray, Peter, Jasper, and many others. Whether it was technical discussions or more ”essential” topics such as culture, language, or cuisine, your support and camaraderie have meant a great deal. A special acknowledgement goes to Jan-Willem for piloting the Diana 2 during the flight test campaign. Your skills and calmness in critical situations saved us from many tricky moments and kept this research airborne.

I would also like to thank my fellow PhD students at NLR. In particular, Jan-Sören who was perhaps the only true ”9-to-5” colleague I will ever have and my multi-talented office mate who could assist with anything from live German translations to constructing professional-grade transport boxes in a spare weekend. Iren, thank you for the many discussions on control laws and aeroelasticity theory as well as for sharing the day-to-day ups and downs of the PhD journey.

At TU Delft, I was fortunate to be part of a vibrant and inspiring research

environment. I would like to thank Sherry and Jurij for their insights and engaging discussions on wind tunnel testing, aeroelasticity and load control and much more. I am also grateful to my fellow PhD candidates Tigran, Mario, Darwin, Natalia, Yasir, Paul, and many others, who are all talented researchers and created an inspiring atmosphere where we all could grow and learn.

I am also deeply thankful for the support of my friends in Estonia, in the Netherlands and beyond. Konsta and Marina, thank you for being my early-morning gym motivators, as well as wonderful hosts for countless dinners, board games, and relaxed weekends including our pig-watching excursions. My hometown boys, Asko, Hendrik, and Jakob - thank you for warming both body and mind during our Christmas sauna gatherings and throughout the year. Jörgen, Siim, and Sander, thank you for the many gaming and rambling sessions that provided a much needed way to unwind. Daniel, Jüri-Mikk, and Karl-Martin, thank you for our yearly wilderness retreats and for introducing me to many new kinds of sports and hobbies.

I would also like to thank Egelyn and Karl-Martin for playing a key role in guiding and inspiring me throughout my studies, and for helping bring me to the Netherlands and supporting my transition to life abroad.

Above all, I am grateful to my family. To my parents, Pille and Alar I want to thank you for your unconditional support and for always encouraging me to pursue my ambitions. From leaving home at the age of 16 to study in Tallinn, to moving abroad for university, you have always found ways to make it possible. I am also grateful to my grandparents for their love and for their efforts to understand what kind of ”model aeroplanes” I have been working on all these years.

Finally, to Eliis, my closest companion throughout this journey. Thank you for your unwavering support, for listening to my endless streams of ideas and half-formed thoughts. I look forward to sharing many more concerts, travels, and hikes together in the years to come. To Mango and Rosin, my silent supervisors, who have spent countless hours by my side or on my keyboard, occasionally contributing a paw stroke or two to this dissertation.

Andres Jürisson
Leiden, May 2026

CURRICULUM VITæ

Andres Jürisson

Andres Jürisson was born in Pärnu, Estonia, on 20^{th} October 1993. He graduated from Tallinn Secondary Science School (Tallinna Reaalkool) in 2013. In the same year, he enrolled in the Aerospace Engineering bachelor program at the Faculty of Aerospace Engineering at Delft University of Technology. After completing his degree in 2017, he continued his studies in the Systems and Control master's program at the Faculty of Mechanical Engineering at Delft University of Technology.

In July 2018, Andres obtained his MSc degree for his research project, titled "Optimal trajectory tracking control design - Emulating fighter aircraft flight test tracks with nonlinear model predictive control." This project, carried out in collaboration with the Royal Netherlands Aerospace Centre (NLR), involved the development of a nonlinear model predictive controller combined with a feedback linearization controller, applied to an F-16 fighter jet model to track aerobatic flight test reference manoeuvres in a simulation environment.

In September 2018, Andres began his PhD research at the Flight Physics and Loads Department at NLR, in collaboration with the Department of Aerospace Structures and Materials at Delft University of Technology.

In April 2023, Andres started as a Research and Development Engineer at the Flight Physics and Loads Department at NLR focusing on aeroelastic aircraft modelling and developing control laws for load alleviation.